In situ Photochemistry on a Benchtop NMR Spectrometer with *p*H_2 Hyperpolarisation

Alastair David Robinson

Doctor of Philosophy

University of York

Chemistry

September 2022

Abstract

High-resolution benchtop NMR spectrometers are uniquely suited for reaction monitoring applications, owing to their portability and accessibility, but the low inherent sensitivity of the approach can limit the observation of low-concentration transient species. In this work, a hyperpolarisation technique called *para*hydrogen induced polarisation (PHIP) was employed to overcome this limitation and observe both thermal and photochemical reactivity.

The developed PHIP hyperpolarised reaction monitoring procedure enabled quantitative analysis of the oxidative addition of H_2 to *trans*-[IrCl(CO)(PPh_3)$_2$], with a k_2 rate constant of (0.89 ± 0.03) $dm^3\,mol^{-1}\,s^{-1}$ showing excellent consistency with established literature. The method was validated against several key experimental parameters (including temperature and relaxation) to establish it as a robust route to accurately monitor reactions at low-field.

Through integration of low-cost *ex situ* and *in situ* photochemistry setups that utilise broadband UV sources, the photochemistry of metal dihydrides (M = Ir, Ru) was explored on a benchtop NMR spectrometer for the first time. Implementation of a photochemical pump - NMR probe method with the *in situ* photochemistry setup allowed observation of photochemistry on the micro-to-millisecond timescale enabling the observation of short-lived hyperpolarised *cis*−[Ru(H)$_2$(dppe)$_2$] (with a hyperpolarised T_1 of (250 ± 20) ms). This setup was employed to detect coherent magnetic evolution of metal complexes formed from addition of *para*hydrogen which has only been observed previously using a laser within a high-field NMR setup. Magnetic evolution was observed for *cis*−[Ru(H)$_2$(dppe)$_2$], [Ru(H)$_2$(CO)$_2$(dpae)], [Ir(H)$_2$(CO)(PPh_3)$_2$I] and [Ir(H)$_2$(^{13}CO)(PPh_3)$_2$I] indicating the viability of a low-cost, benchtop NMR alternative to currently established practices.

Contents

List of Tables

List of Figures

Acknowledgements

I would like to thank my PhD supervisors Dr. Meghan Halse and Prof. Simon Duckett for giving me the opportunity to untake this research project and for all the support and guidance that you have given during my time at the University of York. I am a better researcher today for everything that I have learnt while in your research groups.

To members of CHyM and the MEH research group from past and present, thank you for making my time doing research at York such an enjoyable experience and for all the support you have given along the way. Thank you to Liz, Jenny, Ben, Emma, Denise, Lyndsay, Marianna, Aneurin, Vicky, Marie, Frida, Matt, Helena, Pavan, Alex, Callum, Olga, Kieran, Ahmed, Sean, Tom, Robin, James and Ana. A special thank you to Matheus and Aminata, who have been with me on this PhD journey every step of the way.

Special thanks to the Postdocs who have offered guidance throughout my PhD, in particular Dr. Fraser Hill- Casey, Dr. Pete Rayner, Dr. Pete Richardson, Dr. Barbara Procacci and Dr. Fadi Ahwal. I am also very grateful to the superb technical staff within the Department of Chemistry, with a special mention to the CHyM technical team, namely Dr. Victoria Annis and Dr. Richard John.

I would also like to thank Dr. Arnaud Comment and Dr. Adam Gaunt who graciously lent the Bluewave 75 lamp for use in this research.

Finally, thank you to my family and friends for their unwavering support and ability to keep me positive throughout this experience. And to my brilliant partner, Lewis, I will always and forever be thankful for your constant encouragement and unending belief that I could achieve this.

Author Declaration

I declare that this thesis is a presentation of original work and I am the sole author. This work has not previously been submitted for an award at this, or any other, University. All sources are acknowledged as References.

1 Introduction

Photochemical reactions are present in many aspects of everyday life - for example they underpin many biological processes,[1,2] are used as diagnostic and therapeutic tools in medicine[3,4] and are applied for large-scale industrial synthesis for molecules such as vitamin D.[5,6] These unique applications originate from the dramatically different reactivity available to a reagent species when it is promoted into a higher electronic state upon absorbing a photon of light during a photochemical reaction.[7] To understand and exploit this reactivity, it is essential to have analytical tools that can characterise and probe the kinetics of these systems.

To this end, the ability to monitor the progress of a photochemical process in real-time is an invaluable tool. Using reaction monitoring techniques it is possible to determine the completion point of a chemical process, observe the formation and consumption of transient intermediate species and perform quantitative analysis to obtain kinetic and thermodynamic parameters about a chemical system. With this information, mechanistic insights can be developed and routes to process optimisation can be applied.[8] The key requirement for an analytical technique to be used for reaction monitoring purposes is that the technique provides a characteristic response for all starting materials, intermediates and products of the reaction and that this response is concentration dependent. Furthermore, the spectral acquisition of the technique must be on a suitably fast timescale for the process being observed (as to allow multiple measurements across the reaction coordinate).[9]

Chromatography techniques, such as HPLC, have seen application as highly-sensitive photochemical reaction monitoring methods[10] and are often coupled with UV-visible detection techniques to provide characterisation data.[11,12] One downside of using a chromatography technique is that the monitoring is not performed online - aliquots of the sample taken at different times are analysed externally to the bulk reaction mixture. This limitation is not seen with optical molecular spectroscopy methods (such as IR,[13,14] Raman[15,16] and UV[17,18]) and so

these techniques have seen significant uptake for online non-invasive reaction monitoring of photochemical systems.

One powerful technique that has been used for photochemical reaction monitoring research is Nuclear Magnetic Resonance (NMR) spectroscopy. NMR spectroscopy is a non-invasive technique that provides highly detailed structural information about the species present within a sample through features such as chemical shift, scalar coupling and peak integration. This wealth of structural information can be beneficial in cases where similar compounds are being investigated as the functional group resolution of optical spectroscopy techniques can lead to overlap of key structural features.[19] Furthermore, NMR spectroscopy provides quantitative information about the ratio of reactant to product molecules in a sample without calibration (due to a linear proportionality between signal intensity and nuclei concentration).[20] Owing to the variable temperature functionality of many modern NMR spectrometers[21] and the design and integration of spectrometer compatible flow cells[22,23] and stopped flow apparatuses,[24,25] a wide range of chemical processes are able to be observed using this technique.

To observe photochemical processes using NMR, the incorporation of the initial irradiation step of a photochemical reaction is achieved either through an *ex situ* approach (where irradiation occurs external to the NMR magnet) or an *in situ* approach (where irradiation occurs within the NMR magnet).[26] While *ex situ* irradiation is less complex and cheaper, the requirement to transfer the sample into the NMR spectrometer limits the timescale of reactions that can be observed using this approach.[27] The quicker detection offered through *in situ* irradiation has led to application of this reaction monitoring approach to a wide variety of chemical processes such as photosensitized cycloaddition,[28] photobromination[29] and photoisomerisation.[30]

A significant limitation of using NMR for reaction monitoring is that it is an inherently insensitive analytical technique due to the observed signal resulting from a very small population difference between nuclear energy levels. Owing to this, an array of hyperpolarisation techniques have been developed to boost the sensitivity of NMR spectroscopy. The core principle governing hyperpolarisation is a deviation away from the Boltzmann distribution controlled population of the nuclear energy levels. Through overpopulation of one or more of the nuclear energy levels it is possible to enhance the population difference of the system and thus increase the observed NMR signal. Several robust hyperpolarisation methods have been

developed for use with NMR including Dynamic Nuclear Polarisation (DNP),[31,32] Spin Optical Exchange Pumping (SEOP)[33,34] and *Para*Hydrogen Induced Polarisation (PHIP).[35–37] Of these techniques, the versatility and affordability of PHIP make it a good candidate for use in reaction monitoring NMR experiments. There are two main PHIP hyperpolarisation techniques. The first, hydrogenative PHIP, involves the addition of a molecule of *para*hydrogen into a target analyte with the resulting pair of protons within the product molecule showing enhanced NMR signals for a short period of time.[38] The second route is non-hydrogenative PHIP, referred to as SABRE (Signal Amplification By Reversible Exchange), whereby molecules of *para*hydrogen and the target analyte reversibly bind to a catalyst in the presence of a weak magnetic field to allow for transfer of polarisation from *para*hydrogen into the analyte molecule in order to generate enhanced NMR signals.[39] This work focuses on hydrogenative PHIP which has seen significant application in the observation and monitoring of photochemical reactions on high-field NMR spectrometers.

Research conducted by Duckett and co-workers[40–42] has shown that hydrogenative PHIP hyperpolarisation can be applied to the reactions of metal complexes that include an oxidative addition of H_2 step, enabling the observation of enhanced hydride resonances. This technique has been instrumental in the exploration of the photochemistry of metal hydride complexes, which are important to many catalytic processes, such as C-H bond activation.[43] Following irradiation, many metal hydride complexes undergo degenerate reactions where photodissociation of H_2 from the complex is followed by oxidative addition of a new molecule of H_2 and so they are well suited to being probed using PHIP.[44] To monitor these processes, photochemical pump - NMR probe experiments (where the delay between sample irradiation and NMR detection is varied to allow observation of chemical evolution) have been developed on high-field NMR spectrometers. Using this setup, the reactions of H_2 with several metal dihydrides (such as $[Ir(H)_2(CO)(PPh_3)_2I]$[45] and $[Ru(H)_2(CO)(PPh_3)_3]$)[46] have been followed, allowing the determination of key kinetic parameters and the observation of low-concentration by-products. This approach has also enabled the observation of a unique spin physics phenomenon whereby micro-to-millisecond magnetic evolution of metal hydride complexes is observable immediately following formation. This magnetic evolution can be analysed to gain insight into the mechanism through which the addition of *para*hydrogen results in enhanced NMR signals.[47,48] Most recently, novel high-field NMR research to further optimise photochemically-induced PHIP for metal dihydrides has been published by the Castellano research group.[49] Within this research, the use of a photosensitiser was found to promote H_2 loss from $[Ru(H)_2(CO)(PPh_3)_3]$ resulting in much stronger hyperpolarised signals upon

addition of *para*hydrogen (a 235-fold signal enhancement compared to 35.6-fold without the presence of a photosensitiser).

While impressive results have been obtained using high-field NMR, a limitation of this approach is that high-field NMR spectrometers are expensive (with both large upfront and recurring cryogen costs) and have a large footprint. This has meant that reaction monitoring using NMR spectrometers is limited to specialist laboratory applications. However, the recent resurgence in the development and application of low-field (1 - 2 T) NMR spectrometers has opened up new possibilites for reaction monitoring via NMR.[50] These so-called benchtop NMR spectrometers incorporate a Halbach array of permanent magnets and sophisticated shimming electronics[51,52] to enable magnetic field homogeneities of <10 ppb within the NMR spectrometer. These advancements have allowed for spectral resolutions down to 0.5 Hz linewidths to be achieved, enabling high resolution NMR spectra to be recorded using these permanent magnet spectrometers.[53–55] This movement towards permanent magnet based spectrometers comes with significant advantages for affordability (with lower upfront costs and no requirement for cryogenic cooling) and portability. Furthermore, benchtop NMR spectrometers often contain external locking systems (usually to ^{2}H or ^{19}F) allowing the reaction to be performed with standard protonated solvents.[56] Combined, these benefits allow for *in situ* reaction monitoring with the spectrometer situated close to the reaction vessel or even incorporated into a flow setup for continuous on-line monitoring.[23,57–60] These unique capabilities have resulted in a a plethora of reaction monitoring applications, with benchtop NMR spectrometers being employed to monitor reaction completion,[61,62] investigate reaction pathways[60,63] and calculate kinetic rate information.[64,65] Several studies have validated the use of benchtop NMR spectrometers for reaction monitoring through comparisons to other time-resolved techniques, such as high-field NMR, gas chromatography and IR spectroscopy.[66,67] Similar studies have also highlighted the benefit of using benchtop NMR with complementary on-line reaction monitoring techniques, such as IR[68–70] and mass spectrometry (MS),[71] in order to maximise the information gained about a reaction system.

The use of benchtop NMR spectrometers for reaction monitoring is not without complication. For example, the reduced chemical shift dispersion of the spectra (due to the weaker external magnetic field) can result in broader NMR peaks and strong coupling effects, making signal overlap common within the organic region of ^{1}H spectra even for simple molecules.[72] To address this limitation, research has been

conducted into reaction monitoring using heteronuclear channels,[73,74] and using multidimensional NMR (both with standard[75,76] and ultra-fast[77,78] pulse sequences). Another limitation of benchtop NMR spectrometers is the requirement of strict temperature stabilisation to ensure that the homogeneous magnetic field is maintained within the instrument. For example, the operational temperature of the Spinsolve Carbon (1 T, 43 MHz) is 28.5 °C and so no variable temperature studies are able to be performed with this instrument. However, modern benchtop NMR spectrometers that operate at different temperatures and that can perform variable temperature experiments are becoming commercially available and so a wider range of experimental conditions and more in-depth kinetic studies are beginning to be available for these systems.[79]

A final significant drawback of benchtop NMR spectrometers is that the lower magnetic field strength of the instruments results in a reduced sensitivity compared to high-field NMR spectrometers. NMR sensitivity scales with magnetic field strength approximately according to $B_0^{3/2}$ and so significant reductions in signal are seen when moving to low-field.[80] As a result, spectra on a benchtop NMR spectrometer often need to be acquired using more concentrated samples or with increased numbers of scans to observe sufficient signal. Neither of these requirements are conducive to observing low-concentration transient species for reaction monitoring applications.[81] Therefore, the use of hyperpolarisation techniques to improve the observed signal is crucial for reaction monitoring applications at low-field.

In recent years, PHIP hyperpolarisation methods have been demonstrated to be effective routes to overcome the inherent insensitivity of benchtop NMR spectrometers.[81] Hydrogenative PHIP has shown promise in the monitoring of catalytic processes, with strong signal enhancements and reaction coordinates being obtained for products formed from hydrogenation reactions of both alkene[82–84] and alkyne[85] functional groups. Most recently, this method has also been utilised for the development of novel hydrogenative *para*hydrogen-based hyperpolarisation techniques, such as PHIP-X[86] (where proton exchange is utilised to relay PHIP hyperpolarisation to other analytes within a solution) and RASER (Radiofrequency Amplification by Stimulated Emission of Radiation).[87,88] Comparatively, the SABRE technique has seen more widespread uptake at low-field. This can be rationalised by the wider range of analytes that can be explored using this method, as no direct hydrogenation pathway is required for hyperpolarisation.[79] A significant proportion of the research conducted using SABRE at low-field thus far has been into optimisation of the SABRE process. This research has covered a diverse range of

topics such as catalyst design and catalyst removal (for clinical applications),[89–91] optimisation of the polarisation transfer method[92,93] and improvements to the design and integration of *para*hydrogen generators.[94–97] Additional areas of research where the SABRE technique has been applied at low-field have included hyperpolarisation of heteronuclei (including 1D and 2D experiments for the detection of ^{13}C,[98–100] ^{15}N[101,102] and ^{19}F[103]), reaction monitoring of both organic[104] and organometallic[105] processes and the analysis of biologically-relevant molecules.[106,107]

One potential issue with incorporating PHIP hyperpolarisation into a reaction monitoring experiment is the quantification of the observed signals. In standard NMR, signals can be related directly to concentration as long as the requirement of a sufficient relaxation time between spectra is met. However with hyperpolarised signals, the quantification of the concentration of species is more complex owing to the transient nature of the enhanced signals and the need to account for the efficiency of the hyperpolarisation process. This fundamental difference means that there may not be a direct correlation between the observed signal and the amount of product present within the solution. Within both of the previously highlighted studies into PHIP-hyperpolarised reaction monitoring of hydrogenation reactions at low-field (from the research groups of Jeong *et al.*[84] and Gołowicz *et al.*[85] for reactions involving alkene and alkyne groups respectively), the formation of product was able to be successfully monitored and reaction coordinates were obtained. However, neither study included quantitative analysis in order to obtain kinetic parameters for the observed systems. This suggests a gap within the current literature on the assessment of the robustness and validity of quantitative PHIP hyperpolarised reaction monitoring at low-field.

Similarly to hyperpolarised reaction monitoring at low-field, reaction monitoring of photochemical processes at low-field has seen limited uptake thus far but examples of both *ex situ* irradiation[108,109] and *in situ* irradiation[110] setups are present within the current literature with the most recent study being published in 2022. This indicates that the development of irradiation setups for use with benchtop NMR spectrometers is another currently emerging area of research.

This thesis aims to address these two areas of research through development of robust hyperpolarised reaction monitoring procedures and the design and implementation of *ex situ* and *in situ* irradiation routes on a benchtop NMR system. The background theory for select areas of NMR spectroscopy, PHIP

hyperpolarisation and metal dihydride photochemistry are discussed in Chapter 2, with further theory provided within the relevant chapters as required.

In Chapter 3, a robust and reproducible approach to hyperpolarised reaction monitoring using a benchtop NMR spectrometer is developed. For this a suitable model chemical reaction, the oxidative addition of H_2 to Vaska's complex, is selected for developing the procedure as to allow for clear comparison between experimental and literature results.[111] Details about the experimental design, including the pulse sequence, automated data processing and kinetic model are discussed.

In Chapter 4, the consequences of using *para*hydrogen for quantitative reaction monitoring are discussed. Within this chapter, the concepts of hyperpolarised signal relaxation and the presence of thermally-polarised background signal are presented and their effect on the observed rate of reaction for the system is determined experimentally. Also explored is the robustness of the reaction monitoring method against temperature variations and lower enrichment levels of H_2, where a smaller proportion of the H_2 gas used is the required *para*hydrogen isomer. Finally, to exhibit the potential applications of this reaction monitoring approach, this method is assessed using a complex mixture where several reactions occur simultaneously within the NMR sample.

Chapter 5 concerns the development of an *ex situ* irradiation setup for use with a benchtop NMR spectrometer. Details about the instrumentation used and the irradiation housing designed for *ex situ* irradiation of an NMR sample are discussed. Then, the photochemical reactivity of Vaska's complex is explored and optimised using this setup. Through this optimisation, the advantages and disadvantages of an *ex situ* irradiation approach are discussed and a comparative study to the thermal reaction monitoring of Vaska's complex in Chapters 3 and 4 is performed.

In Chapter 6, the focus is the development and application of an *in situ* irradiation approach on a benchtop NMR spectrometer. An initial comparison between two low-cost broadband UV-lamp *in situ* irradiation setups is performed with a focus on optical properties and the quality of NMR spectra produced. Further optimisation is then conducted on the preferred setup looking at the effect of sample preparation and irradiation length. This *in situ* setup is then applied to a range of iridium and ruthenium complexes that form metal dihydride complexes upon irradiation to enable direct comparison to literature studies performed using a laser-based *in situ* irradiation setup. As a final point of comparison, a photochemical

pump - NMR probe experiment is developed to enable observation of magnetic evolution on the micro-to-millisecond timescale on a benchtop NMR spectrometer.

Chapter 7 presents conclusions alongside potential areas of future work and Chapter 8 provides relevant details about the experimental methods and procedures used throughout the thesis.

2 Background Theory

2.1 Fundamentals of NMR

2.1.1 Zeeman Interaction

The fundamental principle underpinning NMR is the interaction of nuclear spins with external magnetic fields. Nuclei carry an intrinsic total angular momentum ($\hat{I}$), referred to as spin, which is a vector that has contributions from each Cartesian direction ($\hat{I}_x$,$\hat{I}_y$,$\hat{I}_z$). The nuclear spin is described by the spin quantum number, I, which can take either integer or half-integer values. Nuclei with I = 0 (such as ^{12}C), have no intrinsic nuclear spin and so cannot be observed using NMR. Nuclei with non-zero nuclear spin (I $\neq$ 0, seen for nuclei such as ^{1}H and ^{13}C), have a nuclear magnetic moment ($\hat{\mu}$) which is a vector property related to ($\hat{I}$) through the gyromagnetic ratio (γ), a property of the type of nucleus being examined, as shown in Equation 2.1.[80]

$$\hat{\mu} = \gamma \hat{I} \tag{2.1}$$

When nuclei with non-zero spin (I $\neq$ 0) are placed into a static magnetic field, the nuclear magnetic moment ($\hat{\mu}$) will interact with the applied field causing the nuclear energy levels of the nuclei to become non-degenerate. The nuclear energy levels will split into $2I+1$ discrete energy levels and this phenomenon is referred to as Zeeman splitting. The energies of these nuclear spin states are defined by Equation 2.2 where m is the magnetic quantum number (which can take values from +I to -I), γ is the gyromagnetic ratio and B_0 is the strength of the applied magnetic field.[80]

$$E_m = -m\gamma B_0 \hbar \tag{2.2}$$

For a spin-$\frac{1}{2}$ nucleus (such as ^{1}H), only two nuclear energy levels are available, $m = +\frac{1}{2}$ (α) and $m = -\frac{1}{2}$ (β), which represent the nuclear spin being aligned with and against the B_0 field respectively (shown in Figure 2.1).

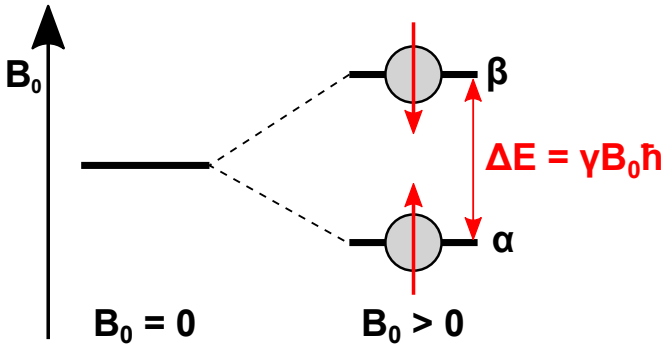

Figure 2.1: Representation of Zeeman splitting for a spin-$\frac{1}{2}$ nucleus in the presence of a magnetic field (B_0).

Within an NMR experiment, transitions between nuclear energy levels that satisfy $\Delta m = \pm 1$ are observed as peaks within the NMR spectrum. For a spin-$\frac{1}{2}$ nucleus, the transition between the α and β energy levels satisfies this condition and so a peak is observed at ΔE (Equation 2.3). This equation can be rewritten using Planck's equation (Equation 2.4), to yield the Larmor equation (Equation 2.5).[80] The Larmor equation highlights that the transition frequency is dependent on only the applied magnetic field (B_0) and the gyromagnetic ratio of the nucleus it is applied to (γ). From this it can be rationalised that all transitions for a specific nucleus (e.g. ^{1}H, ^{13}C) will be centred at the Larmor frequency for that nucleus. Depending on the units required, interconversion between angular frequency (ω, in radians s^{-1}) and frequency (ν, in Hz) is possible using the relationship $\omega = 2\pi\nu$.

$$\Delta E_{\alpha \rightarrow \beta} = \hbar\gamma B_0 \tag{2.3}$$

$$E = h\nu = \hbar\omega \tag{2.4}$$

$$\omega = \gamma B_0 \tag{2.5}$$

Differentiation of nuclei of the same type is possible due to modulation of the Larmor frequency by the electronic environment of each nucleus. The surrounding

electrons will have an induced magnetic field that opposes the applied B_0 field such that each nucleus will experience a different effective magnetic field (B_{eff}). This B_{eff} field will result in a shift to the Larmor frequency, giving chemical environment dependency to the spectral peaks. To ensure that the observed transition frequencies of nuclei are consistent when using NMR spectrometers with different B_0 fields, the frequency is converted to a chemical shift value (δ) using Equation 2.6, where the transition frequency of interest, ν_{sample}, is set relative to a reference frequency of a common NMR species, ν_{ref} (for ^{1}H this is tetramethylsilane).[112] Nuclei in the same chemical environment will appear at the same chemical shift and are referred to as chemically equivalent. Nuclei that are within different chemical environments will have separate chemical shift values and these are termed chemically inequivalent nuclei.

$$\delta_{sample} = 10^6 \frac{\nu_{sample} - \nu_{ref}}{\nu_{ref}} \tag{2.6}$$

Within the B_0 field, there will also be interactions between the magnetic moments of nuclei within the chemical system. These interactions, referred to as scalar spin-spin coupling or J coupling, are mediated through the interactions of shared electrons between the two nuclei. Interactions can occur between nuclei of the same type (homonuclear) or of different types (heteronuclear) but will only be present between nuclei that are either chemically inequivalent or magnetically inequivalent (where both nuclei couple to a third nucleus to different extents). J coupling results in perturbation of the energies of the nuclear energy levels resulting in splitting of the peaks within the NMR spectra. The extent of the splitting is dependent on the strength of the coupling between the nuclei and is quantified as the J coupling constant (measured in Hz). If the J coupling constant between two nuclei is smaller than the difference in chemical shift between them ($J_{12} << \Delta\nu_{12}$) then each peak is split into a multiplet of n+1 peaks (where n is the number of chemically equivalent nuclei being coupled to). This is referred to as weak coupling conditions. In situations where these terms have similar magnitudes ($J_{12} \approx \Delta\nu_{12}$), these are strong coupling conditions and complex second-order splitting patterns are observed.[112] Strong coupling effects are more common at lower B_0 field strengths as the chemical shift is B_0 dependent (so $\Delta\nu_{12}$ will reduce) while J coupling is magnetic field independent (so J_{12} will remain the same).

For an AX-type spin system (where two nuclei, A and X, are coupled and chemically inequivalent) of spin-$\frac{1}{2}$ nuclei, four different combinations of spin are

available: $\alpha\alpha$, $\alpha\beta$, $\beta\alpha$ and $\beta\beta$. According to the selection rule ($\Delta m = \pm 1$), there are four allowed transitions between these spin states. Each nucleus has two transitions where it is the active spin (transitioning between α and β) but the spin state of the coupled passive spin is different. This results in a doublet peak being observed for each nucleus that is centred at its chemical shift (δ_1/δ_2) and split by the J coupling constant to the other nucleus (J_{12}). A diagram of this is given in Figure 2.2.[112]

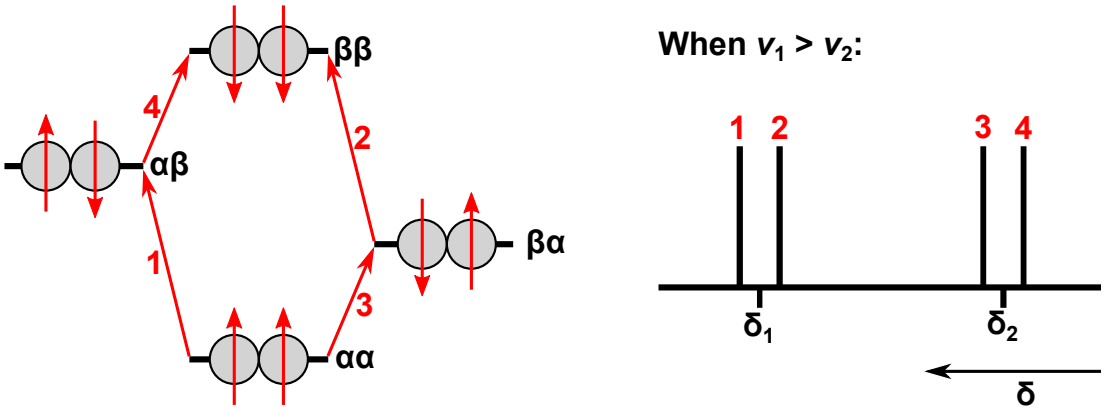

Figure 2.2: Nuclear energy levels and NMR spectrum for an AX-type spin system of spin-$\frac{1}{2}$ nuclei highlighting the available transitions between the energy levels.

2.1.2 The Vector Model

The vector model provides an intuitive method through which the basic principles of NMR can be understood. For all NMR models discussed in this chapter, a Cartesian coordinate system will be used with the z-direction representing the direction of the B_0 field. The interaction of the B_0 field and the magnetic moment ($\hat{\mu}$) can be represented as an interaction between two vector properties (Figure 2.3a). When $\hat{\mu}$ has a component in the x-y plane (a non-zero value of $\hat{\mu}_x$ or $\hat{\mu}_y$), it will experience a torque resulting in precession of $\hat{\mu}$. The frequency of this precession is the Larmor frequency (Equation 2.5).[113]

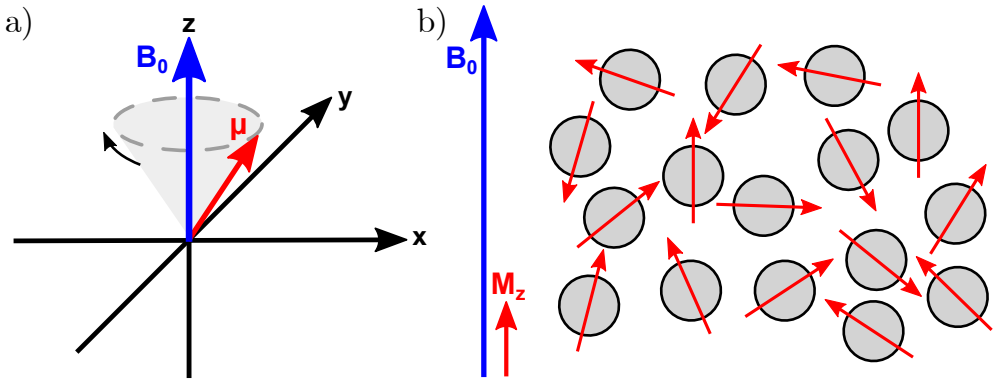

Figure 2.3: Cartoon representations of (a) precession of a magnetic moment ($\hat{\mu}$) about an applied B_0 field and (b) formation of net nuclear magnetisation for an ensemble of nuclear spins.

So far discussion has revolved around a single nucleus but in reality an NMR sample contains millions of nuclei that are all able to interact with B_0. In the absence of a B_0 field, all nuclei have a random orientation and thus have randomly distributed magnetic moments that cancel out. When B_0 is applied, a slight preference to align with the magnetic field rather than against it (owing to the Zeeman splitting making these orientations non-degenerate) results in a net nuclear magnetisation (M_0) forming within the sample (Figure 2.3b).[113] This net nuclear magnetisation will be aligned in the same direction as B_0 (the z-direction) and so at the start of the experiment M_z (the component of M_0 in the z-direction) is equal to M_0.

The vector model can be used to describe the motion of this bulk magnetisation (M_0) across the course of an NMR experiment. To highlight the key aspects of an NMR experiment, a standard pulse and acquire (PA) pulse sequence (Figure 2.4) will be explained through use of the vector model.

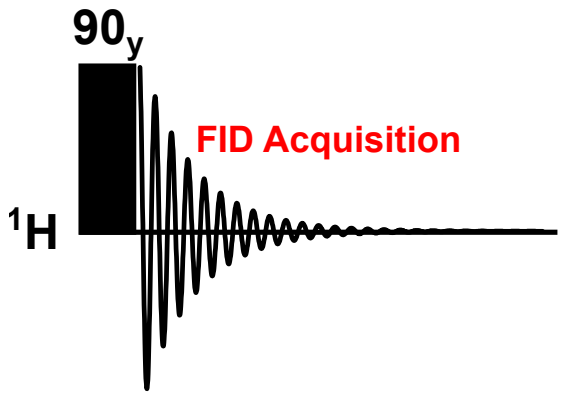

Figure 2.4: Pulse sequence for a standard pulse and acquire (PA) NMR experiment.

As established previously, an initial net magnetisation (M_0) is formed upon application of a B_0 field and this is aligned along the z-direction (M_z = M_0). For M_z to be detected it must be rotated into the x-y plane. To achieve this, an RF pulse (B_1) is applied perpendicular to the z-direction (using a coil orientated in the y-direction in this example). To appear static relative to the M_z magnetisation, the B_1 field is applied at the Larmor frequency of the detection nucleus. This is easiest to picture in the rotating frame (where the frequency of rotation is the Larmor frequency) as B_0 disappears and B_1 appears static and perpendicular to M_z (Figure 2.5a). As a result, M_z will precess around the B_1 field into the x-z plane. The angle of rotation that M_z travels through is proportional to both the amplitude of the RF pulse (B_1) and the time (t) that the pulse is applied for (Equation 2.7). Maximum signal is achieved when M_0 is fully rotated into the xy-plane which occurs after a 90° rotation (Equation 2.8).[113]

$$\theta = \omega_1 t = \gamma B_1 t \tag{2.7}$$

$$M_{xy} = M_0 \sin(\theta) \tag{2.8}$$

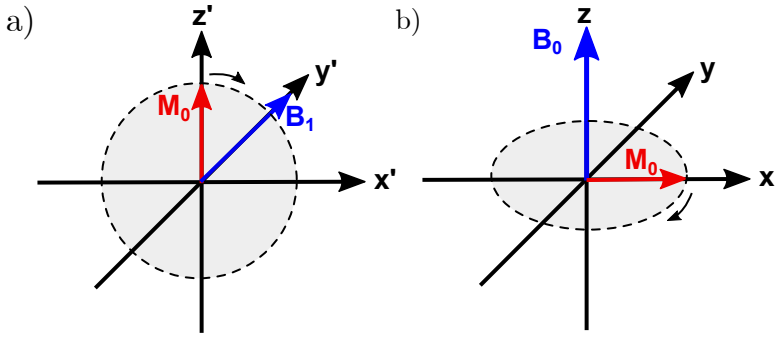

Figure 2.5: Representation of the vector model showing the movement of the bulk magnetisation (M_0) during (a) the application of a B_1 pulse and (b) precession in the x-y plane. (a) is shown in the rotating frame where the rate of rotation is the Larmor frequency and (b) is shown in the laboratory frame.

Once B_1 is switched off, M_{xy} will proceed to precess about B_0 within the xy-plane (pictured within the laboratory frame in Figure 2.5b). During this precession, the magnetisation can be detected by the same coils used to generate the B_1 pulse (via induction of current within the coils due to an oscillating magnetic field) to generate an observable NMR signal in the time-domain. Performing a Fourier transform (FT) on this data creates the standard frequency-domain spectrum that is used for analysis.

During precession, the observable NMR signal appear as a free induction decay (FID). Immediately following the 90° pulse, the individual nuclei that form the M_{xy} bulk magnetisation are precessing in phase with one another. However this phase coherence is lost over time due to random dephasing events caused by interactions with other spins within the system which leads to the decay of the observed signal. This decay is referred to as the transverse relaxation time and is defined by the time constant, T_2, through Equation 2.9. Variation in B_0 field homogeneity can cause transverse relaxation to occur at a faster rate than defined by T_2, and this is referred to as effective transverse relaxation which has the time constant of T_2^* (Equation 2.10, where ΔB is the measured field inhomogeneity).[113]

$$M_{xy}(t) = M_0 \exp\left(\frac{-t}{T_2}\right) \tag{2.9}$$

$$\frac{1}{T_2^*} = \frac{1}{T_2} + \frac{\gamma}{2\pi}\Delta B \tag{2.10}$$

The bulk magnetisation at the start of the NMR experiment (M_0) does not form instantaneously as it requires energy exchange between the spin system and the environment to reach thermal equilibrium. The time required for equilibrium to be reached is known as the longitudinal relaxation time and is characterised by the time constant, T_1, through Equation 2.11.[113] T_1 dictates the time required between sequential scans within an NMR experiments at to ensure thermal equilibrium is reached before the next scan is performed.

$$M_z(t) = M_0\left(1 - \exp\left(\frac{-t}{T_1}\right)\right) \tag{2.11}$$

2.1.3 Polarisation

The magnitude of the NMR signals observed from the NMR experiment, is governed by the initial net magnetisation (M_0) that is aligned with B_0 when it is applied. The net magnetisation for a particular nucleus is given by Equation 2.12 and is dependent upon the total number of that nucleus within the system (N), the percentage excess of spins within the lower energy spin state (termed polarisation,

P) and the size of the magnetic moment for the chosen nucleus (μ).[80]

$$M_0 = NP_0\mu \tag{2.12}$$

In a standard NMR experiment, polarisation (P_0) is governed by the filling of nuclear energy levels according to the Boltzmann distribution. The probability (P_m) of each nuclear energy state (m) being filled is given by Equation 2.13 where E_m is the energy of the state, k_B is the Boltzmann constant and T is the temperature of the system.[80]

$$P_m = \exp\left(\frac{-E_m}{k_B T}\right) = \exp\left(\frac{\gamma B_0 m\hbar}{k_B T}\right) \tag{2.13}$$

To calculate the nuclear polarisation, the difference in population of the nuclear spin states is taken. Under the high temperature approximation, the nuclear polarisation for a spin-1/2 nucleus is approximated using Equation 2.14. From this equation, a dependence of external magnetic field strength (B_0), gyromagnetic ratio (γ) and temperature (T) is seen for the polarisation.[80]

$$P_0 \approx \frac{\gamma B_0 \hbar}{2k_B T} \tag{2.14}$$

For a 9.4 T NMR spectrometer (400 MHz), a population difference of 32.6 ppm is calculated for ^{1}H at 295 K. This means that for every million ^{1}H nuclei, only 32.6 contribute to the observed signal in the NMR spectrum. This population difference reflects an almost equal filling of the nuclear energy levels according to the Boltzmann distribution due to their relatively small energy difference. This inherent insensitivity is one of the key limitations of NMR as an analytical technique. This sensitivity problem is even greater for benchtop NMR spectrometers, with the weaker B_0 field further reducing the population difference (Figure 2.6).[81]

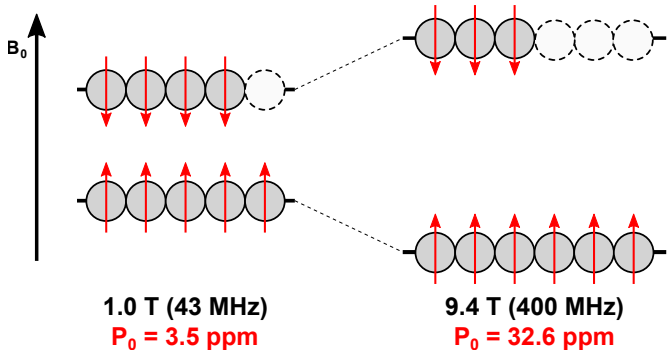

Figure 2.6: Representation of the relative population differences between nuclear spin states using a 1.0 T and 9.4 T NMR magnet. Stated values are given at 295 K.

Due to this inherent sensitivity limitation, large amounts of research have been conducted into how to improve the signal available in NMR spectroscopy. Everyday solutions to this problem tend to come in the form of increasing the concentration of the sample being observed (improving N in Equation 2.12) or by recording several scans (for N scans, SNR improves by $\sqrt{(N)}$). Larger scale improvements have come in the form of improving the NMR magnet itself. From the relationship shown in Figure 2.14, the clearest way to improve polarisation is to increase B_0. This has driven forward the development of stronger NMR magnets with the current strongest NMR spectrometer boasting a 1.2 GHz (28.2 T) superconducting magnet.[114] Other hardware developments, such as liquid-helium cooled cryoprobes (which have enabled up to 3-fold sensitivity improvements relative to conventional NMR spectrometers) have also aided in overcoming these limitations.[115]

2.1.4 The Product Operator Model

When considering more complicated NMR experiments, for example those with multiple coupled spins, the vector model is often insufficient to provide a clear understanding of how magnetisation is being transferred. In these situations, the product operator model can be used to provide a more comprehensive description of the system.

Within the product operator model, the angular momentum of the nuclear spin ($\hat{I}$) is split into its constituent components in the x-,y- and z-directions to give $\hat{I}_x$, $\hat{I}_y$ and $\hat{I}_z$ respectively. For a single spin-$\frac{1}{2}$ nucleus, these three operators represent the component of the bulk magnetisation that is aligned with each of these directions

(a fourth unity operator, $\hat{E}$, is also required for completeness but does not generate observable magnetisation). This gives us a route to probe the state of the spin system at a certain time (t), represented by the density operator ($\hat{\rho}$), by observing the relative contributions of each operator (Equation 2.15).[116] For example, the density operator at the start of an NMR experiment (ρ_0) will only have a non-zero contribution for the $\hat{I}_z$ operator as the bulk magnetisation is aligned with the B_0 field along the z-direction. Therefore, ρ_0 can be denoted as simply $\hat{I}_z$.

$$\hat{\rho}_t = a_t \hat{I}_x(t) + b_t \hat{I}_y(t) + c_t \hat{I}_z(t) \tag{2.15}$$

To understand how the density operator (i.e. the magnetisation) evolves over the course of an NMR experiment, we need to be able to evolve the system under two unique conditions: when an RF pulse is applied and during free evolution periods (where magnetisation can precess about the B_0 field). In both cases, a Hamiltonian operator can be applied to the density operator in order to calculate how the system will evolve with time. Within the product operator model, the Hamiltonian operators used employ the rotating frame as to remove any static components from the analysis. Within this approach, it is useful to define the offset of a spin, Ω, which is the difference between the Larmor frequency of the spin and the reference rotating frame frequency ($\Omega = \omega_0 - \omega_{ref}$).[80] Through developing these Hamiltonian operators, the two stages of the PA experiment (Figure 2.4) will be presented using the product operator model. Going forward, RF pulses will be defined in the form N_x where N indicates the angle of rotation caused by B_1 and x indicates the direction in which the pulse is applied (for example, a 90_y pulse is a pulse applied in the y-direction that rotates the magnetisation through 90°).

The first step of the PA experiment is the application of a hard 90_y pulse (where hard indicates that it is an ideal non-selective rotation of magnetisation within the system). The hard pulse Hamiltonian is given in Equation 2.16 and is dependent upon the amplitude of the B_1 pulse applied (ω_1) and the direction the pulse is applied in (in this case the y-direction). When a pulse (of length t_p) is applied to the density operator, this Hamiltonian results in a rotation of the initial $\hat{I}_z$ magnetisation about the B_1 direction resulting in a distribution of magnetisation in the x-z plane that is dependent upon the angle of rotation applied (Equation 2.17). When the angle of rotation is 90° ($\theta = \omega_1 t_p = \frac{\pi}{2}$ radians), only the second term is non-zero and as such this represents complete rotation of the magnetisation into the x-direction (Equation 2.18).[116] An important stipulation about these rotations is that the application of a

pulse in the same direction as the magnetisation results in no net effect for the system (no rotation will be observed).

$$\hat{H}_y = \omega_1 \hat{I}_y \tag{2.16}$$

$$\hat{I}_z \xrightarrow{\omega_1 t_p \hat{I}_y} \cos(\theta)\hat{I}_z + \sin(\theta)\hat{I}_x \tag{2.17}$$

$$\text{For } 90^\circ : \hat{I}_z \xrightarrow{\frac{\pi}{2}\hat{I}_y} \hat{I}_x \tag{2.18}$$

The second step of the PA experiment is the acquisition of the NMR spectrum which occurs during free evolution of the $\hat{I}_x$ magnetisation. The free evolution Hamiltonian is given in Equation 2.19 and is dependent upon the offset of the spin, Ω. When a free evolution period (of length τ) is applied to the density operator, precession of the NMR signal about the B_0 field at Ω will occur within the x-y plane and so this can be treated as a rotation (Equation 2.20).[116] This evolution accounts for the oscillatory nature of the FID that is acquired and also provides an explanation for why the Fourier transformed peak appears at a particular chemical shift (determined by the value of Ω).

$$\hat{H}_{free} = \Omega \hat{I}_z \tag{2.19}$$

$$\hat{I}_x \xrightarrow{\Omega\tau \hat{I}_z} \cos(\Omega\tau)\hat{I}_x + \sin(\Omega\tau)\hat{I}_y \tag{2.20}$$

The introduction of additional nuclei to the chemical system being examined adds complexity to the product operator model. To describe a two-spin system, all possible combinations of the four operators for one-spin ($\hat{E}$, $\hat{I}_{1x}$, $\hat{I}_{1y}$, $\hat{I}_{1z}$) are required (going forward, operators for spin 1 or spin 2 have an additional subscript notation for clarity). This gives a set of 16 operators required to describe a two-spin system, which are given in Table 2.1. The operators given in blue ($\hat{I}_{1x}$, $\hat{I}_{1y}$, $\hat{I}_{1z}$, $\hat{I}_{2x}$, $\hat{I}_{2y}$ and $\hat{I}_{2z}$) represent magnetisation that is single-spin order (centred on either spin 1 or spin 2). The remaining terms, given in green, indicate two-spin order terms in which both spin 1 and spin 2 contribute to the product operator.

Table 2.1: Product operators required to describe a two-spin system. Those in blue represent one-spin order terms and those in green represent two-spin order terms.

	$\hat{E}_1$	$\hat{I}_{1x}$	$\hat{I}_{1y}$	$\hat{I}_{1z}$
$\hat{E}_2$	$\hat{E}_1\hat{E}_2$	$\hat{I}_{1x}$	$\hat{I}_{1y}$	$\hat{I}_{1z}$
$\hat{I}_{2x}$	$\hat{I}_{2x}$	$2\hat{I}_{1x}\hat{I}_{2x}$	$2\hat{I}_{1y}\hat{I}_{2x}$	$2\hat{I}_{1z}\hat{I}_{2x}$
$\hat{I}_{2y}$	$\hat{I}_{2y}$	$2\hat{I}_{1x}\hat{I}_{2y}$	$2\hat{I}_{1y}\hat{I}_{2y}$	$2\hat{I}_{1z}\hat{I}_{2y}$
$\hat{I}_{2z}$	$\hat{I}_{2z}$	$2\hat{I}_{1x}\hat{I}_{2z}$	$2\hat{I}_{1y}\hat{I}_{2z}$	$2\hat{I}_{1z}\hat{I}_{2z}$

When considering a 2-spin system, a few modifications must be made to the previous NMR experiment description to incorporate the second spin. The first major change is that the starting state of the system contains z-magnetisation for both spin 1 and 2 ($\rho_0 = \hat{I}_{1z} + \hat{I}_{2z}$). The second major change is that the hard pulse and free evolution Hamiltonian operators must account for the interactions of the second spin. For the hard pulse Hamiltonian, a second term is added to account for the interaction of B_1 with the second spin (Equation 2.21) as each spin will only be affected by a Hamiltonian directed at that specific spin.[116]

$$\hat{H}_y = \omega_1 \hat{I}_{1y} + \omega_1 \hat{I}_{2y} \tag{2.21}$$

To account for the presence of the second spin, the free evolution Hamiltonian has to include evolution due to the offset of each spin (Ω_1 and Ω_2) and also due to the coupling between them (J_{12}) resulting in the modified Hamiltonian given in Equation 2.22.[116] The components of this Hamiltonian can be resolved as three successive transformations to the density operator (as long as the operators commute with one another). Rotations due to the J coupling term lead to rotations between single-spin terms (e.g. $\hat{I}_{1x}$) and antiphase two-spin terms (e.g. $2\hat{I}_{1y}\hat{I}_{2z}$) through an angle of $\pi J_{12}\tau$.

$$\hat{H}_{free} = \Omega_1 \hat{I}_{1z} + \Omega_2 \hat{I}_{2z} + 2\pi J_{12} \hat{I}_{1z}\hat{I}_{2z} \tag{2.22}$$

Working through the product operators for the PA experiment for a 2-spin system results in a detectable x-magnetisation term of $\cos(\pi J_{12}\tau)\cos(\Omega_1\tau)\hat{I}_x$ for spin 1. The oscillation of this magnetisation is now dependent on both the offset of spin 1 (Ω_1) and on its coupling to spin 2 (by J_{12}) resulting in the appearance of a doublet at the chemical shift of spin 1 within the NMR spectrum.

Overall, the product operator approach provides a route to understanding the movement of magnetisation during an NMR experiment, making it an excellent tool when designing pulse sequences.

2.1.5 Coherence Order

Another useful concept within the product operator formalisation is that of coherence order. Coherence order (p) is defined as the response of an operator to a rotation about the z-axis, i.e. following a rotation by ϕ about the z-axis, a phase of -pϕ is picked up by the operator. A coherence order of 0 indicates that the operator is unaffected by a z-rotation whereas values of p = ±1 or ±2 will have rotated through $\pm\phi$ or $\pm 2\phi$ respectively. To aid with the description of common NMR product operators in terms of their coherence order, it is useful to define a raising operator ($\hat{I}_+$) and a lowering operator ($\hat{I}_-$). Represented by Equations 2.23 and 2.24 respectively, these operators define states that have p = +1 and p = -1 respectively (i.e. rotations with equal but opposite directions).[116]

$$\hat{I}_+ = \hat{I}_x + i\hat{I}_y \qquad (2.23) \qquad\qquad \hat{I}_- = \hat{I}_x - i\hat{I}_y \qquad (2.24)$$

Using these operators, it is possible to define the product operators for a single spin-$\frac{1}{2}$ nucleus in terms of coherence order (shown in Table 2.2). $\hat{I}_z$ is simple as it is invariant to rotations around the z-axis and so has p = 0. $\hat{I}_y$ and $\hat{I}_x$ are linear combinations of the raising and lowering operators giving them a coherence order of +1 and -1. These terms are commonly referred to as single-quantum (SQ) in reference to their coherence order value. Within an NMR experiment, the detection coil is set to observe one of these coherence orders (commonly the p = -1 coherence) and so we are able to experimentally observe $\hat{I}_x$ and $\hat{I}_y$ magnetisation (one as real signal and the other as imaginary signal).[116]

Table 2.2: Coherence order of product operators originating from a single spin system.

Operator	Definition	p
$\hat{I}_z$	$\hat{I}_z$	0
$\hat{I}_y$	$\frac{1}{2i}(\hat{I}_+ - \hat{I}_-)$	+1 and -1
$\hat{I}_x$	$\frac{1}{2}(\hat{I}_+ + \hat{I}_-)$	+1 and -1

When moving to a two-spin system, the coherence order for each product

operator is calculated through the summation of the individual coherence orders for each spin.[116] For example, the term $2\hat{I}_{1y}\hat{I}_{2z}$ contains p = ±1 (from $\hat{I}_{1y}$) and p = 0 (from $\hat{I}_{2z}$) which when summed give a final value of p = ±1. Through this, it is now possible for multiple quantum (MQ) terms to exist that have p = ± 2 and p = 0 terms within them, such as $2\hat{I}_{1x}\hat{I}_{2x}$ (detailed in Equation 2.25). These coherence orders are described as double-quantum (DQ) and zero-quantum (ZQ) respectively and indicate that they will rotate about the z-axis at double the rate of SQ coherence or not at all. Having terms that interact to different extents with the B_0 field is highly advantageous when designing NMR experiments as it provides a route through which to discriminate which terms are selected for by the pulse sequence performed.

$$2\hat{I}_{1x}\hat{I}_{2x} \equiv \frac{1}{2}(\underbrace{\hat{I}_{1+}\hat{I}_{2+}}_{\text{p = +2}} + \underbrace{\hat{I}_{1-}\hat{I}_{2-}}_{\text{p = -2}} + \underbrace{\hat{I}_{1+}\hat{I}_{2-}}_{\text{p = 0}} + \underbrace{\hat{I}_{1-}\hat{I}_{2+}}_{\text{p = 0}}) \tag{2.25}$$

Revisiting the set of product operators required to define a two-spin system, it is possible to categorise these product operators based on coherence order. The complete set of 16 operator combinations are given again in Table 2.3 but are now grouped according to coherence order. The operators shown in yellow ($\hat{I}_{1z}$, $\hat{I}_{2z}$, $2\hat{I}_{1z}\hat{I}_{2z}$) have a coherence order of p = 0 and represent z-magnetisation. The operators given in blue ($\hat{I}_{1x}$, $\hat{I}_{1y}$, $\hat{I}_{2x}$, and $\hat{I}_{2y}$) represent SQ magnetisation centred on either spin 1 or spin 2. The signals observed from these product operators will appear in-phase with any doublets resulting from scalar coupling between the two nuclei (J_{12}) having all peaks in the same direction. The operators in red ($2\hat{I}_{1x}\hat{I}_{2z}$, $2\hat{I}_{1y}\hat{I}_{2z}$, $2\hat{I}_{1z}\hat{I}_{2x}$ and $2\hat{I}_{1z}\hat{I}_{2y}$) contain SQ anti-phase magnetisation, these spin states are observable by NMR but will show any doublets resulting from scalar coupling between the nuclei (J_{12}) in a antiphase orientation (where the peaks of the doublet are of opposite sign). Terms in green ($2\hat{I}_{1x}\hat{I}_{2x}$, $2\hat{I}_{1y}\hat{I}_{2x}$, $2\hat{I}_{1x}\hat{I}_{2y}$ and $2\hat{I}_{1y}\hat{I}_{2y}$) represent multiple-quantum coherences that contain mixtures of DQ and ZQ coherences.

Table 2.3: Product operators required to describe a two-spin system with colouring denoting coherence order. Colouring indicates the coherence order of the product operator as either in-phase SQ (blue), antiphase SQ (red), a mixture of ZQ and DQ (green) or z-magnetisation with a coherence order of p = 0 (yellow).

	$\hat{E}_1$	$\hat{I}_{1x}$	$\hat{I}_{1y}$	$\hat{I}_{1z}$
$\hat{E}_2$	$\hat{E}_1\hat{E}_2$	$\hat{I}_{1x}$	$\hat{I}_{1y}$	$\hat{I}_{1z}$
$\hat{I}_{2x}$	$\hat{I}_{2x}$	$2\hat{I}_{1x}\hat{I}_{2x}$	$2\hat{I}_{1y}\hat{I}_{2x}$	$2\hat{I}_{1z}\hat{I}_{2x}$
$\hat{I}_{2y}$	$\hat{I}_{2y}$	$2\hat{I}_{1x}\hat{I}_{2y}$	$2\hat{I}_{1y}\hat{I}_{2y}$	$2\hat{I}_{1z}\hat{I}_{2y}$
$\hat{I}_{2z}$	$\hat{I}_{2z}$	$2\hat{I}_{1x}\hat{I}_{2z}$	$2\hat{I}_{1y}\hat{I}_{2z}$	$2\hat{I}_{1z}\hat{I}_{2z}$

2.1.6 Application of Gradients

One final useful tool when designing NMR experiments is the application of magnetic field gradients. Additional gradient coils within an NMR spectrometer can be used to apply a linear gradient across an NMR sample. The result of this is that the effective magnetic field at a certain position in the sample depends on the combination of the B_0 field and the strength of the gradient field (G) at that position in 3d-space (r) - as defined by Equation 2.26.[113] As a result of this, the position of a spin within the sample will change the overall magnetic field strength it experiences and thus shift the Larmor frequency at that position (Figure 2.7).

$$B(r) = B_0 + G \cdot r = B_0 + G_x x + G_y y + G_z z \tag{2.26}$$

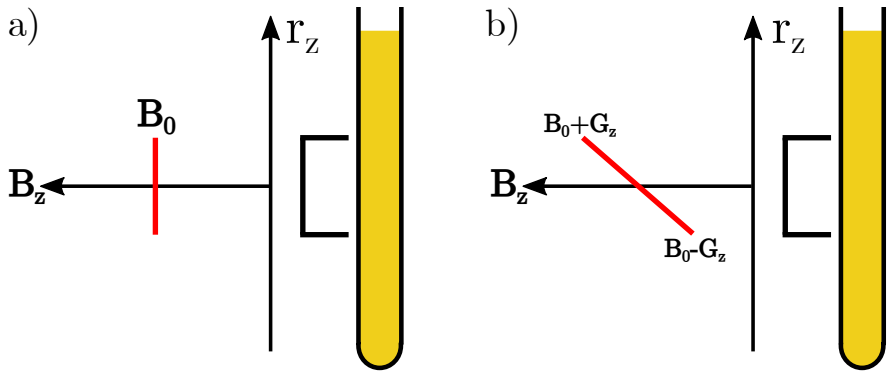

Figure 2.7: Cartoon representation of the B_z magnetic field experienced across an NMR sample in the (a) absence and (b) presence of a G_z gradient.

This encoding of a spatial dependence within the sample is useful for performing coherence selection within a pulse sequence. Evolution of the magnetisation during the application of a gradient will lead to loss of coherence as nuclei at different positions within the sample will be precessing at slightly different frequencies and so dephase relative to each other. However, by applying a gradient in the opposite direction it is possible for the dephasing to be reversed, allowing for coherence to reform later within the experiment. As the rate of dephasing is inherently linked to the coherence order of the product operator term, it is possible to select only for SQ, DQ or ZQ coherences based on the duration and magnitude selected for this second gradient. For example, application of a second gradient of equal duration and magnitude to the original gradient but of opposite sign would allow for refocusing of SQ terms but not DQ terms.

2.2 Principles of Hyperpolarisation

2.2.1 Theory of Hyperpolarisation

As established within the discussion about polarisation (Section 2.1.3), overcoming the sensitivity limitation of NMR is crucial in order to detect short-lived and low concentration species within a sample. While using larger B_0 fields is a valid solution, this raises practical concerns (such as increased cost and footprint) that limit how universally this solution can be applied. One alternative solution that has been pursued is development of pulse sequences that transfer population differences from favourable nuclei to a target nucleus. One example of this is the nuclear Overhauser effect (nOe), whereby the selective excitation of a single nucleus within a system results in signal enhancements for surrounding nuclei due to cross-relaxation mechanisms.[117–119] Another set of NMR experiments focused on the fact that P_0 has a gyromagnetic ratio dependence and so certain nuclei will have an inherently higher sensitivity. This led to the development of pulse sequences such as DEPT[120] and INEPT[121] which transfer the P_0 of ^{1}H nuclei (with a γ of 42.6 MHz T^{-1}) to heteronuclei, such as ^{13}C (γ = 10.7 MHz T^{-1}) or ^{31}P (γ = 17.2 MHz T^{-1}), as to enhance the NMR signals observed.

While the use of stronger NMR magnets and polarisation transfer pulse sequences are successful at producing enhanced NMR signals, it is more beneficial to be able to establish a non-Boltzmann distribution within the nuclear energy levels prior to the NMR experiment itself. This is the general aim of hyperpolarisation. By artificially increasing the population difference between nuclear energy levels (reflected in the schematic shown in Figure 2.8) it is possible to exceed the sensitivity limitation of NMR and record enhanced signals.[122]

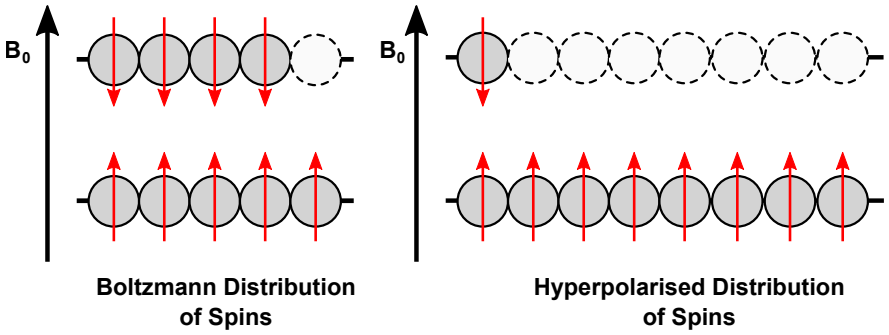

Figure 2.8: Cartoon representation of hyperpolarisation, highlighting the overpopulation of a single spin state when compared to a Boltzmann distribution of spins.

The earliest example of a hyperpolarisation method was found by Gorter in 1934.[123] Through placing an NMR sample within a pre-polarising magnetic field of a higher strength than the detection magnet, signal enhancements were observed upon NMR detection. This application of a stronger magnetic field establishes a greater population difference within the sample which remains detectable upon transfer of the sample into the NMR magnet. This approach was later improved to use both a strong magnetic field and a low temperature to maximise the Zeeman splitting for the system prior to detection.[124] While simplistic, this hyperpolarisation technique paved the way for research in this field and still sees application with compact NMR systems that contain weak B_0 fields.[125]

2.2.2 Overview of Routes to Hyperpolarisation

Recent developments in hyperpolarisation techniques for NMR have focused on the use of an additional species to transfer a favourable population difference onto an analyte species. Through these methods, the polarisation of the species is no longer dependent on the Boltzmann distribution and thus enables polarisation levels of up to 100% to be theoretically possible.[37] The key hyperpolarisation methods that are commonly used within NMR are given below in Table 2.4. Of the listed techniques, the method utilised within this research is *Para*Hydrogen Induced Polarisation (PHIP). This technique pairs well with benchtop NMR as $p\mathrm{H_2}$ is relatively cheap, easy to prepare and generates hyperpolarised signals quickly (down to sub-second timescales).[81]

Table 2.4: Summary of hyperpolarisation methods in NMR, indicating the origin and final location of the hyperpolarised signal and the mechanism through which it is transferred between them.

Technique	Polarisation Source	Polarisation Sink	Polarisation Mechanism
Dynamic Nuclear Polarisation (DNP)[31,32,126,127]	Unpaired electron	Coupled nuclei	Electron polarisation transfer from radical species to analyte through microwave irradiation of the electron paramagnetic resonance (EPR) transition at low temperatures (<4.2 K)
Chemically Induced Dynamic Nuclear Polarisation (CIDNP)[128–131]	Spin correlated radical pairs	Recombination and escape products	Preferential product formation for certain nuclear spin states due to singlet and triplet state interconversion mediated by the electron-nuclear hyperfine interaction
Spin Exchange Optical Pumping (SEOP)[33,34]	Alkali-metal atoms	Noble gas atoms	Spin exchange collisions between noble gas and spin-polarised alkali atoms (the latter formed using a circularly polarised laser beam)
Para-Hydrogen Induced Polarisation (PHIP)[37,38]	$p\mathrm{H_2}$	Nearby bonded nuclei in product	Breaking the symmetry of singlet state *para*hydrogen through incorporation into an analyte
Signal Amplification by Reversible Exchange (SABRE)[39,132]	$p\mathrm{H_2}$	Coupled nuclei on catalyst	PHIP variant where $p\mathrm{H_2}$ and analyte molecules reversibly bind to a catalyst across which polarisation is transferred

2.2.3 Theory of *Para*hydrogen

Molecular hydrogen ($\mathrm{H_2}$) is able to exist as two different spin-isomers, namely *ortho*hydrogen ($o\mathrm{H_2}$) and *para*hydrogen ($p\mathrm{H_2}$). The existence of these spin-isomers originates from the Pauli exclusion principle which states that the wavefunction that describes fermions (like $^1\mathrm{H}$) must be antisymmetric with respect to the exchange of nuclei.[133] Through the Born-Oppenheimer approximation, it is possible to split the overall wavefunction of $\mathrm{H_2}$ into electronic, vibrational, rotational, translational and

spin components (see Equation 2.27).[134]

$$\psi_{tot} = \psi_{elec}\psi_{vib}\psi_{rot}\psi_{trans}\psi_{spin} \tag{2.27}$$

H_2 is a homonuclear diatomic molecule with symmetric electronic, vibrational and translational components. Therefore to satisfy the Pauli exclusion principle, the product of the rotational and spin wavefunctions must be antisymmetric. There are two possible solutions to this wavefunction: a symmetric nuclear spin wavefunction must be coupled with an antisymmetric rotational spin wavefunction (occurs for odd rotational wavenumbers, e.g. J = 1,3,...) or an antisymmetric nuclear spin wavefunction must be coupled to a symmetric rotational spin wavefunction (occurs for even rotational wavenumbers, e.g. J = 0,2...). *p*H_2 is defined as a H_2 molecule with a symmetric rotational and antisymmetric nuclear spin wavefunction, while *o*H_2 is defined as a H_2 molecule with an antisymmetric rotational and symmetric nuclear spin wavefunction.[42]

To determine which spin states of H_2 satisfy these conditions, first a modification has to be made to the four expected product states for two coupled spin-$\frac{1}{2}$ nuclei ($\alpha\alpha$, $\alpha\beta$, $\beta\alpha$ and $\beta\beta$). The $\alpha\beta$ and $\beta\alpha$ states do not fulfill the symmetry requirement for the nuclear spin wavefunction (being neither symmetric or antisymmetric). To correct for this the normalised linear combinations of these two states, $\frac{1}{\sqrt{2}}(\alpha\beta + \beta\alpha)$ and $\frac{1}{\sqrt{2}}(\alpha\beta - \beta\alpha)$, are required which are symmetric and antisymmetric respectively. Overall this gives four spin states of H_2, shown in Figure 2.9a, split into a higher energy *o*H_2 degenerate triplet state and a lower energy *p*H_2 singlet state (the energy difference originating from the restriction of *o*H_2 to higher energy odd rotational wavenumbers).[135]

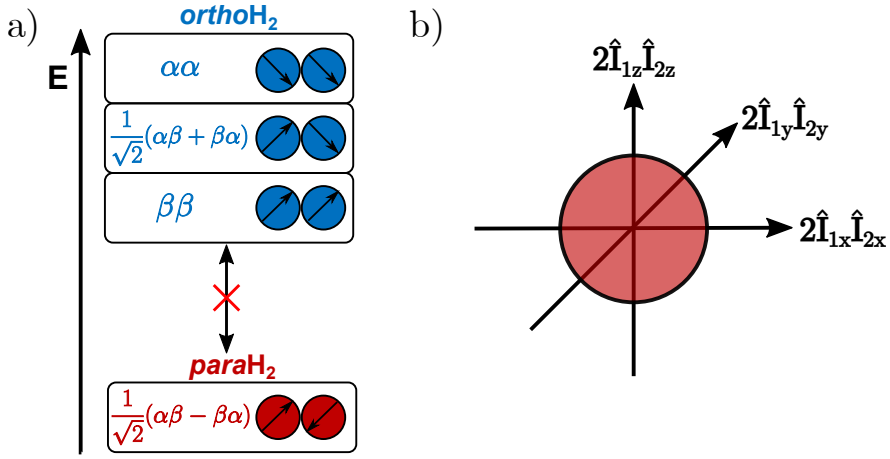

Figure 2.9: (a) Nuclear energy levels of H_2 alongside (b) a representation of the spherical region of nuclear magnetisation present within the $p$$H_2$ spin isomer.

Interconversion between $o$$H_2$ and $p$$H_2$ is symmetry forbidden under standard conditions but can be allowed through interaction of H_2 with a paramagnetic catalyst (such as activated charcoal[136–138] and iron(III) oxide[139,140]). As the population of these spin states is dictated by the Boltzmann distribution, variation of the temperature of H_2 in the presence of a paramagnetic catalyst enables precise control of the distribution of $p$$H_2$ and $o$$H_2$. At room temperature, the relatively small difference in energy of the $o$$H_2$ and $p$$H_2$ nuclear energy levels results in all spin states being populated approximately equally. As $o$$H_2$ is a triplet state while $p$$H_2$ is a singlet state, this results in a distribution of 75% $o$$H_2$ and 25% $p$$H_2$. However through cooling of the gas, population of the lower-energy $p$$H_2$ state is promoted which can result in a composition of up to 99.75% $p$$H_2$ (at 19 K).[141] As removal of the catalyst will result in the transition becoming symmetry forbidden again, isolating H_2 from the catalyst following interconversion at low temperature will enable the gas to be warmed up to room temperature while retaining $p$$H_2$ enrichment. This $p$$H_2$-enriched gas can then be stored for long periods of time prior to use (days or months depending on the mode of storage).[139,142]

2.2.4 *Para*hydrogen Induced Polarisation

Following generation of $p$$H_2$, a PHIP experiment can be performed to produce enhanced signals within NMR spectra. The fundamental principles of this technique will be explained within this section. The PHIP technique being discussed was initially postulated and proved experimentally in the late 1980s by Bowers and

Weitekamp,[37,143] though the effect was unknowingly observed in previous research by the group of Eisenberg.[35,36]

The singlet starting state of pH$_2$ is NMR silent. To understand the origin of this property and how it results in enhancements to the observed NMR signals it is useful to define the pH$_2$ starting state using product operators. For a standard NMR experiment, the starting density operator ($\hat{\rho}_0$) is defined as a linear combination of the z-component of the magnetisation for each spin (e.g. $\hat{\rho}_0 = \hat{I}_{1z} + \hat{I}_{2z}$ for a 2-spin system). However for a singlet state, $\hat{\rho}_0$ is defined by Equation 2.28 which, neglecting the identity operator, comes from the dot product of the total spin angular momentum operators of the two nuclei. As the two H nuclei are magnetically equivalent, the resulting starting state has equal components of the magnetisation in all directions (a representation of which is shown in Figure 2.9b). As a consequence of this, the starting state is invariant to rotation by an RF pulse and so will not produce an NMR signal through a standard NMR experiment. For convenience, $\hat{\rho}_{pH_2}$ is simplified (Equation 2.29) to just a longitudinal term ($2\hat{I}_{1z}\hat{I}_{2z}$) and a transverse term of zero-quantum-x (ZQ_x) - this second term originates from the cancellation of the p = ±2 coherence between $2\hat{I}_{1y}\hat{I}_{2y}$ and $2\hat{I}_{1x}\hat{I}_{2x}$ leaving only the ZQ coherence (p = 0) terms.[38]

$$\hat{\rho}_{pH_2} = \frac{1}{4}\hat{E} - \hat{\mathbf{I}}_\mathbf{1} \cdot \hat{\mathbf{I}}_\mathbf{2} = \frac{1}{4}\hat{E} - \frac{1}{2}(2\hat{I}_{1z}\hat{I}_{2z} + \underbrace{2\hat{I}_{1y}\hat{I}_{2y} + 2\hat{I}_{1x}\hat{I}_{2x}}_{ZQ_x}) \tag{2.28}$$

$$\hat{\rho}_{pH_2} = \frac{1}{2}(2\hat{I}_{1z}\hat{I}_{2z}) + ZQ_x \tag{2.29}$$

The NMR silent pH$_2$ molecule acts as a store of latent polarisation. Through breaking the symmetry of this pH$_2$ singlet state, this latent polarisation is unlocked. In PHIP, the symmetry breaking step is achieved through binding the pH$_2$ molecule to an unsaturated analyte of interest (such as an alkene for an organic system, or metal centre for an inorganic system). A generic scheme for pH$_2$ addition to an inorganic complex is given as Figure 2.10. During this binding, one of two conditions must be met: the two H atoms originating from pH$_2$ must become either chemically-inequivalent ($\Delta\nu_{H_1H_2} \neq 0$) or magnetically-inequivalent ($J_{H_1X} \neq J_{H_2X}$). As this binding occurs in a pairwise and spin-correlated manner, breaking the symmetry of the initial singlet spin configuration of the pH$_2$ molecule leads to selective population of certain spin states within the product molecule. This overpopulation of certain spin states leads to a relatively large population difference

as compared to the standard Boltzmann distribution and so transitions from these spin states lead to stronger signals within the NMR spectra.[135]

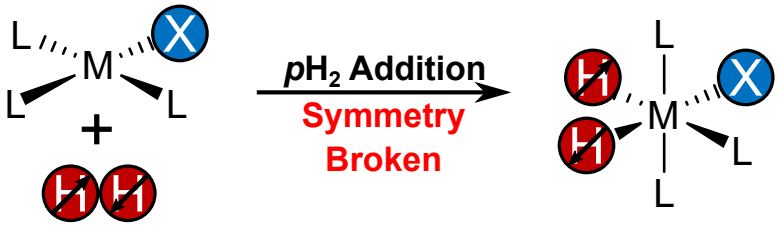

Figure 2.10: General reaction scheme for a PHIP reaction occuring at an unsaturated metal centre where pH$_2$ is represented in red and a coupling heteronucleus is represented in blue.

The symmetry breaking condition for PHIP hyperpolarisation can be represented using the product operator approach. The pH$_2$ starting state (Equation 2.29) will evolve under a free evolution Hamiltonian over the course of the reaction (as the addition is occurring within B$_0$). For an AX-type spin system (where both H atoms are chemically-inequivalent in the product molecule), the complete free evolution Hamiltonian is given in Equation 2.30 and consists of terms for evolution under the Larmor frequency of each nucleus (ω_1/ω_2 in angular frequency units) and the full scalar coupling interaction (J$_{12}$). However, this Hamiltonian can be simplified by removing any terms that commute with the density operator at all points in time, as no net evolution will occur due to these commuting terms. The result includes only the terms that will cause evolution of the density matrix (Equation 2.31, where $\delta\omega = \omega_1 - \omega_2$).[38]

$$\hat{H}_{free} = -\omega_1 \hat{I}_{1z} - \omega_2 \hat{I}_{2z} + \pi J_{12}(2\hat{I}_{1z}\hat{I}_{2z} + 2\hat{I}_{1x}\hat{I}_{2x} + 2\hat{I}_{1y}\hat{I}_{2y}) \tag{2.30}$$

$$\hat{H}_1 = -\frac{1}{2}\delta\omega(\hat{I}_{1z} - \hat{I}_{2z}) + \pi J_{12}(2\hat{I}_{1x}\hat{I}_{2x} + 2\hat{I}_{1y}\hat{I}_{2y}) \tag{2.31}$$

When $\hat{H}_1$ is applied to the initial $\hat{\rho}_{pH_2}$ density operator, the resulting state can be determined by applying each component of the Hamiltonian to the longitudinal ($2\hat{I}_{1z}\hat{I}_{2z}$) and ZQ$_x$ terms independently. The longitudinal term ($2\hat{I}_{1z}\hat{I}_{2z}$) commutes with all terms in $\hat{H}_1$ and so no rotation of this state will occur. The remaining ZQ$_x$ term will be converted into ZQ$_y$ (where ZQ$_y$ is defined as $\frac{1}{2}(2\hat{I}_{1y}\hat{I}_{2x} - 2\hat{I}_{1x}\hat{I}_{2y})$) by the initial term of $\hat{H}_1$ (in blue). This ZQ$_y$ term can then be reconverted back into ZQ$_x$

(via the same term in $\hat{H}_1$) or undergo further conversion by the second term of $\hat{H}_1$ (in red) into $(\hat{I}_{1z} - \hat{I}_{2z})$. Overall, free evolution of the *p*H_2 starting state results in a complex mixture of $2\hat{I}_{1z}\hat{I}_{2z}$, ZQ_x, ZQ_y and $(\hat{I}_{1z} - \hat{I}_{2z})$ states that are given by Equation 2.32 where a(t), b(t) and c(t) represent the relative contributions of each term.[135]

$$\rho(t) = \frac{1}{2}(2\hat{I}_{1z}\hat{I}_{2z}) + a(t)ZQ_x + b(t)ZQ_y + c(t)\frac{1}{2}(\hat{I}_{1z} - \hat{I}_{2z}) \tag{2.32}$$

Through solving a set of coupled differential equations (the details of which are given in the literature by Natterer *et al.*),[135] the relative contributions for each state to the density operator can be determined. These are given in Equation 2.33, where $\xi = \frac{\delta\nu_{12}}{J_{12}}$ and $k = 2\pi\sqrt{\delta\nu_{12}^2 + J_{12}^2}$. The term $\delta\nu_{12}$ represents the chemical shift difference between the nuclei (in Hz).

$$\begin{aligned} a(t) &= \frac{1}{\xi^2+1}(1+\xi^2\cos(kt)) \\ b(t) &= -\frac{\xi}{\sqrt{\xi^2+1}}\sin(kt) \\ c(t) &= \frac{1}{\xi^2+1}(1-\xi^2\cos(kt)) \end{aligned} \tag{2.33}$$

To simplify the density operator, it is assumed that the hydrogenation reaction occurs on a relatively slow timescale and so any evolution due to chemical shift or scalar coupling (which occur on the micro-to-millisecond timescale) will become time averaged and can be ignored.[38] Due to this, any periodic functions within Equation 2.33 are assumed to average to zero on the timescale of the hydrogenation reaction. This removes a large amount of complexity from this evolution period following hydrogenation, resulting in the density operator given by Equation 2.34.[38]

$$\overline{\rho} = \frac{1}{2}2\hat{I}_{1z}\hat{I}_{2z} + \frac{1}{\xi^2+1}ZQ_x + \frac{\xi}{(\xi^2+1)}\frac{1}{2}(\hat{I}_{1z} - \hat{I}_{2z}) \tag{2.34}$$

From Equation 2.34 it can be rationalised that without the presence of a difference in chemical shift ($\delta\nu_{12}$) or scalar coupling (J_{12}) between the two H nuclei, the term ξ would be equal to 0 and as such the density operator would remain unchanged

from the pH$_2$ starting state. As this starting state is NMR silent, no NMR signal enhancement would be observed for the system.

Under symmetry breaking conditions (where $\xi \neq 0$), the change in distribution of spin states in Equation 2.34 will result in enhanced NMR signals. There are two distinct regimes through which the spin system will evolve and these are governed by the strength of the magnetic field in which the reaction takes place. PHIP that occurs within a high-field magnet is referred to as PASADENA (*Para*hydrogen And Synthesis Allow Dramatically Enhanced Nuclear Alignment)[143] while that which occurs in low/zero-fields is classed as ALTADENA (Adiabatic Longitudinal Transport After Dissociation Engenders Nuclear Alignment).[144]

2.2.5 PASADENA Conditions

As stated above, PHIP occurs through the PASADENA regime when the pH$_2$ addition step is performed within a strong magnetic field (i.e. the reaction occurs within the NMR magnet itself). Under these conditions, the breaking of the pH$_2$ singlet state of $\frac{1}{\sqrt{2}}(\alpha\beta - \beta\alpha)$ leads to selective population of only the $\alpha\beta$ and $\beta\alpha$ states of the two H atoms within the product molecule (Figure 2.11a). Four transitions can occur from these overpopulated spin states with the directionality of these transitions resulting in each doublet containing one positively phased and one negatively phased peak. The resulting NMR spectrum will contain two doublets with antiphase character relative to the J_{HH} coupling (Figure 2.11).

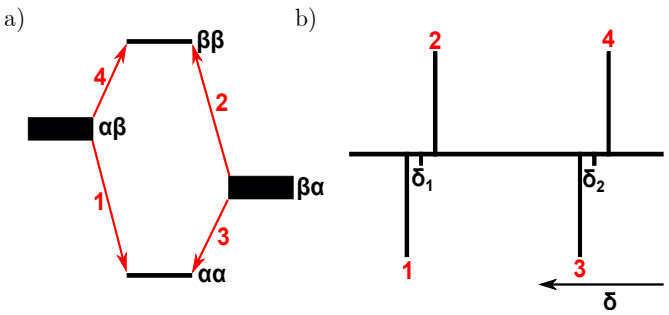

Figure 2.11: (a) Energy level diagram and (b) observed NMR spectrum for an AX-type spin system under PASADENA conditions where pH$_2$ addition occurs within a strong magnetic field.

This spectral appearance can be verified using the product operator approach. Due to the strong magnetic field, the system will be in a weak coupling regime

($\delta\nu_{12} >> J_{12}$, $\xi >> 1$) and so under PASADENA conditions only the $\hat{I}_{1z}\hat{I}_{2z}$ term will survive until NMR detection. Upon application of an RF pulse (θ_y), this is transformed into a single term that is NMR detectable (Equation 2.35). This term corresponds to having antiphase magnetisation on both spin 1 and 2, which is observed as the antiphase doublets shown in Figure 2.11b. Experimentally, the $\sin 2\theta$ term attached to this observable magnetisation means that the use of a 45° pulse angle will produce the maximum signal within an NMR experiment. Therefore, it is common practice to use this smaller pulse angle when performing PHIP experiments under PASADENA conditions.

$$2\hat{I}_{1z}\hat{I}_{2z} \xrightarrow{\theta\hat{I}_y} \frac{1}{2}\sin(2\theta)(2\hat{I}_{1x}\hat{I}_{2z} + 2\hat{I}_{1z}\hat{I}_{2x}) \tag{2.35}$$

2.2.6 ALTADENA Conditions

PHIP occurs through the ALTADENA regime when the pH$_2$ addition step is performed within a weak magnetic field (i.e. the reaction occurs within the Earth's magnetic field and then is transferred into the NMR spectrometer for detection). Under these conditions, the breaking of the pH$_2$ singlet state of $\frac{1}{\sqrt{2}}(\alpha\beta - \beta\alpha)$ leads to selective population of the $\alpha\beta$ state of the two H atoms within the product molecule. This occurs because in the weak magnetic field, the singlet and triplet states originating from pH$_2$ and oH$_2$ are preserved but redistribute in energy with the pH$_2$ singlet state reducing in energy. This reduced energy state is close in energy to the $\alpha\beta$ state in an AX-spin system. Upon application of a strong magnetic field, the singlet state breaks and an adiabatic transfer into only the $\alpha\beta$ state occurs (Figure 2.12a). Two transitions can occur from this overpopulated spin state with the directionality of these transitions resulting in two singlets with antiphase character relative to chemical shift (Figure 2.12b).

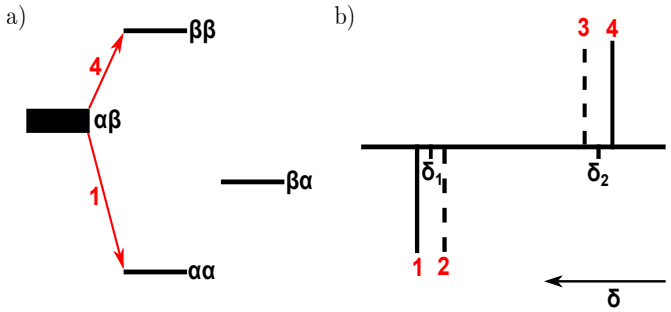

Figure 2.12: (a) Energy level diagram and (b) observed NMR spectrum for an AX-type spin system under ALTADENA conditions where *p*H_2 addition occurs within a weak magnetic field and then the sample is transferred into an NMR spectrometer for detection. Within (b), the dashed peaks for transitions 2 and 3 highlight that the magnitude of these peaks are strongly dependent on NMR pulse angle.

This spectral appearance can be verified using the product operator approach. Due to the weak initial magnetic field, the system has a relatively smaller value of ξ (as chemical shift is B_0 dependent but scalar coupling is B_0 independent) and so it is possible for the $(\hat{I}_{1z} - \hat{I}_{2z})$ state to survive until NMR detection. Upon application of an RF pulse (θ_y), a second NMR observable term is present as well as the original one seen under PASADENA conditions (Equation 2.36). The original term produces antiphase magnetisation while the new term produces in-phase magnetisation, which can lead to the potential cancellation of the inner doublet peaks depending on the pulse angle that is chosen (with smaller pulse angles resulting in greater signal cancellation). ALTADENA experiments are often performed using a 90° pulse angle as this will maximise the in-phase NMR signal (from $(\hat{I}_{1x} - \hat{I}_{2x})$) and remove the anti-phase contribution (from $(2\hat{I}_{1x}\hat{I}_{2z} + 2\hat{I}_{1z}\hat{I}_{2x})$) within the spectrum (enabling the peaks represented by dashed lines in Figure 2.12b to be observed).

$$2\hat{I}_{1z}\hat{I}_{2z} \pm (\hat{I}_{1z} - \hat{I}_{2z}) \xrightarrow{\theta\hat{I}_y} \frac{1}{2}\sin(2\theta)(2\hat{I}_{1x}\hat{I}_{2z} + 2\hat{I}_{1z}\hat{I}_{2x}) \pm \sin(\theta)(\hat{I}_{1x} - \hat{I}_{2x}) \qquad (2.36)$$

2.3 Photochemistry of Metal Dihydrides

2.3.1 Principles of Photochemistry

A photochemical reaction is a chemical reaction that is initiated by light through the generation of electronic excited states of a chemical species. The absorption of a photon of light results in an electronic transition where an electron is promoted to a higher energy molecular orbital. This excited electronic state will have a different electron density distribution to the ground state, leading to changes in bonding within the chemical species. These changes often result in unique reaction pathways for chemical systems that are not available from the ground state in thermal reactions.

For an electronic transition to occur, the wavelength of the absorbed photon must be matched to the energy difference between the ground state (S_0) and excited state (S_1) of the chemical species ($E = \frac{hc}{\lambda}$ where h is Planck's constant, c is the speed of light and λ is the wavelength of the photon). However, simultaneous promotion of the chemical species into a vibrational or rotational excited mode can occur (an example of an electronic transition with multiple vibrational level transitions is given in Figure 2.13a). As a consequence of this, a single electronic transition occurs across a band of discrete wavelengths that correspond to transitions occurring to different vibrational and rotational energy levels (see Figure 2.13b). Typical wavelengths for electronic transitions are within the UV-visible region of the electromagnetic spectrum.[7]

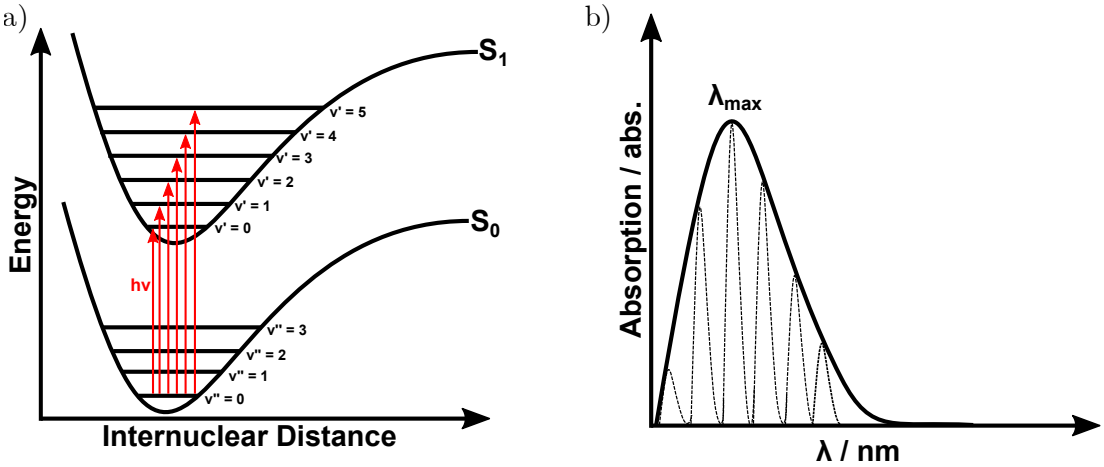

Figure 2.13: (a) Example potential energy curve and (b) UV-visible absorption spectrum for the transition between an electronic ground state (S_0) and excited state (S_1) with vibrational fine structure. Within the UV-vis spectrum, the commonly observed absorption band is shown with a solid line while the vibrational fine structure is shown a dashed line.

2.3.2 Light Sources in Photochemistry

While there are many different routes to irradiation of a sample for photochemistry, this thesis is focused on one particular method: the use of mercury-xenon arc lamps.

Mercury-xenon (Hg-Xe) arc lamps are broad-spectrum and continuous wave. A high voltage electric current is passed between 2 electrodes in the lamp leading to ionization of Hg/Xe atoms within the bulb. Collisions between free electrons and Hg/Xe atoms within the lamp result in excitation of the gas molecules to higher electronic energy levels. As the atoms relax to their ground state, they emit photons with a spectrum characteristic of the Xe and Hg atoms. Strong broadband UV light emissions are characteristic of Hg atoms and so they are ideal sources for initiating a wide range of photochemical reactions. The downside of using broadband UV lamp sources are that there is an inherently low specificity of the irradiation which can make it difficult to selectively observe a single electronic transition. The wide emission spectrum of arc lamp sources can also result in poor efficiency of the required photochemical reaction as there may be poor overlap of the emission band of the lamp and absorption band of the sample or the output power of the lamp at the required wavelength might be low.[145,146]

One common alternative irradiation route used for photochemistry with NMR spectrometers is the use of lasers. Laser sources use stimulated emission from a specific electronic transition within a chemical system to produce a highly coherent light emission at a set wavelength. There are several advantages of using a laser compared to an arc lamp such as the monochromatic nature of the output light (can select for specific electronic transitions), high irradiance of a sample and the ability to pulse the output from a laser (as to enable precise irradiation times for a system).[147] As a point of comparison within Chapter 6, a route to *in situ* irradiation of an NMR sample involving the use of a Nd:YAG laser system is discussed.

More detail about the routes through which these light sources can be integrated into NMR setups will be given in relevant chapters: Chapter 5 for *ex situ* irradiation setups and Chapter 6 for *in situ* irradiation setups.

2.3.3 Reductive Elimination of H_2 from Metal Dihydride Complexes

The reductive elimination of H_2 is a commonly observed photochemical reaction pathway for metal dihydride complexes that contain a pair of mutually *cis* hydride ligands (Figure 2.14). This process results in the formation of molecular hydrogen as both M-H bonds are cleaved in a concerted process (there is no evidence for the formation of hydrogen atoms via this mechanism).[43]

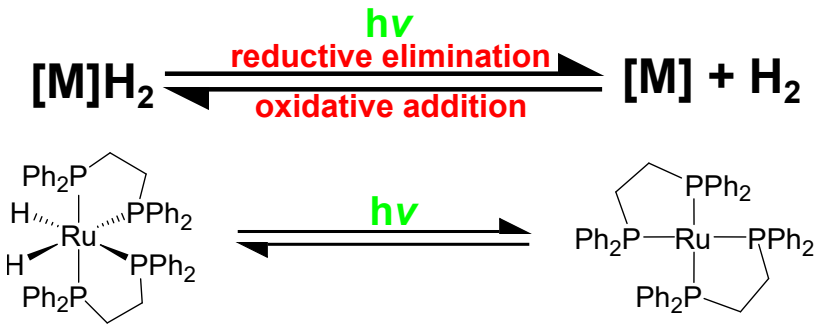

Figure 2.14: Reaction scheme for the reductive elimination of H_2 from a metal dihydride complex with the reaction of *cis*−$[Ru(H)_2(dppe)_2]$ given as an example system.

The absorption bands responsible for these reactions are found within the UV region. These absorption bands can be overlapped with competing processes that have absorption bands at similar wavelengths such as the photodissociation of CO or phosphine ligands within the metal complex.[148] The photodissociation of H_2 occurs due to the excitation of the complex from an electronic ground state into an excited electronic state that is dissociative with respect to H_2 elimination (Figure 2.15). While the exact electronic states being transitioned between are dependent on the nature and symmetry of the metal atom and ligands present, in general this dissociative state results from the transition of an electron into an orbital that has metal-hydrogen antibonding character and hydrogen-hydrogen bonding character.[149] This dissociation process has been determined to occur on the femtosecond-to-picosecond timescale for metal dihydride complexes.[43]

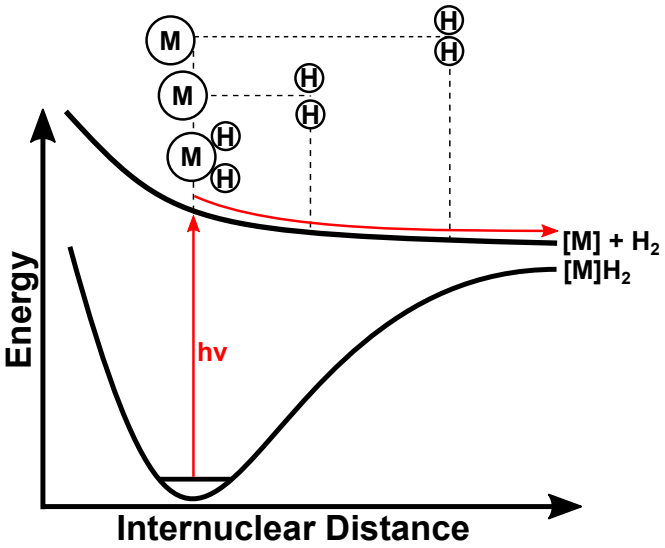

Figure 2.15: Potential energy diagram for the photochemical loss of H_2 from a metal dihydride complex indicating the transition from a bonded ground state to a dissociative excited state.

The 16-electron intermediate metal complex formed following reductive elimination of H_2 is highly reactive and so will participate in further thermal reactions, such as the oxidative addition of small molecules. This can lead to the observation of a degenerate reaction whereby the starting complex is reformed through oxidative addition of a molecule of H_2 (as indicated within Figure 2.14). These degenerate reaction pathways are of great interest for studies involving *para*hydrogen as they provide a clear route to repeatedly produce PHIP enhanced NMR signals in a reproducible manner. The highly reactive nature of the 16-electron intermediate complexes have also seen these dihydride complexes be used as photocatalysts for C-H bond activation.[150–152]

3 Thermal Reaction Monitoring of PHIP Systems

In this chapter, the initial development of PHIP hyperpolarised reaction monitoring protocols on the benchtop NMR spectrometer will be discussed. These initial studies monitor a thermal reaction (rather than a photochemical reaction) as to focus on developing the reaction monitoring procedure itself rather than adding in additional factors such as the design and implementation of an irradiation setup.

PHIP hyperpolarised reaction monitoring has been performed previously using high-field NMR spectrometers but care had to be taken to ensure that the observed enhanced signals within the spectra could be appropriately analysed to yield kinetic parameters for a chemical reaction.[153–155] The currently published literature for PHIP-hyperpolarised reaction monitoring on a benchtop NMR spectrometer, namely studies from Jeong *et al.*[84] and Gołowicz *et al.*,[85] have both shown successful monitoring of product formation over the course of a reaction and in both cases reaction coordinates were obtained. However, neither study included quantitative analysis and so do not present any kinetic parameters, such as rate constants, for the observed systems. This indicates a gap within the currently published research on the assessment of the robustness and validity of quantitative PHIP hyperpolarised reaction monitoring on a benchtop NMR system.

The implementation of a quantitative reaction monitoring procedure within this chapter is performed using a model reaction system, the oxidative addition of H_2 to *trans*-[IrCl(CO)(PPh_3)$_2$]. The choice of this reaction system is discussed in the preliminary section of this chapter, and then, following the implementation of a reaction monitoring procedure, the observed reactivity of this complex is compared to relevant literature studies.

3.1 Model System Development

3.1.1 Vaska's Complex Background

The model system that was chosen for the initial reaction monitoring procedure optimisations was *trans*-[IrCl(CO)(PPh_3)$_2$], which is widely referred to as Vaska's complex. The discovery of this quadrivalent iridium(I) complex is attributed to Vaska and DiLuzio in 1961,[156] as they were the first individuals to correctly formulate the composition of the complex (though the initial synthesis of the complex is attributed to Maria Angoletta).[157,158] Upon its discovery, this complex was observed to have incredible small molecule reactivity, such as with H_2,[159] O_2,[160] and CO[161] under ambient conditions. The adducts formed with these small molecules were of great interest as they were stable enough for full characterisation, had a CO group that could act as an indicator of reactivity and had applicability in homogeneous catalysis[162] and as analogues for important biological molecules.[163]

The reaction of Vaska's complex with H_2 has been studied in-depth, with literature available on the characterisation,[164] kinetics[111] and mechanism (see Section 3.1.2) of the process. Using a well established reaction is advantageous for testing the accuracy of the reaction monitoring procedures that are developed. Furthermore, the reaction has been examined using PHIP hyperpolarisation at high-field, though these studies focused on the observation of hyperpolarised signals and the detection of low concentration reaction byproducts.[165,166] From these studies, the [Ir(H)$_2$(CO)(PPh_3)$_2$Cl] product gave strong signal enhancements that were observable on the NMR timescale.

Looking forward, Vaska's complex is a good starting point for incorporating photochemistry into the reaction monitoring experiments. The photochemistry of Vaska's complex has been studied previously, highlighting that photo-induced reductive elimination of H_2,[43,167] O_2[168] and HCl[169] from their corresponding adduct complexes occurs readily when irradiated by UV-visible light. Starting with a complex with known thermal and photochemical reaction pathways is beneficial as it allows for system optimisations to be carried over and provides a direct route to compare the success of each method. In addition to this, the related iodo-analogue of Vaska's complex, *trans*-[IrI(CO)(PPh_3)$_2$], has been used for photochemical pump - NMR probe experiments at high-field and so this family of complexes are of much

interest for the development of low-field photochemical reaction monitoring methods.[45]

3.1.2 Oxidative Addition of Hydrogen to Vaska's Complex

Vaska's complex, *trans*-[IrCl(CO)(PPh_3)$_2$] (**1**), readily reacts with hydrogen at room temperature. The unsaturated 16e$^-$ metal complex can undergo oxidative addition of H_2 in a concerted fashion to form [Ir(H)$_2$(CO)(PPh_3)$_2$Cl] - a stable 18e$^-$ complex.[111] The reaction passes through a 5-membered transition state where the H_2 molecule binds to the surface of the square planar complex, forcing the complex into a pseudo-octahedral coordination state through displacement of one pair of trans ligands. The presence of two pairs of trans ligands allows for two reaction mechanisms to be followed, with bonding across the the Cl−Ir−CO axis or the P−Ir−P axis resulting in two isomeric products from this reaction: *cis,trans*−[IrH$_2$(CO)(PPh_3)$_2$Cl] (**2a**) and *cis,cis*−[IrH$_2$(CO)(PPh_3)$_2$Cl] (**2b**) respectively (shown in Figure 3.1).[170]

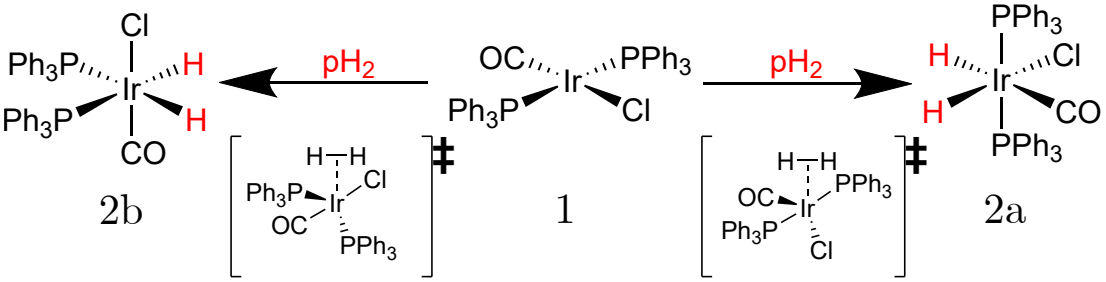

Figure 3.1: Reaction scheme for the addition of *p*H$_2$ to *trans*-[IrCl(CO)(PPh_3)$_2$](Vaska's Complex) highlighting the competing modes of addition.

The selectivity of this reaction is controlled by the favourability of the competing reaction mechanisms. For Vaska's complex, addition over the Cl−Ir−CO axis is strongly preferential. This is evidenced from *ab initio* MO calculations performed by Sargent *et al.*[171,172] on H_2 addition to *trans*−[IrCl(CO)(PH_3)$_2$] and *trans*−[IrCl(CO)(PMe_3)$_2$]. When PH_3 groups were present, a 37.21 kJ mol^{-1} preference for addition over the P−Ir−P axis was calculated. Comparatively, the presence of PMe_3 groups resulted in a 9.51 kJ mol^{-1} preference for addition over the Cl−Ir−CO axis. From this analysis, it was predicted that the π-accepting nature of the PR_3 group was a strong contributor to the favoured mechanism of the reaction, with weaker π-acceptor ligands favouring addition over the Cl−Ir−CO axis.[172] For Vaska's complex (PR_3=PPh_3), which has similar electronic properties to that of

trans−[IrCl(CO)(PMe_3)$_2$] (a Tolman electronic parameter of 2068.4 cm^{-1} compared to 2064.1 cm^{-1}),[173] a similar preference for addition over the Cl−Ir−CO axis is expected. This was verified experimentally by Hasnip *et al.* using PHIP hyperpolarised signals to examine the ratio of the major and minor products of H_2 addition to Vaska's complex. In this study, a ratio of 100:1 for *cis,trans*−[IrH_2(CO)(PPh_3)$_2$Cl] to *cis,cis*−[IrH_2(CO)(PPh_3)$_2$Cl] signals at 295K indicated a preference of 11 kJ mol^{-1} for Cl−Ir−CO addition.[40,165] This selectivity allows for reaction monitoring of the dominant reaction mechanism using NMR. Going forward, reference to [Ir(H)$_2$(CO)(PPh_3)$_2$Cl] will be exclusively referring to the major *cis,trans*−[IrH_2(CO)(PPh_3)$_2$Cl] product.

3.1.3 Practical Considerations

Vaska's Complex is a good choice for the optimisation of reaction monitoring on a benchtop NMR spectrometer. In terms of preparation, the synthesis of the complex is straightforward (shown in Figure 3.2 and detailed within the Section 8.4.1 of the Experimental chapter) and can be easily scaled. Once synthesised, the complex is air stable and does not thermally decompose at room temperature.[160] Therefore, the complex can be stored for long periods without degradation of quality over time.

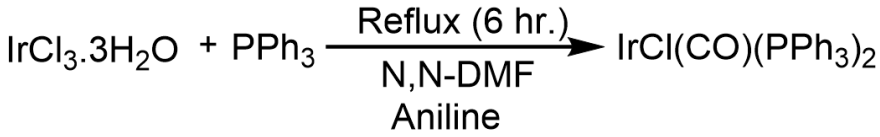

Figure 3.2: Reaction scheme for the synthesis of Vaska's complex, modified from the original report of this method by Collman *et al.*[174]

In terms of practicality, Vaska's complex is a straightforward system to analyse for reaction kinetics. The addition of H_2 to Vaska's complex (Figure 3.3) occurs readily at room temperature with the reaction reaching completion over the course of several minutes. This provides a suitable timescale over which to observe the reaction via NMR. This reaction is also irreversible at temperatures below 343 K and so regeneration of starting material does not need to be accounted for in any analysis performed.[42] Furthermore, the reaction itself is a straightforward bimolecular second-order reaction - the oxidative addition reaction rate is dependent on the concentrations of H_2 and Vaska's complex.[175] Owing to these features, Vaska's complex is a great system with which to monitor pH_2 incorporation over time.

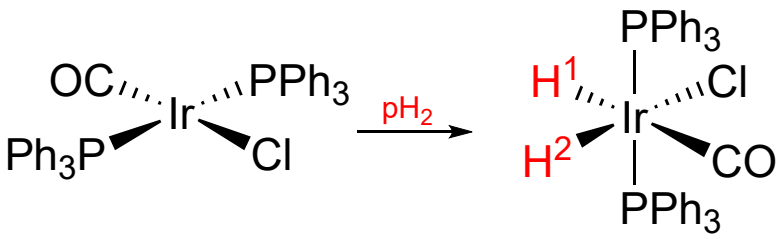

Figure 3.3: Reaction scheme for the oxidative addition of pH$_2$ to Vaska's complex.

3.1.4 Initial NMR Experiments on Vaska's Complex

Initial PHIP experiments were performed using a high-field NMR spectrometer (400 MHz, 9.4 T). Upon initial mixing of Vaska's complex (0.2 mg, 0.43 mM in C_6D_6) and pH$_2$, two strongly enhanced hydride resonances (with a maximum signal-to-noise ratio, SNR, of 296) were observed within the ^{1}H spectra indicating the formation of [Ir(H)$_2$(CO)(PPh$_3$)$_2$Cl] (Figure 3.4a). These hydride resonances were centred at -6.69 ppm and -17.49 ppm and correspond to the hydrides trans to CO (H^1) and Cl (H^2) respectively. The hydride signals appear as triplets of antiphase doublets as they couple to both cis PPh$_3$ groups ($J_{HP_{cis}}$ = 17.6 Hz for H^1 and 14.1 Hz for H^2) and each other (J_{HH} = 4.6 Hz).

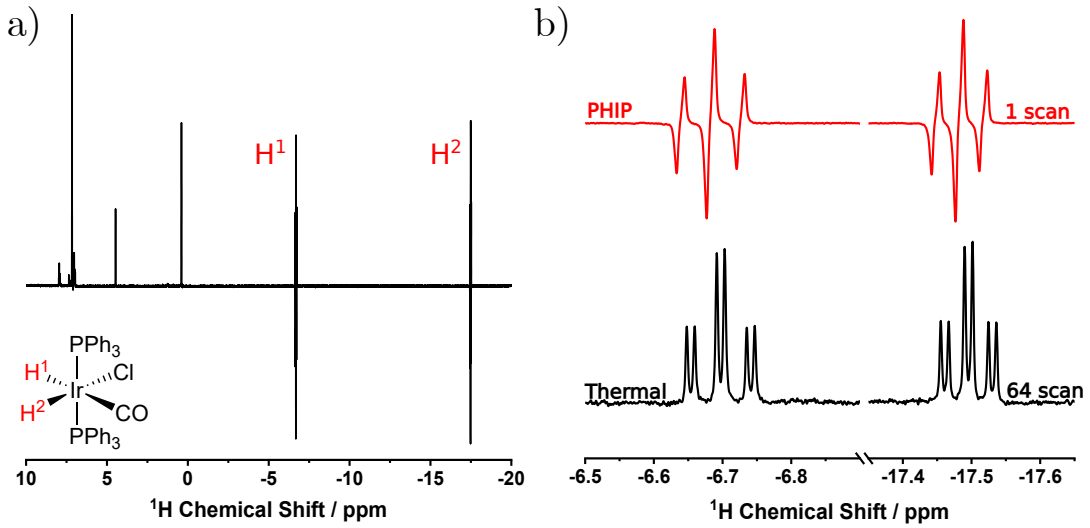

Figure 3.4: ^{1}H spectra obtained at 400 MHz (9.4 T) following the addition of pH$_2$ (4 bar absolute) to Vaska's complex (0.43 mM) showing (a) the full spectrum and (b) the hydride region. Within (b), a thermally-polarised spectrum recorded after completion of the reaction is shown in black.

Upon completion of the reaction, a 64-scan ^{1}H spectrum was obtained for the

sample showing the presence of thermally-polarised $[Ir(H)_2(CO)(PPh_3)_2Cl]$ (Figure 3.4b). This thermally-polarised spectrum has a maximum SNR of the hydride groups of 67. While this value is not directly comparable to that recorded with PHIP (due to this spectrum being recorded following reaction completion and with 64 scans), the over 4-fold signal improvement observed with pH$_2$ highlights the impressive enhancements that can be obtained using PHIP hyperpolarisation.

When a 0.2 mg sample of Vaska's complex (0.43 mM in C_6D_6) is reacted with pH$_2$ and observed at low-field (43 MHz, 1 T), strong enhancements are observed for the hydrides at -6.69 and -17.48 ppm with a maximum SNR of 98.5 (shown in Figure 3.5). Even with the decreased chemical shift dispersion at lower magnetic fields, these hydrides are clearly distinct from all other peaks within the spectrum and from each other. This is advantageous for analysis as well resolved peaks can be integrated in a straightforward manner.

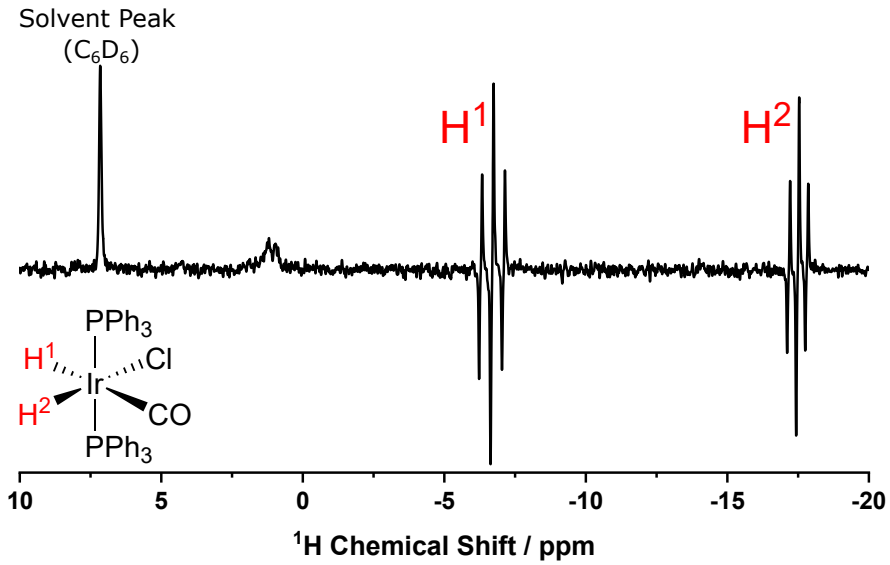

Figure 3.5: ^{1}H spectrum recorded at 43 MHz (1 T) of $[Ir(H)_2(CO)(PPh_3)_2Cl]$ (0.43 mM) following pH$_2$ (4 bar absolute) addition to Vaska's complex.

Obtaining a thermally polarised spectrum of Vaska's complex at low-field required a more concentrated sample (4.3 mM, 2.0 mg of Vaska's complex) and several thousand more scans (4096 scans) than at high-field. A comparison between this spectrum and the one-scan PHIP spectrum is shown in Figure 3.6. This low level of signal produced by thermally polarised Vaska's complex is promising for reaction monitoring as it means that the background signal produced from any $[Ir(H)_2(CO)(PPh_3)_2Cl]$ already in solution will be negligible compared to that produced by a PHIP-hyperpolarised species.

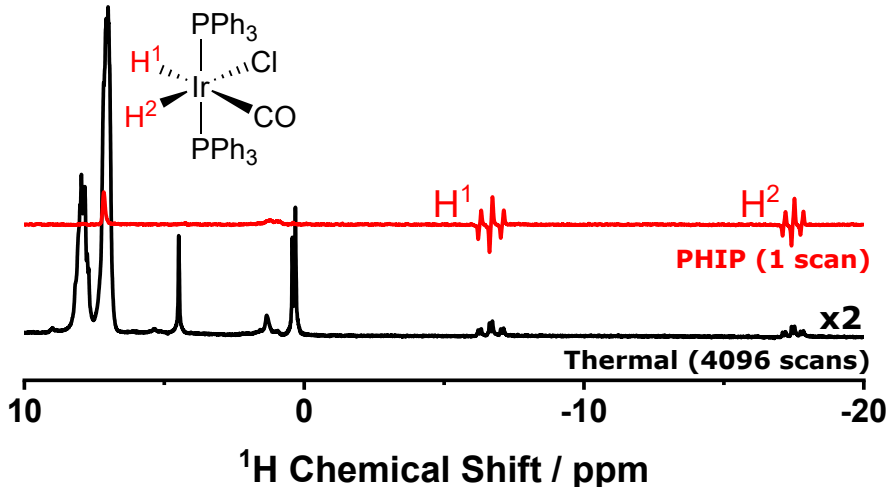

Figure 3.6: Comparison between ^{1}H spectra recorded for $[Ir(H)_2(CO)(PPh_3)_2Cl]$ recorded for a PHIP hyperpolarised sample (0.43 mM) in 1 scan (red) and a thermally-polarised sample (4.3 mM) in 4096 scans (black).

One final preliminary test was performed to check the variation in PHIP hyperpolarised signal over the course of the reaction. A ^{1}H spectrum was recorded every minute for 11 minutes over the course of the reaction of a 0.2 mg (0.43 mM) Vaska's complex sample with pH$_2$ (4 bar absolute). The spectra for the first 8 minutes of the reaction are given as Figure 3.7. From these spectra, a strong decay in observed signal is observed across the first 5 minutes, with a minimal amount of signal persisting until between 7 and 8 minutes. This reaction timescale is promising as it is not too long as to limit repeat measurements but it is not too short as to be difficult to monitor using NMR. Following this experiment, the sample was degassed again and filled with fresh pH$_2$. Upon shaking the sample, no signal was observed within the ^{1}H spectrum recorded. This confirms experimentally that the reaction is irreversible at 28.5 °C and thus goes to completion following the initial addition of pH$_2$.

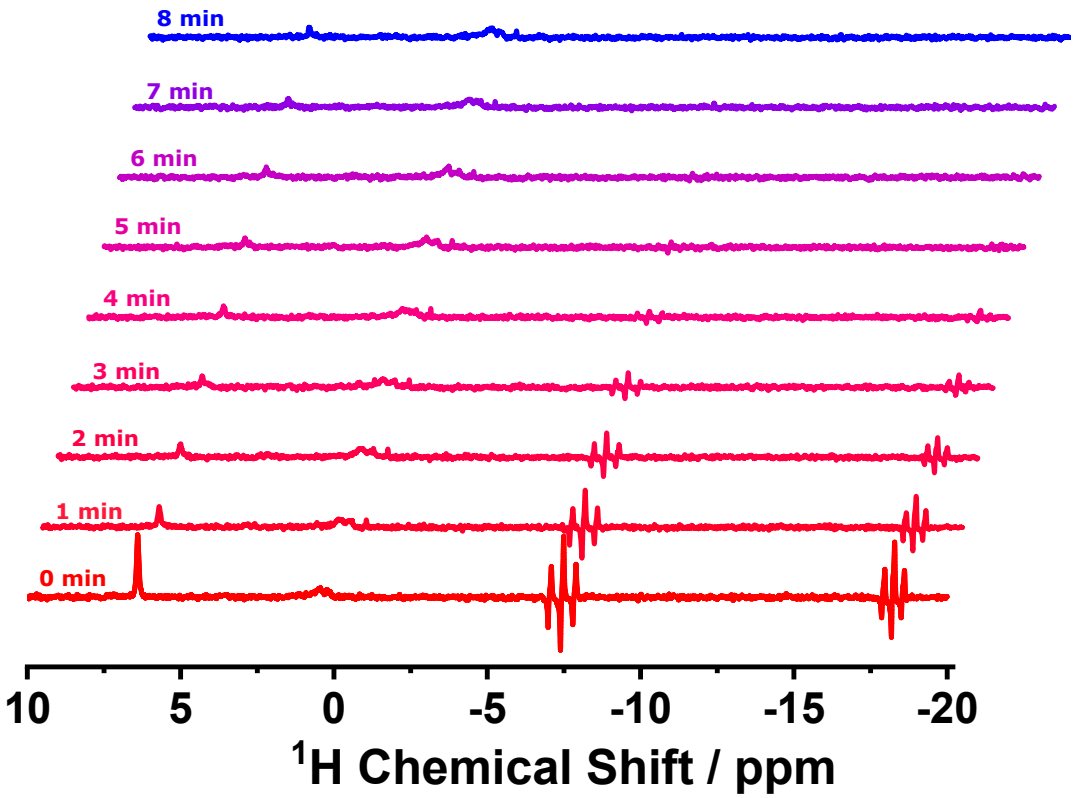

Figure 3.7: Series of ^{1}H spectra recorded at 1 T (43 MHz) monitoring the progress of the addition of pH$_2$ (4 bar absolute) to Vaska's complex (0.43 mM) over 8 minutes.

3.2 Methodology Development

3.2.1 Sample Preparation

Prior to performing reaction monitoring experiments, the required quantity of Vaska's complex was weighed out and then transferred into a glovebox under an N_2 atmosphere. The complex was then dissolved in C_6D_6 to form a bulk solution from which 0.6 mL aliquots were transferred into NMR tubes fitted with J Young taps. Unless otherwise specified, samples were prepared to have a concentration of Vaska's complex of 0.43 mM (0.2 mg). Each sample was degassed using a freeze-pump-thaw method to store them under vacuum prior to experimentation.[176]

To perform each reaction monitoring experiment, the degassed sample is placed into the spectrometer to thermally equilibrate for at least 10 minutes, during which time a ^{1}H spectrum is run to ensure starting material purity. Following this, the

sample is removed from the spectrometer and placed under a pH_2 atmosphere (4 bar absolute). The sample is then shaken for 5 seconds and re-inserted back into the spectrometer, after which data collection can be performed.

3.2.2 Pulse Sequence Design

For the reaction monitoring experiment, a series of ^1H spectra need to be acquired with the exact same parameters over the course of the reaction. One key requirement of the pulse sequence is accurate internal timings to ensure that spectra are collected at regular, well-defined intervals along the reaction coordinate. To achieve this, a pseudo-2D pulse sequence was designed during which a series of spectra are acquired following 45° excitation pulses (Figure 3.8a). A consistent evolution delay (t) was used between successive pulses to ensure that reaction progress was probed at regular intervals as defined by the user. This pulse sequence is a variation of the ROCHESTER (Rates of Catalytic Hydrogenation Estimated Spectroscopically Through Enhanced Resonances) pulse sequence that was developed for monitoring catalytic hydrogenation using PHIP on high-field NMR spectrometers.[155]

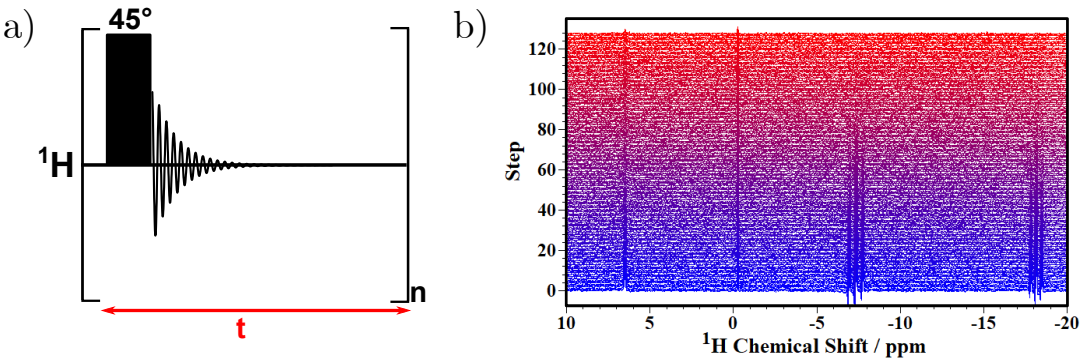

Figure 3.8: (a) Pulse sequence for reaction monitoring experiment showing the acquisition delay, t, and number of loops, n, alongside (b) an example output pseudo-2D stacked spectrum.

To ensure the evolution delay was consistent, the internal clock of the Spinsolve software is checked before and after each spectral acquisition. This duration is subtracted from the requested delay from the user input and then the pulse sequence is paused for the remainder of the delay. To avoid increased computational load during data collection, all plotting and saving of data occurs after the pulse sequence is complete (when left within the experiment, each subsequent

overwriting of the save file increases the time taken for each experimental step). Overall, this allows for an excellent consistency of experimental timings to within ±0.01 s of the required evolution delay. For the reaction monitoring experiments, an acquisition time of 0.8192 s (2048 points, 400 μs dwell time) allowed for down to a 1 second evolution delay to be used (on average, computation added another 0.13 seconds to the pulse sequence loop). Unless otherwise stated, the parameters of t = 5 s and n = 128, giving a total experiment time of 10.7 minutes, were used. The pulse sequence generates a pseudo-2D dataset containing a stacked plot of 1D ^{1}H spectra along the reaction time coordinate (Figure 3.8b).

3.2.3 Data Processing

To elucidate kinetic information for the pseudo-2D dataset, the change in integrals over time for the hydride peaks needs to be measured. By looking at the change in integral over time (shown in Figure 3.9a), the change in PHIP activity over the course of the reaction is observed.

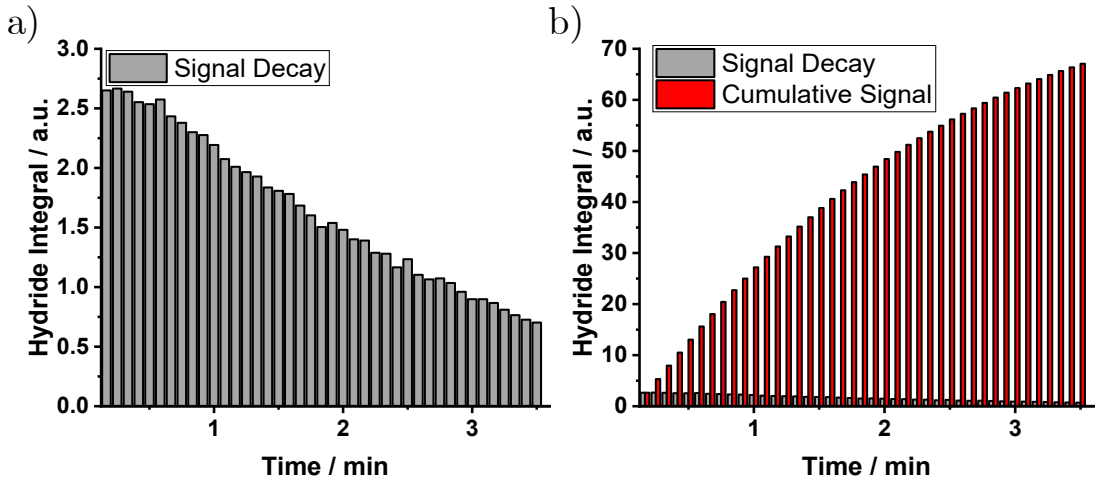

Figure 3.9: (a) PHIP signal decay (measured via hydride peak integrals) and (b) cumulative PHIP signal measured during the reaction of Vaska's complex with pH$_2$.

Each datapoint in Figure 3.9a represents the amount of product that has been formed since the last NMR spectrum was obtained, with one unit of hyperpolarised signal corresponding to the formation of one product molecule. Therefore, this data represents the instantaneous rate at each point during the reaction which decreases over time as starting materials are consumed. It is not important to know the exact value for one unit of hyperpolarised signal as it is the change in amount of signal that

is important rather than the absolute value. Therefore we have a measurement of how much product was formed since the last NMR spectrum, as any previously formed product will have relaxed back to thermal equilibrium and so will not contribute to the hyperpolarised signal. To convert this PHIP activity into rate of product formation, it is necessary to accumulate the integrals of each successive data point as to reflect the total product formed as a function of time. Through this, a product formation curve is obtained (Figure 3.9b).

The first step of processing the pseudo-2D dataset is to discard the first spectrum that is recorded. This is necessary as the initial 5 second window involves the sample travelling from a region of weak magnetic field (external to the spectrometer) to a region of relatively strong magnetic field (within the spectrometer). During this initial window, any PHIP reactions occurring in the weak magnetic field will have ALTADENA character which will interfere with and obscure the anti-phase peaks of PASADENA character once the sample is placed within the spectrometer.

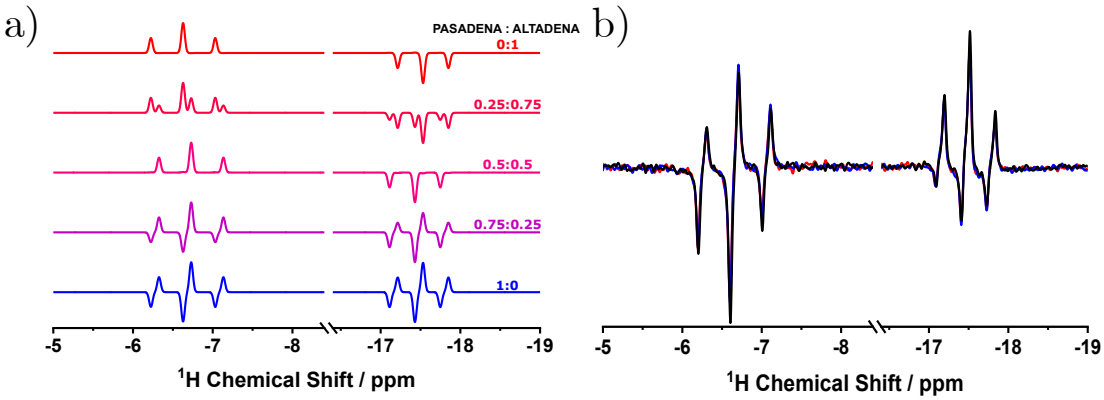

Figure 3.10: (a) Spinach simulations showing the spectra resulting from different PASADENA:ALTADENA ratios and (b) the initial spectrum observed upon reaction monitoring.

NMR simulation studies for Vaska's complex (using the Spinach NMR simulation package developed for use in MATLAB by Ilya Kuprov and co-workers)[177] were used to evaluate how the proportion of PASADENA and ALTADENA character within the sample would affect the appearance of the spectrum. Using the chemical shift and J coupling constant information recorded at 400 MHz, a set of simulations were performed varying the proportions of the two PHIP regimes from full PASADENA character (1:0) to full ALTADENA character (0:1). These simulations are shown in Figure 3.10a. Comparison of these simulated spectra to the experimentally recorded first spectrum from three repeat studies (Figure 3.10b) highlight that there is consistently a small but non-negligible contribution of

ALTADENA hyperpolarisation within the first spectrum produced. Following this initial step, the reaction will take place exclusively under PASADENA conditions and as such the data is directly comparable to itself.

To process the data, the second spectrum is used as a reference. This spectrum is phased, peak picked and then integration regions are determined for each of the peaks within the hydride multiplets. This gives a total of 12 integration regions (6 for each triplet of antiphase doublets). The two hydrides are considered together as the concerted pairwise addition of pH$_2$ ensures that they will reflect the same rate. The reference phase correction is applied to the psuedo-2D spectrum and then each integration window is applied vertically across the dataset. The output of this analysis is a vector containing the integral of each step of the reaction monitoring experiment for that peak. The 12 integral vectors are then accumulated to give a total hydride signal for each spectrum over time (a plot of which is shown in Figure 3.11a).

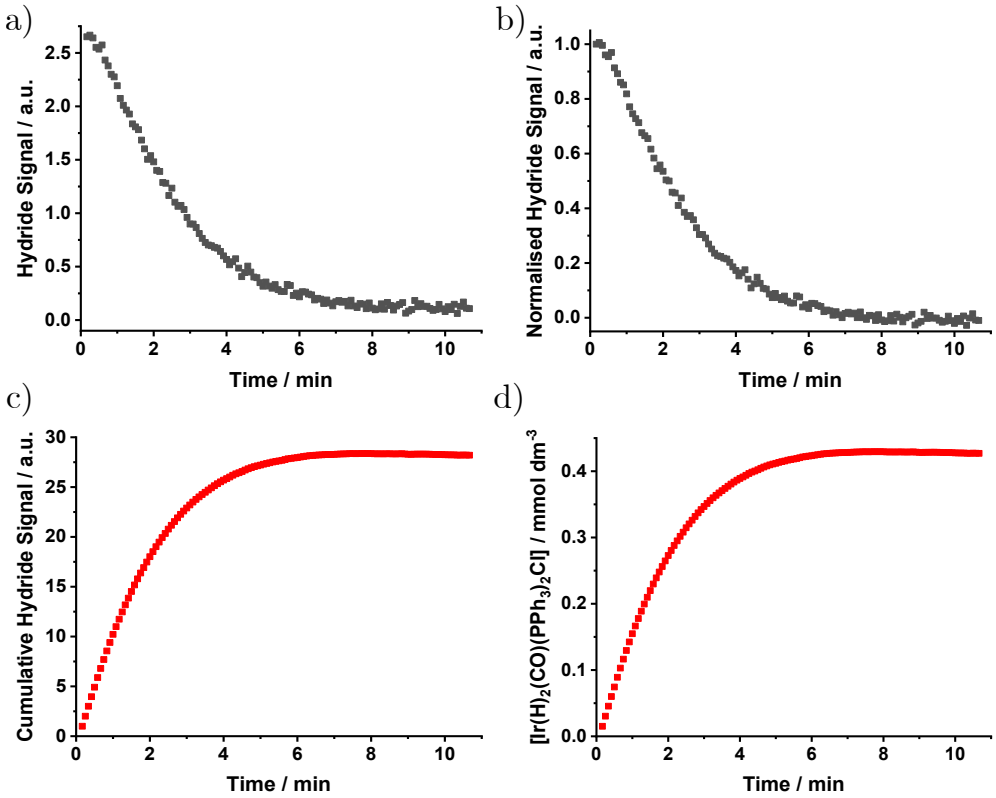

Figure 3.11: Dataset analysis showing the (a) hydride signal decay from integral analysis, (b) normalised hydride signal decay, (c) product formation curve and (b) product formation curve scaled to the known final concentration of the product.

The output data is first baseline corrected and normalised to the first datapoint of the series (Figure 3.11b). A noise correction is then applied to account for the

inherent spectral noise within the integration regions which gives spectra that have no hyperpolarised signal non-zero integrals. This correction is performed by subtracting the average integrals of the last 25 datapoints from all integrals in the series. To account for this requirement experimentally, all reaction monitoring experiments are performed past the point of reaction completion to ensure sufficient spectra are acquired.

Once normalised, the hydride integrals are accumulated to give a product formation curve (Figure 3.11c). To convert the accumulated hydride integrals into concentrations, Equation 3.1 is used where $[P]_t$ is product concentration at time t, $[SM]_0$ is starting material concentration at t = 0 and I_t/ I_f are the cumulative integrals at time t and of the final datapoint respectively.

$$[P]_t = [SM]_0 \times \frac{I_t}{I_f} \tag{3.1}$$

This equation is based upon the knowledge that the starting concentration of Vaska's complex in the solution must be equal to the final concentration of the product. This is known because the reaction goes to completion - any refilling of the headspace of the NMR tube with fresh pH$_2$ does not produce further PHIP enhanced signals (confirmed by examination of spectra recorded at both high-field and low-field). By setting the final concentration to $[\mathrm{SM}]_0$, all other concentrations can be calculated based upon the ratio of the current cumulative integral (I_t) to the final cumulative integral (I_f). This data is then plotted to show the growth in hydrogenated product over the course of the reaction (Figure 3.11d) which can be analysed to elucidate kinetic parameters from the reaction.

3.2.4 Automation of Data Processing

When performed manually, the analysis of reaction monitoring data outlined above is both time-consuming and subject to human errors, particularly in the judgement of peak areas for integration. A more rigorous automated analysis method is desirable, especially when broadening the scope of applications for this technique as this would allow for more complex spectra to be analysed - such as those from complex mixtures or where peak resolution is much poorer. To achieve this goal, a new data processing macro was designed to automatically process the

psuedo-2D dataset to produce a concentration curve (shown in Figure 3.11d).

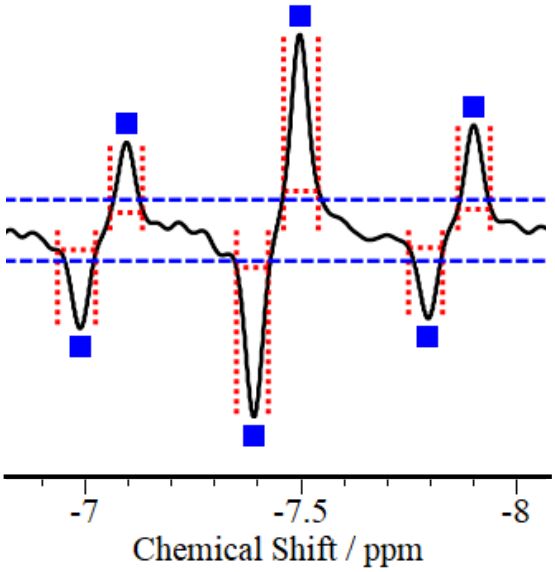

Figure 3.12: Example output of the automatic processing macro, highlighting peak picking (blue dashed lines), integration (red dotted lines) and peak grouping (blue squares) subroutines.

Within the data processing macro, there is an initial parameter loop and then a larger analysis loop. The initial loop is a quick analysis of a 1D reference spectrum allowing for the correct parameters to be determined before doing the full analysis of the pseudo-2D dataset. After providing the location of the raw data to the macro, the parameter loop extracts the second spectrum in the pseudo-2D dataset and phases it. A peak-picking subroutine is then performed that selects for peaks if they are greater than a threshold signal value (set by the user). As the spectrum contains anti-phase hydride signals, the threshold sweep is performed using a positive and negative threshold (shown as the blue dashed lines in Figure 3.12). From the peak list, only peaks that could potentially be hydride peaks (those below 0 ppm) are stored. To remove erroneous peaks, this peak list is compared to a list of peaks to ignore (provided by the user) to ensure only the hydrides of interest are processed. Once all peaks are identified, an integration subroutine is used to generate integration regions for each peak (shown as red dashed lines in Figure 3.12) - more details about this step are given below. At this point an optional grouping script can be performed that allows for peaks to be grouped into discrete sets (highlighted in Figure 3.12 as the blue squares above each peak) - this allows for spectra containing hydrides from multiple species to be differentiated and analysed individually. From this initial loop, a table of peak chemical shifts and integration regions is output to the command line for the user to check prior to full analysis. Upon full analysis, all previous steps are

performed but then the integration windows are applied across the pseudo-2D dataset to acquire the integral changes for each hydride peak. Once acquired, the integrals are converted into a concentration over time for the system (using the steps outlined in Section 3.2.3) with all values saved into an output csv file.

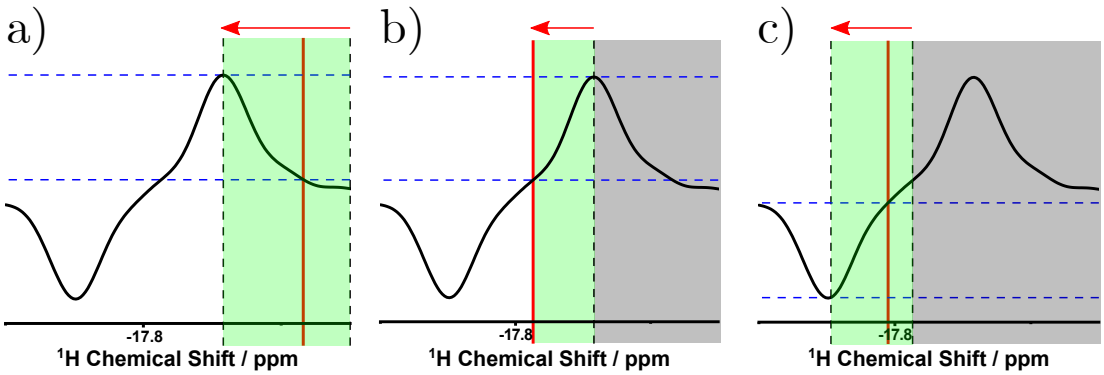

Figure 3.13: Cartoon for the integration window code that highlights (a) the region of interest for the right-hand side of a peak, (b) the left-hand side of a peak and (c) the right-hand side of the following peak. In each case, a green background represents the region being scanned, a grey background represents an ignored region and solid red lines indicate the value being saved by the code. Black and blue lines indicate a limit imposed within the code in terms of chemical shift and peak amplitude respectively.

The integration subroutine was designed to allow individual integration windows to be determined for each peak that could then be applied across the pseudo-2D dataset. The prior peak peaking subroutine provides a list of chemical shifts for which integration regions need defining. Once peak peaking is performed the spectrum is scanned across from lowest chemical shift of the spectrum (defined by the spectral width) up until the chemical shift of the first peak (Figure 3.13a). Within this window, the right-hand side of the integration window needs to be defined. This right-hand limit is defined by the first datapoint that has an amplitude greater than a threshold value, where the threshold value is the maximum amplitude of the peak multiplied by a user input scaling factor (for example the first point that reaches 10% of the peak height). After the right-hand side of the peak is defined, the left-hand side of the peak needs selecting. To find this value, the code starts scanning chemical shifts starting from that for the peak of interest. The condition for the left-hand limit is that it must be the final datapoint that is above the previously determined threshold factor (Figure 3.13b). One caveat to this is that a cut-off case must be established to prevent the overwriting of this value each time that condition is met later within the spectrum. To address this, a limit is added whereby the value cannot be overwritten after the first instance where the amplitude changes sign (for anti-phase peaks) or reaches a point of inflection (for same-phase peaks). After defining the right and left limits, it is facile to calculate the required width of the integration window for that

peak. This process is repeated for each hydride, from most to least negative, with the left-hand side of the previous peak acting as the initial limit from which the code should begin searching from (Figure 3.13c).

To highlight any noticeable improvements to data quality through use of automation, a set of nine reaction monitoring experiments were analysed manually and automatically and then compared (the full details of kinetic analysis are given within the next section and are not needed for this comparison). Automatic analysis carries a higher consistency between the experiments with the standard deviation of the data being 2.7% of the mean rate constant calculated compared to 3.7% with manual analysis. The mean rate constant itself also reduced by 3.0% upon automation of the analysis indicating a slight overprediction in values when manually analysed. Overall, the automation of the analysis allows for rapid and more robust analysis of the large datasets produced through the reaction monitoring experiment.

3.2.5 Developing the Kinetic Model

Once the data has been processed to give a product formation curve, it can be analysed to determine the rate constants for the oxidative addition of H_2 to Vaska's complex (Equation 3.2). Within the available literature, it is known that this oxidative addition reaction is a second-order process with a first-order dependence on both the concentrations of Vaska's complex and H_2.[175] This can be summarised by a rate equation (Equation 3.2) in terms of product formation. For ease of readability in this section, the concentration of Vaska's complex will be given as [Vaska] while the concentration of the product, $[Ir(H)_2(CO)(PPh_3)_2Cl]$, will be written as $[Vaska(H)_2]$.

$$IrCl(CO)(PPh_3)_2 + pH_2 \longrightarrow IrCl(H)_2(CO)(PPh_3)_2 \tag{3.2}$$

$$\frac{d[Vaska(H)_2]}{dt} = k_2[Vaska][H_2] \tag{3.3}$$

One important value within this equation that is currently unknown is the concentration of H_2 dissolved into the solution. To calculate this, the solubility of H_2

in C_6H_6 at 28.5 °C is required. Using a series of mole fractions for H_2 in C_6H_6 over the temperature range of 283.15 - 338.15 K at 1 atm (taken from the IUPAC-NIST Solubility Data Series),[178] interpolation of a mole fraction of 2.680×10^{-4} at 28.5 °C was possible (Figure 3.14).

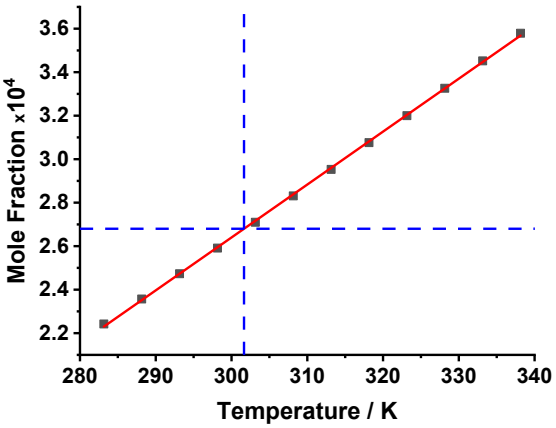

Figure 3.14: Variation of mole fraction of H_2 dissolved in C_6H_6 over the temperature range 283.15 - 338.15 K at 1 atm. Blue line indicates the mole fraction at 28.5 °C (301.65 K). The mole fraction data is obtained from the IUPAC-NIST Solubility Data Series.[178]

To calculate the concentration of H_2 in the solution, the mole fraction can be used to calculate the moles of H_2 from the moles of C_6H_6 present within the sample. Dividing this by the volume of the sample will give $[H_2]$ at 1 atm within the sample.[179] Equation 3.4 is a condensed version of this calculation where $C_{(g)}$ is the gas concentration, ρ_l is the density of the solvent, M_l is the molar mass of the solvent and $x_{1(g)}$ is the mole fraction of the gas. For this system, $\rho_{C_6H_6}$ = 874 g dm^{-3} and $M_{C_6D_6}$ = 78.11 g mol^{-1}. Using the previously determined mole fraction for H_2, this gives a concentration of 3.00×10^{-3} M atm^{-1} (with the atm^{-1} being present as the data used was recorded at 1 atm).

$$C_{(g)} = \frac{\rho_{(l)}}{M_{(l)}} \times x_{1(g)} \tag{3.4}$$

To convert this value to the required pressure (experiments were performed at 4 bar), the $[H_2]$ is multiplied by the pressure of the system (using the proportionality shown in Henry's Law).[179] For a system at 4 bar, this gives a final concentration for H_2 of 0.0118 M. One assumption made during this calculation is that the temperature of the sample upon H_2 dissolution will be exactly 28.5 °C - the validity of this assumption will be explored in Section 4.3.

To simplify the kinetics of the system, a pseudo-first order kinetic model can be used. In order for a pseudo-first order kinetic assumption to hold, there needs to be a high excess of one of the reagents throughout the course of the reaction. A 0.2 mg sample of Vaska's complex in 0.6 mL C_6D_6, has a concentration of 0.427 mM. Using the concentration of H_2 calculated above, this gives a 28-fold excess of pH$_2$ within the solution.

To ensure that pseudo-first order conditions are met with this reactant ratio, a plot of ln(*trans*-[IrCl(CO)(PPh_3)$_2$]) against time across the course of the reaction (640 seconds, 128 steps) is required with the expectation of a linear relationship between these two terms. The concentrations of Vaska's complex throughout the experiment were calculated using Equation 3.5 and plotted as Figure 3.15a. From this data a plot of ln(*trans*-[IrCl(CO)(PPh_3)$_2$]) against time (Figure 3.15b) was constructed to assess the linearity of this relationship. During the first 5 minutes of the reaction, a linear fit provides a good model for the data. Outside of the first 5 minutes, a deviation from linearity is observed. This is attributed to the increasing contribution of noise within the low concentration values as the reaction reaches completion. From this experiment, it was rationalised that it was valid to use a pseudo-first order kinetic model as the reaction closely follows an exponential decay across the majority of the reaction coordinate, with deviations in later datapoints likely originating from noise within the acquired spectra rather than a breakdown of pseudo-first order conditions.

$$[\text{Vaska}]_t = [\text{Vaska}]_0 - [\text{Vaska}(H_2)]_t \tag{3.5}$$

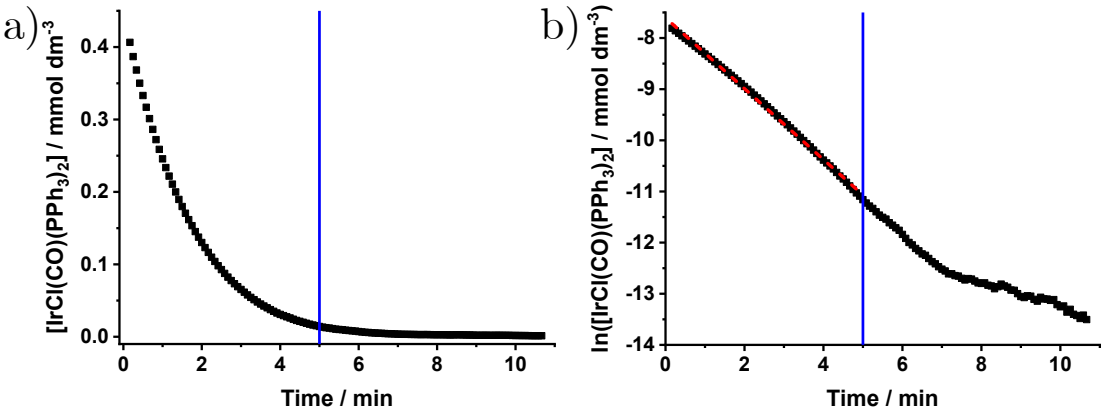

Figure 3.15: Starting material decay curve for the oxidative addition of pH$_2$ to Vaska's complex (0.2 mg, 0.43 mM) portrayed in (a) linear and (b) logarithmic plots to determine pseudo-first order reaction kinetics. A linear fit is shown for the first five minutes of the reaction in (b) by a dashed red line.

Employing pseudo-first order kinetics allows for the rate equation given in Equation 3.3 to be simplified to have sole dependence upon the concentration of Vaska's complex. In this case, the observed effective rate constant is the product of the second-order rate constant and the concentration of H_2, (as shown in Equation 3.6).

$$\frac{d[\text{Vaska(H)}_2]}{dt} = k_{obs}[\text{Vaska}] \quad \text{where} \quad k_{obs} = k_2[\text{H}_2] \tag{3.6}$$

The value of k_{obs} can then be extracted from the fitting of a monoexponential recovery function (Equation 3.7) to the product formation data. An example of this is shown in Figure 3.16.

$$[\text{Vaska(H)}_2]_t = [\text{Vaska(H)}_2]_0(1 - \exp(-k_{obs}t)) \tag{3.7}$$

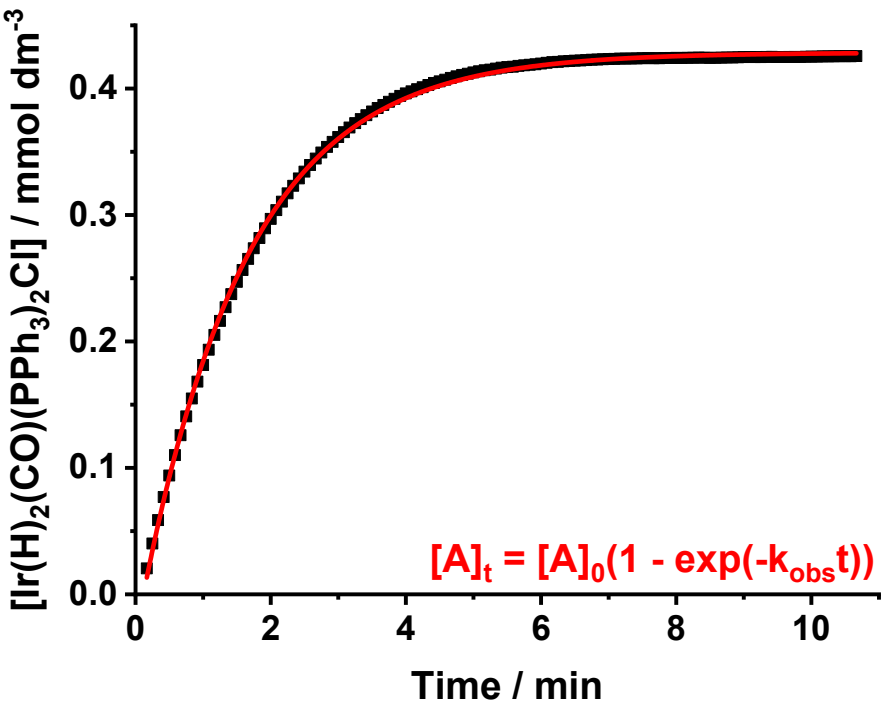

Figure 3.16: Example fitting of a monoexponential recovery function to a product formation curve in order to calculate the pseudo-first order rate constant, k_{obs}.

The second-order rate constant (k_2) for the hydrogenation reaction is then derived by dividing k_{obs} by the concentration of pH_2 (Equation 3.8). The value of $[pH_2]$ used in all calculations was the previously derived value from literature of 11.8 mM.

$$k_2 = \frac{k_{obs}}{[H_2]} \tag{3.8}$$

3.2.6 Sample Regeneration

Within the reaction monitoring experiments, pH$_2$ binds into Vaska's complex to form enhanced hydride signals leading to chemical alteration of the starting material. The irreversible nature of this process at room temperature limits each sample to a single exposure to pH$_2$ before it is completely consumed and unable to be reused. In the interest of reducing the potential wastage of starting materials for the following validation studies (to align more closely with green chemistry principles)[180] and to open up the possibility of testing data reproducibility within a sample, the regeneration of spent samples was considered.

It is well documented within the literature that the oxidative addition of H_2 to Vaska's complex becomes a reversible process at temperatures above 343 K.[42] The position of equilibrium for this process was exploited to attempt the regeneration of the pure starting material. A fully hydrogenated sample of [Ir(H)$_2$(CO)(PPh$_3$)$_2$Cl] was evacuated (to remove any remaining pH$_2$ within the NMR tube headspace), placed under an N_2 atmosphere and heated to 343 K in a water bath for 10 minutes. This cycle was repeated three times before the sample was evacuated a final time. During this process a notable colour change from colourless to pale yellow was observed which indicated the presence of unreacted Vaska's complex within the solution.

To quantify the reversibility of this process, ^{1}H NMR spectra were recorded before and after the regeneration process on a 9.4 T NMR spectrometer (given below in Figure 3.17). As indicated within the proton spectra, there is a significant reduction of 76% in the hydride signal for the [Ir(H)$_2$(CO)(PPh$_3$)$_2$Cl] product. However, owing to the fact that this process is not completely efficient, this could impact the further reactivity of the sample and would affect the reproducibility of the analysis as the concentration of the reactive species following regeneration will be unknown prior to reacting. Overall, due to the disadvantages of the partial regeneration of the sample it was concluded that the preparation of fresh samples for each reaction monitoring experiment would produce the most consistent and valid results.

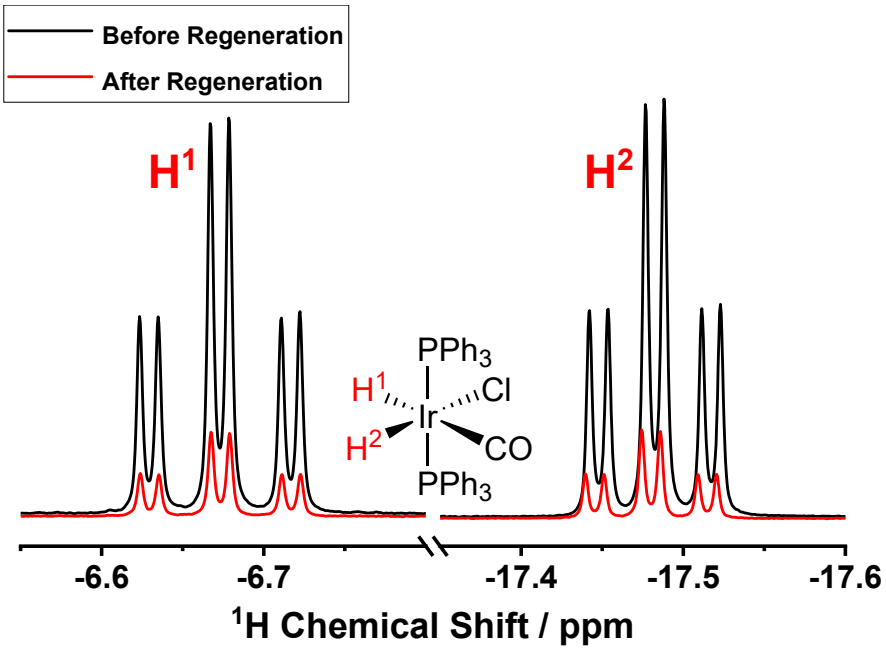

Figure 3.17: Enhanced hydride region of a ^{1}H NMR spectrum for $[Ir(H)_2(CO)(PPh_3)_2Cl]$ both before (black) and after (red) the regeneration of the starting material, recorded at 400 MHz (9.4 T).

3.3 Initial Reaction Monitoring Experiments

3.3.1 Initial Vaska's Complex Reaction Monitoring

A series of three samples of Vaska's complex (0.2 mg, 0.43 mM) were reacted with pH$_2$ and monitored using the experimental method outlined within Section 3.2. The results of the automated analysis of these experiments are given as a product formation curve (Figure 3.18) and as a set of rate constants (Table 3.1). From this data there is a very high constancy within both the product formation curves that are observed and in rate constant values that are obtained. This high reproducibility is exemplified by the 1% standard error that is seen for the set of k_2 second-order rate constants. Therefore these initial experiments appear to indicate that the experimental method is suitable for monitoring this system in a robust and reproducible manner.

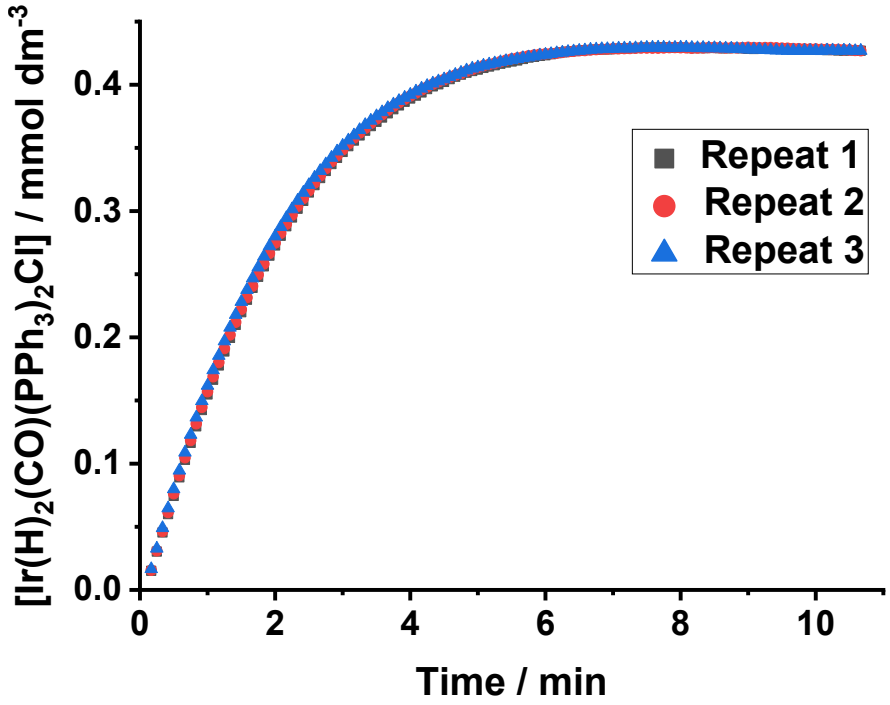

Figure 3.18: Product formation curves for the three repeat measurements for the oxidative addition of pH$_2$ to Vaska's complex (0.2 mg, 0.43 mM).

Table 3.1: Pseudo-first order (k_{obs}) and second-order (k_2) rate constants for the three repeat measurements for the oxidative addition of pH$_2$ to Vaska's complex (0.2 mg, 0.43 mM).

Experiment	1	2	3	Average
k_{obs} / s^{-1}	0.0093	0.0092	0.0095	(0.00935 ± 0.00009)
k_2 / dm^3 mol^{-1} s^{-1}	0.787	0.783	0.807	(0.792 ± 0.008)

3.3.2 Comparison to Literature

To quantify the accuracy of the second-order rate constant obtained from the initial NMR reaction monitoring of Vaska's complex, a comparison to literature was performed. Due to the fixed temperature of 28.5 °C inside the Spinsolve NMR spectrometer, the expected rate constant at this temperature was interpolated from a series of rate constants obtained across a range of temperatures (20 - 35 °C) taken from a study performed by Chock *et al.*[111] This study calculated k_2 rate constants for the addition of H_2 to Vaska's complex by measuring the rate of uptake of H_2 gas at a constant pressure.

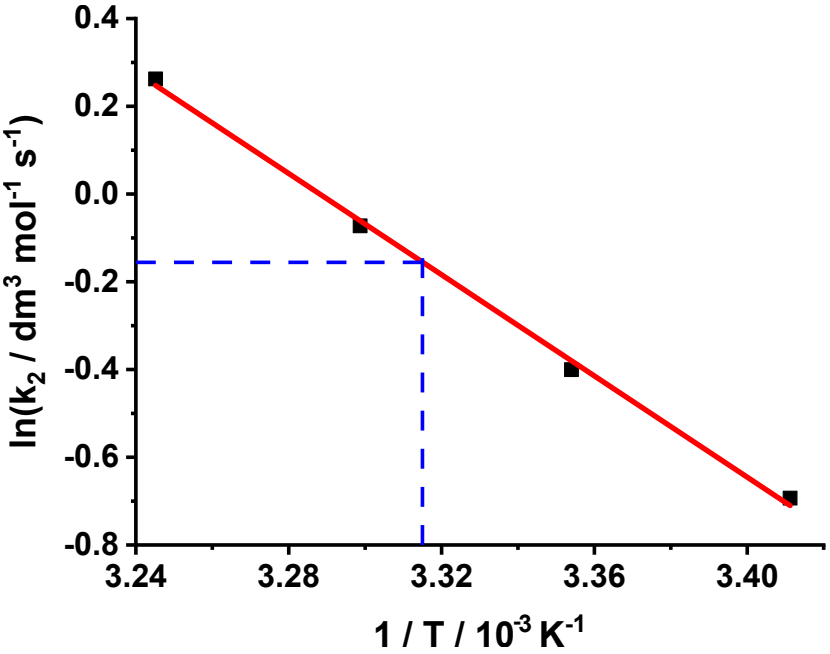

Figure 3.19: Arrhenius plot of literature rate constants for the oxidative addition of H_2 to Vaska's complex in the range of 20 - 35°C to determine k_2 at 28.5 °C.[111]

A plot of ln(k_2) against 1/T was constructed from the literature data (Figure 3.19) and fitted by linear regression analysis. The line of best fit created by this analysis was used to determine a value of k_2 at 28.5 °C of (0.86±0.03) $dm^3\ mol^{-1}\ s^{-1}$. This value is in good agreement with the experimentally determined rate constant (with a percentage difference of 8%) and so this method of analysis was deemed to be appropriate for this chemical system.

3.4 Conclusions

In this chapter, a procedure for monitoring oxidative addition of pH$_2$ into a metal complex through PHIP hyperpolarised NMR was developed for a benchtop (1T, 43 MHz) NMR spectrometer. Within the procedure, the development of a pseudo-2D pulse sequence and data processing macros enabled automatic collection and processing of ^{1}H spectra collected over the course of a reaction. This enabled reaction kinetics to be analysed in a quantitative fashion to produce rate constants for the process being observed.

This procedure was used to monitor the formation of $[Ir(H)_2(CO)(PPh_3)_2Cl]$ from the reaction between pH$_2$ and Vaska's complex. Through analysis of the observed

enhanced hydride resonances, reproducible and accurate kinetic parameters for the reaction were obtained that showed good agreement with the expected literature values. This finding supports the underlying principle of this technique that the change in PHIP hyperpolarised signal across the reaction coordinate is directly proportional to the rate of product formation and so can be used to quantify the kinetics of a reaction. Providing further validation of this statement is the focus of Chapter 4.

4 Validating Thermal Reaction Monitoring using PHIP

In this chapter, the reaction monitoring procedure developed in Chapter 3 is evaluated against several key experimental parameters in order provide further validation that the method is robust and able to produce accurate quantitative information. This is important to determine under what conditions quantification breaks down as to establish the wider applicability of the method.

The validation studies performed were done using *trans*-[IrCl(CO)(PPh_3)$_2$] and investigated the impact of each parameter on the observed NMR spectra and the calculated rate constants. The first studies performed related to the underlying spin physics of the chemical system, namely the impact of hyperpolarised signal relaxation (Section 4.1) and of thermal background signal (Section 4.2). Two physical parameters were also investigated, the impact of sample temperature (Section 4.3) and the level of enrichment of the pH$_2$ used (Section 4.4). In each case, experiments were performed to assess whether the parameter has a non-negligible impact on the reaction monitoring experiment and routes to mitigate the observed effects are explored.

In the final section of this chapter, a further set of studies were performed on complex mixtures containing derivatives of *trans*-[IrCl(CO)(PPh_3)$_2$] with different phosphine ligands. The introduction of multiple competing reactions within an NMR sample provided a challenge for the reaction monitoring procedure and a route to assess how well the method can analyse more complex systems.

4.1 Relaxation of Hyperpolarised Species

4.1.1 Background

The first parameter that could have a large impact on reaction monitoring using hyperpolarised species is relaxation. Once formed, a hyperpolarised species will begin to relax back to equilibrium (as shown in Figure 4.1) and as such the accumulation of bulk hyperpolarised product is time-dependent. Competition between the product formation and product relaxation processes will directly impact the hydride integrals that are detected upon acquisition, causing the observed PHIP activity and thus the calculated rate constants to be lower than expected.

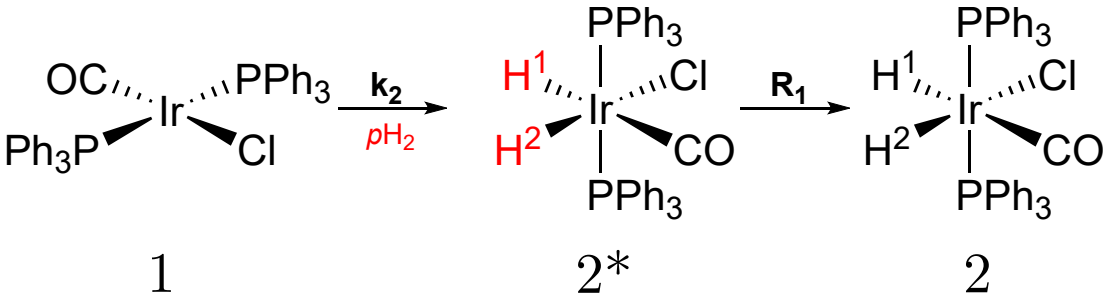

Figure 4.1: Reaction scheme for the oxidative addition of pH$_2$ to Vaska's complex showing both the formation and relaxation of hyperpolarised products.

This relationship is further complicated by the incomplete destruction of PHIP hyperpolarised signal upon detection. When detecting PASADENA hyperpolarisation with a 45° pulse, only 50% of the signal is present as NMR observable terms.[135] The remaining signal, held within non-observable terms, has the potential to persist past the detection window that it was formed in and thus potentially evolve into NMR observable terms within the following acquisition window. This interference from previously formed product could skew the integrals observed within this detection window, depending on the lifetime of this signal, and thus is worth considering within these relaxation studies. To probe the effects of hyperpolarised signal relaxation and of leftover signal between acquisition windows, both computational and experimental methods were employed.

4.1.2 MATLAB Reaction Monitoring Simulation

To investigate relaxation effects within the system, a MATLAB simulation of the NMR reaction monitoring process was developed. The purpose of this simulation was to observe the impact that changing different experimental parameters could have on the rate constants determined for the chemical system. For this simulation to accurately represent the system, it was necessary to consider how the concentration of hyperpolarised species in the sample varies as a function of time. The final MATLAB code for this simulation is given, with annotations for readability, in Appendix A.

One requirement of the simulation is that it needs to be able to correctly model the transient nature of the hyperpolarised signal being observed. This is required as once the product has formed, it will begin to relax to thermal equilibrium and so the bulk hyperpolarised product is able to be depleted over time (as shown in Figure 4.1). To capture the transient nature of the hyperpolarised signal, the simulation is based on a modified form of Equation 3.6 that accounts for not only consumption of the starting material (at a rate of k_{obs}) but also the decay of any pre-existing hyperpolarised species (according to relaxation rate R_1).

$$\frac{d[\mathbf{2}^*]}{dt} = k_{obs}[\mathbf{1}] - R_1[\mathbf{2}^*] \tag{4.1}$$

The simulation monitors the reaction in steps by calculating the concentrations of three species of interest: the starting material ([**1**]), the hyperpolarised product ([**2***]) and the relaxed product ([**2**]). The user is responsible for inputting the gap between each simulation step (Δt) and between each spectral acquisition, the starting material concentration, and the rate constants (k_{obs} and R_1) for the system of interest. At the start of the simulation, [**2***] and [**2**] are set to zero while [**1**] is set to the user input concentration.

For each Δt step, the previous concentration of **1** is depleted through application of k_{obs} while the concentration of **2** increases by the same amount (Figure 4.2b). The concentration of **2*** is calculated by applying R_1 to any leftover **2*** from the previous time step and adding to this to the increase in concentration of **2**. A plot of **2*** over time is representative of the growth and decay of the hyperpolarised signal in the absence of any spectra being recorded (Figure 4.2b).

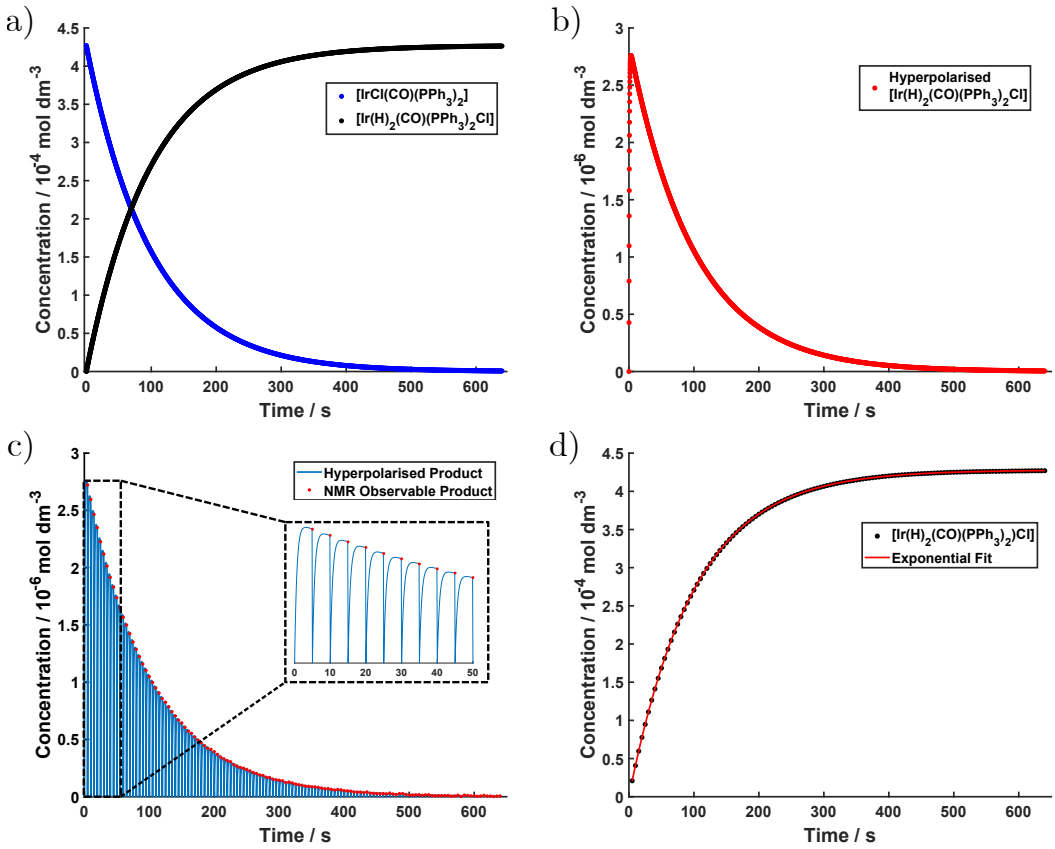

Figure 4.2: Simulated kinetic plots for monitoring the addition of pH$_2$ to *trans*-[IrCl(CO)(PPh$_3$)$_2$] including (a) the rates of reactant consumption and product formation, (b) formation and decay of undetected product, (c) formation and decay of sampled hyperpolarised signal and (d) the overall observed product formation curve fitted to an exponential recovery function.

To account for the collection of spectra at set time intervals, whenever the condition is met that a spectrum would be taken, the concentration of **2*** upon acquisition is reset to 0 as to model the destruction of the NMR signal upon observation. The effect of continually recording NMR spectra on the reaction profile observed is shown in Figure 4.2c. Finally, the observed NMR signal for each spectral acquisition can be processed identically to the experimental data and fitted to an exponential recovery function (Figure 4.2d). Comparison of the observed k$_{obs}$ to the original k$_{obs}$ input by the user indicates if the reaction monitoring method is having a notable impact on the quality of data being collected.

To account for the presence of leftover signal, a modification was made to the above simulation. Rather than resetting the concentration of **2*** to 0 upon acquisition, the concentration at that instant is multiplied by a leftover factor (determined by the user). This factor can take any value between 0 and 1, with 0 being the destruction

of all hyperpolarised product and 1 meaning all signal is carried over into the next acquisition window. Shown in Figure 4.3 is a comparison between the hyperpolarised species concentration when using the standard simulation and the simulation with 50% leftover signal.

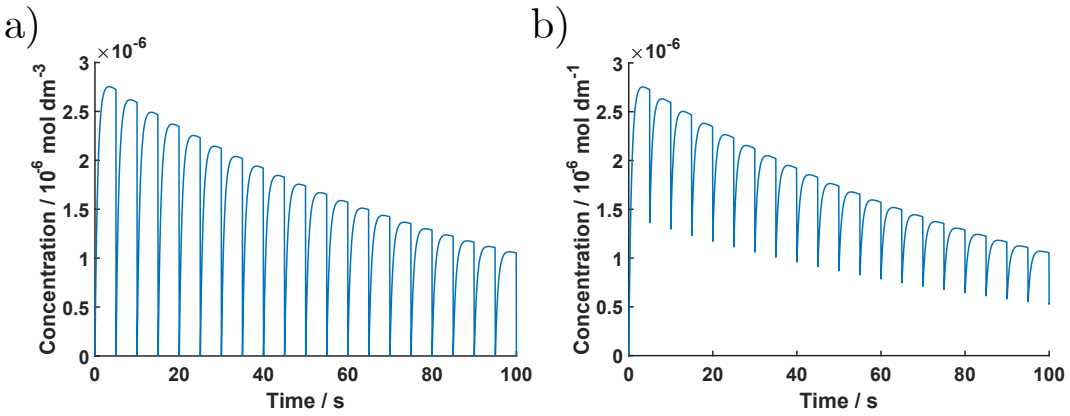

Figure 4.3: Simulated kinetic plots for the formation and decay of the detected hyperpolarised signal for a system without (a) and with (b) the use of a leftover term of 0.5.

4.1.3 Simulation Studies

The first series of simulations performed were for a system that reacts on the same timeframe as the oxidative addition reaction of Vaska's complex, with a k_{obs} of 0.01 s^{-1} and a timestep of 0.01s. For this system, a series of magnitudes of R_1 relaxation rates were tested between 15 s^{-1} (very fast relaxation) and 0.015 s^{-1} (very slow relaxation). In each case, the simulation was performed with three different acquisition window sizes (5.00, 2.50 and 1.25 s) and the k_{obs} and maximum concentration of **2*** were obtained. Differences between the k_{obs} values obtained using different acquisition windows would give a clear indicator that relaxation is having a notable effect on the observed rates of reaction. This is because if relaxation is strongly contributing to the observed signal then reducing the acquisition window size should act to reduce the hyperpolarised signal destruction prior to acquisition and so an improvement to the k_{obs} calculated would be observed.

Table 4.1: Summary of the k_{obs} and maximum observed [2*] values calculated via simulation for a system with an input k_{obs} of 0.01 s^{-1} and a leftover term of 0.

	t = 5.00 s		t = 2.50 s		t = 1.25 s	
R_1 / s^{-1}	k_{obs} / s^{-1}	Max [2*] / mM	k_{obs} / s^{-1}	Max [2*] / mM	k_{obs} / s^{-1}	Max [2*] / mM
15	0.00998	0.00027	0.01000	0.00028	0.01001	0.00028
1.5	0.01000	0.0027	0.01000	0.0027	0.01000	0.0024
0.15	0.01000	0.015	0.01000	0.0088	0.01000	0.0048
0.015	0.01000	0.020	0.01000	0.010	0.01000	0.0053

The calculated rate constants and maximum hyperpolarised species concentrations are summarised in Table 4.1. In all cases, the observed k_{obs} rate constants are within a very small margin of error of the input rate constant of 0.01 s^{-1} and so are seen to be independent of relaxation effects. The most interesting observation from this dataset comes from the maximum concentrations observed in each case. For each acquisition window length, a decrease in the rate of relaxation corresponds to an increase in the observed concentration (which would correspond to a higher SNR in the NMR spectrum experimentally). When R_1 is much larger than k_{obs} (such as R_1 = 15 s^{-1} compared to k_{obs} = 0.01 s^{-1}), the concentration of 2* at each timestep represents the instantaneous concentration - there is no residual 2* being carried across from previous timesteps. In contrast as R_1 gets closer to k_{obs}, the competition between the two processes results in the formation of a bulk hyperpolarised product prior to acquisition - there is residual concentration being carried between timesteps. This allows for higher concentrations to be detected after each acquisition window. This competition is constant across every timestep and so does not impact the overall shape of the observed exponential decay for the PHIP activity. This interaction also explains why the maximum concentration seen with each acquisition window size starts off consistent at R_1 = 15 s^{-1} (as the maximum instantaneous concentration is not dependent on acquisition window size) but as R_1 reduces, longer acquisition windows will allow for the formation of a larger bulk of hyperpolarised species.

The next set of simulations were performed in an identical manner to the above but with the addition of a leftover term of 0.5. Adding this term in a separate set of experiments allows for the impact of relaxation rate and leftover signal to be evaluated independently. For this series of experiments, the calculated rate constants and maximum hyperpolarised species concentrations are summarised in Table 4.2. The main observation for this dataset is that at R_1 values significantly greater that k_{obs}, the results are identical to those seen in Table 4.1. However, for R_1 values

of 0.15 and 0.015 s^{-1} small deviations start to be observed for both the observed k_{obs} and max [2*] values. This would suggest that once k_{obs} and R_1 have similar timescales, the presence of leftover signal acts to skew the observed value of k_{obs} to lower than expected values. However within the experimental error observed for the NMR experiments, the deviations seen would be negligible for this system.

Table 4.2: Summary of the k_{obs} and maximum observed [2*] values calculated via simulation for a system with an input k_{obs} of 0.01 s^{-1} and a leftover term of 0.5.

	t = 5.00 s		t = 2.50 s		t = 1.25 s	
R_1 / s^{-1}	k_{obs} / s^{-1}	Max **[2*]** / mM	k_{obs} / s^{-1}	Max **[2*]** / mM	k_{obs} / s^{-1}	Max **[2*]** / mM
15	0.01000	0.00027	0.01002	0.00028	0.00999	0.00028
1.5	0.01000	0.0027	0.01000	0.0027	0.01000	0.0025
0.15	0.00999	0.017	0.00999	0.012	0.01000	0.0078
0.015	0.00991	0.032	0.00997	0.018	0.00999	0.0097

To investigate the above hypothesis, the simulation studies were performed on a faster reacting system - namely one on the second timescale, with a k_{obs} of 0.1 s^{-1}. This faster reaction rate will be at a similar timescale to the selected R_1 values earlier in the dataset and so a more marked effect due to leftover signal would be expected. Table 4.3 shows the calculated rate constants and maximum hyperpolarised species concentrations for a system with k_{obs} = 0.1 s^{-1} with a leftover term of 0.5. When performed without a leftover term, the observed k_{obs} was identical to the input k_{obs} of 0.1 s^{-1} in all cases, the same result as seen in the previous study with k_{obs} = 0.01 s^{-1}. Once the leftover term of 0.5 is introduced, a much larger deviation in k_{obs} is observed for R_1 values of 0.15 and 0.015 s^{-1} that would lie outside of experimental error if observed using NMR reaction monitoring.

Table 4.3: Summary of the k_{obs} and maximum observed [2*] values calculated via simulation for a system with an input k_{obs} of 0.1 s^{-1} and a leftover term of 0.5.

	t = 5.00 s		t = 2.50 s		t = 1.25 s	
R_1 / s^{-1}	k_{obs} / s^{-1}	Max **[2*]** / mM	k_{obs} / s^{-1}	Max **[2*]** / mM	k_{obs} / s^{-1}	Max **[2*]** / mM
15	0.099	0.0017	0.100	0.0022	0.100	0.0025
1.5	0.100	0.018	0.100	0.023	0.100	0.022
0.15	0.094	0.11	0.095	0.088	0.097	0.060
0.015	0.076	0.17	0.088	0.12	0.095	0.072

To explain the deviation, a comparison between the system when it has fast relaxation (R_1 = 15 s^{-1}) and slow relaxation (R_1 = 0.015 s^{-1}) is useful. Figures 4.4(a)

and (c) show [2*] over the course of the reaction without any NMR detection for fast and slow relaxation respectively. For fast relaxation, only the chemical reaction is detectable on the NMR timescale and so the only process observed is the change in instantaneous [2*] formation over the reaction course. However for slow relaxation, the interplay between the two competing processes is observable resulting in [2*] showing a complex dependency on the rate of both processes and the persistence of [2*] past the end of the chemical reaction at approximately 60 seconds.

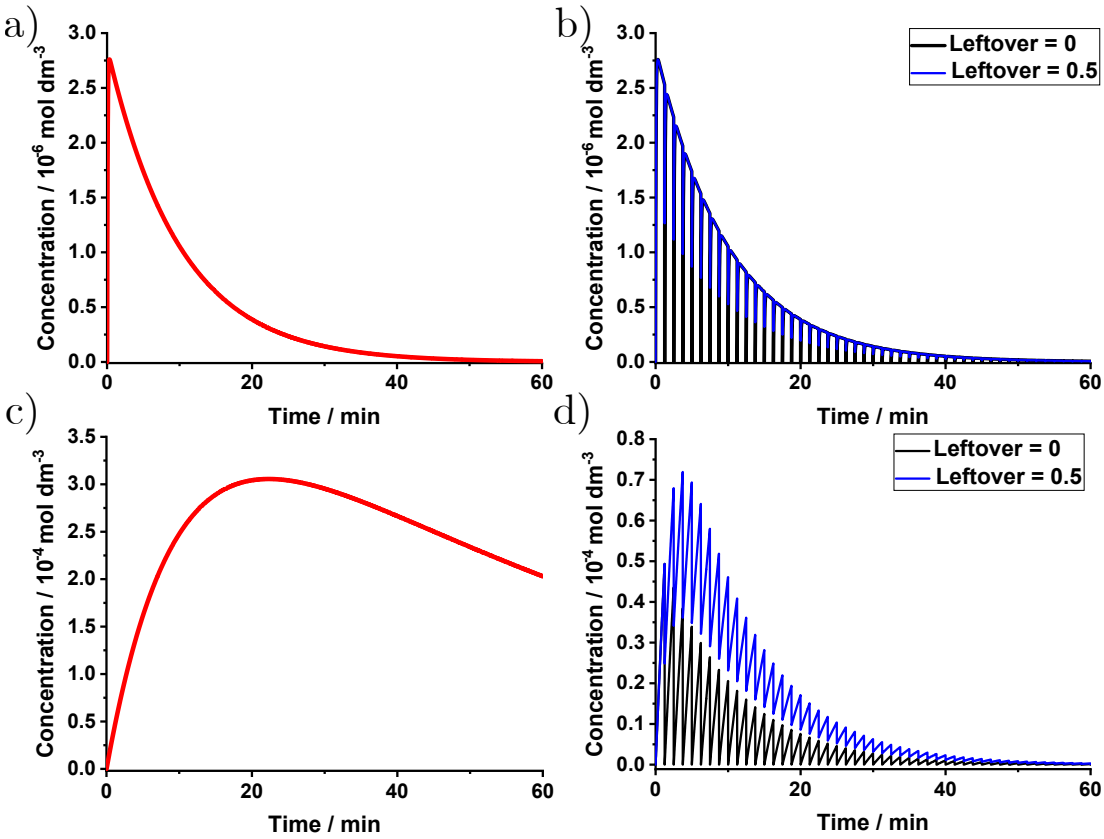

Figure 4.4: Undetected hyperpolarised signal decay curves using k_{obs} = 0.01 s^{-1} with an R_1 of (a) 15 s^{-1} and (c) 0.015 s^{-1} alongside their associated NMR sampling plots, (b) and (d) respectively, highlighting the difference in appearance when using a leftover term of 0.5 or 0.

Figures 4.4(b) and (d) show impacts on NMR detection in each case, with detection at 1.25 second intervals and using a leftover terms of either 0 or 0.5. For fast relaxation, the presence of a leftover term has no lasting impact as any signal that carries over is fully relaxed within the next time step and so the system returns to just observing instantaneous [2*]. However, with slow relaxation there is a significant difference when the leftover term is introduced. When the leftover term is set to 0, the impact of relaxation is negligible as the [2*] growth in each acquisition window remains independent and so the reducing production of 2* as

starting materials are consumed is the dominant observation. Once a leftover term is introduced, acquisition windows are no longer independent and so unrelaxed 2^* inflates the observed $[2^*]$ for subsequent timesteps. When analysed and fit to a monoexponential, the two processes are averaged and so a lower than expected k_{obs} is detected for the system. The observed deviation is higher for larger acquisition windows as $[2^*]$ is allowed to relax for longer periods of time without being detected. Experimentally, once a system satisfies these conditions it is no longer suitable to be considered as an independent reaction monitoring analysis and will require more complex approaches, such as biexponential fitting of the data, to obtain the desired kinetic information.

Overall, the simulation studies highlight some important limits that are imposed on the validity of the reaction monitoring protocol that is being followed when it comes to relaxation. In the case where $R_1 \gg k_{obs}$, we observe the instantaneous rate of the reaction. When $R_1 > k_{obs}$ we still observe the correct k_{obs} but with an improved SNR as bulk hyperpolarisation is able to form prior to detection. Once $R_1 <= k_{obs}$, the competition between relaxation and chemical reaction processes obscures the reaction rate. While this can be improved through use of smaller acquisition windows, more in-depth multi-exponential analysis is likely required to deconvolute the two processes. This result is similar to that found by literature high-field NMR studies using the ROCHESTER pulse sequence to monitor catalytic hydrogenation reactions where the reaction kinetics could be considered independently from the relaxation of hyperpolarised signal if relaxation occurred significantly faster than the reaction being observed.[155]

These computational studies also indicated that there is an inherent limit to how fast a process can be observed using this reaction monitoring method - at some point the frequency of detection required will require a compromise between the number of steps and the NMR acquisition time used. To obtain quality experimental data, the detection window used must be well matched to the expected rate of the reaction of the process to be observed.

4.1.4 Experimental Comparison

To validate the simulation studies performed, a series of variable detection delay experiments (between 5.00 and 1.25 seconds) were performed with Vaska's complex. With similar complexes to Vaska's complex, namely $[Ir(H)_2(CO)(PPh_3)_2I]$, having R_1

values of 1.3 - 1.7 s^{-1} (experimentally determined by Procacci *et al.*[45]) and with Vaska's complexes calculated k_{obs} being 0.01 s^{-1} it is very similar to the second dataset within Table 4.2. Therefore it is expected that the measured rate constants will be independent of the acquisition window size used. The calculated k_2 rate constants and the average SNR of the first usable spectrum for these reaction monitoring experiments are given in Table 4.4. The average product formation curves and starting material decay logarithm plots for each detection window used are give in Figure 4.5.

Table 4.4: Summary of individual and averaged k_2 values calculated for the variable acquisition delay experiments on pH_2 addition to Vaska's complex (0.43 mM).

Delay / s	k_2 / dm^3 mol^{-1} s^{-1}				Avg. SNR
	1	2	3	Average	
5.00	0.787	0.783	0.807	(0.792 ± 0.008)	61.9
2.50	0.763	0.783	0.806	(0.784 ± 0.012)	62.8
1.25	0.764	0.774	0.836	(0.79 ± 0.02	61.3

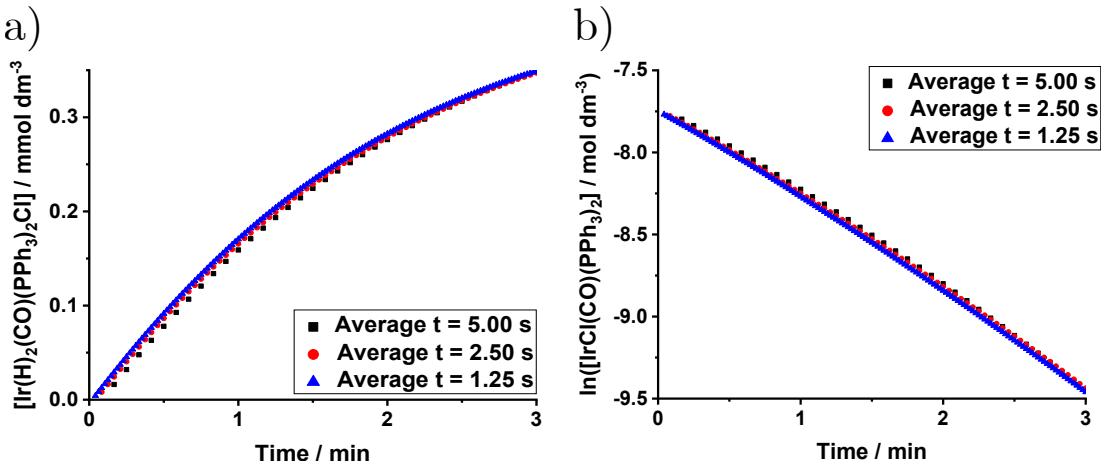

Figure 4.5: (a) Product formation curves and (b) logarithmic starting material consumption plots for the hydrogenation of *trans*-[IrCl(CO)(PPh_3)$_2$](0.43 mM), when using a 5.00, 2.50 and 1.25 second acquisition delay.

Both the product formation curves and calculated k_2 values indicate that there is minimal variation between the observed rate of reaction when changing the detection window size. This aligns well with the expected result based on the simulation studies performed on a similar system. The simulation also correctly predicted that within this regime, the maximum [2*] observed for each detection window would be similar - this is seen by the average SNR of the first usable spectrum for each dataset being within 2% of each other.

Overall, the simulation studies have shown that the impact of relaxation is negligible for the model system being tested. However, for systems that have similar hyperpolarised relaxation and chemical reaction rates a more complex analysis may need to be utilised to separate out the two competing processes. Furthermore for systems that react on faster timescales (second to millisecond), having a suitably short detection window while also a large enough acquisition time might be a challenge for this reaction monitoring approach.

4.2 Formation of Thermal Background Signal

4.2.1 Background

Over the course of the oxidative addition reaction, an increasing concentration of the $[Ir(H)_2(CO)(PPh_3)_2Cl]$ product is present within the sample. This accumulation of product will result in a competing thermally-polarised signal at the hydride resonances of the complex. While the hyperpolarised signal from instantaneous product formation is anti-phase, the bulk thermal signal is entirely in-phase (as transitions are occurring between spin-states filled according to the Boltzmann distribution). The result of this, as shown via Spinach simulations in Figure 4.6, is that the observable signal will be a mixture of the two spectra resulting in constructive and destructive interference of the hyperpolarised signal. This skewing of the observed signal is not a constant effect as the contribution from the thermally polarised species will increase over the reaction coordinate and as such more signal than would be expected will be present at later times in the reaction. Once the reaction has reached completion, no more hyperpolarised signal will be present but the thermal signal will remain. Overall, the increasing presence of a thermally-polarised background signal and the non-zero integrals following reaction completion will result in the reaction appearing to finish at an earlier time and thus any measured rates of reaction will appear faster than expected. In order to investigate this potential limitation, OPSY experiments, that are able to discriminate between thermal and PHIP polarisation, were performed.

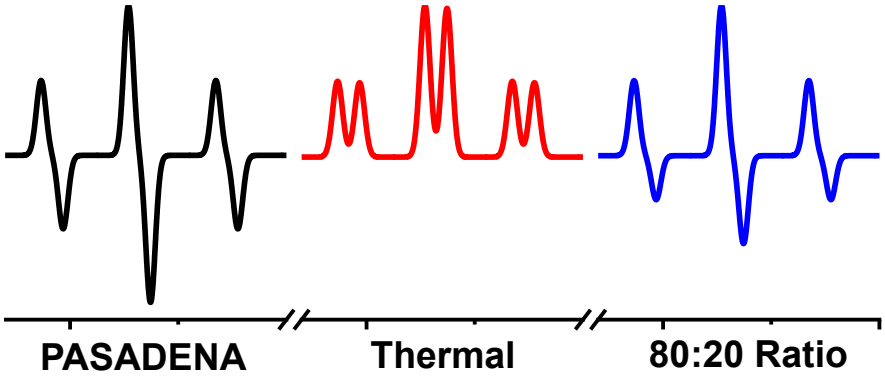

Figure 4.6: Simulated spectra for $[Ir(H)_2(CO)(PPh_3)_2Cl]$, showing the difference in appearance of spectra with PASADENA (black) or thermal (red) polarisation and the resulting spectra when they are combined in a 80:20 PASADENA:thermal ratio (blue).

4.2.2 The OPSY Filter

To quantify the effect of the bulk thermal product on the measured hydride integrals, an Only-Parahydrogen SpectroscopY (OPSY) filter was applied. This method, first published by Duckett *et al.* in 2007,[181] uses a pulse sequence that only allows signals originating from hyperpolarised species to be detected upon acquisition, with all other signals being destroyed through decoherence or placed within NMR unobservable terms.[182] Since inception, several variants of the OPSY pulse sequence have been developed. All OPSY filter pulse sequences work by using a combination of two pulses and two evolution delays, during which gradients may be applied, in order to discriminate between the thermal and hyperpolarised signals present within a sample.

The OPSY filter used for this study (shown in Figure 4.7a) consists of two 90° pulses on the ^1H channel that are interspersed with two z-gradients that are applied with opposite sign and with a 1:2 ratio of magnitudes. This pulse sequence is referred to as the OPSYd-1/2 pulse sequence. The suffix of "d" indicates that the pulse sequence selects for hyperpolarised signal that originates from a double-quantum starting term. The "1/2" details that the gradients applied after each 90° pulse have a 1:2 ratio of duration but the gradients applied during these delays have opposite signs.[183]

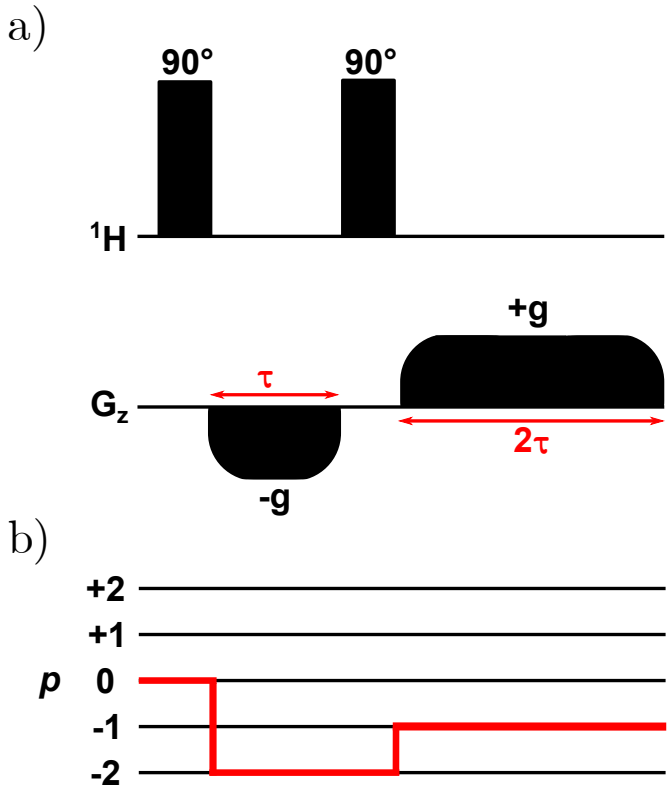

Figure 4.7: (a) Pulse sequence for the OPSY-d1/2 filter and (b) associated coherence transfer pathway.

The OSPY-d1/2 filter works by exploiting the difference in how a magnetic field gradient affects the different starting states of thermally-derived and pH$_2$-derived NMR signals. Within a standard NMR experiment, after a hydrogenation reaction the hydrides within the product will have a starting state defined by $I_{1z} + I_{2z}$. In contrast when pH$_2$ is used, the product starting state is $2I_{1z}I_{2z}$ - in this instance, the ZQ$_x$ term within the product operator formalism of pH$_2$ (detailed in Equation 2.29) is negligible when time-averaged over the timescales being considered.

Considering the pulse sequence without the presence of gradients, the first 90° pulse generates a single-quantum (SQ) coherence, $I_{1y} + I_{2y}$, for thermally-polarised spins, whereas the $2I_{1z}I_{2z}$ term converts to a $2I_{1y}I_{2y}$ term that is a combination of double-quantum (DQ) and zero-quantum (ZQ) coherence order (the term can be written as (ZQ$_x$ - DQ$_x$)). During the first evolution period, this $2I_{1y}I_{2y}$ term will evolve into proportions of $2I_{1y}I_{2y}$, $2I_{1x}I_{2y}$, $2I_{1y}I_{2x}$ and $2I_{1y}I_{2y}$ (with exact amounts being dependent on evolution duration, chemical shift and J-coupling terms). Of most importance are the $2I_{1x}I_{2y}$ and $2I_{1y}I_{2x}$ terms as these will convert into $2I_{1z}I_{2y}$ and $2I_{1y}I_{2z}$ SQ terms upon application of the second 90° pulse. These terms are directly observable upon detection and so signal that originated from a DQ term can

be obtained. However, the SQ and ZQ terms that are also present within the system will also evolve during the pulse sequence and as such must be destroyed prior to observation. This is achieved through application of pulsed-field gradients.

The spread of SQ, DQ and ZQ terms within the system after the initial 90° pulse provides an effective route to discrimination via specific coherence transfer pathways (CTPs). The OPSY-d pulse sequence focuses on ensuring that only coherence originating from the initial DQ terms, and hence the hyperpolarised species, are present upon detection. The initial gradient (of strength -g) is able to differentiate the different terms present as the ZQ terms are unaffected by the gradient (they exist in the z-direction, and thus are unaffected by z-gradients) and the SQ terms will dephase at half the rate as DQ terms (as the DQ terms effectively experience double the magnetic field gradient applied). Upon application of the second 90° pulse, the $2I_{1z}I_{2y}$ and $2I_{1y}I_{2z}$ terms formed from the original DQ coherence can be rephased by applying a second gradient. As these terms are now SQ, to rephase these terms a gradient with double the length and in the opposite direction is required. This gradient will also prevent any SQ terms from the thermally-derived signal from rephasing as compared to the DQ-derived terms they have only half the effective dephasing and so would be rephased and then dephased again upon application of this second gradient. This selection route is summarised by the CTP shown in Figure 4.7b. The overall result of this pulse sequence is therefore the detection of a NMR spectrum that only contains signals derived from the DQ terms from $p\mathrm{H}_2$.[184]

4.2.3 OPSY Experiments at Low-Field

To incorporate the OPSY filter into the reaction monitoring pulse sequence (originally shown in Figure 3.8a), the 90° pulse was replaced with the OPSYd-1/2 block, as shown in Figure 4.8. To generate a gradient in the z-direction gradient the shim coils of the NMR spectrometer were used. For all low-field OPSY experiments performed in this study, a gradient length (τ) of 7 ms was used alongside a gradient strength (g) of 30% of the maximum shim coil strength (with the maximum gradient strength measured to be 14 mT m^{-1} through calibration of the z-shim coil).

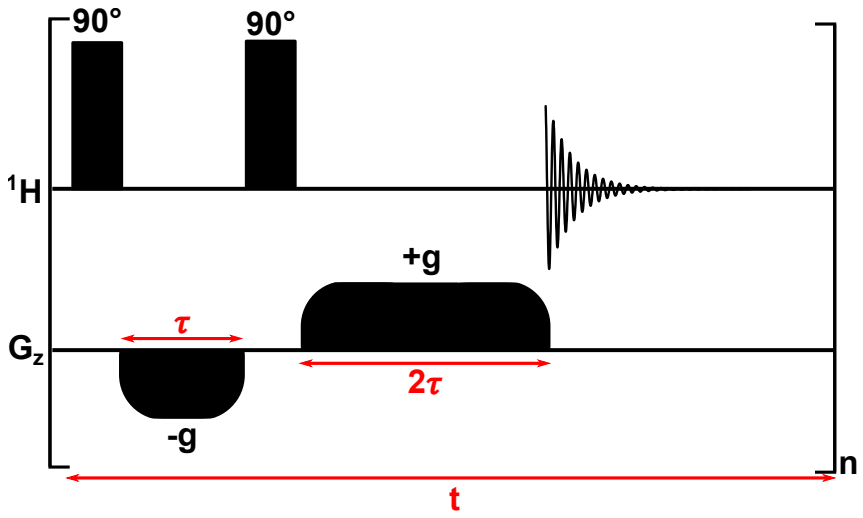

Figure 4.8: OPSY-RM pulse sequence, highlighting the replacement of the 90° pulse in the original reaction monitoring experiment with an OPSYd-1/2 block for each step of the experiment.

To investigate the impact on the rate of reaction due to thermally-polarised signals, a set of reaction monitoring experiments using the OPSY-RM pulse sequence were performed. To ensure a direct comparison, all preparation steps and experimental procedures outlined within Section 3.2 were followed. A series of 3 experiments were performed where the formation of $[Ir(H)_2(CO)(PPh_3)_2Cl]$ was followed for 10.7 minutes with evolution times (t) of 5, 3.5 and 2 seconds. A summary of the kinetic parameters obtained upon analysis of these datasets is given in Table 4.5.

Table 4.5: Pseudo-first order (k_{obs}) and second-order (k_2) rate constants for three repeated measurements using the OPSY-RM Pulse Sequence for pH$_2$ addition to Vaska's complex (0.43 mM).

Experiment	t = 5 s	t = 3.5 s	t = 2 s	Average
k_{obs} / s^{-1}	0.01035	0.01100	0.01095	(0.0108 ± 0.0002)
k_2 / $dm^3\ mol^{-1}\ s^{-1}$	0.877	0.932	0.928	(0.913 ± 0.018)

From these experiments, the average calculated k_2 rate constant for the reaction is $(0.913 \pm 0.018)\ dm^3\ mol^{-1}\ s^{-1}$. When compared to the value obtained using the standard pulse-and-acquire (PA) RM pulse sequence, $(0.792 \pm 0.008)\ dm^3\ mol^{-1}\ s^{-1}$, this value is higher than expected with a 15.3% relative increase. While this difference is non-negligible, it is unlikely to originate from the presence of thermal background signals within the obtained spectra. From the initial studies done on Vaska's complex (Section 3.1.4), it was shown that when studied at low-field the hydride peaks for Vaska's complex are very weak with 4096 scans and a 10-fold

increase in concentration required for them to be observable. To further highlight the absence of thermal signal during reaction monitoring, Figure 4.9 shows the ^{1}H spectra recorded during the first usable and final step of a PA reaction monitoring experiment where only noise is observed during the final step. Overall, the distinct lack of thermal background signal within the reaction monitoring experiments at low-field would suggest that there should be no difference in the k_2 rate constants observed with and without use of an OPSY filter. Therefore, a secondary problem with the OPSY experiment must be responsible for the observed increase in rate constant.

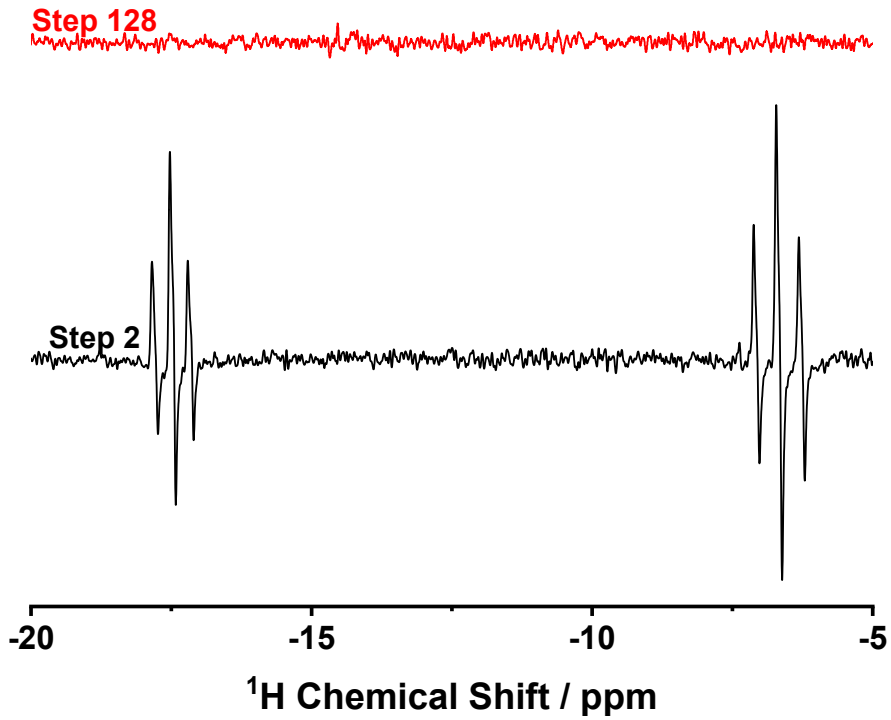

Figure 4.9: ^{1}H NMR spectra at 1 T (43 MHz) for the PA reaction monitoring experiment showing the difference between the first usable spectrum (black) and final spectrum obtained (red).

The origin of the increase in rate constant can be justified by the lower efficiency of the OPSY experiment. From a theoretical standpoint, the OPSY-d pulse sequence has a maximum efficiency of 25%. This means that of the initial magnetisation available, only up to 25% of it will be converted into NMR observable terms by the end of the pulse sequence. This low efficiency originates from the fact that the CTP chosen removes any magnetisation that is present as either ZQ (p = 0) or positive DQ (p = +2) in the system.[182] Experimentally, this lower efficiency manifests as a reduced SNR within the NMR spectra obtained for $[Ir(H)_2(CO)(PPh_3)_2Cl]$. A comparison between the first usable spectrum obtained with the PA and OPSY pulse sequences (Figure 4.10b) shows a drop in SNR of 70% (from 62.5 to 18.9).

Furthermore, the OPSY spectrum is far more difficult to phase into pure dispersion mode lineshapes (as would be expected for anti-phase NMR signals) due to the signals originating from a complex mixture of coherences. As a consequence of this, the data processing code struggles to produce clear, well-defined integration regions for all of the peaks which reduces the overall effectiveness of the analysis. The combination of these issues leads to a PHIP activity decay curve that passes through a much smaller range of values and that is far more affected by spectral noise (Figure 4.10a). These factors work to obfuscate the true PHIP activity of the system and creates an artificial end point for the reaction once the signal is below the threshold of the spectral noise. As a consequence of this, a faster rate of reaction is observed when using the OPSY pulse sequence and this is reflected in the increased k_2 values obtained. Overall, for Vaska's complex, the use of an OPSY pulse sequence at low-field is not required to obtain accurate kinetic parameters and actually negatively impacts data acquisition due to the low SNR of the spectra obtained.

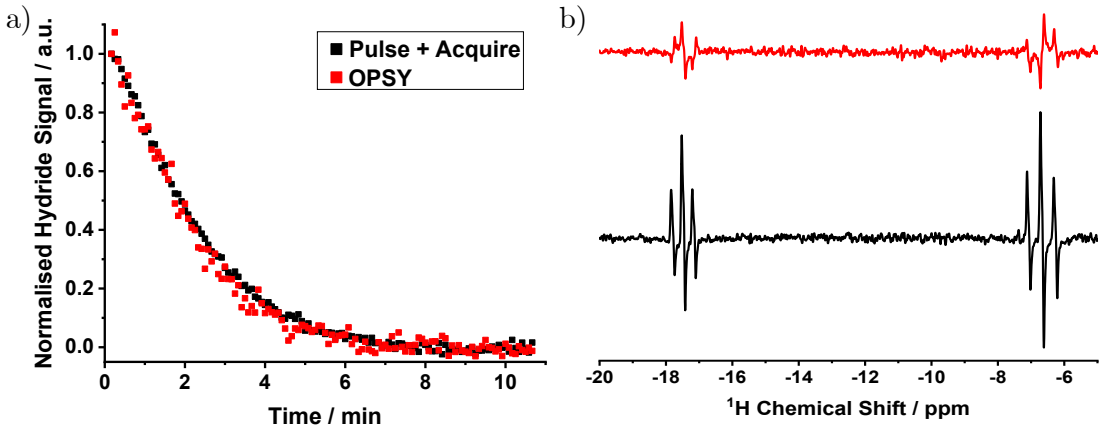

Figure 4.10: Comparison between the (a) PHIP activity decay curves and(b) first usable ^{1}H spectrum at 1 T (43 MHz) when using the PA or OPSY reaction monitoring pulse sequences for pH$_2$ addition to Vaska's complex (0.43 mM).

4.2.4 Comparison to High-Field OPSY Experiments

To provide a comparison to the low-field reaction monitoring with the OPSY pulse sequence, both the PA and OPSY experiments were repeated using a high-field (400 MHz) NMR spectrometer. The experimental protocols followed are analogous to those used at low-field and the spectrometer and samples used were equilibrated to 28.5 °C prior to analysis to more closely replicate the conditions within the benchtop NMR spectrometer. For the OPSY pulse sequence, a gradient length of 1 ms and a gradient strength of 80% were used (with the maximum gradient measured to be 50.8

mT m^{-1}).

In contrast to low-field NMR, the hydride signals for Vaska's complex are more readily observable (strong signals are obtained with 64 scans and with a 0.2 mg sample). This increased signal is observable within the PA reaction monitoring experiments, with the final spectrum showing weak but clearly present thermally-polarised hydride signals (Figure 4.11). To quantify the effect that these signals have on the obtained rate constants for the reaction, both the PA and OPSY reaction monitoring experiments were performed in triplicate. The obtained k_2 rate constants for these experiments are collated within Table 4.6.

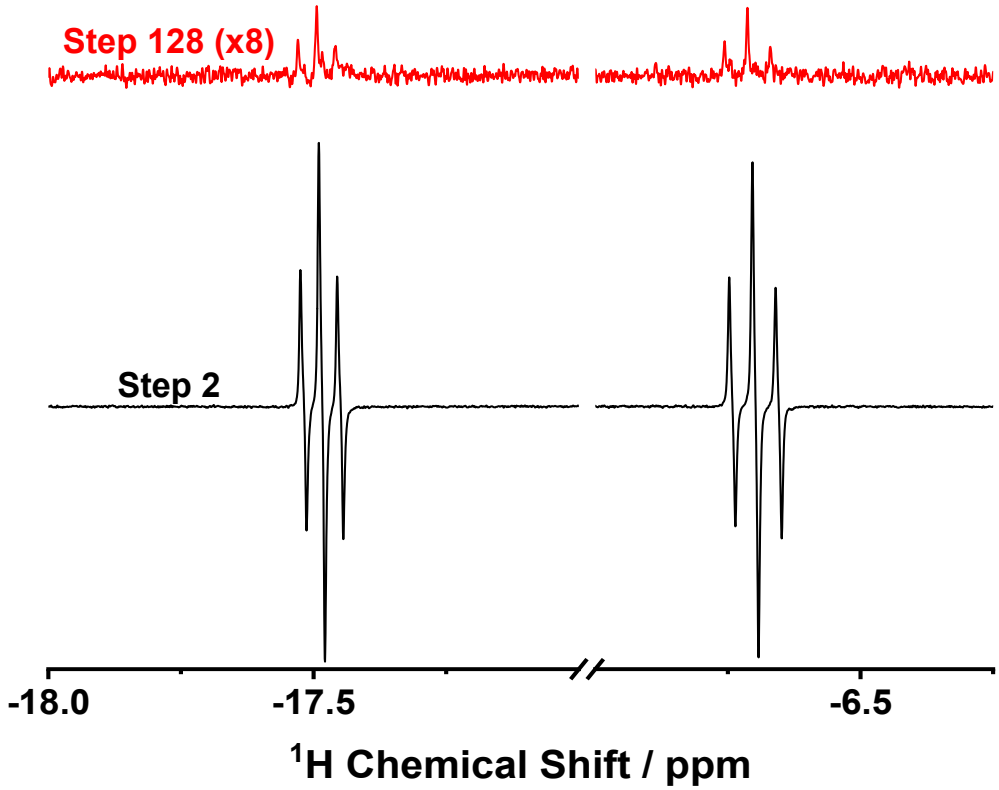

Figure 4.11: ^{1}H NMR spectra at 9.4 T (400 MHz) for the PA reaction monitoring experiment showing the difference between the first usable spectrum (black) and final spectrum obtained (red).

Table 4.6: Summary of individual and averaged k_2 values calculated at high-field (9.4 T) using the PA and OPSY reaction monitoring pulse sequences for pH$_2$ addition to Vaska's complex (0.43 mM).

Pulse Sequence	k_2 / dm^3 mol^{-1} s^{-1}			
	1	2	3	Average
Pulse + Acquire	0.968	0.983	0.938	(0.963 ± 0.013)
OPSY	0.806	0.894	0.833	(0.84 ± 0.03)

From the above experiments, an average k_2 rate constant of (0.963 ± 0.013) $dm^3\,mol^{-1}\,s^{-1}$ is obtained for the reaction when using a PA pulse sequence. Compared to the expected literature rate of (0.86 ± 0.03) $dm^3\,mol^{-1}\,s^{-1}$, this rate of reaction is 12% faster. In contrast, the average k_2 rate constant for the reaction when the OPSY filter is used is (0.84 ± 0.03) $dm^3\,mol^{-1}\,s^{-1}$ which agrees very strongly with the expected rate of reaction (a 2.3% difference). The improvement in accuracy and overall reduction in rate constant seen when using the OPSY pulse sequence indicates that the thermal background signal produced over the course of the reaction is non-negligible at high-field. As seen in Figure 4.12a, relative to the OPSY experiment, the PA PHIP activity decay curve has an increasing deviation to lower values and tends towards a higher non-zero final value. Both of these factors contribute to the higher rate constant seen for the system. Therefore, in contrast to the low-field experiments, at high-field the use of OPSY is recommended for reaction monitoring as to remove the influence of the background signal and improve the obtained kinetic parameters. Another important thing to note is that for the OPSY experiments at high-field, the SNR issues are significantly reduced. When comparing the first usable spectrum from the PA and OPSY experiments (Figure 4.12b), only a 56% reduction in signal is seen and the SNR in both cases is significantly higher than at low-field (an average value of 221 and 97 respectively). This, combined with an easier phasing of the OPSY spectra, ensures that the low SNR issues observed at low-field do not influence the results obtained at high-field.

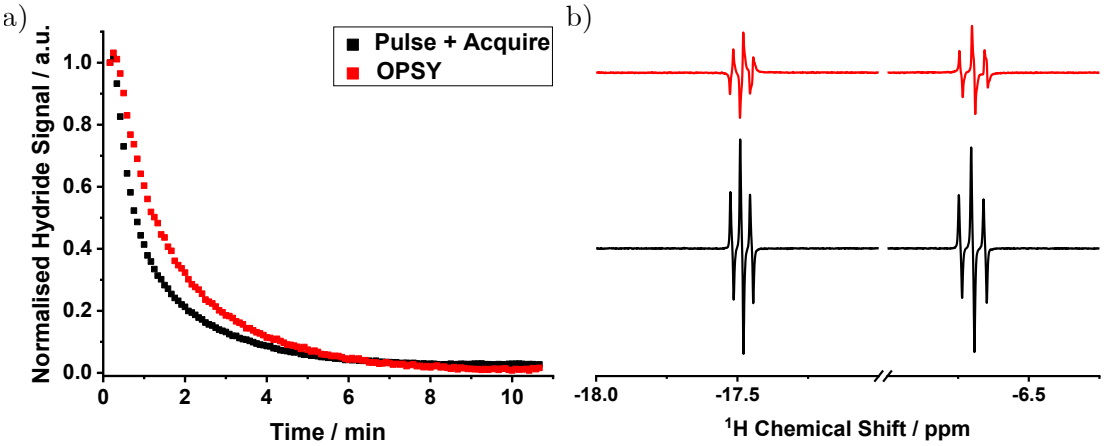

Figure 4.12: Comparison between the (a) PHIP activity decay curve and (b) first usable ^1H spectrum at 9.4 T (400 MHz) when using the PA or OPSY pulse sequences to monitor pH_2 addition to Vaska's complex (0.43 mM).

Overall, while the OPSY pulse sequence is able to remove the presence of thermal background signals within reaction monitoring experiments, the accompanying reduction in SNR can lead to more inaccurate results being obtained.

At low-field, where sensitivity issues are heightened, the negligible presence of any thermal background signal meant that the PA pulse sequence was the correct choice for Vaska's complex. For similar systems, reaction monitoring at low-field can be more beneficial than at high-field as the increased sensitivity at high-field can result in the more complex OPSY pulse sequence being a necessity in order to overcome the increased presence of a thermal background signal. More generally, when considering the correct option for different chemical systems the presence of thermal background signal and the level of enhancement observed with PHIP will determine whether an OPSY filter is required or beneficial for low-field reaction monitoring. In situations where an OPSY filter would be required at low-field, there is potential to reduce the SNR issues present through use of a different OPSY pulse sequence. For example, the OPSY-z pulse sequence selectively allows the ZQ magnetisation to be NMR observable and this carries an increased maximum efficiency of 50% (compared to the 25% efficiency of the OPSYd pulse sequences) which may enable sufficient SNR within the hyperpolarised spectra for reaction monitoring purposes.[182]

4.3 Temperature Variation During Reaction Monitoring

4.3.1 Background

Temperature is a well-known factor that directly impacts the rate of chemical reactions. Through increasing the average kinetic energy of the reactants, more collisions occur above the activation energy for the reaction and as such more successful reactions occur per unit of time. Therefore, when monitoring a reaction it is necessary to ensure that the temperature of the system is constant as to avoid a variable reaction rate being observed.

As mentioned previously, one potential limitation of benchtop NMR is that many instruments in the current generation have their temperatures fixed as to ensure a high magnetic field homogeneity across the detection coil region. If a sample is placed into the spectrometer at a temperature lower than the operating temperature of the spectrometer, there is potential for a temperature gradient to form as the sample equilibrates to the new conditions. This temperature gradient will cause a skew in the

overall observed rate constant as the reaction begins at a slower rate and then speeds up as the sample warms up. In order to investigate the effect of this, it is necessary to find a method via which temperature can be monitored and find effective solutions that mitigate any temperature gradients that are present.

4.3.2 The Methanol Thermometer

To monitor the temperature of the sample within the spectrometer, pure methanol (MeOH) can be used. Methanol is a known NMR thermometer, with the distance between the CH_3 peak and OH peak in the ^{1}H NMR spectrum being indicative of the sample temperature.[185] This technique utilises the fact that lower temperatures facilitate better hydrogen bonding between solvent molecules which increases the shielding of the OH peak but has a negligible effect on the CH_3 peak. As a result, at lower temperatures the OH peak will shift to a lower chemical shift giving a direct indicator of the sample temperature. Within the temperature range of 178 to 330 K, the separation of the two peaks in ppm ($\Delta\delta$) can be used to calculate the sample temperature using Equation 4.2.[185]

$$T(K) = 409.0 - 36.54(\Delta\delta) - 21.85(\Delta\delta)^2 \tag{4.2}$$

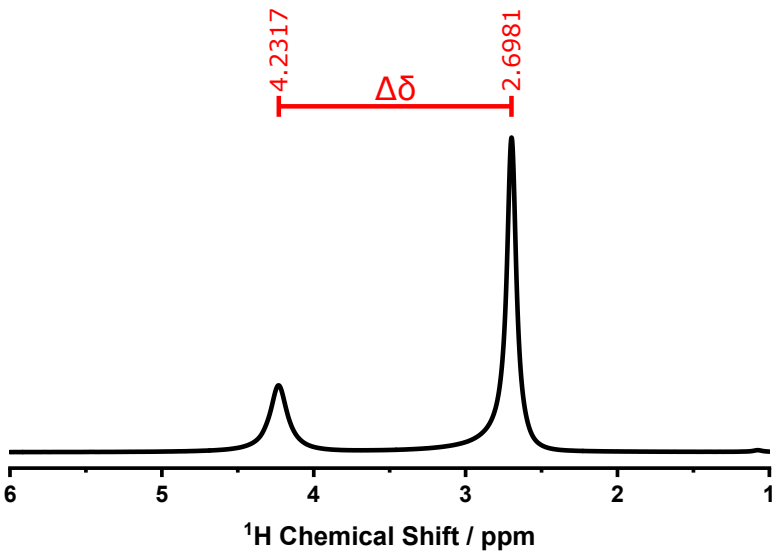

Figure 4.13: ^{1}H Spectrum of MeOH recorded after equilibration within the NMR spectrometer to a temperature of 28.5°C .

To verify Equation 4.2, a sample of pure methanol was inserted into the benchtop NMR spectrometer and left to equilibrate for 1000 seconds (16.7 minutes). Following this, a ^{1}H spectrum was acquired, the chemical shifts for the CH_3 and OH peaks were measured and the distance between them was calculated to be 1.53361 ppm. Inserted into the above equation, this generates a temperature of 301.572 K or 28.422 °C. The operational temperature of the magnet in the Spinsolve spectrometer is 28.5 °C. The temperature measured by the methanol thermometer is clearly close to this value but underpredicts the expected temperature by 0.078 °C. However, this discrepancy is due to a limitation in chemical shift resolution of the spectra acquired rather than a breakdown of the above equation. Using the same parameters as the reaction monitoring experiments (2048 points, 400 μs dwell time and zero-filling to 32,768 points), the spectrum has a 0.0018 ppm spectral resolution. This spectral resolution corresponds to a 0.18 °C resolution of the determined temperatures and as such the recorded temperature of (28.422 ± 0.18) °C is the closest value that can be recorded to 28.5 °C for the experiment. This resolution was deemed acceptable for the following experiments as the main area of interest is the temperature change over the course of the reaction rather than the absolute value of the temperature of the sample. In the limiting case of the temperature change falling within this 0.18 °C range, this would be indicative of an acceptable level of temperature stabilisation for this specific reaction and so would still enable sufficient analysis for the system.

4.3.3 Initial Temperature Experiments

For all following experiments, to monitor the change in sample temperature over time, the reaction monitoring pulse sequence (Figure 3.8a) was used with 128 steps and a 5 second delay (a 10.7 minute experiment). From this experiment, a pseudo-2D dataset of ^{1}H MeOH spectra is obtained. The analysis of this data is performed using a modified version of the automatic processing code used for reaction monitoring experiments. The data is given a chemical shift scale using a 1D reference spectrum and then peak picking is performed across the 2D array to identify the two methanol peaks. Using these values, $\Delta\delta$ is calculated and put into Equation 4.2 to generate a vector of temperatures that are then plotted against the time coordinate of the experiment. From this analysis, chemical shifts, $\Delta\delta$ and temperatures are saved into a csv file for manipulation.

The first experiments performed were to test if removal of the NMR sample during the standard reaction monitoring procedure had any noticeable temperature gradient

issues. For these experiments, the sample was allowed to equilibrate within the spectrometer for 10 minutes and then was removed from the spectrometer for one minute and held in place. The sample was then re-inserted into the spectrometer and the temperature monitoring experiment was performed (an example of the pseudo-2D spectrum produced is given in Figure 4.14a. This experiment was performed in triplicate and the resulting plots are given in Figure 4.14b.

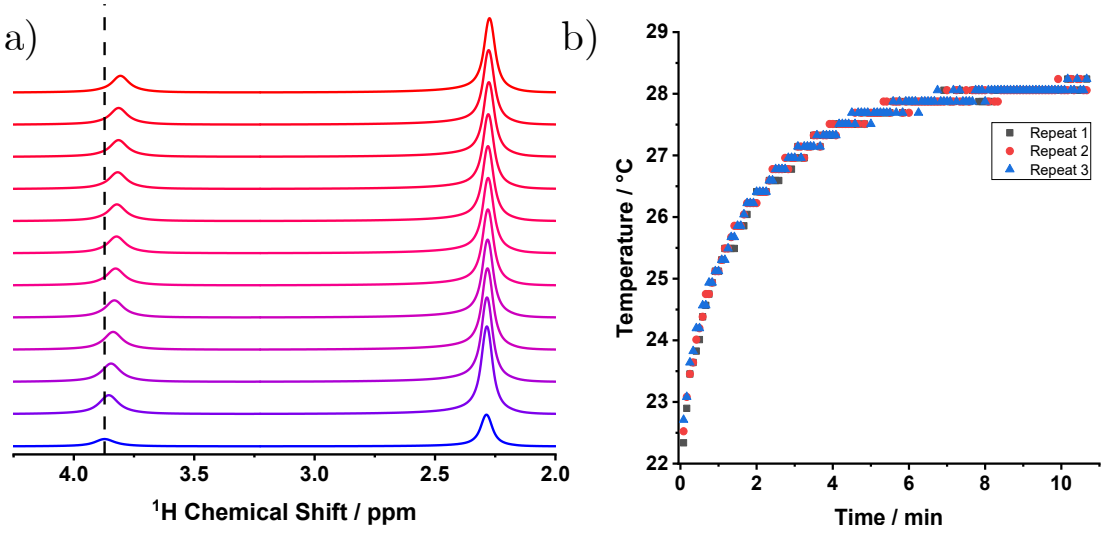

Figure 4.14: (a) Change in ^{1}H NMR signal and (b) sample temperature over 10 minutes for MeOH following 1 minute exposure to external lab conditions.

Figure 4.14b shows that the experiment is fit for purpose as it is able to identify temperature changes within the sample and follow them over time with a high repeatability (the relative standard error of the exponential growth for the three repeats is 1.3%). From these results, it is clear that there is a significant loss of temperature within the sample during the minute that it is exposed to the external laboratory environment. The sample, on average, reaches a minimum temperature of 22.5 °C and after 10.7 minutes is only able to recover to 28.2 °C. This deviation of 6 °C from the spectrometer temperature of 28.5 °C creates a strong temperature gradient over the course of the reaction monitoring experiment. This is highly problematic for the temperature-dependent kinetics being observed during reaction monitoring and thus routes to minimise temperature loss upon sample removal from the spectrometer are essential.

4.3.4 Addressing Temperature Loss External to the Sample

The main source of temperature loss within the sample is the difference in temperature between the spectrometer (28.5 °C) and the external laboratory environment (held at 18 °C). Once the sample has equilibrated to the internal temperature of the spectrometer, it is much warmer than its surroundings and so will immediately begin to cool upon removal from the spectrometer. One solution to this issue is to minimise the contact that the outer surface of the NMR tube has with the external environment. This was achieved through construction of a thermally insulated NMR tube holder (with assistance from Dr. Fadi Ahwal).

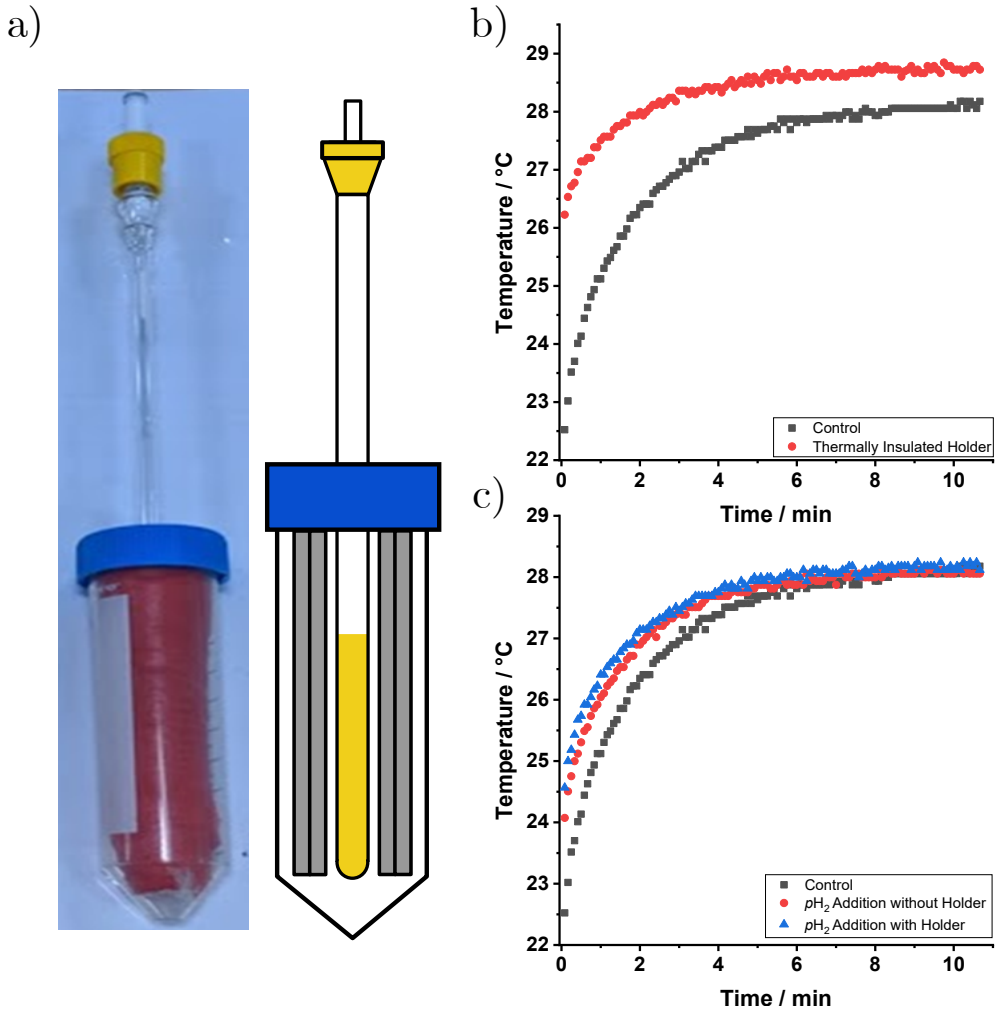

Figure 4.15: (a) Picture and diagram of thermally-insulated NMR tube holder alongside MeOH thermometer studies comparing the benefit of using the holder when the sample is removed from the spectrometer for (b) 1 minute or (c) pH_2 is added and mixed into the sample.

The NMR tube holder (shown in Figure 4.15a) consists of a large screw-top

plastic sample vial with a smaller plastic insert that is wrapped in polyethylene foam (shown in grey in the diagram). A hole has been made in the screw-top of the vial through which an NMR tube can be inserted to create a sealed internal space. The external container acts as a barrier to the laboratory conditions and reduces all airflow around the NMR tube as to prevent the replenishment of cold air. To further insulate the sample, the polyethylene foam localises heat transfer from the sample to its immediate vicinity allowing for heat loss from the sample to occur at a slower rate. To highlight the effectiveness of this holder, the temperature monitoring experiment was repeated in triplicate with the sample being held for 1 minute within the thermally-insulated holder. Figure 4.15b shows the average temperatures observed for this experiment compared to those of the original. A substantial improvement is seen when using the holder, with the sample re-entering the spectrometer with an internal temperature of 26.2 °C - a deviation of only 2.3 °C from the target temperature. Furthermore, in this case the sample is able to reach the desired temperature during the observation window (approximately at 5 minutes into the experiment).

While this method is effective at mitigating external temperature effects, the introduction of pH$_2$ during the PHIP experiments provides a route to temperature loss within the sample itself. The pH$_2$ provided by the pH$_2$ generator within the lab is output at room temperature and as this gas is introduced into the NMR tube itself, external thermal insulation will have a near-negligible effect on any temperature changes within the sample. Evidence of this is given in Figure 4.15c, which compares the change in sample temperature observed with and without using the NMR tube holder when the pH$_2$ filling step is added into the experiment. Fortunately, the MeOH thermometer remains a viable method with which to probe the temperature of these H$_2$ containing samples as previous studies have shown that the introduction of small gas molecules (such as N$_2$ and O$_2$) has a minimal effect on the accuracy of the technique.[186] From these experiments, substantial temperature drops of 4.4 °C and 3.9 °C are observed without and with the holder respectively. Therefore, an alternative solution is required to overcome this secondary route of heat loss.

4.3.5 Addressing Temperature Loss Internal to the Sample

The change in temperature upon addition of pH$_2$ occurs upon the mixing of the room temperature gas into the relatively warmer solvent within the sample. Therefore, one potential route to reduce the temperature loss upon introduction of

pH$_2$ is to increase the temperature of the gas prior to the mixing of the sample. If the sample is allowed to re-equilibrate to a higher temperature after pH$_2$ addition, this would allow both the solution in the base of the NMR tube and the pH$_2$ gas in the headspace to reach the desired temperature prior to mixing. For this to be a viable option, a key requirement is that the sample cannot begin reacting prior to observation and so there needs to be minimal mixing of the pH$_2$ into the solution. To investigate this, pH$_2$ was added to a sample of Vaska's complex and then the sample was placed into the spectrometer without shaking. The sample was observed for 10.7 minutes, after which it was removed from the spectrometer, shaken for 5 seconds and then observed again. The results of this experiment (Figure 4.16) clearly indicate a negligible amount of passive diffusion of pH$_2$ across the liquid-gas interface within the NMR tube as PHIP signals are only observable following the shaking of the sample. The delayed reaction monitoring was also shown to have no noticeable impact upon the quality of the data obtained as analysis of this dataset produced a k_2 for the reaction of 0.81 dm^3 mol^{-1} s^{-1} which of similar quality to the previously obtained k_2 of (0.792 ± 0.008 dm^3 mol^{-1} s^{-1}).

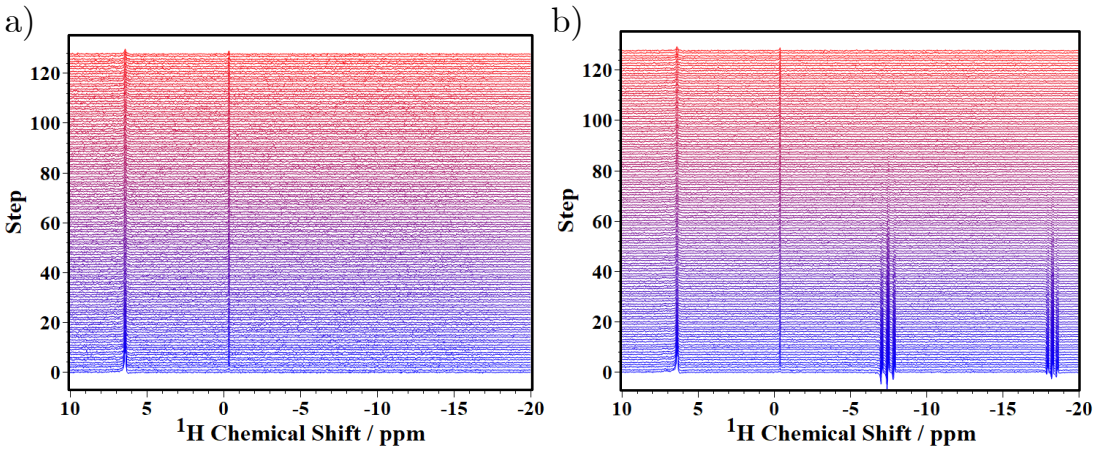

Figure 4.16: Stacked plot of ^{1}H spectra after pH$_2$ addition to Vaska's complex (0.43 mM) with (a) no shaking and (b) 5 seconds of shaking.

With the re-equilibration step proving to be a valid route to increase the temperature of the pH$_2$ within solution, MeOH thermometer experiments were performed to compare the effectiveness of performing this step within a waterbath or within the spectrometer itself. Both approaches have their own advantages with the spectrometer providing a fully-enclosed temperature-stabilised environment for the full length of the NMR tube and the waterbath allowing for the NMR spectrometer to be operational during the re-equilibration period. To compare the two setups, pH$_2$ was added to the MeOH sample and then the sample was placed

into either a waterbath (set to 28.5 °C) or the NMR spectrometer. After 10 minutes the sample was shaken and then placed into the spectrometer for data collection. The results of the experiment, shown in Figure 4.17a, indicate an average temperature range of 4 °C for the waterbath results and of 2.4 °C for the spectrometer results (with respective starting values of 24.5 °C and 26.1 °C). These values indicate that re-equilibrating the sample within the spectrometer enable sufficient heating of the NMR tube headspace as to reduce the temperature loss experienced upon sample mixing.

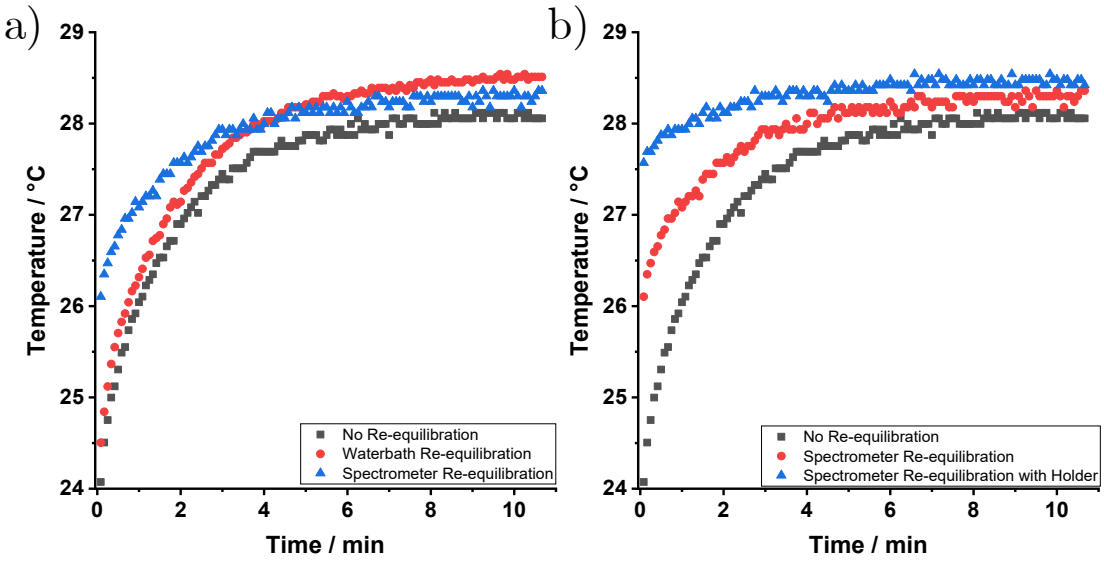

Figure 4.17: MeOH thermometer studies comparing (a) the benefit of sample re-equilibration within the spectrometer or a waterbath and (b) the effectiveness of re-equilibration within the spectrometer with sample shaking occurring in the thermally insulated holder.

A final combination approach was attempted in order to achieve the lowest possible temperature gradient within the experiment, utilising the solutions for both the external and internal temperature loss. The revised experimental procedure leaves the sample within the spectrometer for 10 minutes following pH$_2$ addition. Following this the sample is placed into the thermally insulated holder, shaken for 5 seconds and then replaced within the spectrometer for detection. The results of this experiment are shown in Figure 4.17b (in blue) and are compared to the results when following the original experimental protocol (in grey) and when only the re-equilibration step is performed (in red). This combination of techniques produced only a 0.9 °C drop in temperature for the sample (with a starting temperature of 27.6 °C). Compared to the 4.4 °C drop seen for the original experimental protocol, this improvement highlights a far superior approach to minimise the influence of temperature upon the sample.

4.3.6 Simulating the Effect of Temperature

It is possible to demonstrate the impact that temperature would be expected to have on the reaction monitoring experiments performed with Vaska's complex. The study performed by Chock *et al.* recorded the rate of H_2 addition to Vaska's complex at several temperatures (in the range of 20 °C to 35 °C).[111] From this dataset, a temperature dependence of 0.06 $dm^3\,mol^{-1}\,s^{-1}T^{-1}$ can be obtained for the reaction. This temperature dependence has the potential to have a substantial impact on the reaction monitoring experiments. For example, the 4.4 °C temperature change seen for the original reaction monitoring protocol would translate to an initial rate that is 0.26 $dm^3\,mol^{-1}\,s^{-1}$ lower than expected. To model the impact of these temperature gradients on the final k_2 value calculated for the reaction, a simulation study was performed.

The MATLAB simulation for the formation of $[Ir(H)_2(CO)(PPh_3)_2Cl]$ was modified to include a variable rate constant. To achieve this, the experimental temperature gradient curves for the desired conditions were fit to a mono-exponential recovery function to give the temperature at each time point over the reaction coordinate. This temperature was then converted into a k_{obs} rate constant using the relationship between temperature and rate shown in the literature by Chock *et al.*[111] This new rate is then used for the next step of the simulation, allowing for the system to model the effect of a variable rate constant. The resulting product formation curve is then analysed to give an overall k_2 for that experiment. This simulation was performed for the temperature gradients formed when pH_2 addition is done using the original experimental procedure (the worst case scenario), when re-equilibration is performed and when both re-equilibration and shaking in the holder are done (the best case scenario). A comparison between the best and worst case scenarios is shown in Figure 4.18 and the rate constants obtained for each are summarised in Table 4.7.

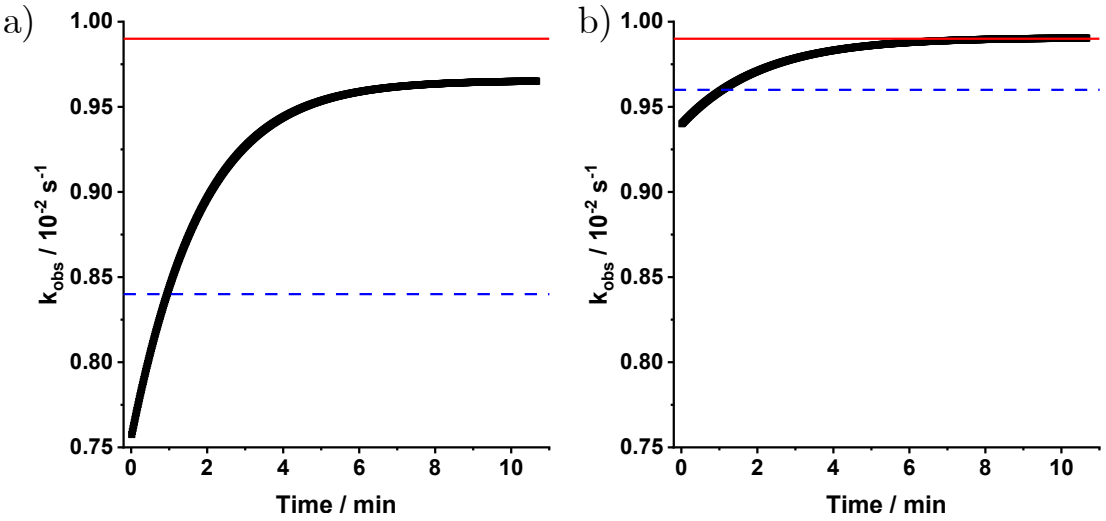

Figure 4.18: Simulated change in k_{obs} for the addition of pH$_2$ to Vaska's complex under the (a) worst and (b) best temperature conditions. Highlighted are the expected rate given no temperature gradient (red, solid line) and the average k_{obs} obtained after analysis (blue, dashed line).

Table 4.7: Calculated rate constants for the addition of pH$_2$ to Vaska's complex under different temperature gradient conditions

Conditions	Starting Temperature / °C	k_{obs} / s^{-1}	k_2 / dm^3 mol^{-1} s^{-1}
Ideal	28.5	0.0099	0.86
Exposed to the Lab	24.1	0.0084	0.72
Re-equilibration	26.1	0.0090	0.78
Holder and Re-equilibration	27.6	0.0096	0.83

From Table 4.7, the 15% decrease in the k_2 rate constant for the worst case data compared to the 3% decrease seen for the best case data shows a marked improvement in accuracy when temperature mitigating methods are employed. Overall, these simulations highlight that temperature effects for the system are non-negligible and so methods for reducing sample temperature fluctuations must be considered when designing a reaction monitoring procedure.

4.3.7 Impact on Low-Field Reaction Monitoring

With this in mind, the oxidative addition of pH$_2$ to *trans*-[IrCl(CO)(PPh$_3$)$_2$] was monitored as previously but with the 10 minute temperature re-equilibration step after pH$_2$ addition and using the thermally-insulated holder for the 5 s shake. Five

samples of Vaska's complex were analysed and the rate constants that they produced are shown in Table 4.8.

Table 4.8: Pseudo-first order (k_{obs}) and second-order (k_2) rate constants for the five repeat measurements for the oxidative addition of pH$_2$ to Vaska's complex (0.43 mmM) with minimisation of the temperature gradient.

Experiment	1	2	3	4	5	Average
k_{obs} / s^{-1}	0.0094	0.0105	0.0108	0.0108	0.0116	(0.0106 ± 0.0008)
k_2 / $dm^3\ mol^{-1}\ s^{-1}$	0.79	0.89	0.91	0.91	0.98	(0.89 ± 0.03)

Using this improved procedure, the average k_2 rate constant increases to (0.89 ± 0.03) $dm^3\ mol^{-1}\ s^{-1}$ which is in excellent agreement with the value expected from literature (0.86 ± 0.03 $dm^3\ mol^{-1}\ s^{-1}$).[111] This value also carries a higher accuracy than that produced previously without the temperature considerations (0.792 ± 0.008 $dm^3\ mol^{-1}\ s^{-1}$). The increased rate constant compared to the previous study is easily rationalised as the low initial temperatures within the original procedure would skew the observed rate constant to lower values (providing evidence that large temperature gradients were present within the original study on Vaska's complex).

Overall for benchtop NMR reaction monitoring, it is important to identify and mitigate the presence of temperature gradients within the experimental procedure being performed. Through simple temperature stabilisation techniques, such as using a thermally-insulated holder or allowing the sample to re-equilibrate to a higher temperature, it is possible to reduce the effect of temperature on the experimental results and thus be able to obtained quantitative data with a high accuracy and in a reproducible manner. A potential future solution to this problem is to develop an approach to performing *in situ* bubbling of pH$_2$ into the NMR sample when it is within the NMR spectrometer. This would alleviate the need to remove the sample from the spectrometer when adding fresh pH$_2$ and as such the sample can remain equilibrated to the internal temperature of the spectrometer. This approach to *in situ* bubbling has already been developed for SABRE experiments at high-field[187,188] and within zero-to-ultra-low-field NMR setups.[189,190]

4.4 $\%pH_2$ Enrichment Variation

4.4.1 Background

The final physical parameter that was investigated was the enrichment of $p\mathrm{H_2}$ within the system. By changing the ratio of [$p\mathrm{H_2}$] to [$o\mathrm{H_2}$] within the NMR tube, the total concentration of $\mathrm{H_2}$ remains constant but the proportion of product that forms in a hyperpolarised state is varied. If any change in rate constant due to $\%p\mathrm{H_2}$ enrichment is observed, this would indicate that the method does not obey the simple quantification assumption made in this protocol that one unit of hyperpolarised signal is independent of experimental conditions. If the hyperpolarisation behaves more akin to SABRE hyperpolarisation, where reaction conditions have a direct impact on the signal enhancements seen, then a more complex model for the reaction monitoring would be required. This would also severely limit the wider applicability of this reaction monitoring technique as using the method on a different setup, for example with a different $p\mathrm{H_2}$ generator (such as one with liquid $\mathrm{N_2}$ cooling that can achieve approximately 50% $p\mathrm{H_2}$ enrichment),[94] could have an impact on the quality of data obtained.

One potential factor that could cause the system to display a dependence on $\%p\mathrm{H_2}$ enrichment is the presence of a $p\mathrm{H_2}$ to $o\mathrm{H_2}$ interconversion pathway within the system. While the rate of reaction would be invariant to additional $o\mathrm{H_2}$ within the sample, due to the total concentration of $\mathrm{H_2}$ remaining constant, the observed rate of reaction would appear slower due to this technique relying on PHIP activity to monitor reaction progress. While the spontaneous interconversion of $p\mathrm{H_2}$ is very slow,[38,137] a secondary reaction pathway within the sample could lead to $o\mathrm{H_2}$ formation, resulting in reduced PHIP activity on the experimental timescale. This could potential occur via nuclear spin initiated conversion through reversible formation of the transition state between Vaska's complex and the dihydride product (as shown in Figure 4.19).

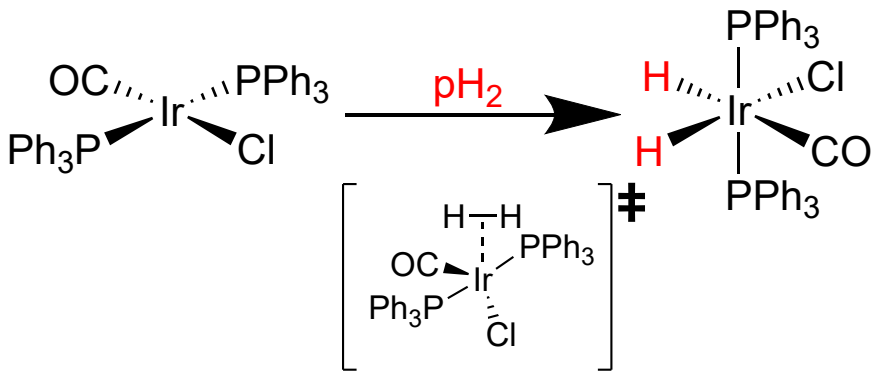

Figure 4.19: Reaction scheme for the addition of pH_2 to Vaska's complex, highlighting the 5-membered transition state of the reaction.

Here the Ir metal centre acts to break the symmetry of the pH_2 state but then this transition state falls apart to reform Vaska's complex and oH_2.[191] This would effectively remove pH_2 from the reaction system without the formation of a hyperpolarised product. The impact of this competing process would be dependent on the initial [pH_2] in the system and as such moving to a lower %pH_2 enrichment would lead to an increase in the observed rate. Previous studies by Vaska *et al.*[192] and Matthes *et al.*[193,194] have indicated that pH_2 to oH_2 conversion is possible for Vaska's complex though in these cases it was observed at low H_2 pressures where the position of the reaction equilibrium is shifted towards the reagents and over much longer reaction times.

4.4.2 Variable *Para*hydrogen Enrichment

In order to investigate this parameter, reaction monitoring experiments needed to be performed with a range of different pH_2 enrichment levels. This can be achieved though tuning the temperature of the pH_2 generator (the design of which is given in detail in Section 8.1). When passed over the paramagnetic catalyst within the pH_2 generator, the H_2 gas can freely interconvert between pH_2 and oH_2 and will stabilise at the equilibrium position between these states. At room temperature (298 K), all of the spin states of molecular hydrogen are approximately equally occupied and so a distribution of 75% *ortho* (the triplet state) and 25% *para* H_2 is obtained. Once removed from the paramagnetic catalyst, spin interconversion between the two states is forbidden and so the distribution of pH_2 to oH_2 remains fixed. Reducing the temperature of the pH_2 generator, will shift the position of equilibrium towards the formation of pH_2 (the lower energy, most stable state) allowing for mixtures of

different pH$_2$:oH$_2$ ratios to be generated.[195]

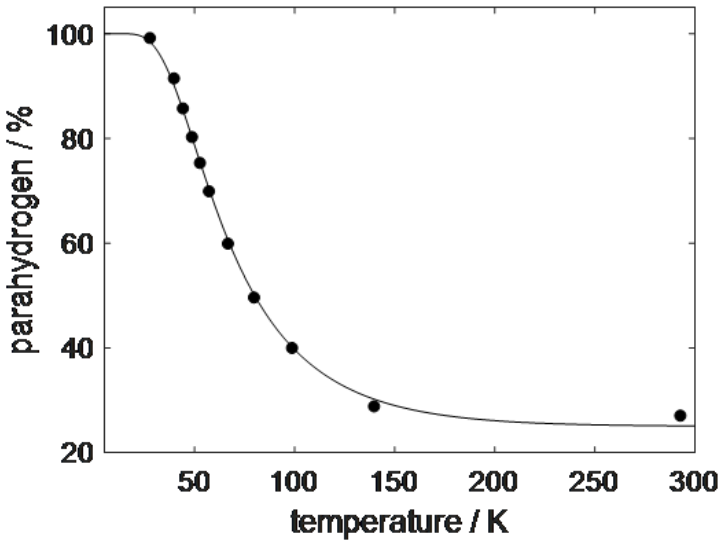

Figure 4.20: Calibration curve of %pH$_2$ enrichment at various temperatures between 28 and 293 K. Reproduced from Ref. 195 with permission from the PCCP Owner Societies.[195]

Previous studies within the group by Richardson *et al.*[195] have verified experimentally the relationship between generator temperature and the %pH$_2$ produced in the range of 25% (at 293 K) to 99% (at 28 K). Using this calibration (shown in Figure 4.20) it is possible to produce a suitable range of pH$_2$ enrichment levels to investigate how changing this parameter affects the observed reaction rate constants for Vaska's complex.

4.4.3 Experimental Results

To measure the effect of %pH$_2$ enrichment on the k_2 rate constant for the Vaska's complex oxidative addition reaction, the pH$_2$ generator was equilibrated to five different %pH$_2$ enrichment levels (in the range of 99% to 60%) with reaction monitoring performed in triplicate for each value. For these experiments, the modified reaction monitoring procedure that includes temperature gradient mitigation effects was used. The corresponding temperatures to each %pH$_2$ enrichment level are given in Table 4.9 alongside the average k_2 rate constants and maximum SNR obtained for each. Figure 4.21 shows the initial 2 minutes of the average product formation curves and logarithmic starting material consumption plot at each %pH$_2$ enrichment level.

Table 4.9: Calculated k_2 rate constants and initial spectral SNR values for the oxidative addition of pH_2 to Vaska's complex (0.43 mM) upon varying the %pH_2 enrichment level within the sample.

%pH_2	T / K	Avg. Max SNR	k_2 / $dm^3\ mol^{-1}\ s^{-1}$			
			1	2	3	Avg.
99.04	28.0	65	0.874	0.918	0.911	0.901 ± 0.014
91.34	40.0	47	0.930	0.920	0.930	0.926 ± 0.003
80.13	49.0	44	0.839	0.893	0.905	0.88 ± 0.02
69.77	57.5	32	0.949	0.925	0.922	0.932 ± 0.008
59.78	67.0	28	1.073	0.982	0.947	1.00 ± 0.04

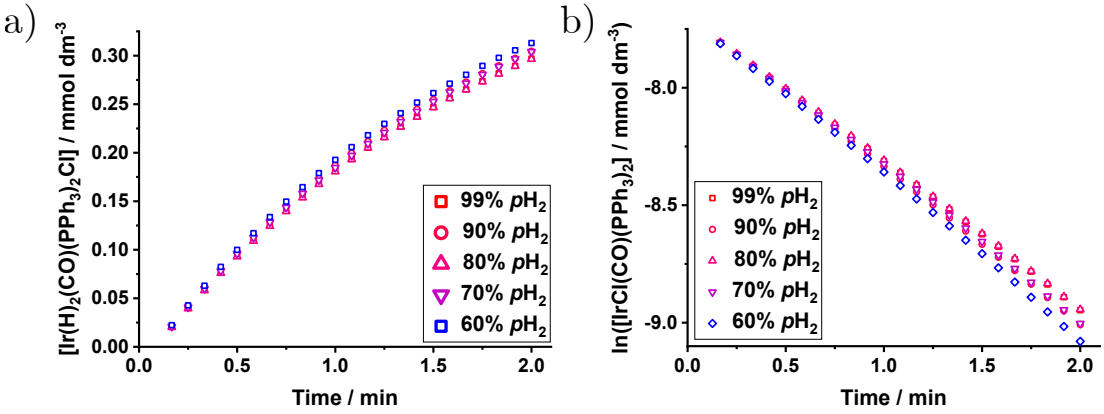

Figure 4.21: Average (a) product formation curves and (b) logarithmic starting material consumption plots for the oxidative addition of pH_2 (4 bar) to *trans*-[IrCl(CO)$(PPh_3)_2$](0.43 mM) in C_6D_6 recorded at 99%, 90%, 80%, 70% and 60% pH_2 enrichment.

As observed from this data, there is a high amount of consistency within the values obtained between 99% and 70% (a maximum range of 0.05 $dm^3\ mol^{-1}\ s^{-1}$ is observed between the average k_2 values) with no apparent trend that would suggest oH_2 conversion. Therefore, this chemical system does not exhibit any %pH_2 enrichment dependency that could affect the obtained kinetic parameters. Of note is the drop is average SNR observed within the first usable spectrum at each %pH_2 level. As PHIP activity is proportional to [pH_2], by introducing more oH_2 into the system, a reduction in SNR is observed. This is problematic for observing the decline in PHIP activity across the reaction coordinate as it will impact both the dynamic range of the hydride integrals being obtained and the number of datapoints able to be collected prior to loss of NMR signal into the noise. This is highlighted by the increasing rate constant observed at 60% pH_2 where the signal is lost to noise earlier in the reaction profile (as shown in Figure 4.22) and as such indicates total completion of the reaction at an earlier time which would correspond to a faster rate

of reaction. This dataset also has the highest error across the series, indicating that this earlier loss of signal into the spectral noise introduces more uncertainty into the calculated rate constants. Therefore, there is an inherent SNR limit within these reaction monitoring experiments that is required to be met to obtain accurate kinetic information from the reaction monitoring experiment. From this study, a provisional SNR limit of around 30 (the SNR between those for the 70% and 60% pH$_2$ enrichment level) can be established.

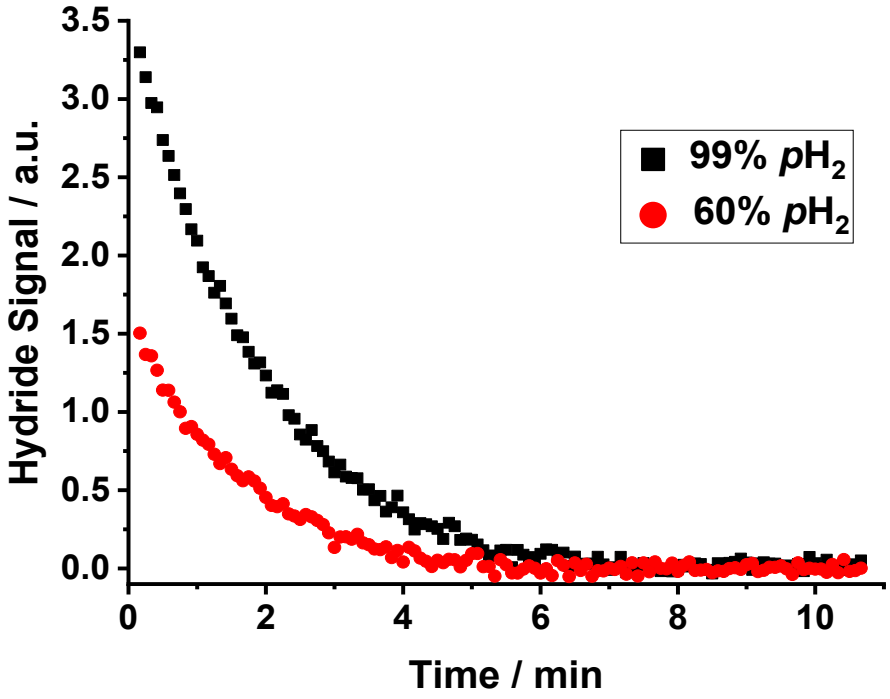

Figure 4.22: Comparison between the PHIP activity decay curves obtained for the reaction of Vaska's complex (0.43 mM) and pH$_2$ recorded at 99% and 60% pH$_2$ enrichment.

The key positive observation from this study is that %pH$_2$ enrichment level is not a factor that influences the observed rate of reaction for a system. Overall, this indicates that the designed experimental procedure should be reproducible regardless of the pH$_2$ generator that is employed. However, moving to lower %pH$_2$ enrichment levels will reduce the hyperpolarised signal observed across the reaction coordinate and can led to inaccurate rate constants being observed for the system. This limitation highlights that generally for this reaction monitoring method to be successful the setup used must enable strong PHIP signal enhancements for the chemical system being observed.

4.5 Expanding Applicability: Mixtures

4.5.1 Mixture Selection

From the validation experiments performed on Vaska's complex, the reaction monitoring protocol established on the benchtop NMR spectrometer has been shown to produce robust and reproducible kinetic information for a reaction. To demonstrate and expand the potential applications of this technique, an investigation into the ability of the technique to handle complex mixtures where there are multiple simultaneous reactions occuring within an NMR sample was performed.

Figure 4.23: Reaction Scheme for the equilibrium established when Vaska's complex is mixed with a suitable PR_3-type ligand, showing the formation of a mixture of unsubstituted, monosubstituted and disubstituted derivatives of the complex.

In order to add the required complexity, the mixtures that were selected to be explored were those of Vaska's complex and the derivatives formed upon addition of excess phosphine within the sample. As shown in Figure 4.23, when additional PR_3-type phosphines are added in excess to Vaska's complex a mixture of unsubstituted, monosubstituted and disubstituted derivatives are formed. This speciation is enabled by the high lability of the phosphine ligands on Vaska's complex and results in the formation of 3 possible complexes, all of which are unsaturated metal centres that are able to bind pH$_2$. This substitution reaction occurs through an associative mechanism whereby an additional PR_3 ligand binds to the square-planar complex to form a 5-coordinate intermediate species. The complex can then reorganise itself and lose one of the original phosphine ligands to form a new square-planar complex.[196] Previous research by Atwood *et al.* has shown that PR_3 ligand exchange via this mechanism occurs rapidly within a sample, with full exchange being established at temperatures of -70 °C and higher temperatures showing broadened resonances - indicating that exchange is competitive on the NMR timescale.[197] This ligand exchange mechanism has seen use synthetically to create derivatives of a complex with different PR_3 ligands.[198] Upon reaction with H_2, the only product formed for each Vaska's complex

derivative is the octahedral 6-coordinate dihydride complex. Therefore, the additional speciation of 5-coordinate species within the reaction mixture is assumed to have a negligible impact on the observed rate of oxidative addition reactions.

To ensure the formation of a suitable mixture of Vaska's Complex derivatives in solution, several different PR_3-type phosphine ligands were compared. The ideal phosphine ligand for this purpose was one that readily exchanged with Vaska's complex to form a distribution of [IrCl(CO)(PPh_3)], [IrCl(CO)(PPh_3)(PR_3)] and [IrCl(CO)(PR_3)]. Futhermore, upon reaction with pH_2 the derivatives formed must produce nicely resolved hydride resonances. To establish the phosphine ligands that met these conditions, NMR samples containing Vaska's Complex (0.43 mM) and 2 equivalents of PR_3 were made up. These samples were placed under pH_2 and then a single-scan hyperpolarised ^1H spectrum was recorded on a 400 MHz (9.4 T) NMR spectrometer. The phosphines that were examined are shown in Figure 4.24 with the pairs of hydrides observed for each complex summarised in Table 4.10. Within Figure 4.24, a green background is indicative of a mixture that led to the formation of Vaska's complex derivatives within the NMR sample while a red background indicates that no additional complexes were observed.

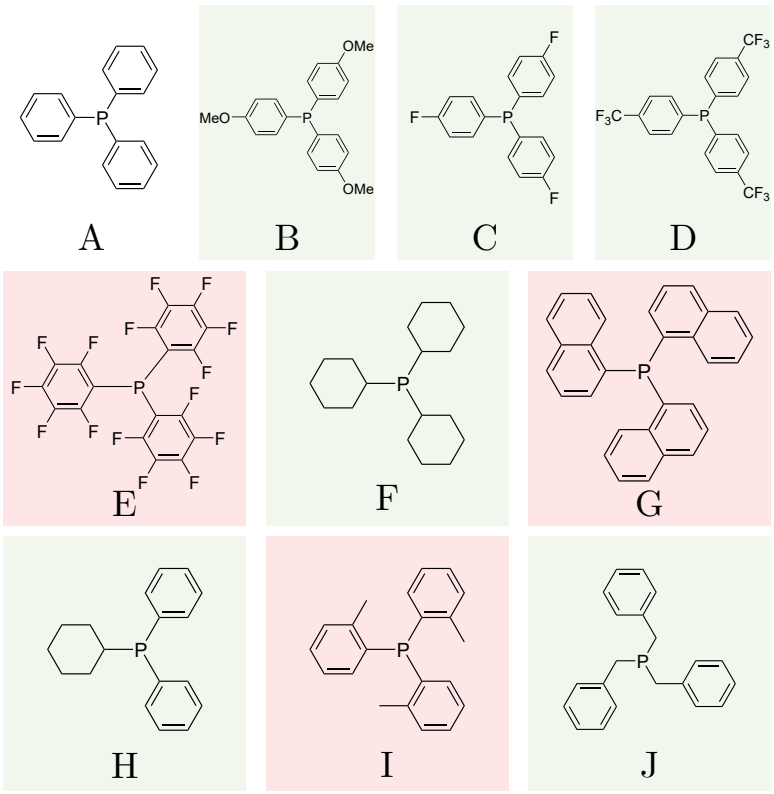

Figure 4.24: Structures for all PR_3 phosphine ligands mixed with *trans*-[IrCl(CO)(PPh_3)$_2$] in C_6D_6. A green background indicates the successful creation of Vaska's Complex derivatives upon addition.

Table 4.10: Chemical shift information for the Vaska's complex derivatives formed upon addition of PR_3 (2 eq.) to *trans*-[IrCl(CO)(PPh_3)$_2$](0.43 mM) in C_6D_6. Recorded at 400 MHz (9.4 T). The values within each column represent δ for H^1/H^2 for the complex.

PR_3	Identity	δ Unsubstituted / ppm	δ Monosubstituted / ppm	δ Disubstituted / ppm
B	$P(p-C_6H_4OMe)_3$	-6.70 / -17.49	-6.52 / 17.49	-6.25 / -17.49
C	$P(p-C_6H_4F)_3$	-6.70 / -17.49	-6.89 / -17.61	-7.10 / -17.73
D	$P(p-C_6H_4(CF_3))_3$	-6.70 / -17.49	-7.00 / -17.58	-7.31 / -17.69
F	PCy_3	-6.70 / -17.49	-7.50 / -18.82	-
H	$P(Cy)(Ph)_2$	-6.70 / -17.49	-7.09 / -18.19	-7.47 / -18.88
J	PBn_3	-6.70 / -17.49	-7.70 / -18.61	-8.38 / -19.61

While the phosphines given in Table 4.10 could all successfully substitute the PPh_3 ligands on Vaska's Complex, two were deemed unsuitable for this initial study. Tris(*p*-methoxy)phenylphosphine (B) was unsuitable due to the very poor resolution of the H^2 hydride region (with all species showing a single resonance at -17.49 ppm) and tricyclohexylphosphine (F) was deemed unsuitable due to the formation of only the monosubstituted [IrCl(CO)(PPh_3)(PR_3)] complex. Of the remaining available phosphines, tribenzylphosphine (PBn_3) was selected to be the best candidate due to the large chemical shift separation between the hydride peaks for each Vaska's complex derivative (as seen in Figure 4.25). This is especially important when considering the reduced chemical shift dispersion present at 1 T, as the broader resonances observed make the potential for peak overlap far greater.

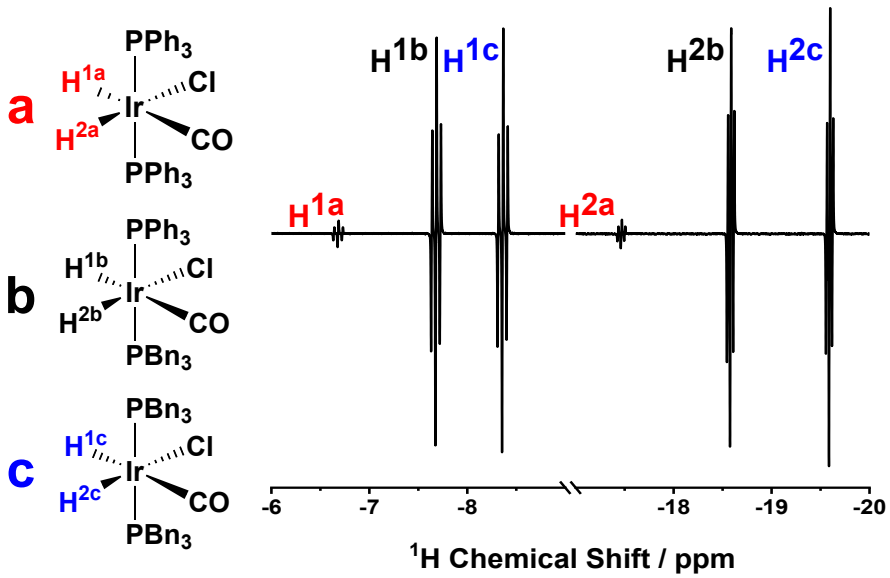

Figure 4.25: ^{1}H Spectrum of a mixture of Vaska's complex (0.43 mM) and PBn_3 (2 eq.) showing the distribution of hyperpolarised products. Recorded at 9.4 T (400 MHz) with 64 scans.

4.5.2 Properties of $[IrCl(CO)(PPh_3)_2]$ and PBn_3 Mixtures

With the selection of PBn_3 as a suitable candidate, a mixture of Vaska's complex (0.43 mM) and 2 equivalents of PBn_3 was made up and analysed on the benchtop NMR spectrometer. The sample was placed under pH_2, shaken to initiate the reaction and then a 64-scan hyperpolarised spectrum, with a repetition time of 100 ms, was recorded (Figure 4.26). Due to the short repetition time this spectrum is not quantitative but does allow for better qualitative analysis of the position and overlap of peaks at low-field. While a high resolution is retained for the H^2 environment for each complex, it is notable that there is significant overlap within the H^1 hydride region between all three species present due to the reduced chemical shift dispersion at low-field. As a result of this, certain peaks within the spectra are representative of the sum of two different chemical species and so will require additional consideration when performing integral analysis in reaction monitoring experiments. Using this spectrum and with confirmation from the high-field spectrum shown previously, chemical shift and J coupling constant information could be collated for each of the derivatives and these value are given in Table 4.11.

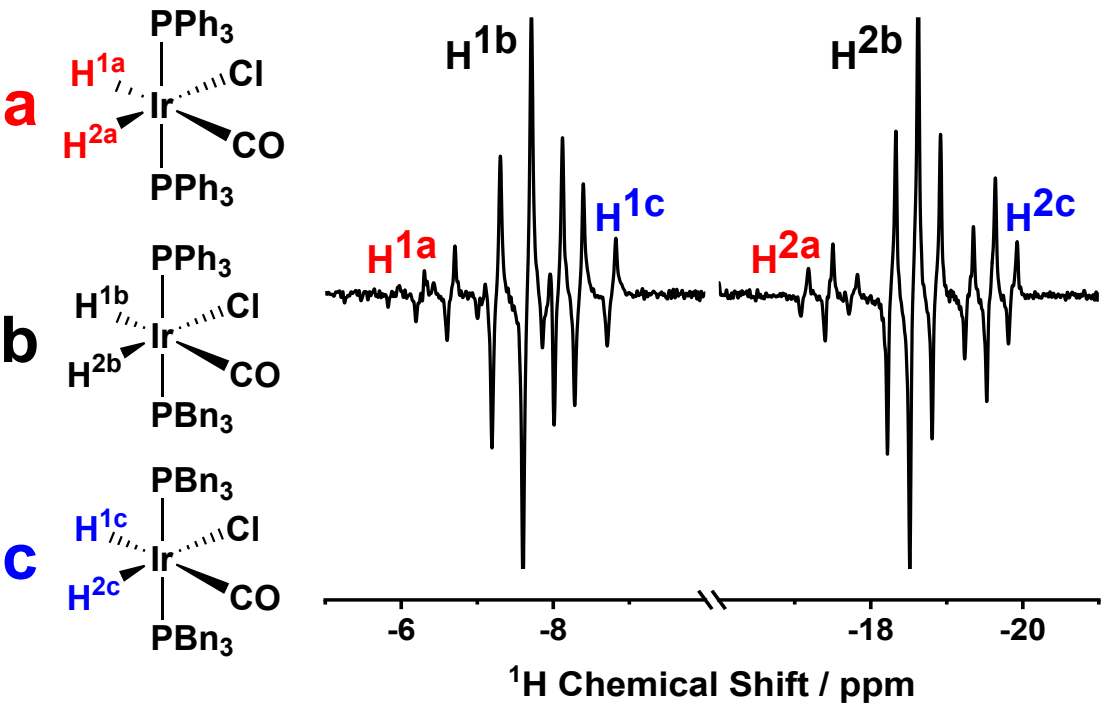

Figure 4.26: ^1H NMR spectrum of a mixture of Vaska's complex (0.43 mM) and PBn_3 (2 eq.) after pH_2 addition showing the distribution of hyperpolarised products. Recorded at 1 T (43 MHz) with 64 scans and a repetition time of 100 ms.

Table 4.11: Chemical shift and J coupling constant values for unsubstituted, monosubsituted and disubstituted Vaska's complex obtained from low-field NMR.

Complex	H^1			H^2		
	δ / ppm	J_{HH} / Hz	J_{HP} / Hz	δ / ppm	J_{HH} / Hz	J_{HP} / Hz
a	-6.69	4.6	17.6	-17.49	4.8	14.1
b	-7.67	4.8	17.7	-18.59	4.8	12.7
c	-8.37	4.9	18.5	-19.61	4.9	12.4

The presence of a dynamic equilibrium within the mixture sample results in there being significant differences between these systems and the original reaction monitoring experiments. Firstly, by changing the excess of phosphine that is present within the sample it is possible to influence the distribution of complexes within the sample. As shown by Figure 4.27, when increasing the excess of phosphine between 0.5 and 3 equivalents, the final distribution of complexes within the sample favours disubstituted product formation. This is a useful feature of the PBn_3 system as it shows the ease at which speciation within the sample can be altered, allowing for the system to be probed under optimal conditions or, alternatively, under limiting conditions as to test the concentration limitations of the reaction monitoring protocol.

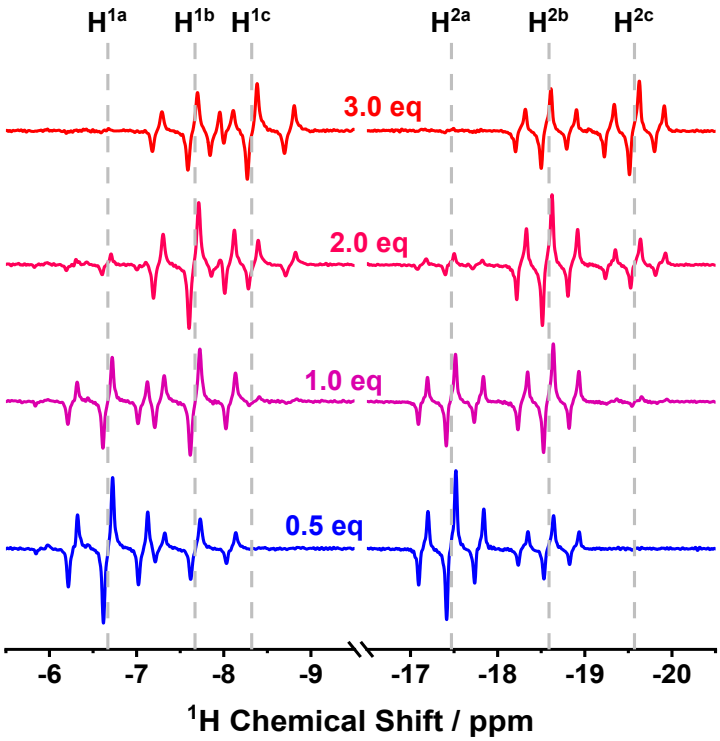

Figure 4.27: Hydride spectrum for mixtures of Vaska's complex (0.43 mM) and 0.5 - 3 equivalents of PBn_3 showing the change in speciation upon addition of different phosphine excesses. Spectra recorded with 64 scan a repetition time of 100 ms.

4.5.3 Properties of *trans*-[IrCl(CO)(PBn_3)$_2$]

Following the selection of PBn_3 as a good candidate, it was necessary to synthesise a pure sample of the disubstituted complex, *trans*-[IrCl(CO)(PBn_3)$_2$], so that kinetic information about the system could be established. The synthetic route given below in Figure 4.28 was modified from a procedure by Burk *et al.*[199] Following synthesis, this complex was characterised by ^{1}H and ^{31}P{^{1}H} NMR and IR spectroscopy, all of which confirmed a high purity of the synthesised complex. Full characterisation data can be found within the Experimental chapter (Section 8.4.2).

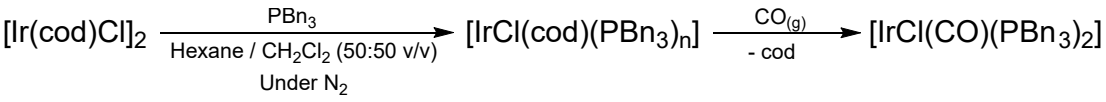

Figure 4.28: Synthetic route for the preparation of [Ir(Cl)(CO)(PBn_3)$_2$] adapted from a procedure by Burk *et al.*.[199]

Following the synthesis of *trans*-[IrCl(CO)(PBn_3)$_2$], low-field NMR reaction monitoring was performed to obtain kinetic information about the system. Two samples of *trans*-[IrCl(CO)(PBn_3)$_2$] (0.2 mg, 0.39 mM) in C_6D_6 (0.6 mL) were prepared, degassed and reacted with pH_2 (4 bar). Figure 4.29a is an example ^{1}H spectrum recorded during the reaction monitoring experiment highlighting the two hyperpolarised hydride peaks generated at -8.4 and -19.6 ppm for H^1 and H^2 respectively.

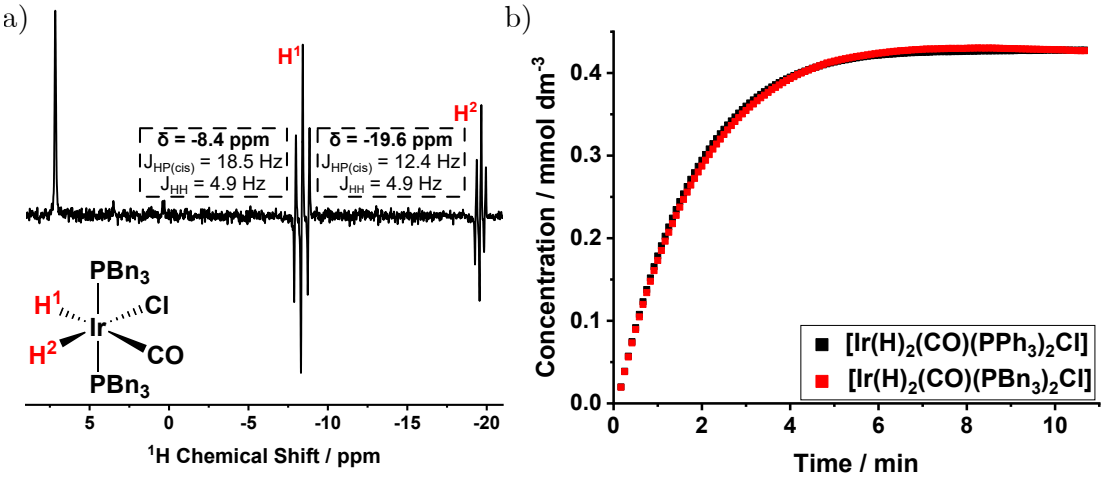

Figure 4.29: (a) Hyperpolarised single-scan ^{1}H spectrum and (b) a product formation curve for the reaction between pH_2 and *trans*-[IrCl(CO)(PBn_3)$_2$] (0.39 mM) in C_6D_6. A comparative reaction rate for *trans*-[IrCl(CO)(PPh_3)$_2$] is overlaid onto (b).

Analysis of the reaction monitoring data (Figure 4.29b) produced a k_2 of

(0.83 ± 0.03) $dm^3\ mol^{-1}\ s^{-1}$ for the reaction. The slower rate of reaction observed for the oxidative addition of pH_2 to *trans*-[IrCl(CO)(PBn_3)$_2$] relative to *trans*-[IrCl(CO)(PPh_3)$_2$] is expected for both electronic and steric reasons. To break the H-H bond of pH_2, the Ir metal centre must donate electron density from either the d_{xy} or d_{yz} orbital into the $\sigma^*(H_2)$ antibonding orbital of pH_2. Therefore, an increase to the electron density of the metal centre will result in a faster rate of addition. As phosphine ligands act as σ-donor and π-acceptor ligands, improving the σ-donor capability of the ligand will increase the electron density on the metal centre. One method to measure the relative electron richness of the Ir-centre is through examination of the carbonyl stretching frequency within the complex, with a lower value of ν_{CO} indicating a more electron-rich metal centre.[175] From recorded IR spectra, *trans*-[IrCl(CO)(PBn_3)$_2$] has a ν_{CO} of 1959 cm^{-1} and from characterisation data (Section 8.4.1), *trans*-[IrCl(CO)(PPh_3)$_2$] has a ν_{CO} of 1949 cm^{-1}. This means that *trans*-[IrCl(CO)(PPh_3)$_2$] would be expected to react at a faster rate due to electronic reasons. In terms of steric interactions, the Tolman Steric Parameter gives an indication of the cone angle for different phosphine ligands. A larger cone angle would increase the crowding within the coordination sphere of the metal complex and as such a slower rate of reaction would be expected. For PPh_3 and PBn_3 the ligand cone angles are 145° and 165° respectively and therefore this parameter also indicates that Vaska's complex would be expected to react faster.[173]

While steric and electronic properties can justify which reaction should occur on a faster timescale, determination of the activation energies of the two reactions is useful to quantify the expected difference in reaction rate. To investigate this, a series of reaction monitoring experiments for both complexes were performed at variable temperatures (these experiments had to be performed at high-field due to the fixed stabilisation temperature of the benchtop NMR spectrometer). The obtained rate constants for both complexes at temperatures between 10 °C and 30 °C are given in Table 4.12.

Table 4.12: k_2 rate constants for the oxidative addition of pH_2 to *trans*-[IrCl(CO)(PPh_3)$_2$] (0.43 mM) and *trans*-[IrCl(CO)(PBn_3)$_2$] (0.39 mM) recorded between 283 and 303 K. Data was collected on a 400 MHz (9.4 T) spectrometer using an OPSY pulse sequence.

Complex	k_2 / $dm^3\ mol^{-1}\ s^{-1}$				
	283 K	288 K	293 K	298 K	303 K
trans-[IrCl(CO)(PPh_3)$_2$]	0.27	0.34	0.49	0.64	0.92
trans-[IrCl(CO)(PBn_3)$_2$]	0.28	0.35	0.48	0.62	0.88

To extract thermodynamic properties for each complex, the Eyring equation can be used (Equation 4.3) where k is the rate constant for the reaction, T is the temperature, $\Delta H^{\ddagger}$ is the activation enthalpy, R is the ideal gas constant, k_B is the Boltzmann constant, h is Planck's constant and $\Delta S^{\ddagger}$ is the activation entropy.[200] Using this equation, the values of $\Delta H^{\ddagger}$ and $\Delta S^{\ddagger}$ can be determined through linear fitting of $\ln(\frac{k}{T})$ against $\frac{1}{T}$. Once these thermodynamic properties are determined, the Gibbs free energy of activation ($\Delta G^{\ddagger}$) at a specific temperature can be acquired (Equation 4.4).[201] Eyring equation plots for both complexes are given in Figure 4.30 and the extracted thermodynamic parameters, alongside $\Delta G^{\ddagger}$ at 301.5 K, are given in Figure 4.13.

$$\ln\left(\frac{k}{T}\right) = \frac{\Delta H^{\ddagger}}{R}\frac{1}{T} + \ln\left(\frac{k_B}{h}\right) + \frac{\Delta S^{\ddagger}}{R} \tag{4.3}$$

$$\Delta G^{\ddagger} = \Delta H^{\ddagger} - T\Delta S^{\ddagger} \tag{4.4}$$

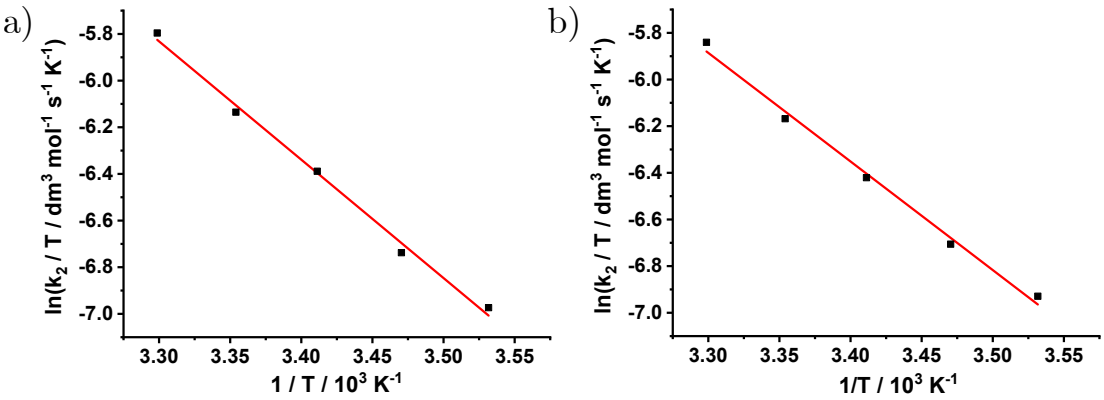

Figure 4.30: Eyring equation plots for (a) *trans*-[IrCl(CO)(PPh_3)$_2$] (0.43 mM) and (b) *trans*-[IrCl(CO)(PBn_3)$_2$] (0.39 mM) for the addition of pH_2 between 283 and 303 K.

Table 4.13: Thermodynamic activation energy parameters for the addition of pH_2 to *trans*-[IrCl(CO)(PPh_3)$_2$] and *trans*-[IrCl(CO)(PBn_3)$_2$].

Complex	$\Delta H^{\ddagger}$ / kJ mol^{-1}	$\Delta S^{\ddagger}$ / J K^{-1} mol^{-1}	$\Delta G^{\ddagger}$ (T = 301.5 K) / kJ mol^{-1}
trans-[IrCl(CO)(PPh_3)$_2$]	(42 ± 2)	(-107 ± 7)	(74 ± 3)
trans-[IrCl(CO)(PBn_3)$_2$]	(39 ± 2)	(-119 ± 9)	(75 ± 3)

The values for $\Delta H^{\ddagger}$ and $\Delta S^{\ddagger}$ obtained for *trans*-[IrCl(CO)(PPh_3)$_2$] are well matched to those previously obtained within the literature by Chock *et al.* (where

$\Delta H^{\ddagger}$ = 45 kJ mol^{-1} and $\Delta S^{\ddagger}$ = -96 J mol^{-1} K^{-1}).[111] The accuracy of the *trans*-[IrCl(CO)(PPh_3)$_2$] values indicates that those obtained for *trans*-[IrCl(CO)(PBn_3)$_2$] will be valid (as these have not been previously reported) and so comparisons can be made between the two systems. The most significant result from this experiment is that the values of $\Delta G^{\ddagger}$ calculated for both complexes are within error of each other, with only a slightly higher activation energy for the *trans*-[IrCl(CO)(PBn_3)$_2$] complex. This finding suggests that although the reaction of *trans*-[IrCl(CO)(PBn_3)$_2$] would be expected to occur at a slower rate (for steric and electronic reasons), these properties of the complexes cause a near negligible difference in the activation energy barriers for the reactions. Therefore, within the accuracy of the PHIP hyperpolarised reaction monitoring technique, both reactions will occur on near identical timescales. This is beneficial for simultaneous reaction monitoring as the progress of both reactions can be monitored using the same experimental parameters.

In terms of routes to form mixtures of unsubstituted, monosubstituted and disubstituted complexes in solution, the synthesis of *trans*-[IrCl(CO)(PBn_3)$_2$] provides two additional options. The first option is the addition of excess PPh_3 to a solution of *trans*-[IrCl(CO)(PBn_3)$_2$], providing an opposite starting state for the solution but that should equilibrate to the same distributions seen when performing PBn_3 addition to *trans*-[IrCl(CO)(PPh_3)$_2$]. The second option is to put a mixture of *trans*-[IrCl(CO)(PBn_3)$_2$] and *trans*-[IrCl(CO)(PPh_3)$_2$] into the sample. While there is not an excess of PR_3-type ligands within the solution, research by Rominger *et al.*[202] has indicated the mixing of two iridium-centred square-planar complexes that contain different PR_3-type ligands can lead to scrambling of the phosphine ligands to form a mixtures of complexes that contain all possible combinations of the PR_3-type ligands present. The route for this was theorised to likely be a dissociative mechanism of initial loss of PR_3 ligands from the complexes following which the free phosphine can bind to another complex to form a 5-coordinate intermediate that can reorganise and lose a different PR_3 ligand.

4.5.4 Mixture Reaction Monitoring Protocol

Before reaction monitoring can be performed on these complex mixtures, the problem of having peak overlap within the ^{1}H hydride region needs to be addressed within the automated processing procedure. In order to achieve this, simulation studies can be performed in order to understand which peaks within the spectrum

are contributed to by several species and which represent a single species. For this, a MATLAB script was written that uses the Spinach package to plot each species individually (using the characterisation information given in Table 4.11) and then allows the user to define the proportion of each species that contributes to an overall spectrum. For this, all spectra are normalised so that the maximum signal within each spectrum is equal to 1. To prove that the simulated spectrum could accurately predict the spectra of mixtures, the MATLAB script was used to try to replicate the spectrum shown in Figure 4.26. To simulate this spectrum, the contribution of each species was calculated using the unsubstituted: monosubstituted: disubstituted ratio of integrals within the experimental data of 0.10:0.65:0.25 and a Gaussian filter with a width of 25 was applied to mimic the peak width seen within the data. The resulting simulated spectrum (shown in Figure 4.31) strongly matches the experimental spectrum and as such can be used to determine where major incidents of peak overlap are occurring.

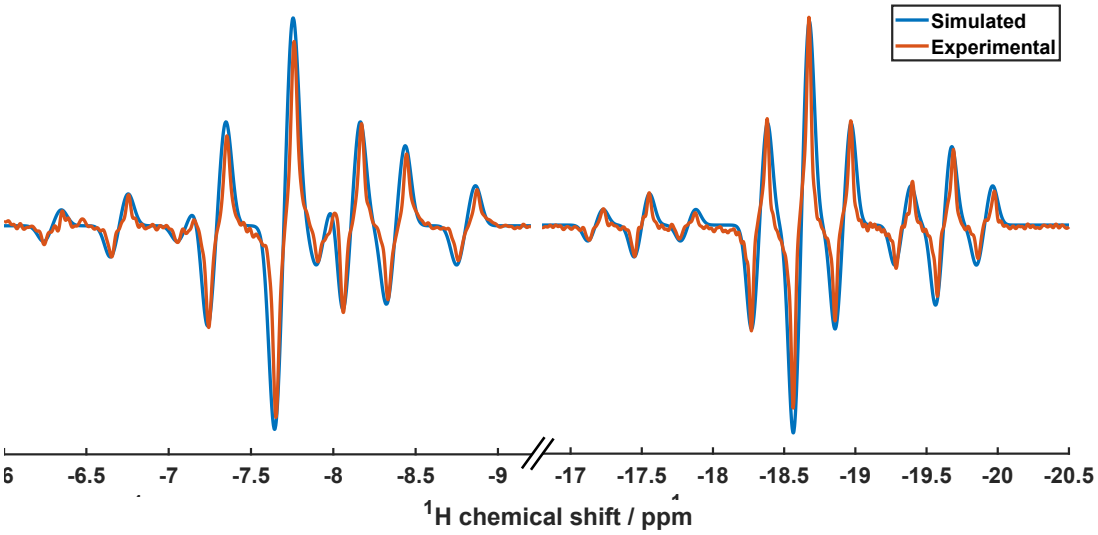

Figure 4.31: Comparison between simulated and experimental hydride region spectra of a mixture of Vaska's complex (0.43 mM) and 2 equivalents of PBn_3.

To identify the regions of peak overlap, the MATLAB script was performed with identical parameters to before but rather than plotting the combined spectrum, the script overlaid the ^{1}H hydride regions for each species, the result of which is given in Figure 4.32. Within the simulated spectrum, there are two clear regions of non-negligible peak overlap: a smaller region between $[Ir(H)_2(CO)(PBn_3)_2Cl]$ and $[Ir(H)_2(CO)(PPh_3)(PBn_3)Cl]$ and a large overlap between $[Ir(H)_2(CO)(PPh_3)(PBn_3)Cl]$ and $[Ir(H)_2(CO)(PPh_3)_2Cl]$. For these overlapped regions, the two options for analysis are to use more sophisticated data processing to extract the individual components of the peaks or to ignore these peaks and remove them from the calculated integrals for each species. While resolving peak components is

preferable, due to retention of more signal for each species, there are substantial difficulties with quantification of the contribution of each peak. To be able to calculate these contributions, it would be necessary to precisely know the concentration of hyperpolarised product formed for each species within each evolution delay and also the amount of hyperpolarised signal that is observed per hyperpolarised product formed (and how relaxation will affect this). Trying to solve for this many unknown variables would make complete analysis of these peaks difficult, even with the use of simulations. Therefore, the optimal approach for initial testing of mixture reaction monitoring is to remove these peaks from the analysis, only integrating the peaks without significant overlap. The limitation of this approach is that not all of the available signal is used reducing the sensitivity of the analysis for components that give low SNR ^{1}H spectra.

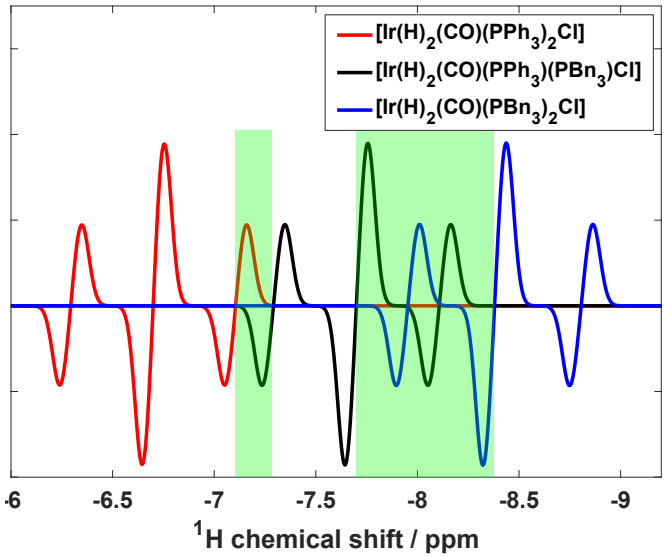

Figure 4.32: Simulation of the H^1 region of the mixture of Vaska's complex derivative formed upon addition of PBn_3. Highlighted in green are the regions of significant overlap between species.

4.5.5 Mixture Reaction Monitoring at Low-field

To test the capability of the reaction monitoring procedure to handle the analysis of a complex mixture, an initial performance test was done using an equimolar mixture of 0.43 mM of *trans*-[IrCl(CO)(PPh_3)$_2$] (0.20 mg) and 0.43 mM of *trans*-[IrCl(CO)(PBn_3)$_2$] (0.23 mg). This increased total concentration of iridium in the sample (0.86 mM) was used to counteract the reduced SNR that is observed when observing the speciation within these mixtures. This concentration is double that used previously (i.e. a 0.4 mg sample of Vaska's complex). This increase in

complex concentration reduces the overall excess of pH$_2$ in the solution to a 14-fold difference. To ensure that this does not have a substantial impact on the observed rate constants, 0.86 mM samples containing only *trans*-[IrCl(CO)(PPh$_3$)$_2$] and *trans*-[IrCl(CO)(PBn$_3$)$_2$] were reacted with pH$_2$ and found to have rate constants of (0.82 ± 0.04) and (0.83 ± 0.03) dm^3 mol^{-1} s^{-1} respectively. Compared to the values obtained using a concentration of 0.43 mM of (0.89 ± 0.03) and (0.83 ± 0.03) dm^3 mol^{-1} s^{-1}, these rates obtained with a reduced pH$_2$ excess were found to within acceptable limits to proceed with the increased concentration.

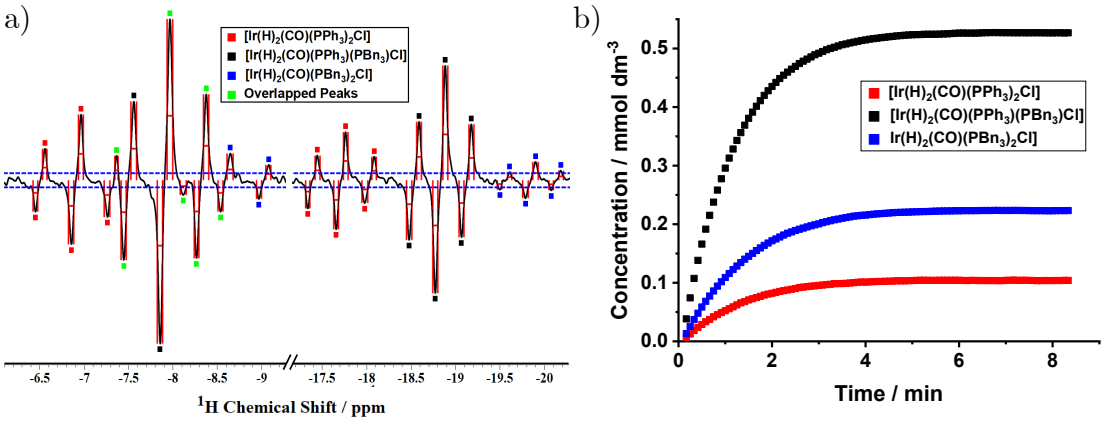

Figure 4.33: (a) Hyperpolarised single-scan ^{1}H spectrum and (b) the product formation curves for the reaction between pH$_2$ and a mixture of *trans*-[IrCl(CO)(PPh$_3$)$_2$] (0.43 mmM) and *trans*-[IrCl(CO)(PBn$_3$)$_2$] (0.43 mM).

The reaction monitoring experiment was performed in triplicate using the standard reaction monitoring procedure with temperature stabilisation. To perform the analysis, the first spectrum with pure PASADENA character was used to determine suitable integration windows for each peak within the mixture (an example of which is shown in Figure 4.33a) and then these peaks were grouped based on the complex they originated from. Any overlapped peaks within the ^{1}H region were discarded into a separate group (shown by the green labels within the figure) as to prevent them from influencing the integral analysis. Once suitable parameters for peak selection were determined, integration across the pseudo-2D matrix of spectra was performed with these integrals then being summed, normalised and accumulated to produce product formation curves. To scale the product formation curves to the final concentration of each species, a 64-step ^{1}H spectrum was recorded at high-field (9.4 T) at the end of the reaction monitoring experiment and the ratio of the integrals for each complex was used to determine the proportion of the overall concentration of Ir within the solution attributed to each complex. Following this, data could be fitted to a mono-exponential recovery function to determine individual rate constants for each component in the mixture.

Figure 4.33b shows the resulting product formation curves obtained for the mixture of *trans*-[IrCl(CO)(PPh_3)$_2$] and *trans*-[IrCl(CO)(PBn_3)$_2$]. The appearance of this data was very promising as it clearly showed that individual product formation curves could be obtained through simultaneous reaction monitoring within a complex mixture. However upon calculation of the k_2 rate constants for each complex, discrepancies to those calculated using the single species samples were observed. Average rates of (0.82 ± 0.04), (1.07 ± 0.09) and (1.05 ± 0.03) $dm^3\ mol^{-1}\ s^{-1}$ were determined for the formation of [Ir(H)$_2$(CO)(PPh_3)$_2$Cl], [Ir(H)$_2$(CO)(PPh_3)(PBn_3)Cl] and [Ir(H)$_2$(CO)(PBn_3)$_2$Cl] respectively. While the k_2 rate observed for [Ir(H)$_2$(CO)(PPh_3)$_2$Cl] is within the expected range, the observed rates for the other two species are much faster than expected.

To investigate this discrepancy and to assess the quality of kinetic data that can be obtained for complex mixtures via this method, a series of reaction monitoring experiments were performed with different mixture compositions. A series of mixtures containing Vaska's complex and PBn_3 were made up with ligand excesses of 0.5, 1, 2 and 3 equivalents. To complement this, a series of mixtures containing Vaska[PBn_3]$_2$ (a shorthand for the *trans*-[IrCl(CO)(PBn_3)$_2$] complex) and PPh_3 were made up with ligands excesses of 0.5, 1, 2, and 3 equivalents. Finally, a mixture containing equal concentrations of Vaska's complex and Vaska[PBn] was made. For all samples, the total concentration of iridium present is consistent and each sample was made up in triplicate. The results for the reaction monitoring experiments are given in Tables 4.14 - 4.16 for the formation of [Ir(H)$_2$(CO)(PPh_3)$_2$Cl], [Ir(H)$_2$(CO)(PPh_3)(PBn_3)Cl] and [Ir(H)$_2$(CO)(PBn_3)$_2$Cl] respectively. Each table summarises the calculated rate constants for the formation of that particular complex within each of the mixtures along with the SNR for the first usable spectrum in the experiment and the proportion of that complex seen within a high-field spectrum obtained post reaction monitoring.

Table 4.14: Calculated k_2 rate constants and signal-to-noise for the formation of $[Ir(H)_2(CO)(PPh_3)_2Cl]$ upon pH_2 addition over a range of different mixture compositions.Dashed lines indicate no available data for that complex within the associated mixture.

Sample	Proportion	k_2 / $dm^3\ mol^{-1}\ s^{-1}$				Avg. SNR
		1	2	3	Avg.	
Vaska	1.00	0.858	0.775	0.832	(0.82 ± 0.04)	(127 ± 1.9)
Vaska$[PBn_3]_2$	-	-	-	-	-	-
Vaska + Vaska$[PBn_3]_2$	0.26	0.942	0.889	1.118	(0.98 ± 0.07)	(32 ± 3)
Vaska + 3 eq PBn_3	-	-	-	-	-	-
Vaska + 2 eq PBn_3	-	-	-	-	-	-
Vaska + 1 eq PBn_3	0.22	-	1.203	1.192	(1.198 ± 0.006)	(32.7 ± 1.8)
Vaska + 0.5 eq PBn_3	0.55	0.909	0.895	0.909	(0.904 ± 0.005)	(68.1 ± 1.8)
Vaska$[PBn_3]_2$ + 3 eq PPh_3	-	-	-	-	-	-
Vaska$[PBn_3]_2$ + 2 eq PPh_3	-	-	-	-	-	-
Vaska$[PBn_3]_2$ + 1 eq PPh_3	-	-	-	-	-	-
Vaska$[PBn_3]_2$ + 0.5 eq PPh_3	-	-	-	-	-	-

Table 4.15: Calculated k_2 rate constants and signal-to-noise for the formation of $[Ir(H)_2(CO)(PPh_3)(PBn_3)Cl]$ upon pH_2 addition over a range of different mixture compositions. Dashed lines indicate no available data for that complex within the associated mixture.

Sample	Proportion	k_2 / $dm^3\ mol^{-1}\ s^{-1}$				Avg. SNR
		1	2	3	Avg.	
Vaska	-	-	-	-	-	-
Vaska$[PBn_3]_2$	-	-	-	-	-	-
Vaska + Vaska$[PBn_3]_2$	0.62	1.043	0.931	1.245	(1.07 ± 0.09)	(78 ± 5)
Vaska + 3 eq PBn_3	0.12	1.018	-	1.226	(1.12 ± 0.10)	(13.4 ± 1.9)
Vaska + 2 eq PBn_3	0.36	1.065	1.130	1.131	(1.11 ± 0.02)	(42.5 ± 1.3)
Vaska + 1 eq PBn_3	0.68	-	1.146	1.113	(1.129 ± 0.017)	(90.2 ± 0.7)
Vaska + 0.5 eq PBn_3	0.43	1.271	1.290	1.289	(1.283 ± 0.006)	(60 ± 3)
Vaska$[PBn_3]_2$ + 3 eq PPh_3	0.34	1.008	1.048	1.128	(1.06 ± 0.04)	(27.2 ± 0.4)
Vaska$[PBn_3]_2$ + 2 eq PPh_3	0.28	1.234	1.237	1.217	(1.229 ± 0.006)	(20.3 ± 1.9)
Vaska$[PBn_3]_2$ + 1 eq PPh_3	0.19	1.334	1.194	1.264	(1.26 ± 0.07)	(14.60 ± 0.10)
Vaska$[PBn_3]_2$ + 0.5 eq PPh_3	0.13	1.256	1.334	1.125	(1.24 ± 0.06)	(8 ± 2)

Table 4.16: Calculated k_2 rate constants and signal-to-noise for the formation of $[Ir(H)_2(CO)(PBn_3)_2Cl]$ upon pH_2 addition over a range of different mixture compositions. Dashed lines indicate no available data for that complex within the associated mixture.

Sample	Proportion	k_2 / $dm^3\ mol^{-1}\ s^{-1}$				Avg. SNR
		1	2	3	Avg.	
Vaska	-	-	-	-	-	-
Vaska$[PBn_3]_2$	1.00	0.869	0.779	0.847	(0.83 ± 0.03)	(63.5 ± 1.6)
Vaska + Vaska$[PBn_3]_2$	0.12	0.982	0.986	1.19	(1.05 ± 0.07)	(13.1 ± 0.9)
Vaska + 3 eq PBn_3	0.88	0.844	-	0.888	(0.87 ± 0.02)	(93.6 ± 0.3)
Vaska + 2 eq PBn_3	0.64	0.921	0.928	0.978	(0.942 ± 0.017)	(74 ± 3)
Vaska + 1 eq PBn_3	0.11	-	1.592	1.271	(1.43 ± 0.16)	(18.1 ± 0.8)
Vaska + 0.5 eq PBn_3	-	-	-	-	-	-
Vaska$[PBn_3]_2$ + 3 eq PPh_3	0.66	0.894	0.998	0.981	(0.96 ± 0.03)	(51.2 ± 0.8)
Vaska$[PBn_3]_2$ + 2 eq PPh_3	0.72	0.891	0.922	0.917	(0.96 ± 0.02)	(51 ± 3)
Vaska$[PBn_3]_2$ + 1 eq PPh_3	0.81	0.961	0.936	0.949	(0.949 ± 0.013)	(60.2 ± 1.5)
Vaska$[PBn_3]_2$ + 0.5 eq PPh_3	0.87	0.936	0.927	1.005	(0.91 ± 0.01)	(62 ± 2)

There are several key observations that can be made when assessing the large amount of data obtained for the reaction monitoring of these equilibrium mixtures. The most important observation is that there is a non-negligible deviation in the observed rate constants for the formation of both $[Ir(H)_2(CO)(PPh_3)_2Cl]$ and $[Ir(H)_2(CO)(PBn_3)_2Cl]$ across the data series that are shown. The formation of both species is shifted to higher k_2 rate constants as the proportion of that species within the final mixture is reduced. There are two likely factors that contribute to this trend.

First is that the reaction monitoring experiment is capturing the complex interplay between two competing processes: the irreversible formation of the hyperpolarised product and the reversible formation of different Vaska's complex derivatives due to the dynamic equilibrium present within the sample. Over the course of the oxidative addition reaction, there will be a continual adjustment of the proportions of *trans*-$[IrCl(CO)(PPh_3)_2]$, *trans*-$[Ir(CO)(PPh_3)(PBn_3)Cl]$ and *trans*-$[IrCl(CO)(PBn_3)_2]$ present to try and maintain the equilibrium within the sample. This underlying change to available starting material for each reaction will impact the amount of hyperpolarised product formed prior to each spectral acquisition. Therefore, the PHIP activity observed for each species becomes dependent on both the rate of the oxidative addition reaction and the rate of equilibration of the sample. As both processes occur on the NMR timescale, the resulting k_2 for the reaction is skewed to higher than expected values. This complex interplay helps to explain why the recorded values for the formation of $[Ir(H)_2(CO)(PPh_3)(PBn_3)Cl]$ are consistently fast as there are two underlying equilibrium processes that are obscuring the k_2 rate constant. One strong piece of evidence that supports this interpretation rather than the higher rate constants being due to a pH_2 effect is that there is no systemic deviation across the rate constants for all species within a mixture. If the rate constants for all components within a sample showed an overprediction of the rate constant this would be indicative of pH_2 consumption influencing the reaction rates (as the pseudo-first order kinetics would break down). However, as different complexes within a mixture show higher and lower than expected rate constants the variation cannot be caused by a pH_2 effect.

A second factor that compounds the trend seen above is that having a lower proportion of a species within the mixture will result in the observed hyperpolarised signals for that species being weaker. This is reflected within the measured maximum SNR observed for all complexes across the the two phosphine addition series (where

additional equivalents of either PPh_3 or PBn_3 are added) as decreases in the proportion of a complex across the series results in a reduction in SNR. Within the previous $\%pH_2$ enrichment study (Section 4.4), an approximate SNR limit of 30 was found where the reduced hyperpolarised signals across the reaction resulted in deviation of the observed rate constant to higher values. Therefore, for complexes that do not meet this SNR threshold the observed k_{obs} will likely show a further increase and a higher uncertainty in the measured value. This previous finding is supported within the rate constants obtained within this experiment as a general trend is seen that for samples that have an initial SNR below 30, a higher variability is observed in the calculated rate constants for that species.

While the reaction monitoring experiment is not equipped to separate the competing processes present within the sample, the rate constants produced for components within each mixture are shown to have a good reproducibility if the SNR threshold is met. This indicates that the underlying reaction monitoring method is still robust and so any deviations that are observed from the expected values for these components are likely to be real and indicative of additional complexity within the sample being explored. One caveat to this statement are the mixtures containing equimolar proportions of *trans*-[IrCl(CO)$(PPh_3)_2$] and *trans*-[Ir(CO)$(PPh_3)(PBn_3)$Cl] which showed much greater variability between repeat measurements. In this case, the increased complexity of the phosphine substitution mechanism (due to the lack of free phosphine in solution) may have led to a worse performance of the reaction monitoring procedure.

Overall, the mixtures study highlighted a few key features to be aware of when using this reaction monitoring method. Firstly, the presence of competing processes that have comparable timescales to that of the required reaction can lead to the observation of skewed rate constants. Secondly, the reaction monitoring method is robust permitting that a threshold SNR value is achieved for this system. This may lead to issues for systems that have lower enhancement factors than Vaska's complex. Finally to successfully monitor several species, the hyperpolarised signals obtained need to have sufficient resolution from one another. For the mixture of Vaska's complex and PBn_3, enough peaks were well-resolved to allow for analysis of each component within the mixture. However, for systems containing more similar components or that require analysis of peaks within the organic region of the spectrum, it may not be possible to remove overlapped peaks from analysis. Overcoming these limitations could be achieved through implementation of heteronuclear decoupling within the NMR experiments as to reduce the multiplicity

of the resonances to be analysed. This solution could not be implemented with the current reaction monitoring setup as the Spinsolve Carbon benchtop NMR spectrometer does not have a ^{31}P channel.

4.6 Conclusions

In this chapter, the effects of several experimental parameters on the PHIP hyperpolarised reaction monitoring procedure were investigated. Of these parameters, only temperature was observed to have a significant impact on the rate of $[Ir(H)_2(CO)(PPh_3)_2Cl]$ formation and this effect was mitigated through appropriate changes to the experimental procedure: the introduction of a thermally-insulated holder and of equilibration periods prior to reaction monitoring. Using this procedure, the higher k_2 for $[Ir(H)_2(CO)(PPh_3)_2Cl]$ formation of (0.89 ± 0.03) $dm^3\,mol^{-1}\,s^{-1}$ observed showed excellent agreement with the expected value of (0.86 ± 0.03) $dm^3\,mol^{-1}\,s^{-1}$ from literature.[111] The reaction monitoring technique was also seen to successfully analyse multiple competing reactions of Vaska's complex derivatives within a mixture, with the automated data processing able to extract multiple product formation curves from a single experiment.

Within the reaction monitoring of mixtures containing *trans*-$[IrCl(CO)(PPh_3)_2]$ and *trans*-$[IrCl(CO)(PBn_3)_2]$, deviations of the measured rate constants from those recorded on pure samples of each complex were observed. These deviations were not indicative of a breakdown of the analysis method but rather attributed to the presence of competitive phosphine ligand substitution processes that occurred on a similar timescale to the oxidative addition reaction. This result is similar to that observed within the study of PHIP signal relaxation whereby simulation studies highlighted that relaxation will have a negligible effect on the rate of reaction unless it occurs on a similar or slower timescale than pH_2 addition. These findings indicate that not all hydrogenation reactions are suitable for monitoring with this technique as it is unable to distinguish between multiple processes occurring on similar timescales.

Within these studies, the lower sensitivity of the benchtop NMR spectrometer relative to standard high-field NMR spectrometers was observed to be both advantageous and disadvantageous. While the lower sensitivity reduced the presence of signals from thermally-polarised product molecules (alleviating the need for more complex OPSY-type pulse sequences), low concentration

hyperpolarised complexes or setups that use lower $p\mathrm{H_2}$ enrichment levels may observed SNR issues that prevent easy analysis of the reaction coordinate. The limit found with this experimental setup was that an initial SNR above 30 was required to allow for a sufficient decay in PHIP activity to be monitored for a chemical reaction.

With the validation of this reaction monitoring method, future experiments could focus on applying this technique to an industrially relevant hydrogenative process (such as the catalytic hydrogenation reactions that have previously been monitored using high-field ROCHESTER experiments).[155] Additionally, showcasing the simultaneous reaction monitoring capabilities on a more suitable mixture of chemical species would provide a clearer demonstration of this wider application of the technique. In terms of improvements to the method itself, the development of *in situ* bubbling within the NMR magnet would provide a route to further improve the mitigation of temperature effects within the experiments.[187] Furthermore to improve resolution of hydrides from similar species within $^{1}\mathrm{H}$ spectra, it would be beneficial to develop experiments that utilise heteronuclear decoupling (such as from $^{31}\mathrm{P}$ to reduce the multiplicity of the peaks) or ultrafast-2D pulse sequences (to separate peaks out in multiple dimensions).[203]

Overall, the work within this chapter demonstrates the robust nature of PHIP hyperpolarised reaction monitoring at low-field and the potential it has for use in the observation of hydrogenative reactions. Chapter 5 intends to build on this foundation through the incorporation of an *ex situ* irradiation setup as to broaden the scope of this method to include photochemical reactions.

5 *Ex situ* Photochemistry on a Benchtop NMR Spectrometer

In this chapter, the use of PHIP hyperpolarisation to analyse photochemical reactions on a benchtop NMR spectrometer is considered. With the methods developed in Chapters 3 and 4 providing quantitative results for thermal reaction monitoring, the next development required for observing photochemistry on a benchtop NMR spectrometer was the incorporation of an irradiation step. The design and optimisation of an *ex situ* irradiation setup is the focus of the initial section of this chapter. The assessment of this *ex situ* irradiation approach focuses on the reproducibility of the observed NMR signals and the influence of experimental parameters such as irradiation length and sample transfer time. These studies are performed using the photochemistry of $[Ir(H)_2(CO)(PPh_3)_2Cl]$, allowing for comparisons to be drawn to the thermal reactivity of the complex.

5.1 Instrumentation

5.1.1 Routes to *ex situ* Irradiation

The key requirements for the *ex situ* irradiation setup are that it integrates well with the benchtop NMR spectrometer and is appropriate for observing the required photochemical processes. For NMR incorporation, the choice of a setup that is relatively affordable and portable is desirable as to match the unique advantages of the benchtop NMR spectrometer. As the light source is not being directed into the spectrometer, it is also important that a suitable housing is designed as to ensure that an NMR sample can be quickly and safely transferred between irradiation and NMR detection as to enable hyperpolarised signals to be observed on a suitable timescale. In terms of matching the required photochemistry, as the main focus of

this research is on the loss of H_2 from metal dihydrides, a light source that provides a strong UV output is required.[43]

In terms of *ex situ* irradiation setups that have been incorporated with high-field NMR spectrometers, there are two main approaches that are seen within the literature. The first places the irradiation setup close to the NMR spectrometer and manually transfer the sample for detection.[204] The second method utilises a pneumatic flow system to automatically shuttle the sample between an irradiation housing and the NMR spectrometer.[205,206] Both methods have advantages and disadvantages, with the first approach being simple and cheaper but the second method offering full automation and precise control over the transfer of the sample. For the initial proof-of-concept studies being performed within this chapter, the less complex manual transfer method was chosen.

5.1.2 Irradiation Source

The most important component of the *ex situ* irradiation setup is the irradiation source. As stated previously, the source must have a strong UV output to facilitate the loss of H_2 from the initial complex. Previous studies into H_2 loss from inorganic complexes within the group have made use of Hg,[207,208] Xe[46] or Hg-Xe arc lamps.[209] Of these options, the Hg-Xe arc lamp is the optimal choice as it provides the high intensity output seen from mercury in the UV-visible region but with the improved lifetime and stability of xenon arc lamps.[210] An Oriel high-pressure 200 W Hg-Xe lamp was selected for use in the *ex situ* photochemical irradiation setup. This was chosen based on both the availability of the source and the high intensity UV-visible output of the lamp (a spectral irradiance plot for the Hg-Xe lamp was provided by Newport and is given within Appendix B).

One disadvantage of using a broadband UV lamp source is the heat output during irradiation. The non-negligible emission of longer wavelength IR irradiation during irradiation coupled with the multi-second irradiation windows required to generate the required photochemical product means there is potential for considerable sample heating during irradiation (which is undesirable due to the potential thermal reactivity that could occur). To minimise heating effects within the sample, the output of the lamp was coupled with a 5 cm water filter to act as a heat sink within the setup.

5.1.3 Irradiation Chamber Design

To safely irradiate the NMR sample using the lamp source a custom housing was designed with help from Dr Fraser Hill-Casey. The requirements for this housing were that it would fully encase the output of the lamp (to protect the user), couple to the water filter and provide a route to insert and remove an NMR sample while the lamp was on.

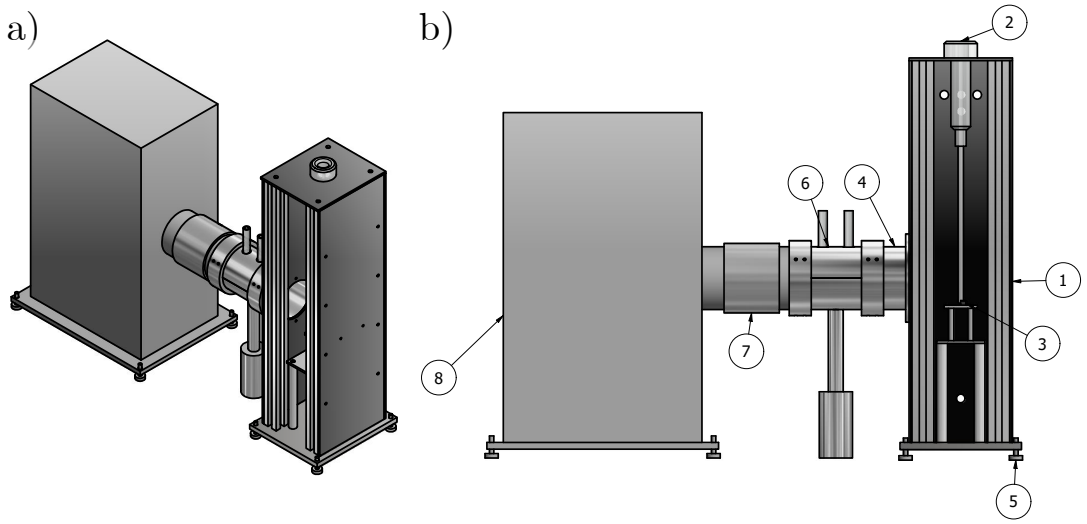

Figure 5.1: (a) 3D and (b) 2D CAD drawings for the *ex situ* photochemistry setup designed for manual insertion and removal of a J Young tap NMR tube for irradiation. Drawings were prepared by and used with permission from Dr. Fraser Hill-Casey.

The final design for the irradiation chamber is given in Figure 5.1. The outer casing of the chamber (1) is made out of aluminium sheet (2.5 mm thickness) with the internal faces painted black to minimise reflections within the casing. The result is a fully enclosed container that provides complete shielding of the lamp source to protect the user from the input irradiation. The top of the casing (2) has a central circular hole (diameter matched to the NMR sample holder) to allow for easy insertion and removal of the NMR sample. To aid with sample positioning, a central mount (3) is present within the chamber that is set to a height so that it sits just below the NMR sample when inserted. At the top of this mount is a foam pad that has a central recess which is matched to the round-bottom of the NMR tube. Overall, this allows samples to be securely held within the irradiation chamber without placing unnecessary strain on the glass NMR tube. To ensure adequate irradiation the sample, the coupling window for the water filter (4) is situated so that the NMR detection region is aligned with the centre of the UV lamp. To couple the lamp to the the

water filter, a joining ring containing three pairs of Grub screws (set 120° apart) was designed to allow for a tight connection between the metal casing of the water filter and the irradiation chamber. Finally to allow for alignment of the housing with the lamp source, a set of adjustable feet (5) were attached to the base plate of the housing allowing for easy vertical adjustments.

Upon confirmation of the above design, the irradiation chamber was machined and constructed by the mechanical workshop at the University of York. Following alignment of the Hg-Xe lamp, water filter and sample housing the *ex situ* photochemistry setup was ready for use with the benchtop NMR spectrometer. The completed setup is given in Figure 5.2.

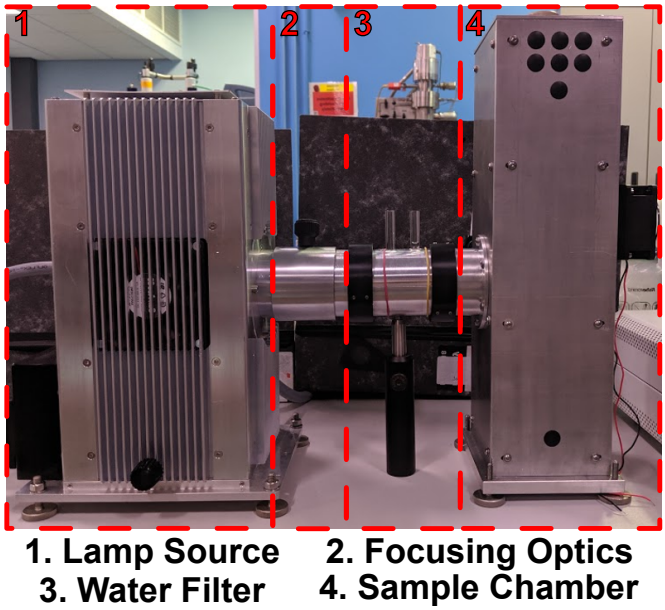

Figure 5.2: Photograph of the complete *ex situ* photochemical setup with individual sections labelled and highlighted within red boxes.

5.1.4 Experimental Design

To perform *ex situ* photochemistry experiments on the benchtop NMR spectrometer, the following method was used. Prior to any experiments, the Hg-Xe lamp is turned on and left to warm up for 5 minutes. During this time, the sample of interest is placed under pH$_2$, shaken for 5 seconds and then a ^{1}H spectrum is recorded to check that no PHIP reactivity is observed in the absence of irradiation. The experiment is then performed according to the pulse sequence given in Figure 5.3. The sample is placed into the irradiation chamber and left for a set irradiation

period (t). Subsequently, the sample is transferred into the NMR spectrometer and a ^{1}H spectrum is recorded.

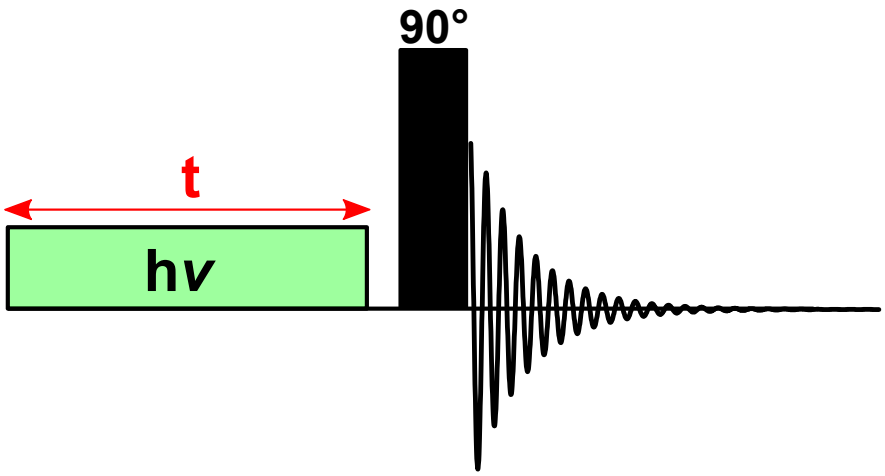

Figure 5.3: Pulse sequence used when performing *ex situ* photochemistry experiments.

The main difference between this pulse sequence and the one used for thermal reaction monitoring is the inclusion of a 90° rather than a 45° pulse angle. This change is required due to the formation of hyperpolarised species now occurring externally to the magnetic field of the spectrometer. The consequence of this is that the system is now under ALTADENA conditions and as such the maximum hyperpolarised signal is observed upon application of a 90° pulse.

5.2 Initial Exploration of Method

5.2.1 Photochemical Properties of Vaska's Complex

To continue on from the experiments performed under thermal conditions, Vaska's complex was chosen as the initial complex to explore with the *ex situ* photochemical setup. To confirm that the photochemical reactivity of Vaska's complex is matched well to the output of the Hg-Xe lamp, UV-visible spectra of both the unreacted complex and the dihydride product were recorded. The UV-visible spectra were recorded between 200 and 1200 nm, with the region of interest (300 - 600 nm) shown as Figure 5.4. In order to observe the necessary peaks within the

UV-vis spectrum of $[Ir(H)_2(CO)(PPh_3)_2Cl]$, a concentration of 21.35 mM was required (a 50-fold increase compared to Vaska's complex).

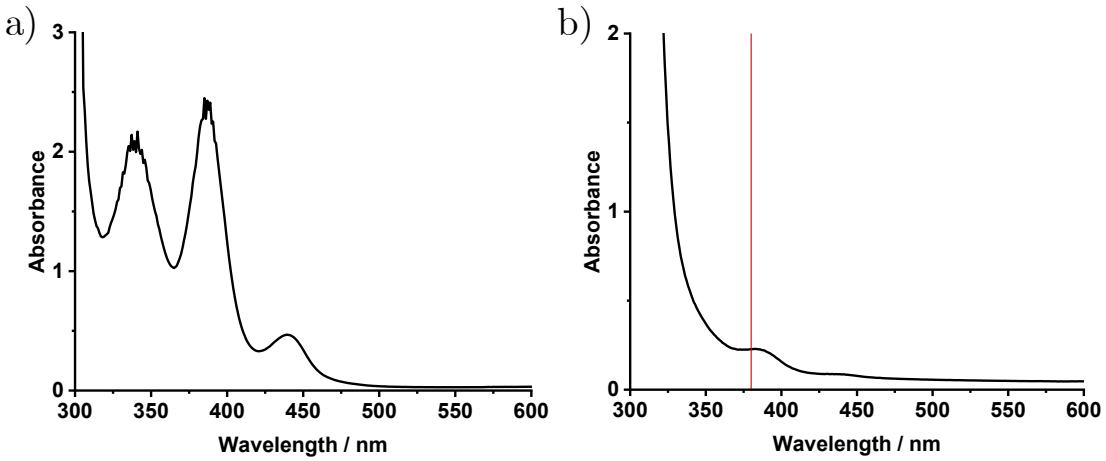

Figure 5.4: UV-Vis spectra of (a) *trans*-$[IrCl(CO)(PPh_3)_2]$ (0.43 mM) and (b) $[Ir(H)_2(CO)(PPh_3)_2Cl]$ (21.35 mM) recorded between 300 - 600 nm. The red line indicates the literature λ_{max} for $[Ir(H)_2(CO)(PPh_3)_2Cl]$ at 380 nm. Spectra were recorded using a quartz cuvette with a 1 cm pathlength.[169]

The photochemical pathway of interest is the loss of H_2 from $[Ir(H)_2(CO)(PPh_3)_2Cl]$ which is known from literature to occur at 380 nm.[169] This transition aligns with the single band observed within the UV-vis spectrum of $[Ir(H)_2(CO)(PPh_3)_2Cl]$ (Figure 5.4b). This photochemical pathway leads to the reformation of the Vaska's complex starting material which is then available to react with a new molecule of pH_2 to produce a new pair of enhanced hydride signals (a reaction scheme is given in Figure 5.5). The second step of this degenerate reaction process is observable via NMR and corresponds to the thermal reaction that was the focus of Chapter 3. Therefore, the previous optimisations are applicable to this system and direct comparisons can be made to the reactivity observed under thermal conditions.

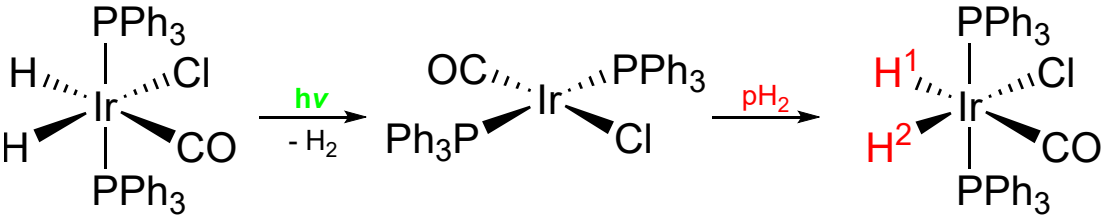

Figure 5.5: Reaction scheme for degenerate photochemical reaction of $[Ir(H)_2(CO)(PPh_3)_2Cl]$ involving the reductive elimination of H_2 and oxidative addition of pH_2.

Prior to performing NMR experiments with the *ex situ* photochemistry setup, it

was important to ensure that the irradiation of the sample was not subject to any primary inner filter effects (IFEs). Primary IFEs are a common problem in fluorescence spectroscopy where the intensity of the excitation wavelength has been attenuated prior to reaching the observation region of the sample.[211] IFEs occur when the optical density of the sample is such that the absorbance of incident light attenuates across the volume of the sample. These effects are problematic for the *ex situ* photochemistry experiments as an attenuation gradient will reduce the overall effectiveness of the irradiation source (which could result in lower SNR within the observed spectra) and could add an unwanted spatial dependence across the NMR active region. One simple method to minimise the presence of IFEs within a sample is to ensure that $A < 0.1$ is satisfied (where A is the absorbance of the sample).[212]

Using the Beer-Lambert Law (Equation 5.1), where A is absorbance, ϵ is the molar absorption coefficient, c is concentration and l is optical pathlength, it is possible to determine ϵ at λ_{max} for $[Ir(H)_2(CO)(PPh_3)_2Cl]$. For this UV spectrum, c is 21.35 mM, A at λ_{max} (383 nm) is 0.229 and the quartz cuvette has a pathlength of 1 cm. This gives an ϵ_{max} of 10.7 $dm^3\ mol^{-1}\ cm^{-1}$.

$$A = \epsilon c l \tag{5.1}$$

Using the value of ϵ_{max} it is possible to determine the absorbance of the NMR sample during irradiation within the *ex situ* setup. The maximum concentration used for the photochemistry experiments is 4.27 mM (2 mg) and as the incident irradiation is perpendicular to the NMR tube, the pathlength is only the inner diameter of the NMR tube which is ≈ 4.2 mm. Overall, this gives a value of A = 0.019 which meets the $A < 0.1$ requirement and so inner filter effects are not likely to affect the following experiments using Vaska's complex.

5.2.2 Initial Photochemistry

To ensure that the *ex situ* photochemistry setup was suitable to observe the degenerate reaction of Vaska's complex (Figure 5.5), initial experiments were performed to ensure that PHIP hyperpolarised signals were observable for the system. These were performed using a 1 mg (2.14 mM) sample of Vaska's complex that had previously been reacted with pH_2 so that the sample only contained

$[Ir(H)_2(CO)(PPh_3)_2Cl]$. For the experiments, the procedure outlined in Section 5.1.4 was followed and an irradiation time of 30 seconds was used. An example of the spectra obtained using this method is given in Figure 5.6b.

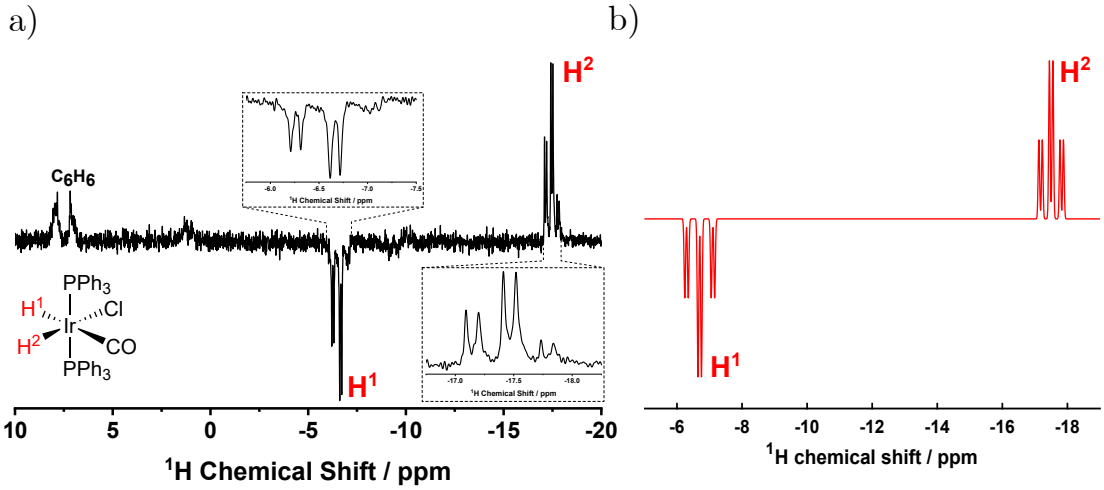

Figure 5.6: (a) Experimental and (b) simulated ^1H spectra for $[Ir(H)_2(CO)(PPh_3)_2Cl]$ recorded under ALTADENA conditions. The experimental spectrum was recorded following 30 seconds of irradiation and is shown with enhanced hydride resonance insets.

From Figure 5.6a, it is evident that the *ex situ* photochemistry setup is suitable for observing the formation of $[Ir(H)_2(CO)(PPh_3)_2Cl]$ following reformation of the Vaska's complex starting material. Both hydride peaks for the complex are observed and occur at the expected chemical shifts (-6.69 and -17.48 ppm for the hydrides trans to CO and Cl respectively). Owing to the ALTADENA conditions of the PHIP hyperpolarisation, H^1 and H^2 appear with opposite phases with one multiplet being positively phased while the other is negatively phased. This is supported by a Spinach simulation of the system performed using an ALTADENA starting state with a 90° pulse (given in Figure 5.6b).

A key difference between the experimental and simulated spectra for $[Ir(H)_2(CO)(PPh_3)_2Cl]$ is the ratio of peak integrals within the hydride peak multiplets. While the simulated spectrum follows the expected distribution for a triplet multiplicity of 1:2:1, the experimental results deviate from this with the right-hand peak of each triplet having near negligible intensity. This deviation from the expected multiplet peak intensities is a common feature of spectra obtained under ALTADENA conditions, with this effect being noted within the seminal work on the technique, where the methylene and methyl resonances for ethylbenzene displayed triplet and doublet multiplicities respectively rather than the expected

quartet and triplet.[144] The origin of this feature is explained by the presence of both in-phase and anti-phase magnetisation terms under ALTADENA conditions which can lead to partial cancellation of lines within the spectra.[135,213] Commonly, the anti-phase term is cancelled out when using a 90° pulse resulting in the spectrum shown in Figure 5.6b. However, the B_1 coil calibration of the Spinsolve spectrometer being used is imperfect and thus a slight deviation in flip angle could enable some anti-phase character to be present within the spectrum leading to the signal cancellation observed in Figure 5.6a. As this feature is consistent between *ex situ* photochemistry experiments, it will not negatively impact the analysis of the hyperpolarised spectra obtained.

5.2.3 Repeatability Studies

The addition of an initial irradiation step into the experimental design requires the optimisation of an additional parameter: the irradiation time. For the *ex situ* photochemistry setup, poor signal enhancements were observed for short irradiation times (up to 10 seconds). The need for longer irradiation periods is common when using broadband UV sources as to ensure sufficient product formation from the desired photochemical pathway.[208]

To determine the optimal irradiation time for use with Vaska's complex, a 1 mg sample (2.14 mM) was irradiated for between 10 - 60 seconds and then a ^{1}H NMR spectrum was recorded. This was repeated 5 times for each irradiation time. The average hydride integral for each irradiation time, along with the standard error between the 5 repeat measurements, are given in Figure 5.7.

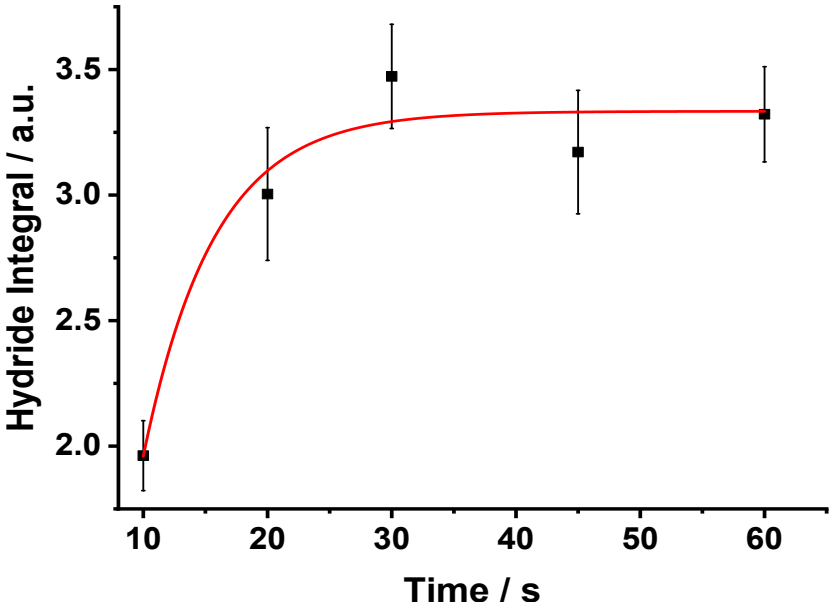

Figure 5.7: Average hydride integrals measured for pH$_2$ addition following irradiation of [Ir(H)$_2$(CO)(PPh$_3$)$_2$Cl] (0.43 mM) under ALTADENA conditions. Data was collected for 10, 20, 30, 45 and 60 seconds of irradiation within the *ex situ* photochemical setup.

Within Figure 5.7, the observed NMR signal shows increasing enhancement with longer irradiation times up to 30 seconds. This relationship indicates the formation of a bulk of Vaska's complex over the course of the irradiation period. As H_2 is continually cycling onto and off Vaska's complex during this time, a bulk of this intermediate species would form if the rate of the photochemical reductive elimination step is relatively fast compared to the thermal oxidative addition step (which is the case with loss of H_2 from metal dihydride complexes which has been been determined to occur on the femtosecond-to-picosecond timescale).[43] Upon removal from the irradiation chamber, the concentration of Vaska's complex is fixed. Assuming consistent transfer time to the spectrometer (so the same proportion of [Ir(H)$_2$(CO)(PPh$_3$)$_2$Cl] has been lost for all irradiation times during transfer), the observed signal will be primarily dependent on this initial concentration.

Above 30 seconds, this trend is no longer observed and the NMR signal appears to plateau. This is indicative of a steady state condition being met within the sample where the formation and consumption of Vaska's complex are in equilibrium with one another. Therefore, any increase in irradiation time above this limit will not produce improved NMR signal and can have potential detrimental effects as the additional consumption of pH$_2$ within the sample can reduce the proportion of product formed in a hyperpolarised state once the sample is removed from the irradiation chamber. This factor could provide an explanation for why the integrals observed at 45 and 60

seconds are lower compared to that seen at 30 seconds. Overall it appears that, under these conditions, using a 30 second irradiation period provides the best enhancements for the complex.

One wider issue that this set of experiments highlights is the reproducibility of the hyperpolarisation using the *ex situ* setup. Within this dataset, a maximum percent error of 8.8% is observed within the integrals at 20 seconds of irradiation. The source of this uncertainty is likely due to the manual transfer steps of the experimental protocol, both in terms of the irradiation time of the sample and the transfer time to the spectrometer. For the former, additional irradiation time will lead to a larger bulk concentration of Vaska's complex within the solution. For the latter, a longer transfer time allows for additional product formation under ALTADENA conditions prior to observation. Therefore, the presence of human reaction times in both of these stages has a direct impact on the NMR signal enhancements observed and thus will limit the achievable consistency between measurements for this experimental protocol. One potential route to solving this particular issue is to implement the use of the flow system. Pneumatically controlled flow systems (such as that detailed by Mewis *et al.*[214]) have been employed previously on benchtop NMR spectrometers to perform SABRE hyperpolarised studies.[98] The setup enabled automated $p\mathrm{H}_2$ bubbling outside of the spectrometer followed by automated transfer into the spectrometer for detection. Through modification of this setup it would be possible to perform automated transfer between the photochemical housing and the NMR spectrometer to improve the consistency of the observed hyperpolarised signals.

5.3 Exploring the Photochemistry

5.3.1 Sample Degradation

Within the repeatability study discussed in the previous section, a further problem was observed upon repeated irradiation of the Vaska's complex sample. Within the later experiments performed, the hydride region of the $^1\mathrm{H}$ spectrum began to show additional peaks, most notably between -9 and - 11 ppm (Figure 5.8). These peaks indicated that photodegradation of the sample was beginning to occur and as such new reactive species were present within the reaction mixture. This is problematic for the applicability of this setup for quantitative applications and as a

potential route to regenerating the Vaska's complex starting material (which would enable multiple PHIP experiments per sample) as additional reaction pathways will affect the consistency of the results that are obtained. In order to establish the structure and prevalence of these photodegradation products, a series of experiments were performed using the *ex situ* photochemistry setup with a 9.4 T high-field NMR spectrometer.

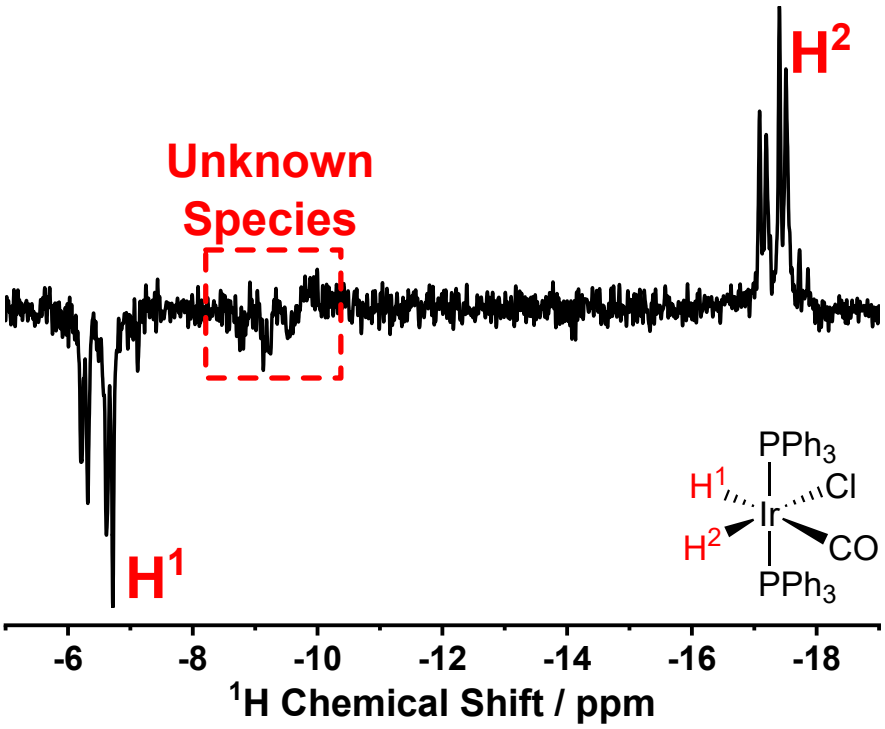

Figure 5.8: ^{1}H spectrum of Vaska's complex (2.14 mM) under pH$_2$, following irradiation for 60 seconds within the *ex situ* photochemical setup. The highlighted region between -9 and -11 ppm indicates the presence of additional species within the sample.

To investigate the photodegradation of Vaska's complex, a 0.2 mg sample (0.43 mM) was irradiated for a total of 12 minutes with spectra being recorded after 1, 2, 7 and 12 minutes. To enable hyperpolarised signals for the degradation products to be observed, the sample was irradiated under vacuum and then placed under pH$_2$ prior to placement into the spectrometer. For each irradiation period, 1- and 16-scan hyperpolarised ^{1}H and ^{1}H{^{31}P} spectra were collected along with a ^{1}H{^{31}P}-^{31}P HMQC thermal spectrum (performed with 128 steps each with 4 scans).

Figure 5.9a shows the 16-scan ^{1}H{^{31}P} spectrum collected after 2 minutes of irradiation of the sample. Within this spectrum, there are several additional hydride signals present. These signals have a relatively low intensity (they are obscured by noise within the fully-coupled ^{1}H spectrum) but indicate that even at short

irradiation times that additional speciation of the sample is occurring. As the sample continues to be irradiated up to 12 minutes (Figure 5.9b), the number of additional hydride peaks is seen to increase, especially within the -9 to -11 ppm region, which indicates further degradation of the initial sample and also aligns with the additional signals that were observed at low-field.

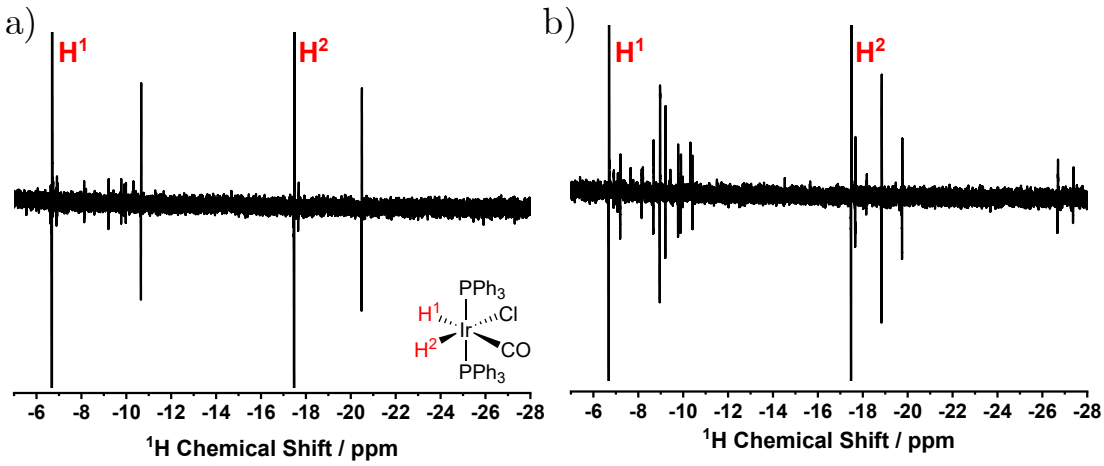

Figure 5.9: $^{1}H\{^{31}P\}$ hydride spectra (16 scan) recorded at 400 MHz for Vaska's complex (0.43 mM) upon pH_2 addition following (a) 2 minutes and (b) 12 minutes of irradiation in the *ex situ* photochemical setup.

The $^{1}H\{^{31}P\}$-^{31}P HMQC spectra collected during these experiments can be used to identify the structure of the unwanted degradation products being formed in solution. From the HMQC spectrum collected after 2 minutes of irradiation, Figure 5.10, two additional complexes can be positively identified. Complex **2**, is determined to be *cis,cis*−$IrH_2(CO)(PPh_3)_2Cl$ - the minor isomeric form of Vaska's complex following addition over the P−Ir−P axis. The peaks observed for this species at -8.1 ppm for ^{1}H and -5.9 ppm for ^{31}P are in agreement with those observed in literature by Hasnip *et al.*[40,165] who observed this species as a minor product (100-fold weaker signals) upon H_2 addition to Vaska's complex at 295 K. Due to the irradiation of the sample leading to H_2 re-addition to Vaska's complex, this allows for reformation of the complex with this alternative structure and thus the presence of this minor species was to be expected within these spectra. The second new species present in the sample, Complex **3**, was determined to be the trisphosphine complex $[IrH_2(PPh_3)_3Cl]$ with hydride resonances observed at -10.6 and -20.4 ppm (which matched the chemical shift values seen in literature).[215] Previous studies have observed the formation of this complex thermally when Vaska's complex is in the presence of excess PPh_3. Photochemical loss of CO from Vaska's complex is well established[216] and the lability of the phosphine ligands within Vaska's complex has been highlighted previously with the addition of excess phosphine into a sample of Vaska's complex producing

substituted derivative complexes. Therefore, the formation of this complex during irradiation is possible and occurs via the route given in Figure 5.11. The formation of this complex is significant as it highlights that even after a relatively short period of irradiation ligand exchange pathways are present that can produce unwanted by-products within the sample.

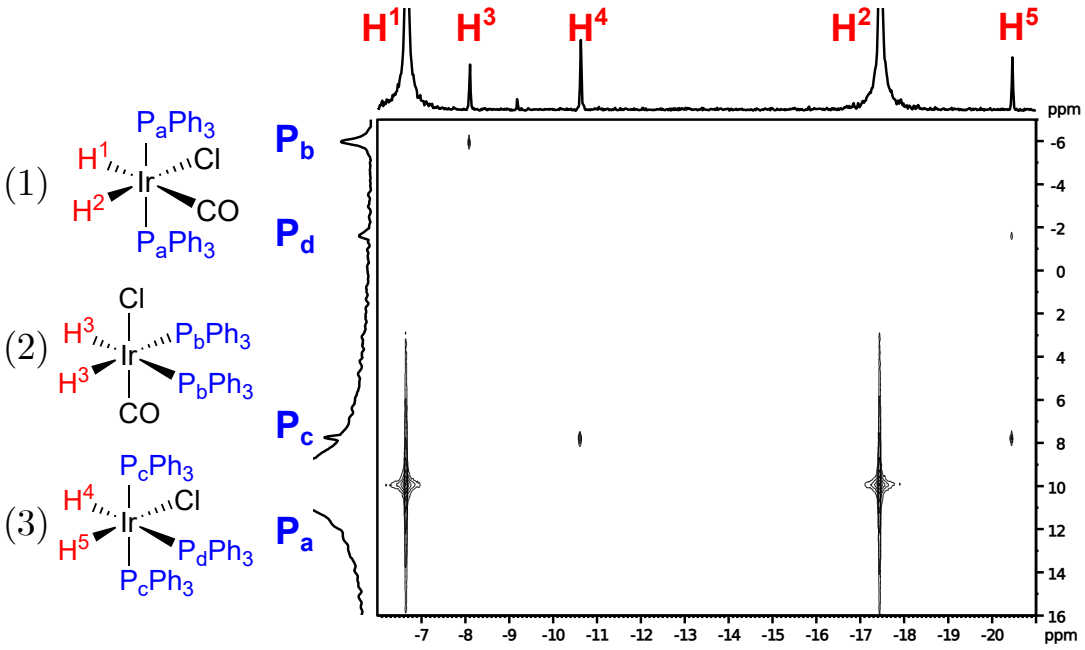

Figure 5.10: $^{1}H\{^{31}P\}$-^{31}P HMQC spectrum (4 scan, 128 step, J_{HP} = 32 Hz) recorded for $[Ir(H)_2(CO)(PPh_3)_2Cl]$ (0.43 mM) mixed with pH_2 following 2 minutes of irradiation in the *ex situ* photochemical housing.

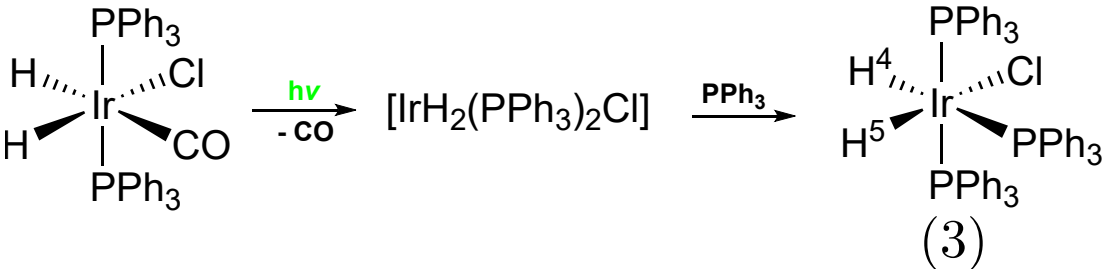

Figure 5.11: Reaction scheme for the formation of $[IrH_2(PPh_3)_3Cl]$ following irradiation of Vaska's complex.

Upon irradiation for 12 minutes, the HMQC spectrum indicates the presence of additional hydride-containing complexes within solution. Of those formed, the easiest to identify are the related complexes **4a** and **4b** with the structure $[IrH_3(CO)(PPh_3)_2]$. Both complexes are trihydride species that have hydride peaks at -9.2 / -9.9 ppm (for complex **4a**) and -9.4 / -10.4 ppm (for complex **4b**) and these assignments are corroborated by those seen in literature.[217] These complexes are

formed via the photochemical elimination of HCl from the complex (scheme given in Figure 5.13) which allows for a new molecule of pH_2 to bind into the complex to produce the two conformers shown. The presence of HCl is unfavourable as it both introduces a new species within the sample and also will begin to acidify the solution, changing the experimental conditions.

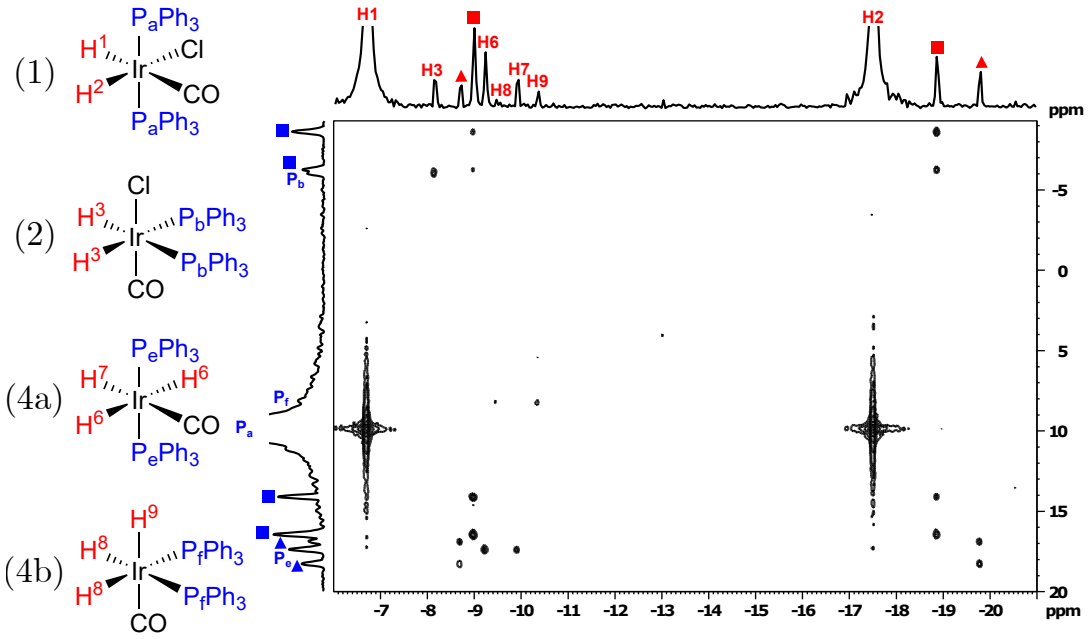

Figure 5.12: $^{1}H\{^{31}P\}$-^{31}P HMQC spectrum (4 scan, 128 step, J_{HP} = 32 Hz) recorded for $[Ir(H)_2(CO)(PPh_3)_2Cl]$ (0.43 mM) mixed with pH_2 following 12 minutes of irradiation in the *ex situ* photochemical housing.

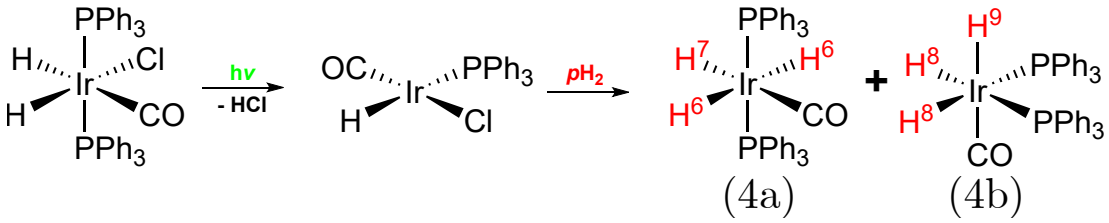

Figure 5.13: Reaction scheme for the formation of $[IrH_3(CO)(PPh_3)_2]$ following irradiation of Vaska's complex.

The full assignment of the two other major species within the sample (indicated by the square and triangle assignments within the HMQC spectrum) is outside the scope of the experiments performed but these preliminary results indicate that they are from complexes that contain functionalised phosphine groups (where the nature of the phosphine ligand has been altered and is no longer PPh_3). This hypothesis is rationalised by the presence of multiple ^{1}H-^{31}P cross-peaks for each hydride resonance in the complexes, and by the large ^{31}P-^{31}P splittings observed (380 Hz

and 230 Hz for the square and triangle assignments respectively) which requires the presence of asymmetric phosphine ligands to be present. Within the literature around Vaska's complex speciation, ^{31}P-^{31}P couplings of similar magnitudes have been observed for species that contain two different phosphine ligands (such as PPh_3 and PPh_2Cl which is shown in Figure 5.14a).[40] Alternatively, Vaska's complex can be used as a photochemical C-H activation catalyst which enables carbonylation of benzene within the PPh_3 ligands.[167] The photochemical carbonylation process results in the functionalisation of one of the PPh_3 ligands, resulting in the phosphine ligands no longer being chemically equivalent and thus large ^{31}P-^{31}P couplings can be observed for these complexes (as shown in Figure 5.14b). While both options could account for the signals seen, further narrowing down of the correct complexes is not achievable from this spectrum as the exact ^{31}P chemical shift for these complexes cannot be established, due to the small spectral width of the ^{31}P axis leading to folding over of the spectrum. Even without exact assignments, evidence for the presence of complexes with asymmetric phosphine ligands is highly problematic as this indicates that not only is ligand exchange present but, upon extended irradiation, these ligands can be chemically altered leading to far more complex speciation within the sample which will deviate it further from the initial composition.

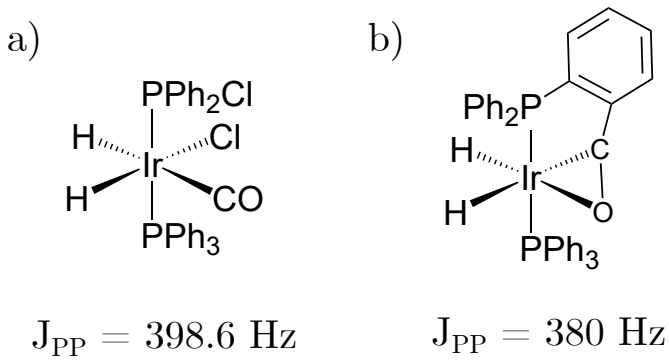

Figure 5.14: Vaska's complex derivatives with asymmetric phosphine ligands that have been characterised previously within literature. Full characterisation for each species is given by Hasnip *et al.*[40]

Within Figure 5.9b, there are also hyperpolarised signals that lie at -26.7 and -27.4 ppm. These strongly shielded hydride resonances are common indicators of the presence of dimeric species within the solution. The formation of dimers following irradiation of the Vaska's complex derivatives $IrCl(CO)(PMe_3)_2$[40] and $IrI(CO)(PPh_3)_2$[45] have been previously reported within the literature. In both cases, the resonances for the terminal hydride atoms appear below 20 ppm (see Figure 5.15). Given the similarity of both complexes to Vaska's complex and the strong shielding observed

for the two peaks, it is highly likely that these hyperpolarised signals originate from dimeric species.

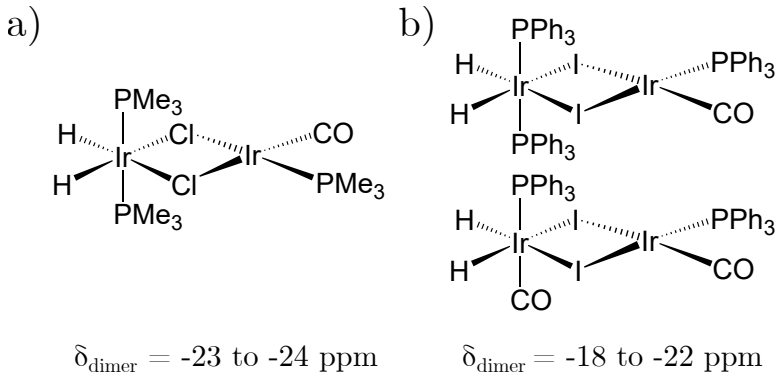

Figure 5.15: Dimeric species formed by Vaska's complex derivatives that have been characterised previously within literature. Full characterisation for each species is given by (a) Hasnip *et al.*[40] and (b) Procacci *et al.*[45]

Overall, the prolonged irradiation of Vaska's complex with broadband UV-visible light results in complex speciation occurring within the sample. A comparison between a thermal spectrum recorded prior to irradiation and following irradiation (Figures 5.16a and b respectively) indicates that while some of the irradiation products are short-lived (namely those observed for the trisphosphine, mixed phosphine and dimer species), irreversible changes have been made to the composition of the sample. In addition to those complexes assigned previously, species that have formed but do not show strong PHIP enhancements can also be observed such as the monohydride species seen at -7.7 and -14.5 ppm respectively.[40] The presence of these additional species affects the enhancements observed for $[Ir(H)_2(CO)(PPh_3)_2Cl]$ (evidenced by a 12% reduction in integrals between the two spectra) and makes repeat studies using this setup unfavourable as conditions within the sample are not identical between runs.

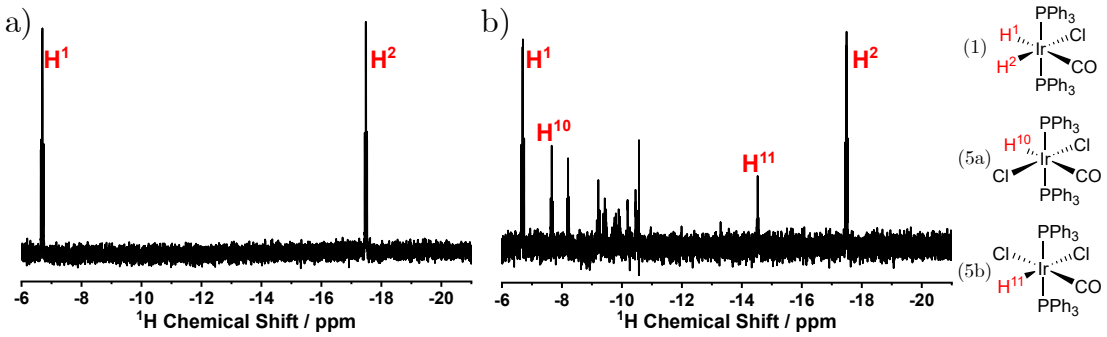

Figure 5.16: Thermal ^{1}H spectrum recorded at 400 MHz (a) before and (b) after 12 minutes of irradiation of $[Ir(H)_2(CO)(PPh_3)_2Cl]$ (0.43 mM). Highlighted in (b) are the additional monophosphine species that are observed following sample irradiation.

5.3.2 Selective Irradiation

One route to address the speciation of the sample upon irradiation is to place filters between the UV-visible lamp source and the photochemical housing as to only permit certain wavelengths of light to reach the sample. By selecting for the wavelengths of light that promote H_2 loss from the complex and minimise other reaction pathways, the degradation of the sample could be slowed down as to allow for multiple measurements to be collected using a single sample of Vaska's complex. To explore this possibility, a series of high-pass band filters (that prevent irradiation below a certain wavelength threshold from reaching the sample) were tested with the *ex situ* photochemical housing.

The high-pass band filters available for this study came in several increments in the range of 280 to 515 nm. Of these filters, those in the range of 280 - 385 nm were of most interest as the wavelengths these filters allow to pass through still contain the absorption band that is responsible for H_2 loss from the complex (as highlighted by Figure 5.17a). To test each filter, each one was placed into the *ex situ* photochemical setup between the water filter and the sample irradiation chamber as shown in Figure 5.17b. For each filter, a sample of $[Ir(H)_2(CO)(PPh_3)_2Cl]$ (0.43 mM) was degassed, irradiated for a set period of time and then filled with fresh pH_2 for observation using a 400 MHz NMR spectrometer. Each sample was irradiated for three 1 minute periods and one 5 minute period to show the change in speciation present within the sample after 1, 2, 3 and 8 minutes of total irradiation.

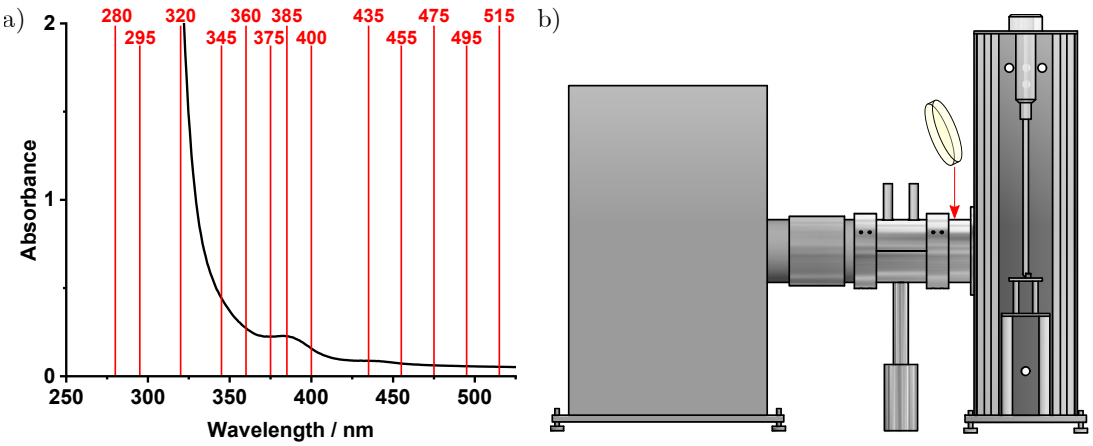

Figure 5.17: (a) UV-visible spectrum for $[Ir(H)_2(CO)(PPh_3)_2Cl]$ with the wavelengths of each high-pass band filter overlaid alongside (b) a diagram indicating the position of the filter within the *ex situ* photochemical setup.

Figure 5.18a is a series of single-scan ^{1}H spectra recorded after 1 minute of irradiation for each filter examined. The key finding of this set of data is the abrupt disappearance of any hyperpolarised signals for Vaska's complex when wavelengths lower than 345 nm are cut off. From both literature data from Geoffroy *et al.*[169] and previously recorded UV-vis spectra, the λ_{max} for the $[Ir(H)_2(CO)(PPh_3)_2Cl]$ complex is known to be 380 nm and so it would be expected that PHIP signals should still be observed. This disparity could potentially be explained through the lower efficiency of the photochemical process for wavelengths higher than 320 nm resulting in a smaller steady state concentration of *trans*-$[IrCl(CO)(PPh_3)_2]$ in the sample relative to the previous filters. Once irradiation stops, the *trans*-$[IrCl(CO)(PPh_3)_2]$ could react with the oH_2 present in the solution and so by the time that the sample is refreshed with pH_2, shaken and placed within the spectrometer the amount of available *trans*-$[IrCl(CO)(PPh_3)_2]$ is insufficient for PHIP signal detection. This reduced efficiency for filters above 345 nm makes them unsuitable for use as they prevent observation of the desired reaction pathway.

A further problem with this setup, as seen from from Figure 5.18b, is that the filters that permit the detection of hyperpolarised signals from $[Ir(H)_2(CO)(PPh_3)_2Cl]$ (in the range of 280 - 320 nm) do not select against the sample degradation pathways examined in Section 5.3.1. From the previous study, it is clear that continued irradiation will only cause further speciation within the sample. Overall, both of these findings indicate that regeneration of Vaska's complex through irradiation is not a suitable use of this *ex situ* photochemical setup.

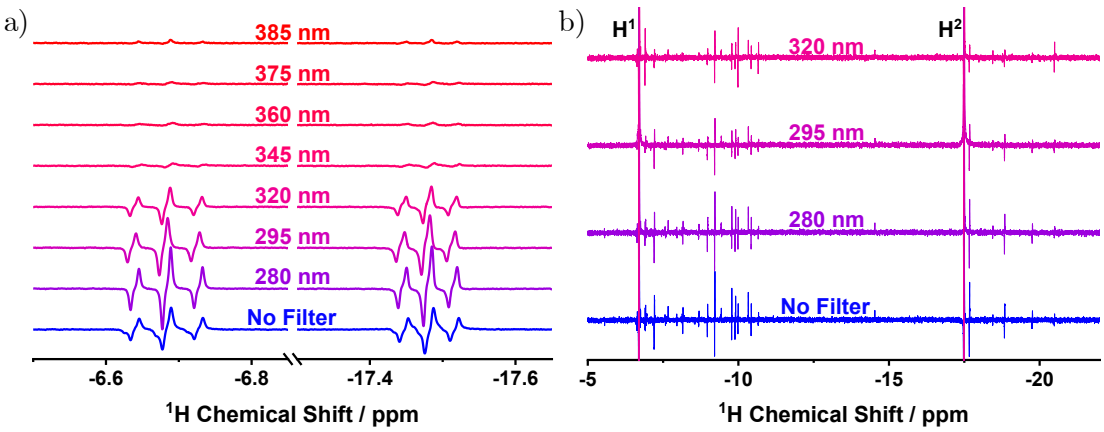

Figure 5.18: Single scan hyperpolarised ^{1}H spectra (at 9.4 T) for $[Ir(H)_2(CO)(PPh_3)_2Cl]$(0.43 mM) recorded after 1 minute of irradiation for a range of high-pass filters (A) and a set of 64 scan $^1H\{^{31}P\}$ spectra recorded after 8 minutes of irradiation with < 345 nm high-pass filters.

5.3.3 Reaction Monitoring

A final set of experiments performed using the *ex situ* photochemical setup was a reaction monitoring study for the reformation of $[Ir(H)_2(CO)(PPh_3)_2Cl]$ following the photochemical loss of H_2 (the second step shown within the reaction scheme in Figure 5.5). This step of the reaction is identical to that monitored thermally allowing for a comparison between the two methods. As established previously within this chapter, repeated irradiation of a single sample of Vaska's complex results in the presence of several unwanted photodegradation products. Therefore, each sample used for reaction monitoring purposes was only irradiated once to minimise the potential formation of any additional species.

To perform the reaction monitoring experiments, the same procedure was followed as for the thermal reaction monitoring experiments. Each sample of Vaska's complex (0.43 mM) was placed under a headspace of pH$_2$ (4 bar absolute) and left to equilibrate to the internal temperature within the NMR spectrometer for 10 minutes. The sample was then placed into the *ex situ* photochemical housing and irradiated for 30 seconds. Following this, the sample was placed into the thermally insulated holder and shaken for 5 seconds before placement into the spectrometer. The reaction was then monitored over the course of 11 minutes with a ^{1}H spectrum recorded every 5 seconds (128 steps in total). Analysis of the data was performed using the data processing macros detailed previously. The calculated rate constants for the 5 repeats performed are collated in Table 5.1 and an example product formation curve is given as Figure 5.19.

Table 5.1: Pseudo-first order (k_{obs}) and second-order (k_2) rate constants for the five repeat measurements for the oxidative addition of pH$_2$ to Vaska's complex following a 30 s irradiation period on $[Ir(H)_2(CO)(PPh_3)_2Cl]$ (0.43 mM) within the *ex situ* photochemical setup.

Experiment	1	2	3	4	5	Average
k_{obs} / 10^2 s^{-1}	1.136	1.142	1.141	1.124	1.089	(1.130 ± 0.010)
k_2 / dm^3 mol^{-1} s^{-1}	0.963	0.968	0.967	0.967	0.923	(0.958 ± 0.009)

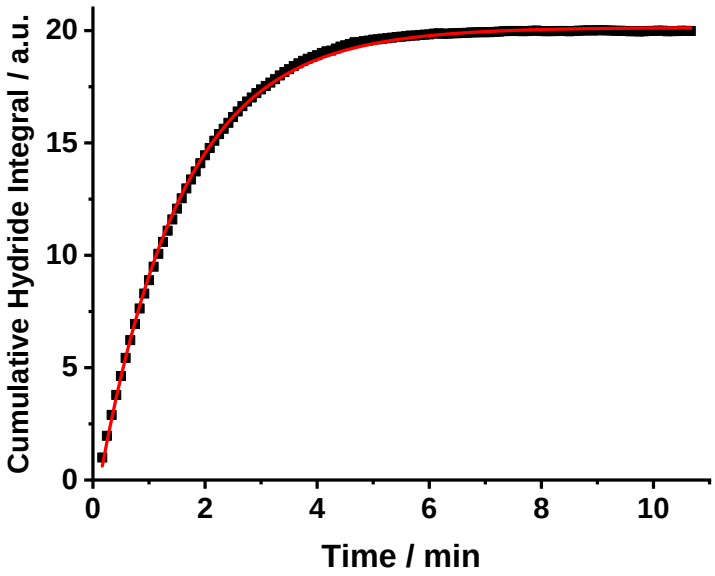

Figure 5.19: Average cumulative integral curve for 5 repeat measurements for the oxidative addition of *p*H_2 to Vaska's complex following 30 seconds of irradiation on $[Ir(H)_2(CO)(PPh_3)_2Cl]$ (0.43 mM) using an *ex situ* irradiation setup

From the reaction monitoring experiments, an average k_2 rate constant of (0.958 ± 0.009) $dm^3\,mol^{-1}\,s^{-1}$ is obtained. Compared to both the expected literature value (0.86 $dm^3\,mol^{-1}\,s^{-1}$) and the value obtained when performing thermal reaction monitoring (0.89 $dm^3\,mol^{-1}\,s^{-1}$), an increase in the rate constant is observed (by 11.4% or 7.6% respectively). Owing to the very high reproducibility of the data, the observed deviation is likely to originate from a source of systematic error due to the additional *ex situ* irradiation step.

One potential contributor to this systematic error is the reduced SNR that is observed for these reaction monitoring experiments. Unlike the thermal reaction monitoring experiments, the starting concentration of Vaska's complex present within the solution is unknown. This is because only a steady state concentration of Vaska's complex is reformed during the 30 second irradiation period. Not knowing the exact initial concentration of the solution prevents the scaling of the product formation curve against concentration which is why Figure 5.19 is plotted using the cumulative hydride integral data. Importantly, having a smaller starting concentration of Vaska's complex will result in a smaller proportion of $[Ir(H)_2(CO)(PPh_3)_2Cl]$ being produced during each 5 second window and so the observed hydride signals will be reduced compared to thermal reaction monitoring. To rationalise the impact of this reduced SNR, a comparison to the *para*hydrogen enrichment study in the previous chapter (Section 4.4) is beneficial.

Within the *para*hydrogen enrichment study, a reduction in SNR was observed as the proportion of pH_2 within the solution reduced. Whilst the underlying change to the system is different to that for the irradiated samples, a similar drop in SNR due to the reduced concentration of hyperpolarised product is observed. To compare the *ex situ* photochemistry reaction monitoring to the pH_2 enrichment study, the cumulative hydride signals (Figure 5.20a) and the SNR of the first usable spectrum (Figure 5.20b) for the *ex situ* photochemistry reaction monitoring and select pH_2 enrichment levels (99%, 70% and 60%) were plotted against one another.

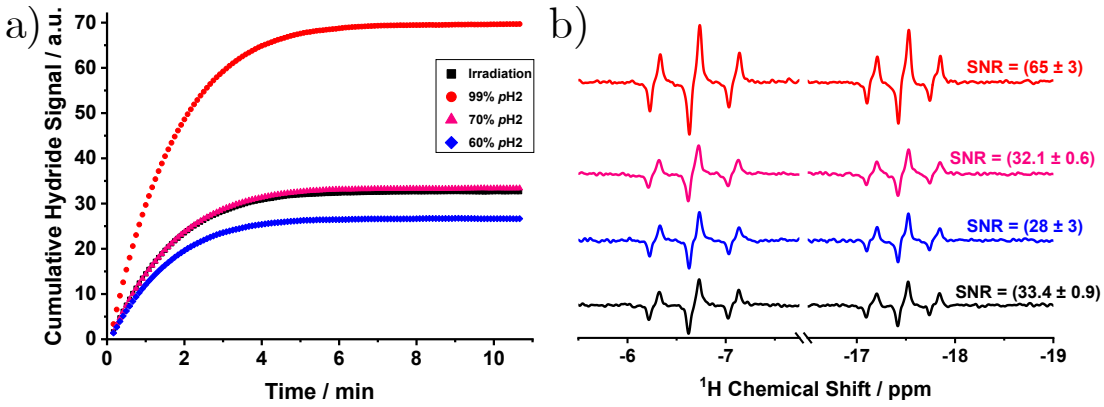

Figure 5.20: (a) Cumulative hydride growth curves and (b) first usable ^{1}H spectra collected for the reaction of Vaska's complex (0.43 mM) with pH_2 following 30 seconds of irradiation compared to those collected when using 99%, 70% and 60% pH_2 enrichment in Section 4.4.

In terms of both initial SNR and the hydride integrals observed over the course of the reaction, the *ex situ* photochemistry experiment shows a close resemblance to those observed with a 70% *para*hydrogen enrichment level. Within the original study, this enrichment level produced an average k_2 rate constant of (0.932 ± 0.008 $dm^3\,mol^{-1}\,s^{-1}$) which was within a 5% difference to the rate observed using a 99% pH_2 enrichment level (0.901 ± 0.014 $dm^3\,mol^{-1}\,s^{-1}$) but showed the greatest deviation from this value outside of the 60% pH_2 enrichment level (1.00 ± 0.04 $dm^3\,mol^{-1}\,s^{-1}$). Therefore, it was rationalised that the 70% enrichment level lies close to the SNR limit (of approximately 30) of the reaction monitoring experiment. Using this comparison, it can be postulated that the smaller initial concentration of Vaska's complex formed during the 30 second irradiation period will contribute to the increased rate of reaction seen as the hydride signal will decay into spectral noise on a shorter timescale so that the reaction appears to reach completion sooner. From this finding, it would be beneficial for a larger bulk of reactants to form during the irradiation period as to make reaction monitoring using the *ex situ* irradiation setup more viable. Solutions to this problem require a more powerful UV source or

use of a complex with a greater photochemical efficiency or slower thermal reaction (to increase the steady state concentration of reactant in solution).

The deviation caused by a low SNR is likely further compounded by the presence of temperature fluctuations during the experimental procedure. As shown in Section 4.3, the formation of temperature gradients due to the introduction of a relatively cold sample into the spectrometer can have a noticeable effect on the observed rate of a reaction. While the thermally insulated holder can be used for transfer steps, no temperature stabilisation is present during the irradiation period. While the sample is within the irradiation chamber, there is potential for sample heating from unfiltered IR irradiation from the lamp source and also sample cooling due to the external temperature of the lab. The inability to mitigate these temperature effects using the current *ex situ* irradiation setup make it unsuitable for measurements where precisely controlled temperatures are required to ensure a high experimental accuracy.

5.4 Conclusions

Through development of a route to irradiate NMR samples in a consistent manner within an *ex situ* irradiation setup, the exploration of hydrogenative reactions involving photochemistry was possible within a benchtop NMR spectrometer. The *ex situ* irradiation setup utilised a Hg-Xe lamp to provide the required UV output and was designed to enable quick and safe transfer of NMR samples into the NMR spectrometer. The utility of this setup was showcased through the photochemistry of $[Ir(H)_2(CO)(PPh_3)_2Cl]$ which showed showed strong hydride signal enhancements with optimal signal being observed after a 30 second irradiation period.

Signal reproducibility was observed to be an issue for the photochemistry of $[Ir(H)_2(CO)(PPh_3)_2Cl]$. While this could partially be attributed to the degradation of the sample upon repeat irradiation (verified through high-field NMR studies), the manual transfer requirement of the *ex situ* setup introduces a source of uncertainty in the delay between irradiation and NMR detection. This uncertainty propagated into the variation seen between the integrals measured for spectra obtained under identical conditions. One route to potentially address this limitation is to use a flow system to automatically transfer the sample into the NMR spectrometer following irradiation. The use of flow cells with pH$_2$ bubbling on a benchtop NMR has been

published previously[99,214] and so expansion of this method to include an irradiation step could provide a route to well defined transfer timings with the *ex situ* irradiation setup.

The photochemistry of $[Ir(H)_2(CO)(PPh_3)_2Cl]$ also highlighted the major limitations of the *ex situ* setup for reaction monitoring, namely the presence of temperature gradients, long sample transfer times and low steady state concentrations of reactive species. One route to address these issues is to use an *in situ* irradiation method that removes the requirement for sample transfer thus enabling observation of chemical species at an earlier time and allowing for the sample to equilibrate to the temperature of the spectrometer prior to analysis. The development of this approach will be the focus of Chapter 6.

6 In situ Photochemistry on a Benchtop NMR Spectrometer

In this chapter, the development of an *in situ* irradiation method for use on a benchtop NMR spectrometer is discussed. Addressing the limitations of the *ex situ* irradiation approach, the use of an *in situ* irradiation method removes the requirement to manually transfer the sample into the NMR spectrometer for detection enabling the observation of shorter-lived hyperpolarised species in solution.

An initial discussion of the instrumentation required for an *in situ* irradiation setup is presented with the comparison of two potential setups being performed. Upon selection and optimisation of the chosen setup, the photochemistry of several metal dihydride complexes is examined to establish the potential applications of this approach. One such application, the observation of magnetic evolution on the micro-to-millisecond timescale, is explored in greater detail with the development of a photochemical pump - NMR probe experiment at low-field.

6.1 Instrumentation

6.1.1 Literature Routes to *in situ* Irradiation

Most requirements for the *in situ* irradiation setup are similar to those of the *ex situ* setup with the need for a light source that has an output within the UV region and preferably one that is relatively compact so that it can be operated on a benchtop. The major difference to the *ex situ* approach is that there must be a route for the light source to provide light to the NMR sample while it is in the NMR spectrometer. There are three main routes through which this has been achieved at high-field, either from underneath the NMR sample (Figure 6.1a), through an optical fibre (Figure 6.1b) or

through the the NMR probe (Figure 6.1c).

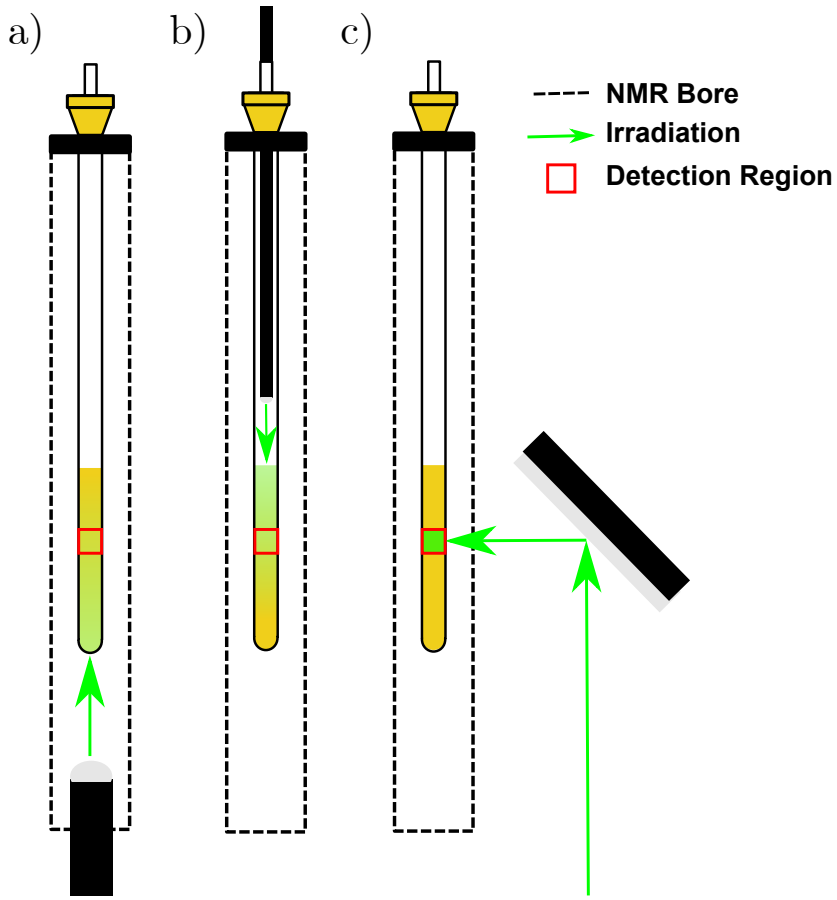

Figure 6.1: Cartoon demonstrating the published routes to *in situ* irradiation of a sample within an NMR spectrometer, highlighting the (a) through-bore, (b) optical fibre and (c) through-probe approaches.

The first route to sample irradiation to be integrated with a NMR spectrometer was the through-bore approach whereby light is directed into the NMR sample from underneath using an optical fibre.[218] This approach was initially implemented by Kaptein *et al.*[219,220] in 1978 for the study of proteins using the photo-CIDNP hyperpolarisation method (described in Table 2.4, with the additional irradiation step generating the required spin-correlated radical pairs). Within the setup used, the output of an argon ion laser was directed into the bottom of the NMR probe through use of a aluminium coated mirror. A similar approach was used by Miller *et al.* in 1981 when using photo-CIDNP to perform flash photolysis of ketones with a nitrogen laser.[221] As research into *in situ* photochemical setups continued, the approaches used moved away from this particular method. One reason for this is that the through-bore approach required permanent modification of the NMR probe for light transmission to the sample. Furthermore, the through-bore approach was more prone to inner filter effect (IFE) issues where the large passive volume of the

NMR sample that the irradiation has to pass through could result in non-uniform irradiation across the NMR sample for optically-dense samples. However, this approach has seen more recent application by Koeppe *et al.*[222,223] in 2011 within a combined UV-Vis and NMR spectroscopy setup. One large improvement utilised within this setup is the modification of a round-bottomed NMR tube to have a 0.4 mm quartz flat-bottom as to improve the transition between the sample and halogen-deuterium lamp used.

The second route shown (Figure 6.1b) uses an optical fibre that is inserted into the NMR tube as to provide irradiation from above the sample. This approach was first developed by Lerman *et al.*[224] in 1980 as an advancement in techniques for use within photo-CIDNP studies of proteins. This initial approach utilised a krypton laser coupled to a quartz optical fibre that was placed directly into the NMR sample. This technique also found application in organometallic chemistry during the late 1990's with the Ball laboratory using a 100W Hg arc lamp with a 1.5 mm diameter fibre-optic cable to deliver light to the top of an analyte solution.[26] Since inception many iterations of this setup have been developed. Optimisation of this approach has seen the incorporation of coaxial inserts to hold the optical fibre above the NMR sample,[225,226] and changes to the design of the tip of the optical fibre either by adding a pencil-shaped tip[227] or through etching the optical fibre[228] to enable uniform irradiation within the sample.[44] The most recent designs feature LED light sources, allowing for a large range of wavelengths to be examined, coupled to roughened optical fibres, to allow for uniform and efficient irradiation of the sample.[49,229] The most recent variant of this approach, termed NMRtorch, opts to replace the optical fibre with a custom-designed NMR tube where a lighthead containing LEDs is fitted to the top of a double-walled NMR tube and shone between the two walls to enable direct irradiation of the NMR active region of the sample. This design has the benefit of being easily customised (by changing the LED used in the lighthead) and removing the presence of an optical fibre within the sample.[110]

The through-probe approach (Figure 6.1c) allows for irradiation of only the NMR detection region of the NMR sample with the light being directed into the NMR sample using mirrors. This route to irradiation was first utilised by Kaptein in 1982 as an improvement to the through-bore approach originally employed for CIDNP research. Through the addition of a quartz lightguide and cylindrical mirror to the original setup, it was possible to direct the output of the argon laser to irradiate the sample from the side of the NMR tube. More recently, this approach has been implemented by the research groups of Duckett[230] and Gescheidt.[231] The benefit of

this approach is that it allows for focused, high powered irradiation of the important portion of the NMR sample. Similarly to the through-bore approach, one significant downside of this method is the requirement to drill through the probehead of the NMR spectrometer as to provide a path for the light to reach the sample.

6.1.2 Available Irradiation Setups

Of the methods outlined above, research conducted on a high-field NMR spectrometer using *in situ* irradiation at York have utilised a through-probe approach. Within these experiments, the unfocused output of the light source was reflected off an initial mirror into the spectrometer and then reflected within the probehead by a secondary mirror into the NMR active region of the sample (a scheme of this setup is shown in Figure 6.2).[47] The initial mirror was positioned on a kinematic mount allowing for facile alignment of the setup. This setup has be utilised with a continuous-wave 25 mW He-Cd laser (with a 325 nm output),[46,232,233] a pulsed 85 mW Nd:YAG laser (with a 355 nm output)[45,234,235] and a 200 W Hg-Xe arc lamp.[209] This through-probe approach is incompatible with the Spinsolve spectrometer as there are no interchangeable probeheads on the spectrometer (so modifications could not be limited to a single component of the system) and the 5 mm width bore does not provide sufficient room for the placement of a mirror within the NMR active region of the spectrometer. Accommodating a through-probe approach would therefore require drilling a hole through the spectrometer casing which would both compromise the Halbach array of magnets required to produce a homogeneous magnetic field and the temperature stabilisation of the system.

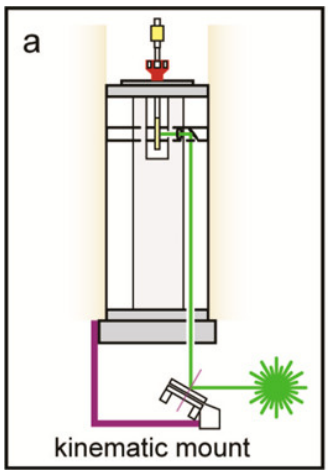

Figure 6.2: *In situ* irradiation setup used previously with a 600 MHz NMR spectrometer at York utilising a through-probe approach. Reproduced from Ref. 47 with permission from the American Chemical Society.[47]

At first glance, the use of an optical fibre internal to the NMR sample appears to be a suitable alternative choice and one that has seen use on low-field NMR spectrometers.[110] However, the requirement for the samples to be under high-pressure $p\mathrm{H_2}$ atmospheres makes the reality of designing a suitable setup far more complex. This approach would require designing an NMR tube that allows an optical fibre to be placed into the sample whilst also enabling the sample to be filled with $p\mathrm{H_2}$ and retain an adequate pressure seal during the experiments performed.

One desirable feature of the Spinsolve spectrometer that differentiates it from high-field NMR spectrometers is the fully open bore nature of the spectrometer. The greater accessibility of the magnet allows for a through-bore irradiation approach to be implemented without any permanent modification to the spectrometer. This removes one of the significant limitations that was observed previously when coupling the approach with high-field NMR spectrometers. Within this approach, the optical fibre can be situated just below the base of the NMR sample to minimise the optical pathlength into the NMR detection region. A further advantage of this irradiation route is that it allows for complete irradiation of the sample without impacting the ease of sample removal from the spectrometer as it does not require interfacing with the NMR tube. This is crucial for PHIP experiments as it enables facile addition of $p\mathrm{H_2}$ to the NMR sample as no modification is made to the NMR tube. As a proof of concept for this setup, it was logical to first use UV-visible lamp sources as these provide an affordable initial starting point and allow for direct comparisons to the previous *ex situ* studies. A cartoon representation of this *in situ* irradiation route is provided as Figure 6.3.

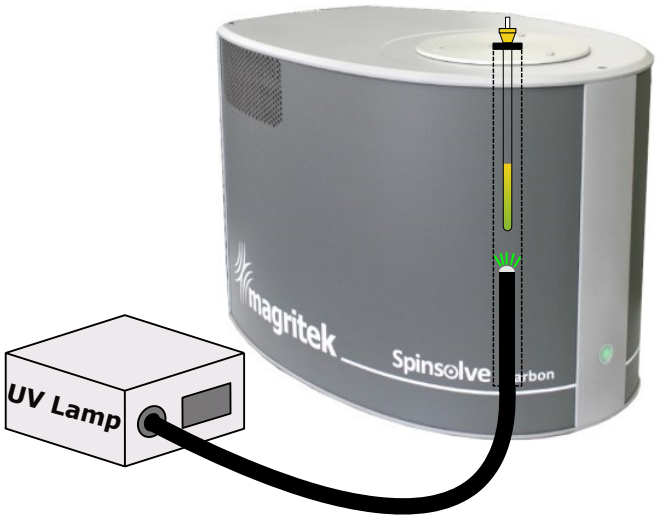

Figure 6.3: Cartoon schematic for the *in situ* irradiation setup to be used with the Spinsolve NMR spectrometer.

For this *in situ* photochemical setup, two UV-visible lamp sources were available. The first was the Oriel 200 W Hg-Xe lamp used within Chapter 5 (which will be referred to as Oriel 200 going forward). To convert the *ex situ* setup into an *in situ* setup, the sample chamber was removed and an adaptor was connected to the end of the water filter. Through this adaptor, an ethanol liquid light guide could be coupled to the lamp. The light guide was then placed inside of the NMR spectrometer to direct the UV-visible irradiation through the NMR sample. To hold the light guide in place and ensure it was directed in-line with the sample, a plastic cylindrical insert was 3D printed. The insert had an outer diameter that matched the open bore of the spectrometer with a central hole cut precisely to match the diameter of the light guide. This setup is shown as Figure 6.4.

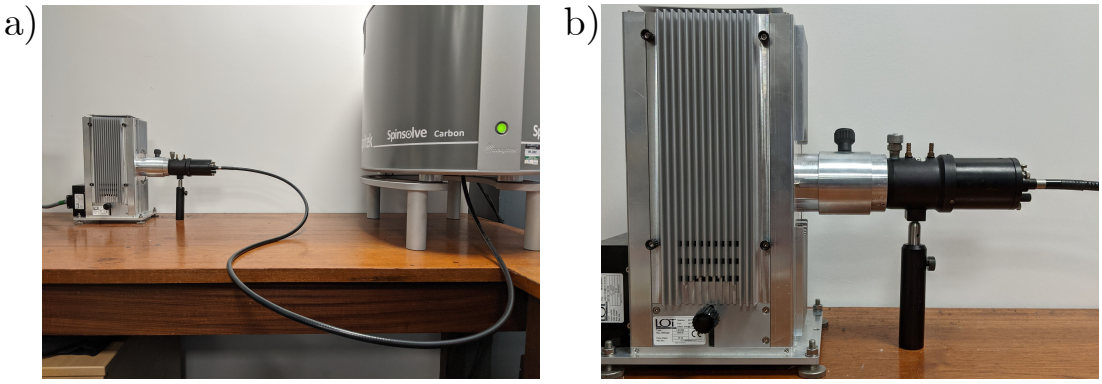

Figure 6.4: Pictures of the *in situ* irradiation setup using the Oriel 200 source, highlighting (a) the overall setup and (b) the coupling of the optical fibre to the lamp source.

The second lamp source was a Bluewave 75 Spot Curing Lamp (Dymax Europe GmbH, Wiesbaden, Germany) which was graciously provided by the research group of Dr. Arnaud Comment. The Bluewave 75 lamp source is primarily marketed as a high intensity UV light-curing spot lamp for use in industrial processes such as curing adhesives or coatings. The lamp itself is a 75 W short-arc bulb that is capable of emitting strong UV irradiation within the 300 - 450 nm wavelength range (a spectral irradiance plot provided by Intertronics is given in Appendix B). The lamp source was provided with a liquid light-guide (comprising of a light-conducting liquid that is transparent from 270 to 720 nm and sealed with quartz glass on either terminus) and with an internal mechanical shutter that can be operated manually (using a foot pedal) or automatically through use of an internal timer. Contained on the faceplate of the unit is a screen that enables the user to set how long the shutter is open for (between 0.01 and 99.99 seconds) and a screen to track the unit and bulb lifetime in hours. As with the above setup, a 3D printed insert was designed as to ensure the

optical fibre was held directly underneath the NMR sample. This setup is shown as Figure 6.5.

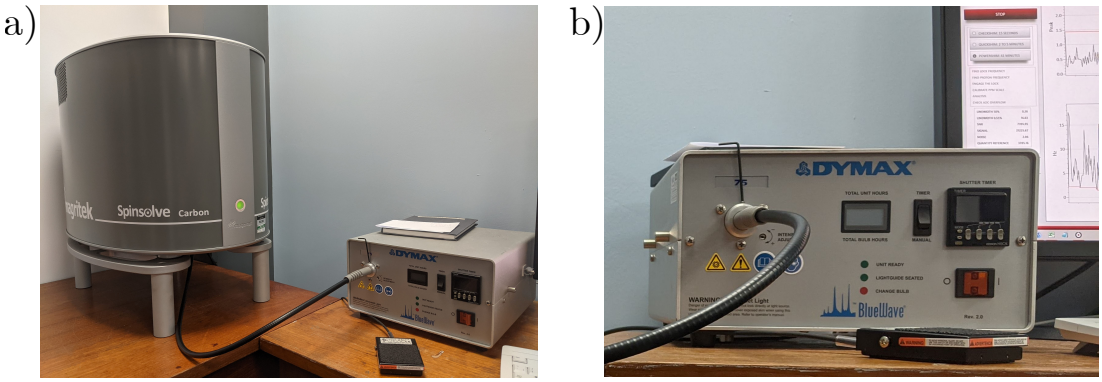

Figure 6.5: Pictures of the *in situ* irradiation setup using the Bluewave 75 source, highlighting (a) the overall setup and (b) the faceplate of the lamp control unit.

6.2 Comparison of Systems

6.2.1 Comparison of Features

The first point of comparison between the two *in situ* setup options is the features that are unique to each system. Table 6.1 compares the features available for each system across 6 categories: shutter operation, irradiation time, automation options, focusing optics, unit cooling and safety features. While both systems compare favourably in design elements such as their safety features and cooling systems, the ease of incorporation of the Bluewave 75 with the NMR spectrometer make it a superior option in this regard. In particular, the ability to position the foot pedal trigger close to the spectrometer computer and set predetermined irradiation times within the unit made the triggering of the lamp source followed by the NMR pulse sequence more reliable and enabled the application of shorter irradiation periods than achievable by human operation (less than 1 second).

Table 6.1: Summary of key features for the Bluewave 75 and Oriel 200 broadband UV lamp sources.

Feature	Bluewave 75	Oriel 200
Shutter Operation	Manual foot pedal trigger	Manual switch trigger on setup
Irradiation Time	Controlled by user or internal timer	User control only
Automation Options	Auxiliary cable input port	TTL pulse controlled external shutter
Focusing Optics	Internal to system	Requires manual focusing
Unit Cooling	Internal Fan	Water filter between source and optical fibre
Safety Features	Requires optical fibre to be present for shutter to open	All components are locked in place by Grub screws

6.2.2 Comparison of Light Output

To determine the power output of each lamp source, a study was performed using a power meter. Power meters are commonly used to measure the output of laser sources at specific wavelengths by measuring the power of the incident irradiation upon the active region of the sensor. For a broadband lamp source, a power meter will measure the power of all individual wavelengths of light that are incident on the sensor and thus an overall power output for a broadband source can be approximated. For these studies, a Coherence FieldMax II power meter equipped with a PM30 head was used. The PM30 head is able to measure the power of incident irradiation between 250 nm and 11 μm in the range of 100 mW to 30W making it a suitable option to observe these two lamps with strong outputs in the UV-visible region. To record measurements, the power meter was set to operate at 532 nm. The operation wavelength of the power meter determines the correction factor applied to the observed power based on the efficiency of the power meter at that wavelength. As the lamp sources are not monochromatic, the use of an identical operational wavelength just ensures that both sources have the same correction factor applied to the observed power output to ensure that a comparison can be made between the two. For both sources, the end of the optical fibre that is placed into the spectrometer was placed against the PM30 head (to mimic the distance between the NMR tube and optical fibre within the spectrometer) and clamped in place within the 3D printed plastic insert. The power meter was then

zeroed to the ambient light level within the laboratory. Both lamp sources were left to reach operational temperature for 15 minutes and then the output power was monitored for the following 30 minutes, with a reading being taken every minute. Table 6.2 contains the average power (in W) and power density (in W cm^{-2}) for each setup. As a further point of comparison, the power output of the *ex situ* setup used in Chapter 5 (using the Oriel 200 lamp source) was also observed where the power meter replaced the irradiation chamber of the setup.

Table 6.2: Average output power and power density measured for the Bluewave 75 and Oriel 200 lamp source using a Coherence FieldMax II power meter equipped with a PM30 head. Measurements for the Oriel 200 system were taken using both the *in situ* and *ex situ* photochemistry setups.

Instrument	Power / W	Power Density / W cm^{-2}
Bluewave 75	4.03	515
Oriel 200	0.07	9
ex situ Setup	1.37	174

The key finding from Table 6.2 is the output power of 4.03 W for the Bluewave 75 is approximately 58 times more powerful than that observed from the Oriel 200 setup (of 0.07 W). The major limitation of the Oriel 200 setup appears to be the coupling of the optical fibre to the lamp source as when compared to the *ex situ* setup (which is identical to the *in situ* setup up to that component) a 20-fold decrease in power is observed. While this means that the Oriel 200 setup could be improved through optimisation of the adaptor and lightguide combination used, the maximum possible output of 1.37 W for the system is still below that observed for the Bluewave 75 system. This large disparity in output power is a strong indicator that the Bluewave 75 is the optimal system to use going forward as a low output power is likely to lead to smaller concentrations of photoproduct molecules in solution and thus reduce the PHIP enhancements observed for a species. Furthermore, irradiation of a sample from underneath introduces an increased passive volume through which the irradiation must penetrate through in order to reach the NMR detection region of the sample. Choosing to use the more powerful irradiation source will minimise incident irradiation attenuation across the passive volume of the sample and thus will enable the use of more concentrated samples within this setup.

While the maximum power output was used for all future studies, a further benefit of the Bluewave 75 lamp is that it has a dial with which to tune the output power to lower values. This enables more precise control of the power being put into the NMR sample. This functionality provides an additional route through which to control

the conditions that are experienced by the NMR sample and thus enables the user to fine-tune experiments to their requirements (for example, reducing the observed NMR signal to increase the stability of a sample against photodegredation) or run additional NMR experiments, such as calibrating signal integrals against irradiation intensity. Repeating the power meter experiment at different dial positions showed a linear attenuation of the output power with a range of 4.03 - 0.10 W being established for the system.

6.2.3 Comparison of NMR Spectra

A final point of comparison is how effectively each setup can irradiate a photoactive NMR sample. The simplest metric through which to perform this comparison is through the appearance of the NMR spectra obtained for a particular species both in terms of the resolution and SNR of the observed peaks. For each *in situ* setup, the optical fibre was aligned within the spectrometer (by shining a torch through the fibre and observing the positioning of the fibre from the top of the spectrometer bore) and then the spectrometer was shimmed to ensure a <0.5 Hz FWHM was achieved. Following setup, a sample of Vaska's complex (0.43 mM) was placed under an atmosphere of pH$_2$, shaken to dissolve the pH$_2$ into solution to form [Ir(H)$_2$(CO)(PPh$_3$)$_2$Cl] in solution, and then placed into the spectrometer. The sample was then irradiated for 5 periods of 1 second with a spectrum being recorded immediately following each irradiation period. A comparison between the hydride signals observed using the two *in situ* setups is given in Figure 6.6. The appearance of the spectra using the *in situ* setup is expected to match that seen with the thermal reaction monitoring experiments with each hydride having a multiplicity of a triplet of antiphase doublets. This is because, unlike the *ex situ* setup, the irradiation step occurs within the magnet and as such PHIP will occur under PASADENA conditions.

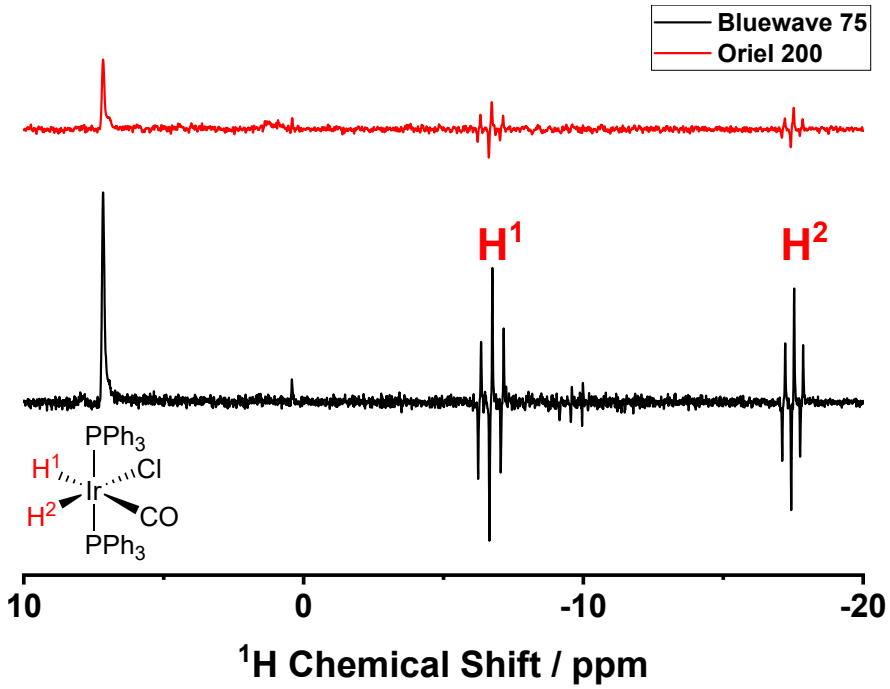

Figure 6.6: ^{1}H spectra of $[Ir(H)_2(CO)(PPh_3)_2Cl]$ (0.43 mM) recorded following 1 second of irradiation from a Bluewave 75 (black) or Oriel 200 (red) UV lamp source.

As evidenced from the above figure, the Bluewave 75 performed better than the Oriel lightsource, with stronger and more reproducible hydride signal enhancements being observed with that *in situ* setup. Using these unoptimised *in situ* setups, the Bluewave 75 delivered an average SNR of (47 ± 3) for the hyperpolarised hydride signals compared to the SNR of 17 for the Oriel lightsource, which is an increase of 2.8 times signal. Furthermore, the Oriel setup was far more unreliable with only one of the five recorded spectra showing observable signal for the sample even with identical conditions being used throughout. The increased difficulty with aligning and operating the Oriel setup combined with this lower reproducibility of results make it an undesirable choice for further experimentation.

Overall, the improved lamp power and observed NMR signals observed using the Bluewave 75 combined with the easier control of irradiation times for the user make this setup the most suitable candidate to use for further experimentation. Therefore, all further experiments performed using an *in situ* photochemical setup will feature the Bluewave 75 setup that is shown in Figure 6.5.

6.3 Optimisation of Chosen System

6.3.1 Inner Filter Effects

As discussed in Chapter 5, the presence of inner filter effects (IFEs) across the irradiation region within the NMR sample is undesirable as it can lead to the formation of concentration gradients within a sample and reduced observable species within the NMR detection region. By choosing to irradiate the sample from underneath, there is an increased potential for IFEs to be present due to the irradiation having to pass through a passive volume of the sample to reach the NMR detection region. The total pathlength within the *in situ* setup includes both the distance from the base of the NMR tube to the NMR detection coil (2.9 cm) and the diameter of the NMR detection region (0.5 cm). Overall, this 3.4 cm pathlength is an almost 7-fold increase from that within the *ex situ* setup (0.5 cm) and so a lower maximum concentration for the samples will be tolerated within this setup. By rearranging the Beer-Lambert Law, it is possible to calculate the new sample concentration maximum that ensures that the A < 0.1 condition (to minimise the presence of IFEs) is still met (Equation 6.1).[212]

$$c = \frac{A}{\epsilon l} \tag{6.1}$$

For Vaska's complex, using A = 0.1, ϵ_{max} = 10.7 dm^3 mol^{-1} cm^{-1} and a pathlength of 3.4 cm gives a maximum concentration of 2.7 mM for a sample of $[Ir(H)_2(CO)(PPh_3)_2Cl]$ which equates to 1.3 mg of starting material. Overall, this concentration limitation is stricter than that observed with the *ex situ* setup but is still greater than the 0.43 mM concentration that is used within the reaction monitoring experiments performed with Vaska's complex.

6.3.2 Irradiation Length Optimisation

Similarly to the *ex situ* irradiation setup, one feature that can be optimised is the irradiation time for the sample. With changes to the overall power of the lamp source and direction of irradiation, a different trend to that observed with the *ex situ*

setup (whereby the NMR signal increased to a steady state value with increasing irradiation time) may be present. To perform a comparable test, a 1 mg sample of Vaska's complex (2.14 mM) was reacted with pH$_2$ to form [Ir(H)$_2$(CO)(PPh$_3$)$_2$Cl]. The pH$_2$ was then replenished and the sample was irradiated for between 5 - 60 seconds with a ^{1}H spectrum recorded immediately after. Each irradiation period was repeated 3 times with the pH$_2$ being refreshed between each experiment. Given in Figure 6.7 is the average integral for each irradiation period examined. From this dataset, only one experiment was performed with a 60 second irradiation time due to loss of shim stability at this length of irradiation period.

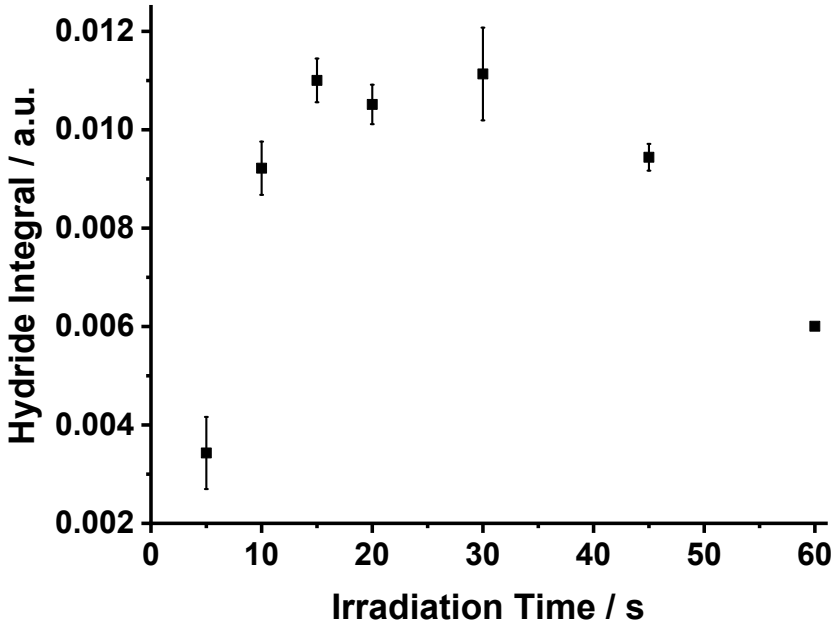

Figure 6.7: Average hydride integrals measured for [Ir(H)$_2$(CO)(PPh$_3$)$_2$Cl] (2.14 mM) under PASADENA conditions following 5, 10, 20, 30, 45 and 60 seconds of irradiation within the *in situ* photochemical setup.

The trend observed for the *in situ* irradiation setup is notably different from that observed previously with the *ex situ* setup with two key changes being identifiable from Figure 6.7. The first major change is that, while the maximum integral is still observed at 30 seconds (0.0111 ± 0.0009), a highly comparable value of (0.0110 ± 0.0004) is observed at 15 seconds. This implies that the steady state formation of Vaska's complex in solution (where the photochemical formation and thermal reactivity of the species are balanced) is reached much sooner with this setup which can be justified by the increased power of the Bluewave 75 lamp source (4.03 W as compared to 1.37 W for the Oriel 200 *ex situ* setup). This more powerful lamp source, alongside the removal of the transfer step prior to acquisition, has the added benefit of improving the overall SNR observed under the same irradiation period. For 30 seconds of irradiation, an SNR of (51 ± 6) is observed for the *in situ* setup

while for the *ex situ* setup, the SNR is only (33 ± 2). The ^{1}H spectrum with the best SNR for each setup is shown in Figure 6.8a, which highlights that not only does moving to an integrated *in situ* irradiation approach improve the observed signal but also enables observation of the expected multiplicity of the hydride signals as there is no ALTADENA character within the spectrum.

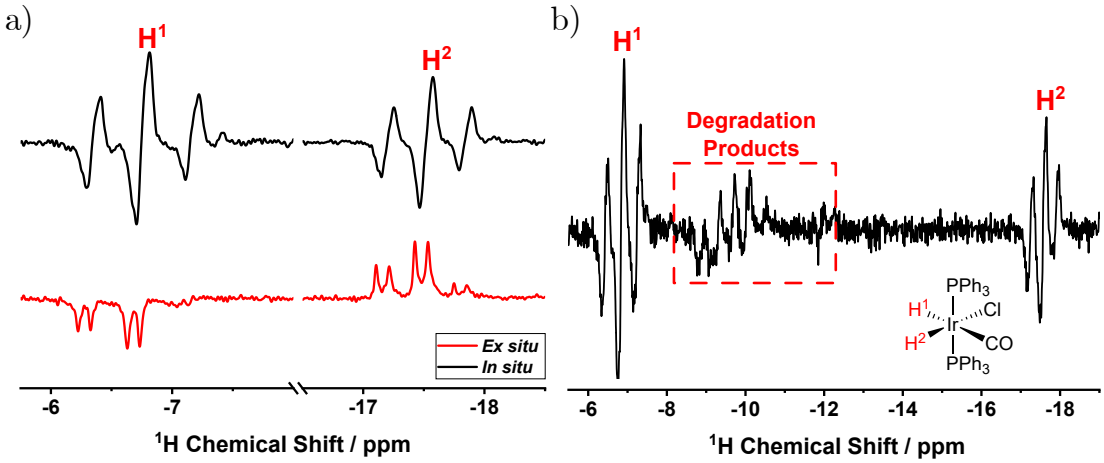

Figure 6.8: (a) Comparison between ^{1}H spectra obtained for $[Ir(H)_2(CO)(PPh_3)_2Cl]$ (2.14 mM) obtained followed 10 seconds of irradiation with an *in situ* (black) or *ex situ* (red) irradiation setup. (b) ^{1}H spectrum recorded for $[Ir(H)_2(CO)(PPh_3)_2Cl]$ (2.14 mM) following 60 seconds of sample irradiation highlighting the additional peaks observed between 9 - 12 ppm.

The second major difference observed from this experiment is that for irradiation times above 30 seconds, there is not a plateau in the hydride integrals but rather a decay is observed. One possible reason for this decay is due to the high consumption of pH$_2$ within the sample during the irradiation period. During irradiation, a high rate of H$_2$ cycling onto the complex will occur prior to NMR observation. However, any H$_2$ that reforms following photodissociation of $[Ir(H)_2(CO)(PPh_3)_2Cl]$ will form according to the room temperature distribution of pH$_2$ and oH$_2$ and so subsequent reactions occur under thermally-polarised conditions. For short irradiation periods, the large excess of pH$_2$ in solution results in a negligible loss of signal from this redistribution. For longer irradiation periods (above 30 seconds), the [pH$_2$]:[oH$_2$] ratio will move towards a room temperature distribution and so competition between oH$_2$ and pH$_2$ binding will result in lower overall enhanced NMR signals being observed for the product hydride signals. An alternative reasoning is that continued exposure to this intense irradiation source promotes photodegradation of the $[Ir(H)_2(CO)(PPh_3)_2Cl]$ in solution. As such sustained irradiation of the sample reduces the concentration of $[Ir(H)_2(CO)(PPh_3)_2Cl]$ in the sample resulting in smaller signals. There is clear evidence of photodegradation within the sample over

the course of the experiment, as shown by the spectrum recorded after 60 seconds of irradiation (Figure 6.8b) with very clear hyperpolarised signals seen between -9 and - 12 ppm (which strongly suggests trihydride species formation based on the analysis performed in Section 5.3.1). Both of these problems likely contribute to the trend shown above and as such the use of shorter irradiation periods (such as 10 seconds) appears to be favourable as strong signals can still be observed but the consumption of pH$_2$ and degradation of the sample can be reduced.

While moving to an *in situ* irradiation setup has improved the observable signal for Vaska's complex, there are still some issues that persist from the original *ex situ* setup experiments that need to be addressed. The first issue is that the reproducibility of the signal observed following irradiation is only slightly improved (with a maximum percentage variation of 8.5% seen during the irradiation study compared to 8.8% for the *ex situ* experiments). This variability is likely due to the coordination of the irradiation period and the NMR acquisition which is controlled manually by the user. This non-negligible human reaction time delay to NMR acquisition needs to be eliminated to further improve the consistency of the observed NMR signals. A second issue is that sample degradation of Vaska's complex is still present and limits the usability of this complex to further optimise parameters for *in situ* irradiation experiments. Therefore, finding a more appropriate complex that gives sufficient hyperpolarised signals but is more resistant to photodegradation is necessary.

6.3.3 NMR Tube Design

An alternative route to further improve the observed NMR signal is to optimise the design of the NMR tube used for these experiments. To explore how NMR tube design could impact the observed signal, the air-glass interface between the optical fibre and the NMR tube in this through-bore approach needs to be considered.

For an air-glass interface where the incident irradiation is normal to the surface, it is expected that around 96% of the incident irradiation will transmit through the glass in accordance with Snell's Law (with 4% lost to specular reflection).[236] However usually for an NMR experiment, the standard NMR tube that is used has a rounded surface at the base. This rounded surface is non-ideal as moving away from a normal angle of incidence increases the proportion of light that will be reflected (Fresnel's Law) and thus reduce the penetrating power of the irradiation into the

sample itself.[236] Previous literature using this *in situ* irradiation approach have opted to utilise flat-bottomed NMR tubes as to improve the penetration of light into the sample by increasing the area over which the incident irradiation will be normal to the interface.[222] Therefore, a set of flat-bottomed NMR tubes (S-5-400-FB-7, Norell) were purchased. These NMR tubes were adapted to have J Young tap valves (as to enable the samples to be placed under a pH$_2$ atmosphere) by the glass workshop at the University of York. For these experiments, the further glass-solvent interface was not considered as both types of NMR tube are made from the same material and contain the same solvent (C_6D_6) and as such a negligible difference would be expected between the samples.

To determine if the use of flat-bottomed NMR tubes improved the observed signal in *in situ* irradiation experiments, two samples of Vaska's samples (0.43 mM) were prepared with one in a round-bottomed NMR tube and the other in a flat-bottomed NMR tube. Each sample was placed under pH$_2$, reacted to completion to form [Ir(H)$_2$(CO)(PPh$_3$)$_2$Cl] and then the pH$_2$ was refreshed. To perform the *in situ* irradiation experiments, each sample was irradiated for 10 seconds and then a single-scan ^{1}H spectrum was recorded. Between each of the 5 repeats performed the NMR sample was shaken to dissolve fresh pH$_2$ into the sample. A comparison between the best spectra obtained with each setup is given in Figure 6.9.

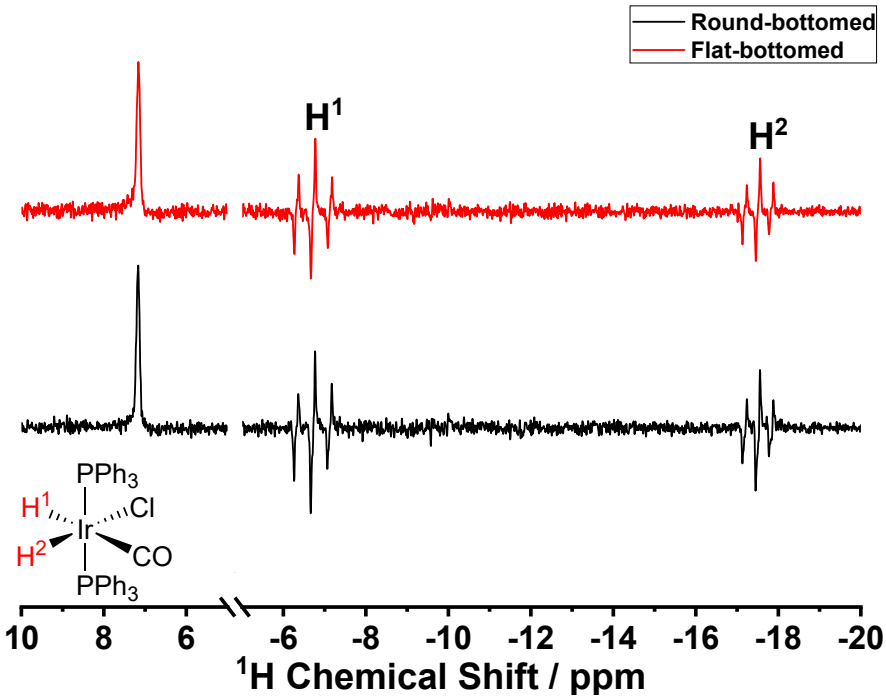

Figure 6.9: ^{1}H spectra of [Ir(H)$_2$(CO)(PPh$_3$)$_2$Cl] (0.43 mM) recorded following 10 seconds of irradiation with the sample within a round-bottomed (black) and flat-bottomed (red) NMR tube.

The standard round-bottomed NMR tube performed best with an average SNR of (22.4 ± 1.2), compared to the value of (17.7 ± 1.2) obtained for the flat-bottomed NMR tube. Whilst the quality of spectra obtained with the flat-bottomed NMR tube is comparable to that observed with the round-bottomed NMR tube, the lack of substantial SNR improvements suggests that there is no advantage to improving the interfacing surface between the sample and the optical fibre indicating that this feature is not a limiting factor within the current setup. Furthermore as the flat-bottomed NMR tubes have to be modified for use with pH$_2$, this finding confirms that it is preferable to use the commercially available round-bottomed alternative.

6.4 Initial Exploration of Photochemistry with an *in situ* Irradiation Setup

6.4.1 Selection of Complexes

With the faster timescale of detection available through use of the *in situ* photochemistry setup, a suite of new complexes capable of forming dihydride products upon irradiation were explored. The complexes that were used within these studies are shown in Figure 6.10.

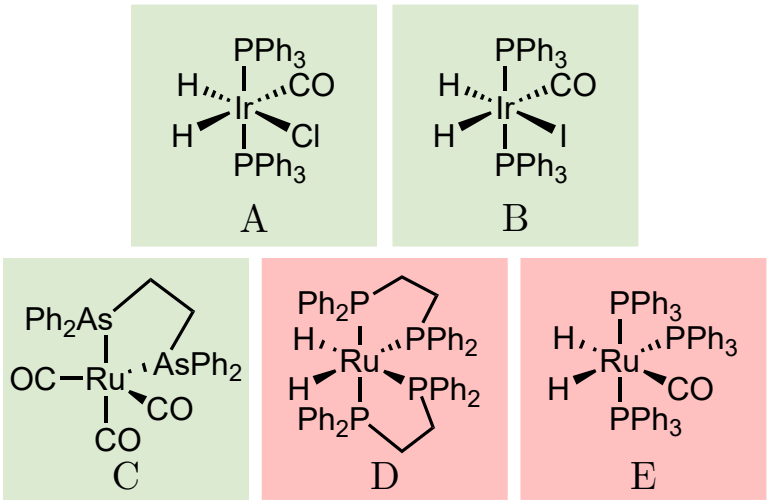

Figure 6.10: Chemical structures for 5 complexes of interest for their reactivity with pH$_2$ to form metal dihydride complexes. Background colour indicates if hyperpolarised signal was observed at low-field (1T, 43 MHz) when the complex was reacted with pH$_2$ following sample irradiation (with green representing success and red representing failure).

This selection of complexes was chosen as each complex has been explored within previous research at the University of York using a high-field NMR photochemistry setup, enabling facile benchmarking of the results obtained using a low-field NMR setup.[45,47,48] These studies showed hyperpolarised hydride signals for all complexes after irradiation at 355 nm and so the strong UV output of the *in situ* photochemical setup should enable observation of these complexes using the benchtop NMR setup.

The first new complex explored was the iodo-derivative of Vaska's complex, $[Ir(H)_2(CO)(PPh_3)_2I]$ (**B**), whose photochemically-initiated degenerate reaction had been previously explored using a photochemical pump - NMR probe technique.[45] The second new complex explored was $[Ru(CO)_3(dpae)]$ (**C**), where dpae is 1,2-bis(diphenylarsino)ethane, whose reaction with pH_2 to form $[Ru(H)_2(CO)_2(dpae)]$ creates a high purity singlet state that was explored for use in quantum computing.[237] A final set of ruthenium complexes, *cis*−$[Ru(H)_2(dppe)_2]$ (**D**) where dppe = 1,2-bis(diphenylphosphino)ethane and $[Ru(H)_2(CO)(PPh_3)_3]$ (**E**) were also explored. These two complexes were used as part of a study on observing milli-to-microsecond oscillations of the NMR signal due to magnetic evolution (a more detailed description of this phenomenon will be given in Section 6.5).[47,48] Whilst all of these complexes are of interest going forward, the initial motivation for testing this range of complexes was to find a system that gave strong reproducible signals with minimal degradation to allow for further optimisation of the *in situ* irradiation setup to be conducted.

For an initial study, 0.2 mg samples of all complexes were made up in 0.6 mL of C_6D_6. Each sample was degassed and the headspace of the NMR tube was filled with pH_2 . Before any NMR experiments, each sample was shaken to dissolve pH_2 into solution and then irradiated within the NMR spectrometer before detection. After multiple experiments with each sample, varying irradiation lengths between 0.5 and 2 seconds, hydride signals were observed only for complexes **A**, **B** and **C** (as shown by the green background coloration of the complexes in Figure 6.10). Following the study at low-field, a ^1H thermal spectrum was recorded at high-field for each complex which confirmed all samples contained the desired complex (identifying information can be found in Section 8.4). The following subsections within this section detail the further experiments performed with each of complexes **A** - **C** along with a discussion of why signal was not observed for complexes **D** and **E**.

6.4.2 Vaska's Complex Reaction Monitoring

Of all the complexes investigated within this section, Vaska's complex has already been explored in detail during the initial instrumentation optimisation performed for the *in situ* irradiation setup. As found with the *ex situ* irradiation setup, photodegradation of Vaska's complex limits the usability of the complex for detailed repetition studies using this irradiation setup (see Figure 6.8 for evidence of sample degradation). However, one useful experiment to perform using this *in situ* irradiation setup is to do a comparison reaction monitoring experiment to those performed both thermally and with the *ex situ* irradiation setup.

To monitor the reformation of $[Ir(H)_2(CO)(PPh_3)_2Cl]$ following photochemically induced reductive elimination, 5 samples of Vaska's complex (0.43 mM) were placed under pH$_2$ to allow full conversion of the sample to $[Ir(H)_2(CO)(PPh_3)_2Cl]$. Fresh pH$_2$ was then added to the sample prior to reaction monitoring. To perform the reaction monitoring experiment, each sample was shaken for 5 seconds and placed into the spectrometer for 10 minutes to equilibrate to the temperature of the spectrometer. The sample was irradiated for 10 seconds and then the standard reaction monitoring procedure was followed. Similarly to the *ex situ* irradiation setup, the k_{obs} rate constant is obtained via fitting of a monoexponential recovery function to the cumulative hydride integral curve (as the initial concentration of Vaska's complex is unknown). The determined rate constants are summarised within Table 6.3. The cumulative integral curves for each experiment are shown in Figure 6.11a and a comparison between the average growth curve observed for the *in situ* , *ex situ* and thermal reaction monitoring experiments is given in Figure 6.11b (with the maximum value of each normalised to 1 as to remove differences due to absolute integral values).

Table 6.3: Pseudo-first order (k_{obs}) and second-order (k_2) rate constants for the five repeat measurements for the oxidative addition of pH$_2$ to Vaska's complex following a 10 second irradiation period on $[Ir(H)_2(CO)(PPh_3)_2Cl]$ (0.43 mM).

Experiment	1	2	3	4	5	Average
k_{obs} / s^{-1}	0.0154	0.0164	0.0159	0.0153	0.0157	(0.0158 ± 0.0004)
k_2 / dm^3 mol^{-1} s^{-1}	1.33	1.41	1.38	1.32	1.35	(1.36 ± 0.02)

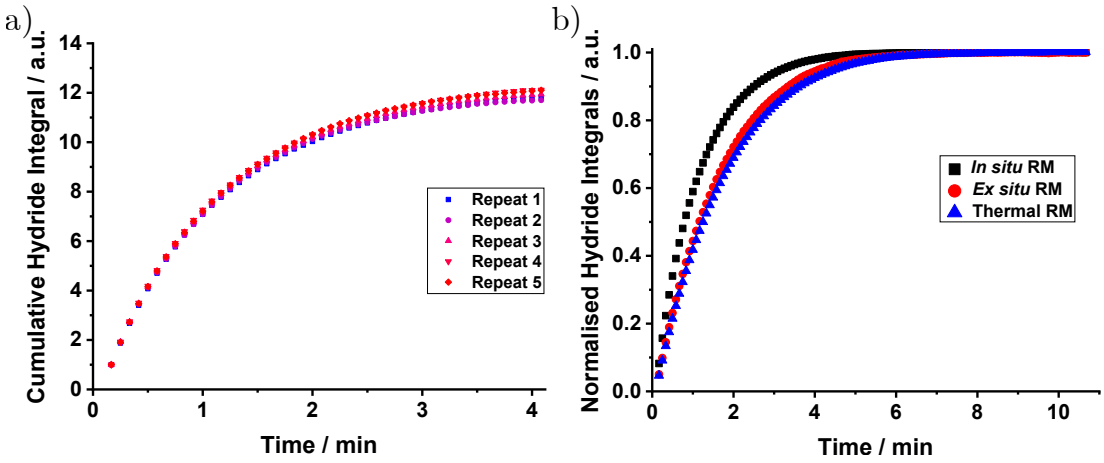

Figure 6.11: Cumulative integral curves for the the oxidative addition of $p\mathrm{H_2}$ to Vaska's complex for (a) 5 repeat measurements recorded following 10 seconds of irradiation using an *in situ* irradiation setup and (b) average measurements recorded using no irradiation, *ex situ* irradiation and *in situ* irradiation.

The most notable difference observed for reaction monitoring following *in situ* irradiation is that the overall k_2 rate constant, (1.36 ± 0.02) $\mathrm{dm^3\,mol^{-1}\,s^{-1}}$, is significantly higher than that expected from the literature, (0.86 ± 0.03) $\mathrm{dm^3\,mol^{-1}\,s^{-1}}$, and from those observed when monitoring the reaction thermally, (0.89 ± 0.03) $\mathrm{dm^3\,mol^{-1}\,s^{-1}}$, or with the *ex situ* setup, (0.958 ± 0.009) $\mathrm{dm^3\,mol^{-1}\,s^{-1}}$. Each of the 5 repeats for the reaction monitoring experiment produced highly consistent growth curves (see Figure 6.11a) giving a maximum difference from the average k_2 rate of 3.7%. Because of this high reproducibility, it suggests that there is a systematic source for this increase in rate that must originate from the difference in setup compared to the other experimental datasets. A slight increase in the observed rate constant was previously seen with the *ex situ* reaction monitoring experiments which was attributed to drop in the SNR of the observed hydride signals. However, this is unlikely to be the origin of the rate increase for the *in situ* setup as the averaged measured SNR of the first usable spectrum for each reaction monitoring experiment was (68 ± 3) which is of a similar magnitude to that obtained for thermal reaction monitoring (with an SNR of 65).

The origin of the increase in rate constant that is observed is likely to be a result of sample heating during the 10 second irradiation period. While temperature effects were discussed in the case of the *ex situ* irradiation setup, stronger temperature effects are likely to be present for the *in situ* setup for two main reasons. The first factor is that the sample is no longer being transferred into an external housing during irradiation and so is not exposed to the laboratory temperature during irradiation. This means that sample cooling during the irradiation period and transfer period will

not occur. Secondly, the *in situ* lamp source sits much closer to the NMR tube and has a higher output power (4.03 W) and as such heating effects would be expected to be increased. To explore the extent of sample heating during irradiation, a thermocouple was placed into a 0.6 mL sample of water which was then placed into the spectrometer. The sample was irradiated and then allowed to cool before repeat measurements were taken. Triplicate measurements for irradiation periods between 1 and 10 seconds were recorded with the data collated within Table 6.4.

Table 6.4: Average temperature increase following irradiation of a sample of H_2O (0.6 mL) for between 1 - 10 seconds. Temperatures were measured using a thermocouple placed inside the solution.

Irradiation Time / s	Average Final Temperature / °C
1	32.2
2	33.4
5	35.2
10	37.2

The results of this experiment indicate that there is non-negligible heating of the sample during irradiation and, intuitively, a longer irradiation time leads to increased heating of the sample prior to observation. While an exact comparison to what is occurring within the Vaska's complex sample cannot be made here (due to water and C_6D_6 having different thermal properties), a similar temperature increase would explain the extent of the rate constant change seen in this reaction monitoring experiment. Assuming a 8.7 °C increase in temperature during the 10 second irradiation period (between 37.2 and 28.5 °C) and using the fact that Vaska's complex displays a 0.06 $dm^3\,mol^{-1}\,s^{-1}T^{-1}$ temperature dependence (established in Section 4.3.6), this would correspond to an expected rate increase of 0.52 $dm^3\,mol^{-1}\,s^{-1}$. Adding this value to the literature rate constant at 28.5 °C leads to an expected initial rate constant for the reaction of 1.38 $dm^3\,mol^{-1}\,s^{-1}$ which is of similar magnitude to the observed rate constant of 1.36 $dm^3\,mol^{-1}\,s^{-1}$. While this calculation assumes a similar degree of heating in the sample to that of water and does not account for the variation in rate that will occur as the sample cools, the fact that a temperature increase can lead to the correct magnitude of deviation from the expected rate constant is an indicator that temperature is a likely source for the observed change.

Importantly, the change in rate constant observed for the *in situ* reaction monitoring setup suggests that care needs to be taken when performing temperature-controlled experiments, such as taking kinetic measurements, with this

setup. While the heating effects could be mitigated by reducing the irradiation time (as observed in Table 6.4) or by reducing the power output of the lamp this will also affect the SNR of the observed resonances in the NMR spectrum and so a compromise will have to be made.

6.4.3 $[Ir(H)_2(CO)(PPh_3)_2I]$ Complex Studies

$[Ir(H)_2(CO)(PPh_3)_2I]$ reacts with pH_2 following irradiation in an analogous manner to the chloro-derivative, with reductive elimination of H_2 followed by oxidative addition of pH_2 in a degenerate reaction (reaction scheme given in Figure 6.12). Upon observation, a pair of triplets of antiphase doublets are observed centred at -8.4 ppm ($J_{P_{cis}H}$ = 17.4 Hz, J_{HH} = 4.2 Hz) and -14.9 ppm ($J_{P_{cis}H}$ = 13.6 Hz, J_{HH} = 4.2 Hz) for the hydride trans to CO and I respectively.

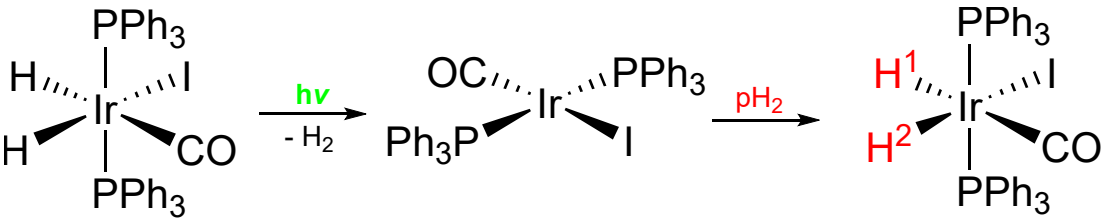

Figure 6.12: Reaction scheme for the degenerate photochemical reaction of $[Ir(H)_2(CO)(PPh_3)_2I]$ in the presence of pH_2.

Initial signal quality and reproducibility experiments were performed using a 0.2 mg sample of *trans*-$[IrI(CO)(PPh_3)_2]$ (0.38 mM). The sample was reacted with pH_2 to form $[Ir(H)_2(CO)(PPh_3)_2I]$ in solution and then fresh pH_2 was added to the headspace of the NMR tube. A series of 5 experiments were performed whereby the sample was irradiated for 1 second and then observed by ^1H NMR. Between experiments the sample was shaken to refresh the pH_2 in solution. An example hyperpolarised spectrum of $[Ir(H)_2(CO)(PPh_3)_2I]$ is given as Figure 6.13.

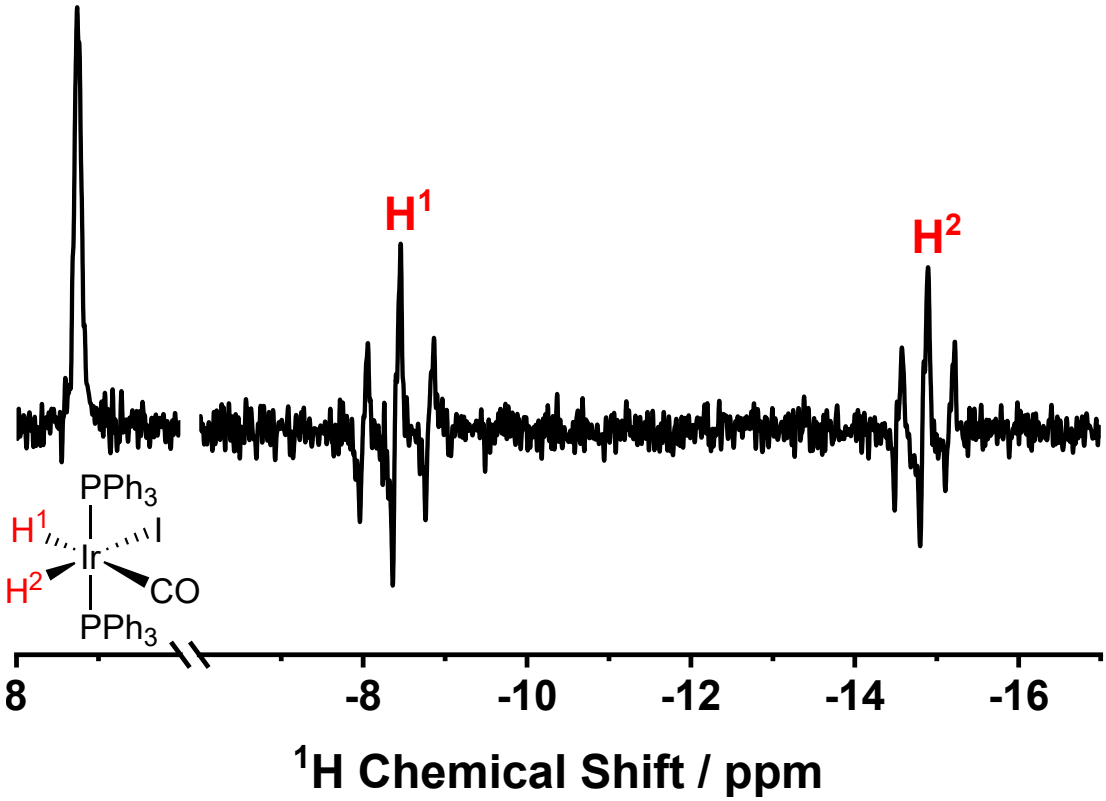

Figure 6.13: Single-scan ^{1}H spectrum of $[Ir(H)_2(CO)(PPh_3)_2I]$ (0.38 mM) after pH_2 addition recorded following irradiation of the sample for 1 second.

The reformation of $[Ir(H)_2(CO)(PPh_3)_2I]$ within this reaction occurs within a substantially faster timeframe than that of Vaska's complex, with a rate of $k_2 = (3.26 \pm 0.42) \times 10^2$ M^{-1} s^{-1} for the reaction being established by Procacci *et al.*[45] This rate of reaction is 379 times faster than that of Vaska's complex and as such reaches completion on the second timescale (within 5 seconds) rather than spanning over several minutes. Therefore, even the observation of these signals represents a significant leap forward using this *in situ* irradiation setup as these signals would not be able to be detected using the *ex situ* irradiation setup (due to the significant contribution of transfer times). From the five repeat measurements, an average SNR of (14.2 ± 0.8) was obtained which showed a high consistency of observed hyperpolarisation using this setup and is only slightly poorer than that observed for 0.43 mM sample of $[Ir(H)_2(CO)(PPh_3)_2Cl]$ irradiated for 1 second (22.4 ± 1.2). However, $[Ir(H)_2(CO)(PPh_3)_2I]$ is not a good option for continued optimisation of the *in situ* photochemical setup as it shares similar degradation pathways to the chloro-derivative. Within the aforementioned study, Procacci *et al.* identified several additional species following continued irradiation of $[Ir(H)_2(CO)(PPh_3)_2I]$ including ligand rearrangement products, trisphosphine complexes and dimer formations .[45]

The short-lived nature of the signal during the reaction of *trans*-[IrI(CO)(PPh_3)$_2$] with pH_2 also highlights a software limitation within the current approach to reaction monitoring. This limitation is best exemplified when trying to perform the standard reaction monitoring procedure following irradiation of [Ir(H)$_2$(CO)(PPh_3)$_2$I]. To maximise the number of spectra to be recorded over the reaction course, the parameters for this experiment were set so that a spectrum could be recorded every second (with an acquisition time of 409.6 ms). The resulting first 5 seconds of this reaction monitoring experiment are shown in Figure 6.14. While clear signals are observable for the first 2 seconds of the reaction, all signal is quickly lost to noise. The second timescale of this reaction makes it so that a conventional reaction monitoring method where spectra are recorded continuously over the reaction coordinate is unsuitable. While shorter acquisition times can be used there is a limit to how short the acquisition can be used before the signals of interest become obscured. Proceeding towards monitoring faster processes, such as reactions on this timescale or magnetic evolution of systems, will require development of a photochemical pump - NMR probe experiment at low-field so that datapoints can be collected individually and with enough signal in order to be analysed.

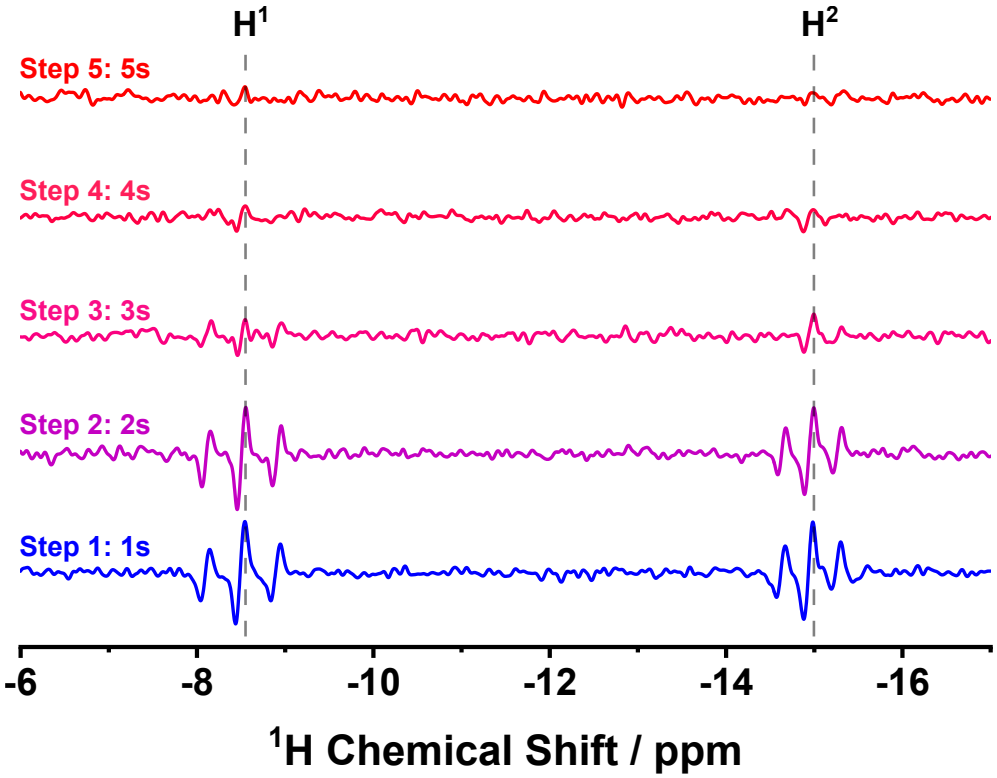

Figure 6.14: Stacked ^{1}H spectra showing the first five steps of a reaction monitoring experiment between [Ir(H)$_2$(CO)(PPh_3)$_2$I] (0.38 mM) and pH_2 following a 1 s irradiation period.

6.4.4 [Ru(CO)$_3$(dpae)] Studies

One very promising complex that produces strong and reproducible hydride signals from the high-field NMR literature is [Ru(CO)$_3$(dpae)]. Research by Blazina *et al.*[237] observed that upon irradiation by a 12 ns XeCl eximer laser pulse, the hyperpolarised signal obtained had an enhancement factor of 31,284 when compared to a thermally-polarised spectrum. This enhancement corresponded to (106 ± 4)% of the theoretical maximum of signal that could be obtained for this complex. This value indicates that the method is generating essentially a pure nuclear state (i.e. all nuclear spins populate the same energy level thus resulting in the maximum population difference for that species). This generation of a pure starting state for a system is what makes this complex of interest to research into NMR-based quantum computers.[238] Recent research by Adams *et al.*[239] has shown that the reaction proceeds in a similar manner to that of [Ru(CO)$_3$(dppe)] (which had been previously established in the literature) with photochemical loss of CO from [Ru(CO)$_3$(dpae)] which results in the formation of an unstable [Ru(CO)$_2$(dpae)] intermediate. This unstable intermediate then adds pH$_2$ on the sub-microsecond timescale to form the dihydride product (the overall reaction scheme is given in 6.15).[240,241]

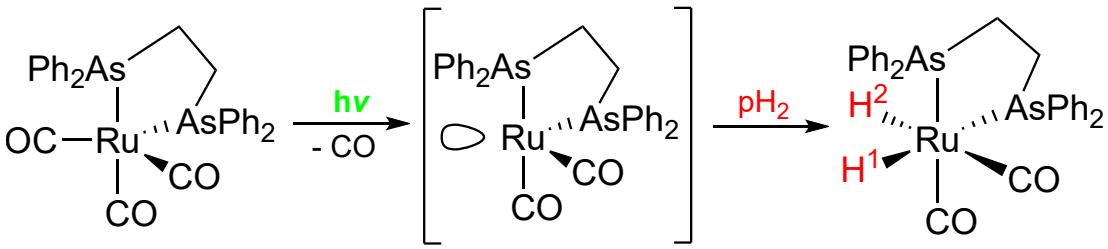

Figure 6.15: Reaction scheme for the photochemical reaction of [Ru(CO)$_3$(dpae)] to form [Ru(H)$_2$(CO)$_2$(dpae)] in the presence of pH$_2$.

Initial spectra were obtained with a 0.2 mg sample of [Ru(CO)$_3$(dpae)] (0.49 mM). The sample was placed under pH$_2$ and then irradiated for 0.5 s prior to detection (the observed spectrum is given in Figure 6.16). Due to the known difficulty of obtaining a thermally-polarised spectrum for this complex (noted by Blazina *et al.*[237]), an enhancement factor for comparison with the high-field study could not be obtained with this sample.

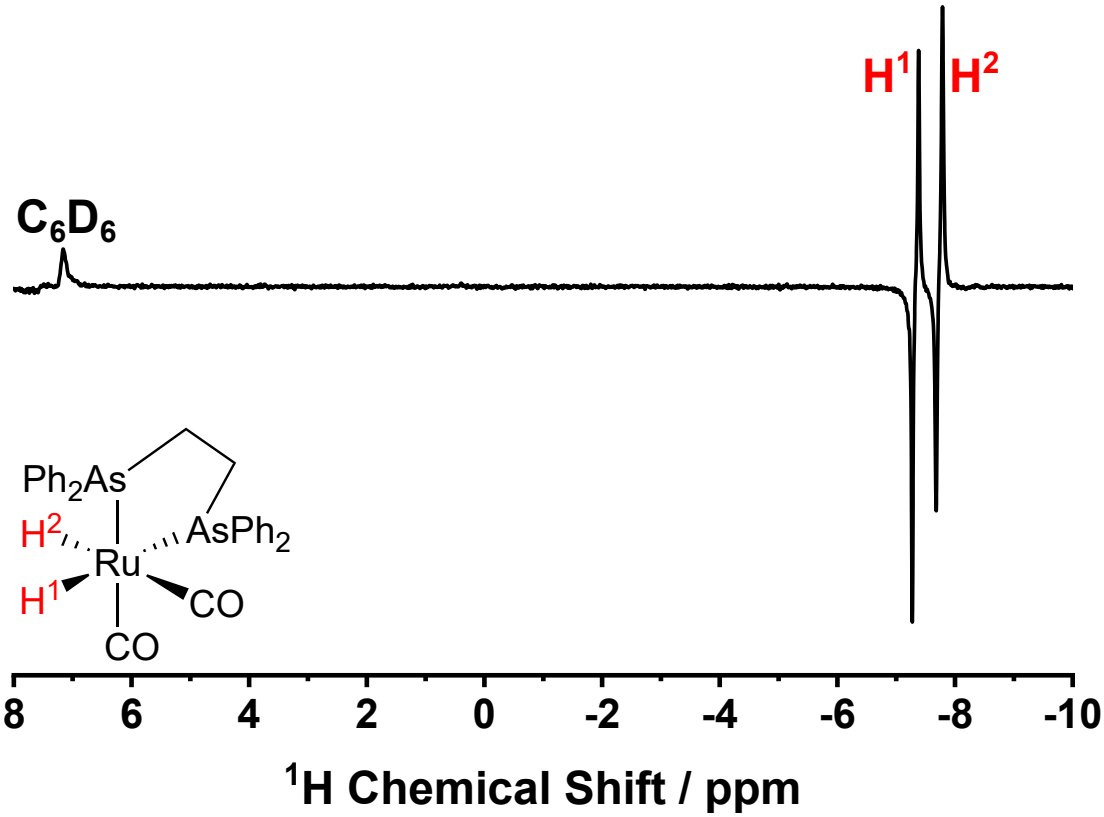

Figure 6.16: Single-scan ^{1}H spectrum of [Ru(H)$_2$(CO)$_2$(dpae)] following the reaction of pH$_2$ with [Ru(CO)$_3$(dpae)] (0.49 mM) upon irradiation of the sample for 0.5 seconds.

The hyperpolarised signals observed for [Ru(H)$_2$(CO)$_2$(dpae)] appear at -7.3 and -7.7 ppm for the hydrides trans to dpae and CO respectively and they share a J_{HH} coupling constant of 4.7 Hz (well-matched to the literature values observed by Adams *et al.*[239]). The average SNR of the 5 repeat measurements was (345 ± 10) which represents a significant increase in SNR relative to the complexes that have been explored thus far. With such a strong signal enhancement, at first glace this complex appears to be an ideal candidate for further optimisation of the *in situ* irradiation setup.

One important factor to consider when selecting a complex to use for optimisation is the rate of pH$_2$ depletion upon repeat irradiation of the sample. A finite concentration of pH$_2$ will be dissolved within the sample at the start of an experiment and upon irradiation a portion of the available pH$_2$ will be consumed. The first potential route to replenish the pH$_2$ in solution is to shake the sample to dissolved fresh pH$_2$ from the NMR tube headspace. Due to poor diffusion across the gas-liquid interface at the surface of the sample, shaking the sample will allow the large excess of pH$_2$ contained within the headspace to be redistributed into the solution. However, a point will be reached where the proportion of oH$_2$ within the

sample is non-negligible and so the observed NMR signal will begin to decline even with shaking of the sample. At this point the pH$_2$ within the sample needs to be replenished by the pH$_2$ generator. Determining the maximum number of shakes that can be performed on a sample before refreshing the pH$_2$ is important as reducing the number of times the pH$_2$ generator is used reduces the overall experiment time and the amount of solvent evaporation that occurs upon degassing the sample (which can change the concentration of the sample as more repeats are performed). As a point of comparison, a literature study on [Ir(H)$_2$(CO)(PPh$_3$)$_2$Cl] (0.7 mM in C_6D_6) performed using through-probe irradiation (Nd:YAG laser, 5 ns pulse) required the sample to be shaken every 4 experiments and showed consistent signal for 16 repeats.[45]

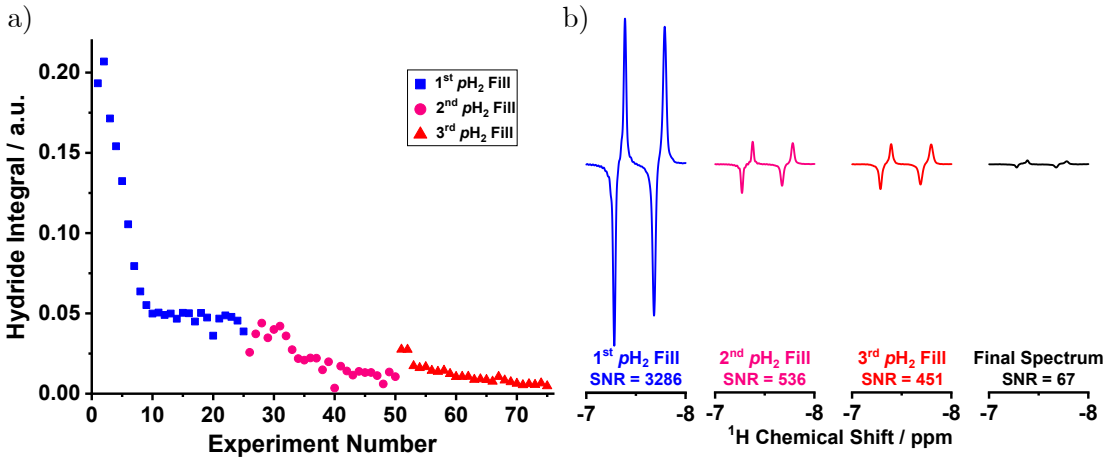

Figure 6.17: Observed decay in hydride integrals for [Ru(H)$_2$(CO)$_2$(dpae)] (2.65 mM) upon irradiation of the sample for 2 seconds. Data for (a) three repeats of the experiment with refreshment of pH$_2$ between and (b) select ^{1}H spectra (1 scan) recorded during the experiment are shown.

To determine this property for [Ru(H)$_2$(CO)$_2$(dpae)], experiments were performed using a 1.1 mg (2.65 mM) sample which was irradiated for 2 seconds and then detected. 25 repeats were performed on the sample and between each repeat the sample was removed from the spectrometer and shaken for 5 seconds. After all repeat measurements were performed, the pH$_2$ within the sample was refreshed and a second series of identical experiments were performed. This process was repeated three times to produce a total of 75 ^{1}H spectra. Using the automated peak picking and integration macros that were designed for thermal reaction monitoring, the hydride integrals for each spectrum were integrated and summed. To examine the NMR signal decay over repeat experiments, the hydride integrals were plotted against experiment number (Figure 6.17a). To provide indication of how the decay of the hydride integrals translates to the appearance of the spectra, the hydride

peaks observed at select times during the experiment are given in Figure 6.17b. These peaks are shown with the exact same scaling factor as to enable comparison between them.

While excellent signal enhancements were observed for the initial spectra (an SNR of 3286) recorded during the experiment, by the third spectrum a significant drop in the observed NMR signal was observed. This drop in signal continued through the first 25 experiments with the decay plateauing at around 1/4 of the original integral value. From this first dataset, it suggests that pH$_2$ might need refreshing after every two irradiation periods to enable consistent integral measurements. This value is significantly lower than that used in the high-field study using [Ir(H)$_2$(CO)(PPh$_3$)$_2$I] but factors such as increased sample concentration, higher irradiation times and irradiation of the entire sample with the *in situ* setup could explain this difference. However, the continued loss of signal upon both refreshments of the pH$_2$ within the sample is problematic as this was an unexpected trend within the experiment. As the signal decay continues between pH$_2$ refreshment stages, this indicates that a secondary feature must be reducing the amount of observable signal that is dependent on the overall irradiation that the sample has experienced.

To investigate the potential cause of the signal decay upon prolonged irradiation of [Ru(CO)$_3$(dpae)], a repeat of the above experiment with a fresh 2.65 mM sample of the complex was performed but with an irradiation period of only 0.5 seconds. The aim of this experiment was to determine if the loss of signal showed a strong dependence on the total amount of time that the sample had been irradiated for as this would be indicative of photodegradation of the sample. The results of this experiment (shown in Figure 6.18) showed a stronger consistency of signal within the first 25 experiments. While slight signal increases are observed upon refreshment of the pH$_2$ in this experiment, ultimately a continual decrease in the hydride signals is observed across the entire dataset. This finding is similar to that seen for the 2 second irradiation period, but the decay occurs at a slower rate (it is only after the third pH$_2$ fill that the signal drops below 1/4 of the starting signal in this instance). Overall, this suggests that the decay of the sample has been somewhat mitigated by using a shorter irradiation period. To confirm that the sample had not undergone photodegradation, a thermally-polarised ^{1}H spectrum (64 scan) of this sample was then recorded at 9.4 T (Figure 6.19). Within the hydride region of this spectrum the only observable signals were those of [Ru(H)$_2$(CO)$_2$(dpae)] and so it is reasonable to assess that the signal decay is not caused by the formation of additional complexes in the sample.

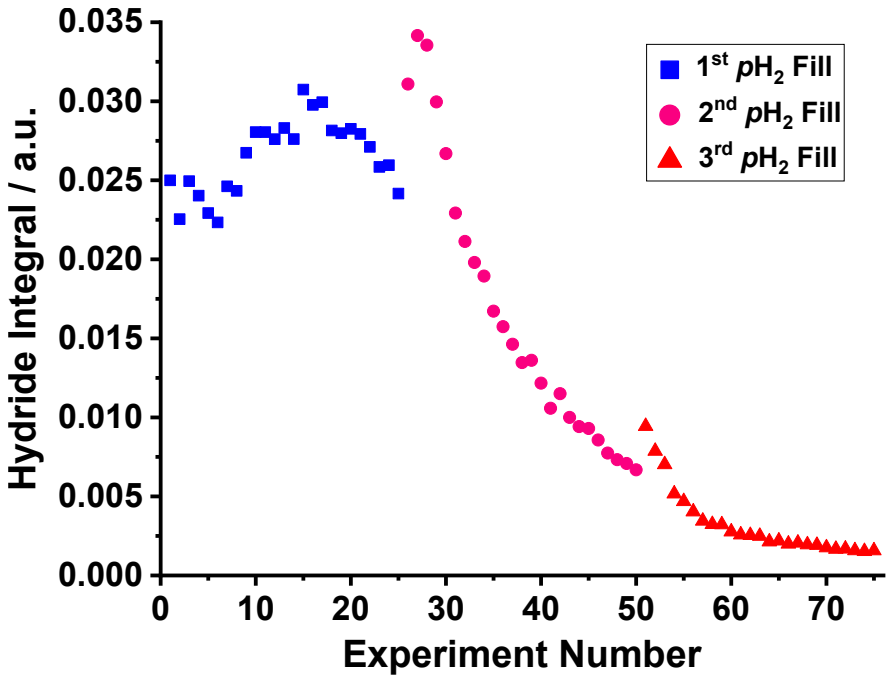

Figure 6.18: Observed decay in hydride integrals for $[Ru(H)_2(CO)_2(dpae)]$ (2.65 mM) upon irradiation of the sample for 0.5 seconds. Data for three repeats of the experiment with refreshment of pH_2 between them is shown.

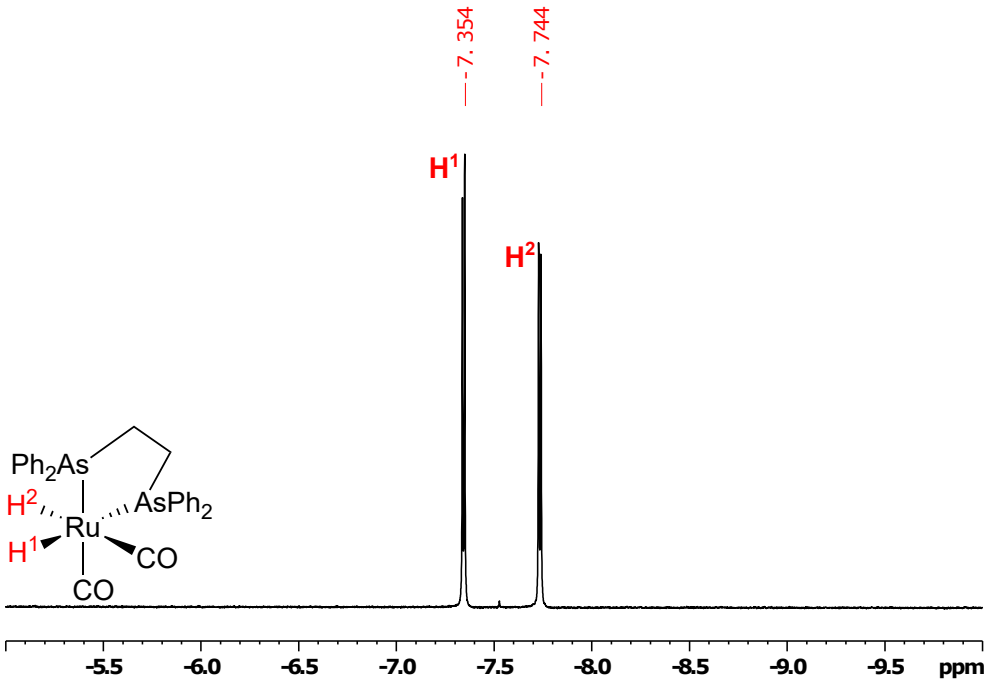

Figure 6.19: Hydride region of a ^1H spectrum (64 scan) of $[Ru(H)_2(CO)_2(dpae)]$(2.65 mM), recorded following irradiation of the sample during the pH_2 refreshment experiments performed at low-field. This spectrum was recorded at 9.4 T (400 MHz).

Using the accumulated evidence that shorter irradiation periods reduce the rate of signal loss and that no photodegradation products were observed, it is likely that the issue within the sample is a fast rate of consumption of the $[Ru(CO)_3(dpae)]$ starting material. As this photochemical reaction is not degenerate, once a molecule of $[Ru(CO)_3(dpae)]$ has reacted with pH_2 to form $[Ru(H)_2(CO)_2(dpae)]$, the product molecule can no longer react via the same mechanism. Future irradiation of $[Ru(H)_2(CO)_2(dpae)]$ will lead to a degenerate reaction via the scheme shown in Figure 6.20. This change of the mechanism via which pH_2 addition occurs to the complex can then result in poorer signal enhancements within the product molecule.

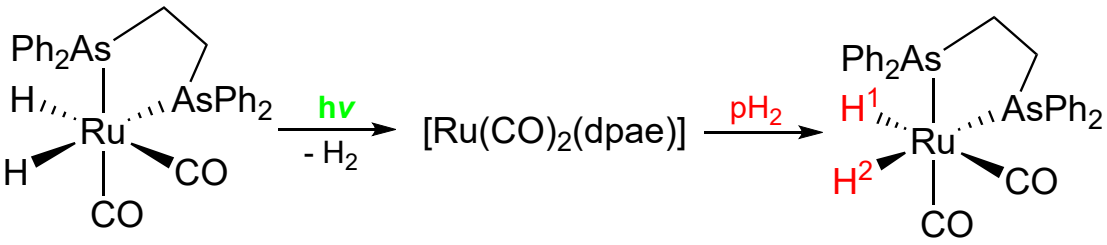

Figure 6.20: Reaction scheme for the photochemically initiated degenerate reaction of $[Ru(H)_2(CO)_2(dpae)]$ with pH_2.

Within the previous high-field studies performed with this complex, the conversion of $[Ru(CO)_3(dpae)]$ to $[Ru(H)_2(CO)_2(dpae)]$ over the course of 1000 laser pulses (each a 12 ns pulse from the XeCl excimer laser) was determined to be only 2.3% and so it was assumed that a near-negligible portion of the sample would be converted during each irradiation period.[237] However, this assumption does not hold true for the experiments performed with the *in situ* irradiation setup. The origin of this faster-than-expected consumption of starting material is likely due to the irradiation occurring across the entirety of the sample when using the *in situ* irradiation setup (rather than just in the NMR detection region as with a through-probe approach) and the requirement for longer irradiation periods when using the broadband UV lamp source. Overall, the rapid decay of the $[Ru(CO)_3(dpae)]$ sample when used in conjunction with the current *in situ* irradiation setup excludes it from being a suitable candidate for optimisation experiments.

6.4.5 Other Ruthenium Complex Studies

The remaining Ruthenium(II) complexes that were tested at low-field (**D** and **E**) did not yield any observable signals using the *in situ* setup. This is an unexpected

result as both of these complexes have been observed at high-field within photochemical pump-NMR probe experiments performed by Torres *et al.*[47] One factor that contributes to the difficulty of detecting these complexes is the presence of phosphorus couplings. As shown in Figure 6.21, each hydride resonance of $[Ru(H)_2(CO)(PPh_3)_3]$ has a complex multiplicity owing to multiple different phosphorus environments present in the complex. Increasing the multiplicity of the NMR signals will reduce the prominence of the peak above the noise and thus the limit of detection for these complexes is increased. As the Spinsolve spectrometer utilised within these experiments does not have a ^{31}P channel, it is not possible to use decoupling pulse sequences in order to simplify the spectra and improve the magnitude of the observed signals.

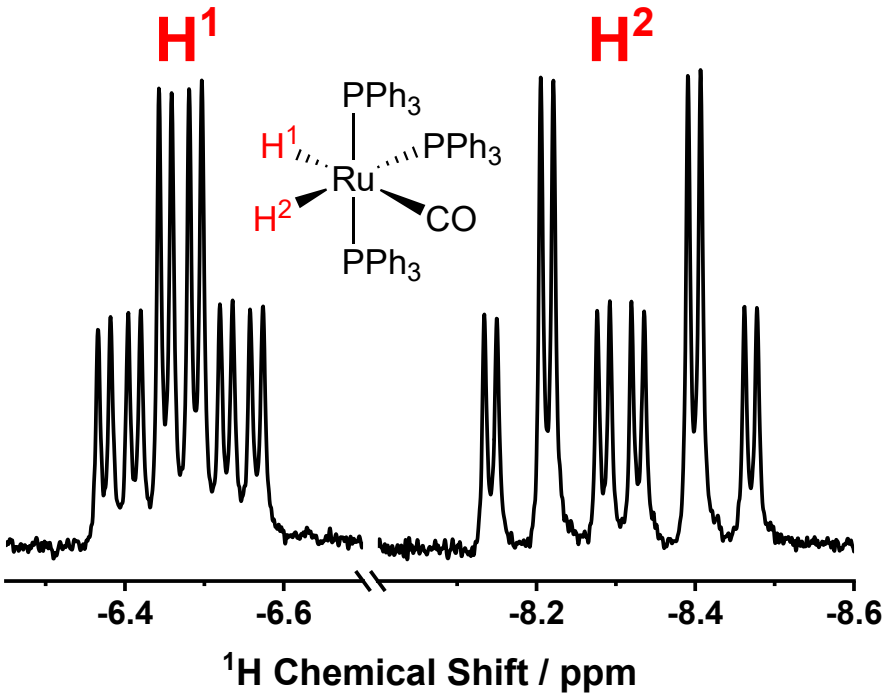

Figure 6.21: Hydride region of ^1H spectra recorded at 9.4 T (400 MHz) highlighting the multiplicity of the peaks for $[Ru(H)_2(CO)(PPh_3)_3]$.

Another contributing factor is the relaxation rate of the hyperpolarised signal. Because the photochemical initiation provides synchronous product formation for these Ruthenium(II) complexes, there will be no continuation of product formation post-irradiation and so the hyperpolarised signals present will begin to decay. For the observed complex $[Ru(H)_2(CO)_2(dpae)]$, the T_1 for the hyperpolarised signal is given in literature as (1630 ± 30) ms whereas the hyperpolarised T_1 for *cis*−$[Ru(H)_2(dppe)_2]$ is significantly lower at (301 ± 27) ms (when measured in C_6D_6 at 298 K).[48] As there is currently no communication between the light source and the NMR spectrometer, the manual initiation of NMR detection will add a

non-negligible delay to spectral acquisition. When combined with these very short T_1 values, this prevents observation of hyperpolarised signals for these fast relaxing complexes within the current *in situ* irradiation methodology.

6.5 Pump-Probe Development and Optimisation

6.5.1 Background Theory

The previous research in this chapter has shown that it is possible to observe photochemically initiated processes on a benchtop NMR system and even follow the chemical evolution for a system at longer timescales. However, many of the photochemical reactions of interest, such as those involving the reaction of Ru(II) complexes with pH$_2$, occur at timescales that are currently inaccessible using the *in situ* irradiation setup described above.

To be able to monitor processes occurring on fast timescales relative to the detection method, time-resolved (TR) pump-probe spectroscopy techniques are commonly utilised (such as flash photolysis for UV-visible spectroscopy).[240] Within these methods, the pump refers to the irradiation period that initiates the chemical process to be observed and the probe refers to the spectroscopic observation. As the whole chemical process cannot be captured within a single experiment, each pump-probe experiment interrogates the evolution of the chemical system at a single point in time. Through variation of the evolution period (τ) between the pump pulse and the probe detection, the entire reaction course can be captured in a series of 1D experiments. This dataset can then be analysed to obtain kinetic parameters about the observed system.

A photochemical pump - NMR probe method for capturing fast processes using NMR spectroscopy was first published in 2014 by Torres *et al.*[47] using a 600 MHz spectrometer. The pulse sequence for this technique (Figure 6.22a) is initiated by a 10 ns laser pulse from a Nd:YAG laser. This is followed by evolution of the system for τ and then the state of the system is captured using a 45° pulse. By repeating this experiment for several evolution delays (n_τ), a pseudo-2D dataset is obtained. Integration of the spectral peaks across this dataset can then be performed to analyse the kinetics of the reaction (Figure 6.22b).

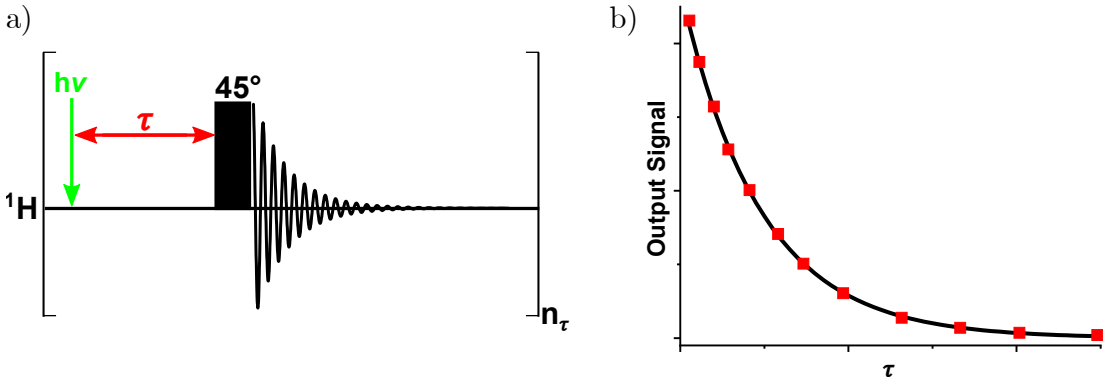

Figure 6.22: Example (a) pulse sequence and (b) data output for a photochemical pump - NMR probe experiment.

6.5.2 Designing the Arduino-Relay Device

To develop a photochemical pump - NMR probe experiment at low-field, the experimental timing limitations need to be addressed. When using the current *in situ* irradiation setup, the user is required to both initiate the irradiation of the sample (using the foot pedal connected to the lamp source) and, once irradiation has finished, initiate spectral acquisition (using the computer running the NMR spectrometer). This introduces a component of user reaction time into the experiment which results in uncertainty in when spectral acquisition is initiated. This inconsistency would have a large impact when performing a pump-probe experiments as the evolution delay (τ) would be poorly defined. This limitation also becomes more pronounced as faster processes are observed as the user reaction time corresponds to a more significant proportion of the overall reaction time. Overall, without solving for this, the applications for a pump-probe experiment at low-field would be limited.

The major difference between the current *in situ* setup at low-field and the literature setup at 600 MHz is the presence of spectrometer-laser communication. At high-field, the NMR pulse sequence controls both the firing of the laser and the NMR detection and so these processes can be synchronised with well-defined τ delays. To replicate this at low-field, a connection must be established between the UV lamp source and the computer running the NMR spectrometer (the red linkage in Figure 6.23a). The shutter within the UV lamp is operated through a simple electronic switch which is controlled via the manually operated foot pedal (when pressed the electronic circuit within the lamp is complete, opening the shutter). Replacing the foot pedal with a fully automated switch was achieved through development of a shutter controller that can parse commands between the computer

and the auxiliary port of the lamp source.

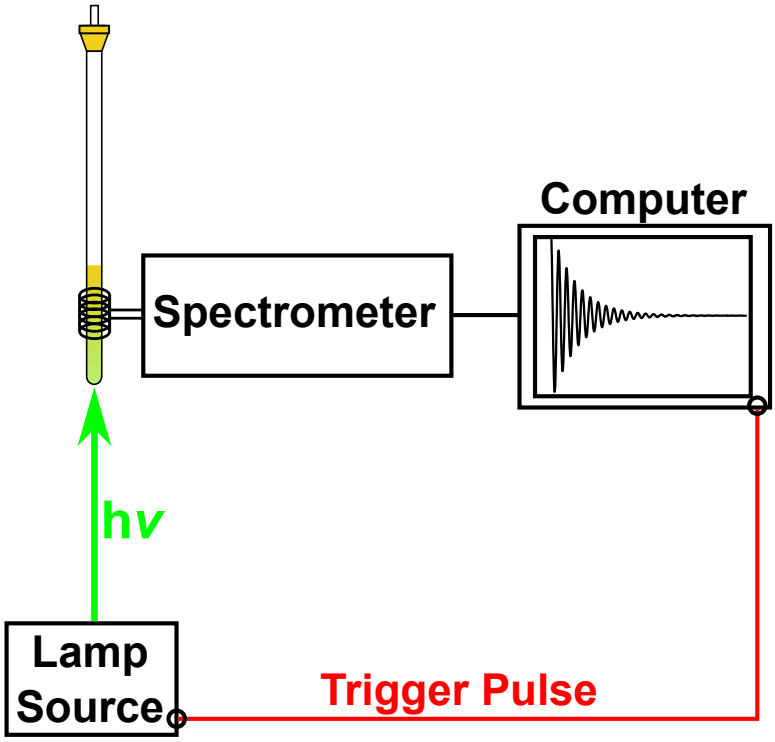

Figure 6.23: Schematic of the *in situ* irradiation setup on the benchtop NMR spectrometer. Highlighted in red is the missing communication between the computer running the spectrometer and the UV lamp source.

The shutter controller consists of two components: a microcontroller (Arduino Nano) and a mechanical SPDT (Single Pole Double Throw) relay module (shown in Figure 6.24a). The microcontroller is connected to the computer through a USB cable allowing for commands to be sent to the Arduino through the virtual serial port. The relay replaces the foot pedal attachment for the lamp source and is connected using a $\frac{1}{4}$ inch jack into the auxiliary port.

To aid with explanation of how the shutter controller works, a circuit diagram is provided as Figure 6.24b. The controller consists of two main circuits, one between the Arduino and the relay (**1**) and the other between the relay and the UV lamp (**2**). These two circuits are isolated from one another allowing the 3.3 V control signal from the Arduino to be able to safely switch a signal up to 240 V. Without a serial input, both circuits are open meaning that the shutter remains closed.

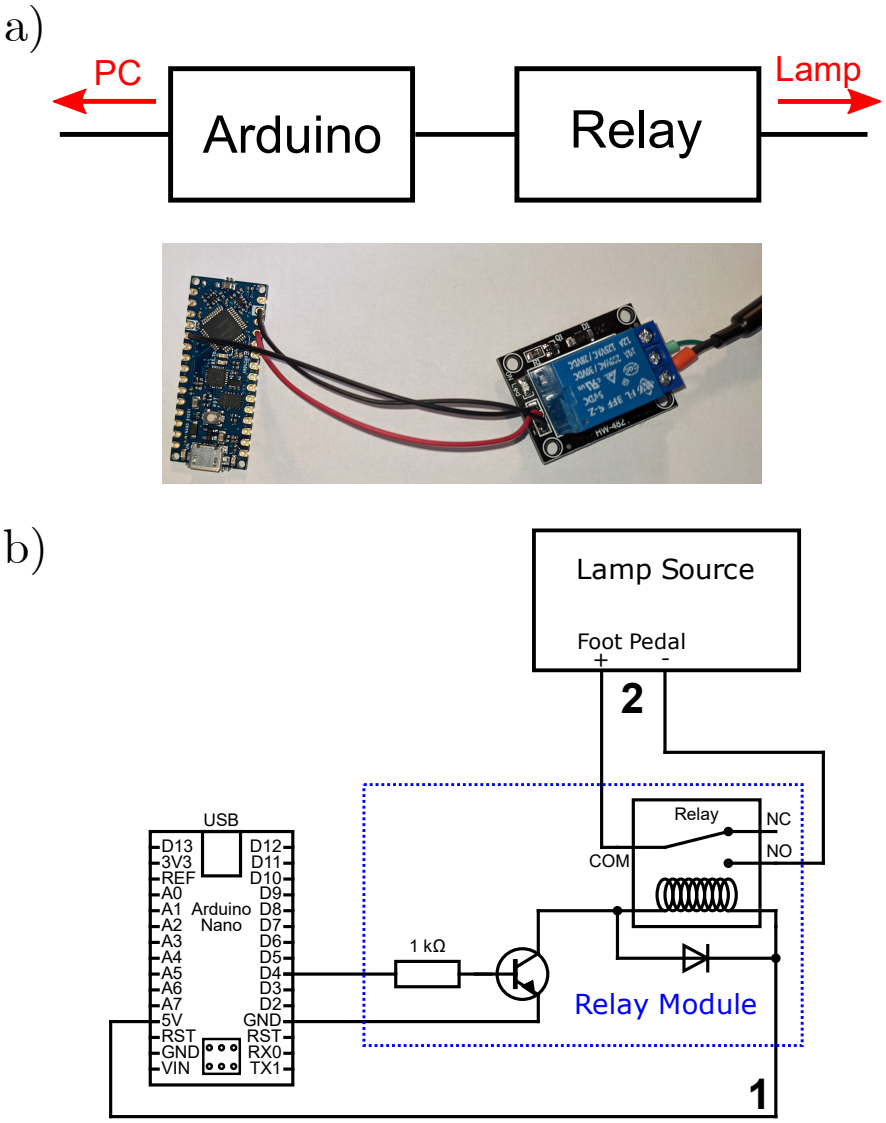

Figure 6.24: (a) Diagram and picture of the Arduino-relay for automated shutter control in the *in situ* irradiation setup with a (b) circuit diagram of the system shown below.

When a serial command is read, the output of the digital pin on the Arduino is written high and provides a voltage to the transistor gate within circuit **1**. This transistor allows current to flow from the 5V rail to ground energising the coil. The electromagnetic field from the coil switches the reed's position in circuit **2** from normally closed (NC) to normally open (NO) completing circuit **2** and causing the shutter on the lamp to open. A secondary serial command can then write the output of the digital pin to low which will de-energise the coil and return circuit **2** to NC, closing the shutter. Typical response times for a relay switch are approximately 50 milliseconds, providing much faster and more consistent shutter operation.

6.5.3 Designing the Arduino Code

In order for the Arduino microcontroller to precisely control the shutter on the UV lamp, the unit must be programmed. Code for the Arduino is written in the C++ programming language and then is uploaded onto the microcontroller. Unlike code for a pulse sequence which runs once, code uploaded to an Arduino is continuously running and so must be programmed with a looping set of functions. The code written for operation of the shutter is described below. For reference, the full code written for the Arduino is given in Appendix C.

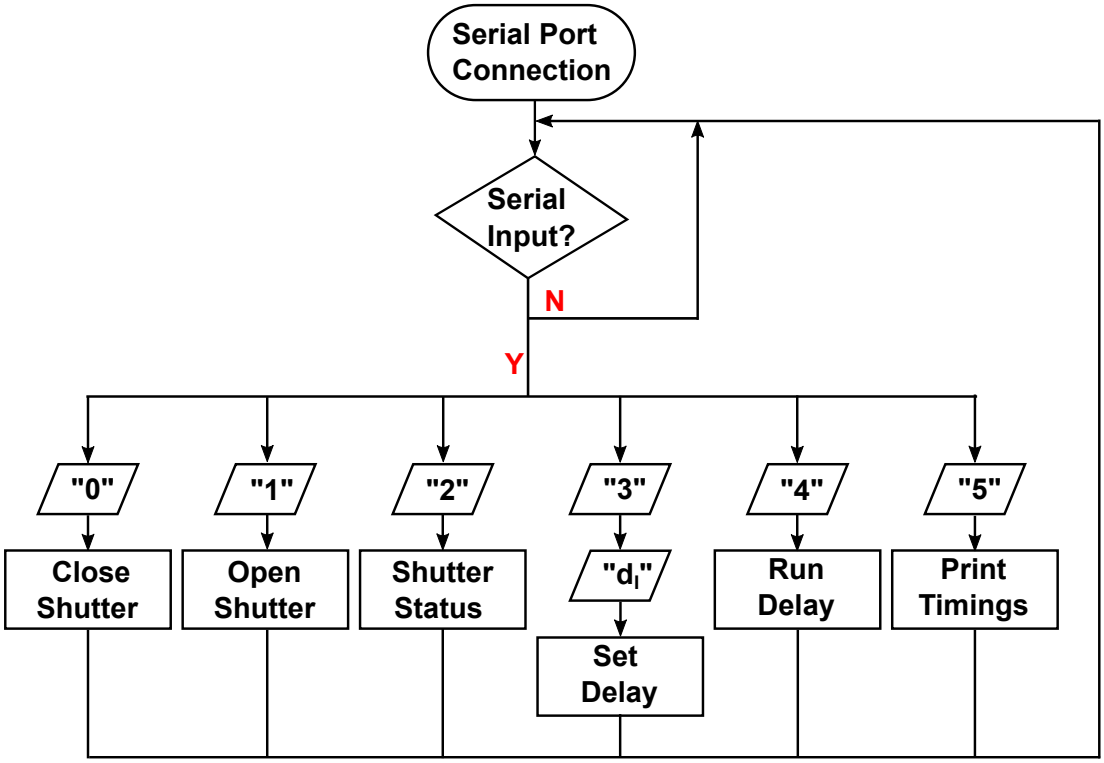

Figure 6.25: Flow diagram representation of the Arduino code required to run pump-probe experiments.

The main function of the code is to determine when the digital pin connected to the relay needs to be written high (to open the shutter) or low (to close the shutter). To do this the Arduino is required to parse serial commands through a USB connection to the spectrometer computer. The first step required for this is a single-time initialisation step in which a serial connection is established between the Arduino and computer. Following this, the Arduino enters a holding loop where it will wait until a serial input is identified. Once a serial input is present, the Arduino enters a switch statement. In a switch statement, the value of the serial input is read and then compared to a number of different expected input values

(referred to as cases). If the serial input matches one of the case values then all commands within that case are executed. The Arduino will then return to the holding loop until a new serial input to evaluate is present. A flow diagram describing this code is given as Figure 6.25.

As seen in Figure 6.25, there are six different cases programmed into the Arduino. The first two cases, "0" and "1", correspond to writing the digital pin to low and high respectively. Case "2" sends a statement from the Arduino to the computer to tell the user the current status of the shutter. Cases "3" allows the user to input a set irradiation period (labelled d_I) and then case "4" will automatically open and close the shutter using the d_I delay. Finally, case "5" will print the time between opening and closing the shutter to allow the user to check that d_I was set correctly. Using these six cases, it is now possible to use serial port communication to operate the UV lamp shutter.

On the topic of safety, an internal timer has been set up within the Arduino code that starts when the shutter is opened and only resets once the shutter has been closed. If the internal timer reaches 30 seconds, the digital pin will instantly be written to low to ensure that the shutter on the lamp is never open for longer than 30 s.

6.5.4 Designing the NMR Experiment Code

With the Arduino now accepting serial port communication, new code needed to be written within the Spinsolve NMR experiments so that commands could be sent to the Arduino at specific times during an experiment. The code developed for this purpose can be split into two sections: general procedures and experiment commands. The code written for the Spinsolve (in Prospa, the coding language of the Spinsolve) is given in Appendix D with annotations for readability.

In terms of general procedures, five different procedures were written to handle general communication with the Arduino: "Initialise Arduino", "Close Arduino", "Write to Arduino", "Send to Arduino" and "Reply to Arduino". The "Initialise Arduino" and "Close Arduino" procedures are required to initiate and cease Arduino communication at the start and end of the NMR experiment respectively. "Write to Arduino" allows for the switch command inputs (0 - 5) to be sent to the Arduino. "Send to Arduino" enables the user to write two values to the Arduino in quick

succession, this is required for case "3" where the value of d_1 needs to be set. Finally, "Reply to Arduino" is used for cases where the Arduino sends a value back through the serial connection (such as shutter status in case "2" or timings in case "5").

These building blocks enable an NMR experiment to be written with the required Arduino interactions. The standard progression for an NMR experiment is given in Figure 6.26a. Going forward, the phrase "pulse sequence" will only refer to the stage of the NMR experiment during which the spectrometer is active. All other stages shown in Figure 6.26a are localised on the computer. Highlighted in red on the figure are the additional steps required to perform a pump-probe experiment using the *in situ* irradiation setup.

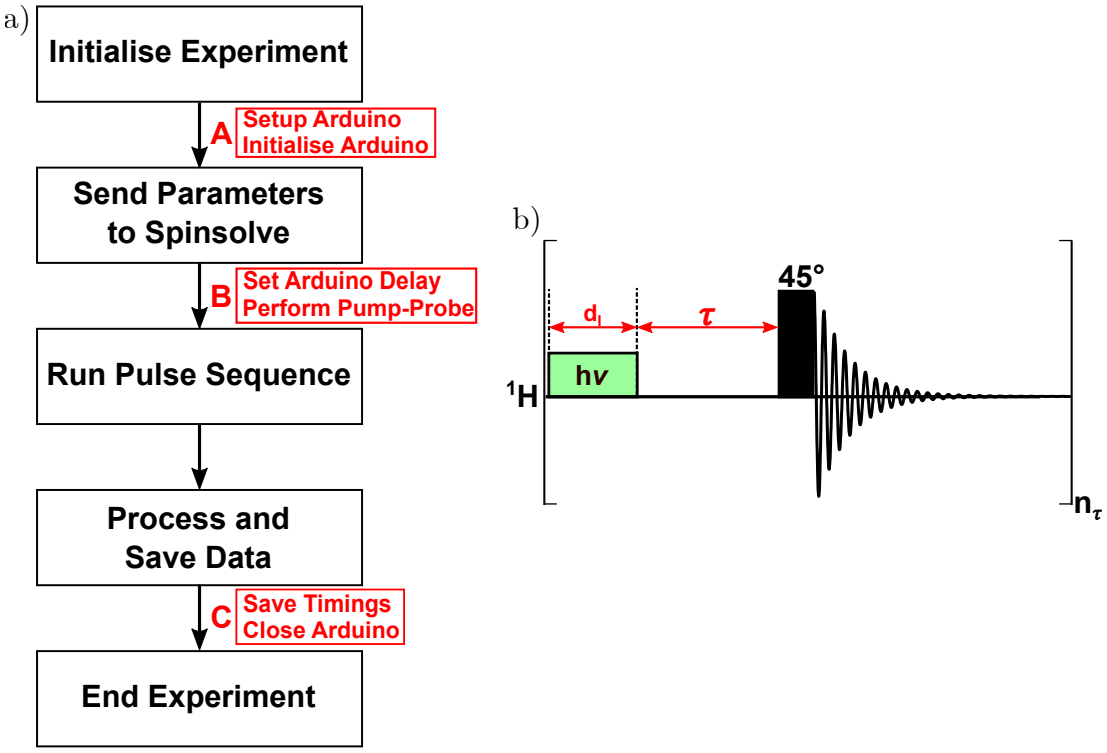

Figure 6.26: (a) Outline of an NMR experiment on the Spinsolve spectrometer alongside (b) a modified pump-probe pulse sequence that accounts for irradiation time.

Three additional blocks of code must be added to an NMR experiment in order for it to be converted into a pump-probe experiment. The first block (**A**) is placed at the start of the experiment and is required to setup the computer-Arduino communications. Within this block the parameters required to use the "Initialise Arduino" command are stated (such as the serial port, baudrate and parity being used) and then the command is run.

The second block (**B**) is placed directly before the pulse sequence is run and is essential to performing a pump-probe experiment. Within this block, the d_I parameter is sent to the Arduino (using the "Send to Arduino" procedure) and then irradiation is performed (using the "Write to Arduino" procedure with an input value of "4"). Following the "Write to Arduino" command, two delay periods are observed. The first delay has a length of d_I to ensure that the irradiation period is observed on the computer. This is required because unlike with laser initiation, the pump pulse is on a similar timescale to the NMR experiment. The second delay has a length of τ, allowing for a specific probe delay to be observed before the pulse sequence is run. This step of the experiment is shown in Figure 6.26b.

The final block (**C**) is placed just before the end of the NMR experiment. This block is required to save the important experimental timings (including delays from the Arduino which can be obtained using the "Reply to Arduino" procedure) and close the Arduino communication.

With communication between the Arduino and computer being established and with pump-probe procedures being developed for NMR experiments, it is now possible to perform time-resolved NMR experiments without user interaction.

6.6 Pump-Probe Optimisation on [Ru(H)$_2$(dppe)$_2$]

6.6.1 Observation of *cis*−[Ru(H)$_2$(dppe)$_2$]

With the development of computer-lamp communication, it is now possible to address the time resolution issue that was established within Section 6.4. Automation of the pump pulse now enables the use of irradiation times down to 10 ms (a limit set by the speed of the mechanical shutter) and probe delays down to the millisecond timescale. As a result of this, the short-lived hyperpolarisation for *cis*−[Ru(H)$_2$(dppe)$_2$] could potentially be observed. The degenerate reaction of *cis*−[Ru(H)$_2$(dppe)$_2$] following photochemical loss of H_2 is given in Figure 6.27.

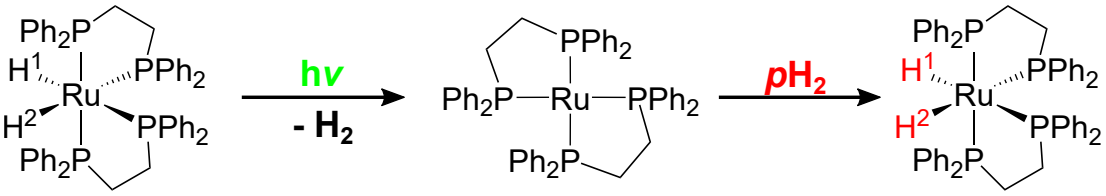

Figure 6.27: Reaction scheme for the degenerate photochemical reaction of *cis*−[Ru(H)$_2$(dppe)$_2$] when placed under a *p*H$_2$ atmosphere.

cis−[Ru(H)$_2$(dppe)$_2$] is a unique system compared to those previously examined as both hydrides within the complex are chemically-equivalent. This complex is still able to perform PHIP experiments as the hydrides are magnetically inequivalent, each hydride will couple to the equatorial ^{31}P atoms to a different extent through a *trans* or *cis* coupling (where $J_{HP(trans)} > J_{HP(cis)}$). This coupling system is referred to as AA'XX'Y$_2$ (where A/A' are H atoms, X/X' are equatorial P atoms and Y are axial P atoms).

When a thermally polarised spectrum of *cis*−[Ru(H)$_2$(dppe)$_2$] is recorded, such as that in Figure 6.28a, a complex second-order multiplet is observed at -8.3 ppm. The multiplet observed is made up of 36 components (though resolution limitations mean that not all components are visible). The predominant feature of this spectrum is a pseudo doublet with a 53 Hz coupling constant. Previous literature studies have attributed this splitting to $|J_{HP(trans)} + J_{HP(cis)}|$ where $J_{HP(trans)} = \pm 68$ Hz and $J_{HP(cis)} = \mp 15$ Hz.[47,242]

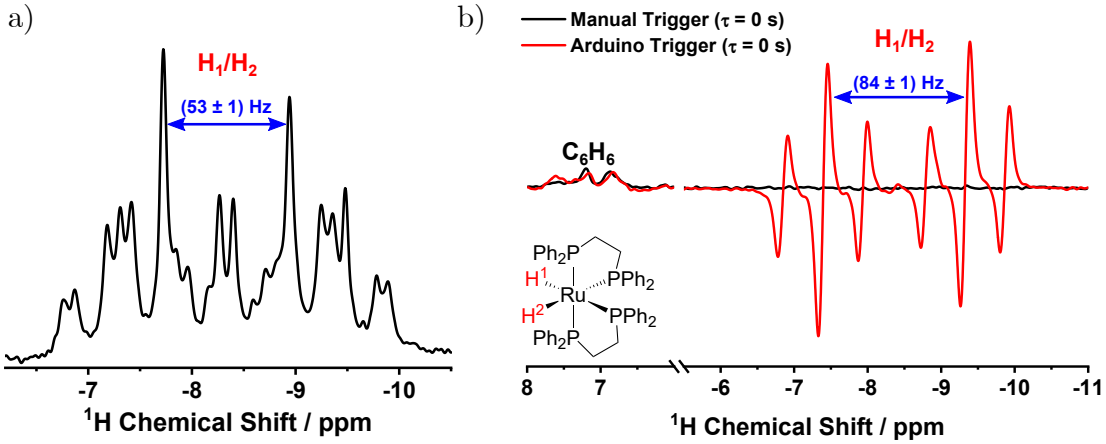

Figure 6.28: (a) Thermal 16384-scan and (b) hyperpolarised 1-scan spectra of *cis*−[Ru(H)$_2$(dppe)$_2$] (2.59 mM) recorded at 1 T. For the hyperpolarised spectra, a 0.5 s irradiation period was used with both the manual and automated *in situ* irradiation setup.

To determine if *cis*−[Ru(H)$_2$(dppe)$_2$] hyperpolarised signal was observable with

the new pump-probe approach, a 1.4 mg sample (2.59 mM) of *cis*−[Ru(H)$_2$(dppe)$_2$] was irradiated under fresh pH$_2$ for 0.5 s using both the manual and automated variants of the *in situ* irradiation experiment. In both cases the NMR spectrum was recorded as soon as the irradiation period ends (τ = 0 s). The result of this experiment, shown in Figure 6.28b, clearly highlights the advantage of using the automated NMR experiment as strongly enhanced NMR signals are now observable for this species. From these experiments, it can be rationalised that even with no evolution delay prior to acquisition, the user within the manual irradiation experiments adds a non-negligible interaction delay. By replacing the user with a shutter control device, hyperpolarised species with sub-second relaxation times can now be observed.

In terms of the spectral appearance, the PHIP hyperpolarised spectrum of *cis*−[Ru(H)$_2$(dppe)$_2$] simplifies to a doublet of triplets of doublets (as shown in Figure 6.28b). This spectral appearance change is due to only certain energy levels of the spin system being overpopulated and so only a select few transitions are enhanced. Within this system, the dominant doublet splitting has a value of 83 Hz. The origin of this splitting is $|J_{HP_{(trans)}} - J_{HP_{(cis)}}|$.[47]

With an SNR of 273, the enhancements observed with this complex are very promising and well above the spectral noise. Unlike the iridium systems previously studied, the oxidative addition reaction occurs on a much faster timescale than the NMR experiment as it has been measured to occur on the microsecond timescales (based on time-resolved absorption spectroscopy study performed by Cronin *et al.*[240]). This difference is beneficial as it means that changes in the observed signal are purely from the relaxation of the hyperpolarised state of *cis*−[Ru(H)$_2$(dppe)$_2$] and not from a competing chemical reaction producing additional hyperpolarised species (as the reaction has reached completion prior to NMR observation).

6.6.2 Optimisation using *cis*−[Ru(H)$_2$(dppe)$_2$]

With signal from *cis*−[Ru(H)$_2$(dppe)$_2$] now being observable, it was possible to optimise the *in situ* irradiation experiment with respect to this chemical system. The first stage of this was to determine an appropriate irradiation time for the system and to determine the reproducibility of the signal upon repeat irradiation (as to ensure continual signal decay isn't observed such as with [Ru(H)$_2$(CO)$_2$(dpae)]). For both these studies, the same 2.59 mM sample of *cis*−[Ru(H)$_2$(dppe)$_2$] was used.

To optimise irradiation time, *in situ* irradiation experiments were performed for irradiation times between 0.1 and 10 seconds. Compared to previous irradiation studies, much shorter times could be tested due to all experimental timings being controlled centrally within the NMR experiment. For each irradiation time, three repeats were performed with pH$_2$ bring refreshed between each experiment. The results of this experiment are given in Figure 6.29a. From this experiment, the observed NMR signal increased with increasing irradiation times up to 2 seconds. This trend is similar to that seen previously with longer irradiation periods enabling a bulk of unreacted intermediate species to build up in solution. One difference to previous studies is that optimal irradiation period is shorter than those previously observed (such as 15 seconds for [Ir(H)$_2$(CO)(PPh$_3$)$_2$Cl]) which reflects the greater efficiency of the photochemical reductive elimination step for Ruthenium(II) complexes. Then the following decrease in signal with longer irradiation periods also matches that seen previously with the likely source being an over consumption of pH$_2$ within the solution leading to lower levels of hyperpolarisation.

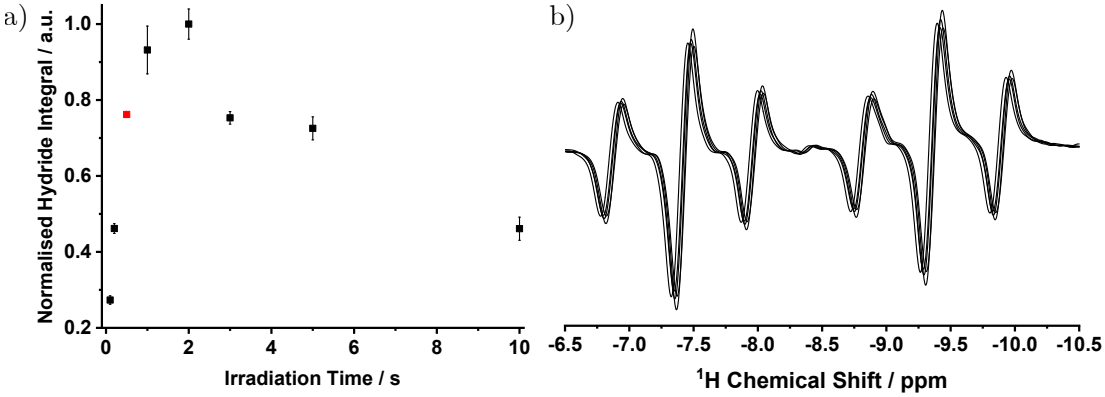

Figure 6.29: (a) Irradiation time dependence of *cis*−[Ru(H)$_2$(dppe)$_2$] (2.59 mM) hydride integrals alongside (b) 5 repeat ^{1}H spectra collected following 0.5 s irradiation periods.

Considering the previous temperature study performed using the *in situ* irradiation setup (Table 6.4), shorter irradiation periods are preferable to ensure that minimal heating occurs during irradiation. Therefore, a compromise value of 0.5 seconds was selected for future experiments as this allows for strong hyperpolarised signals to be obtained (highlighted in red within Figure 6.29a). These initial experiments using *cis*−[Ru(H)$_2$(dppe)$_2$] also highlighted a strong reproducibility of signal between NMR experiments with pH$_2$ refreshment (shown by the 5 repeats in Figure 6.29b). Subsequent experiments on a 400 MHz spectrometer did not show any additional peaks within the NMR spectrum, confirming that repeat irradiation does not lead to substantial degradation of *cis*−[Ru(H)$_2$(dppe)$_2$] making this an ideal system to test variable delay pump-probe experiments with.

Before performing a variable delay pump-probe experiment, a further set of experiments were performed to determine the frequency with which pH$_2$ must be refreshed within the NMR tube (as discussed previously with $[Ru(H)_2(CO)_2(dpae)]$ in Section 6.4.4). For reference, for pump-probe experiments performed with *cis*$-[Ru(H)_2(dppe)_2]$ using the 600 MHz spectrometer, the sample is filled with pH$_2$ once and is then shaken after 4 irradiation periods to replenish the pH$_2$ in solution.[47]

The first series of experiments focused on signal reproducibility upon repeat irradiation with no change made to the sample (no addition of fresh pH$_2$ or shaking of the sample). The sample was irradiated for a series of 15 steps and then pH$_2$ was refreshed. This was repeated three times and the hydride integrals for each step were averaged and normalised (Figure 6.30a). From these experiments, it was clear that the observed signal dropped substantially upon continued irradiation of the sample. This is because through-bore irradiation results in the entire sample being irradiated and as such the pH$_2$ within the solution is rapidly depleted. The reason why 4 repeats could be performed with the 600 MHz spectrometer is due to through-probe irradiation. This approach selectively irradiates the NMR active region and as such the concentration of dissolved pH$_2$ falls less rapidly with each irradiation and so diffusion within the sample can replace the consumed pH$_2$.

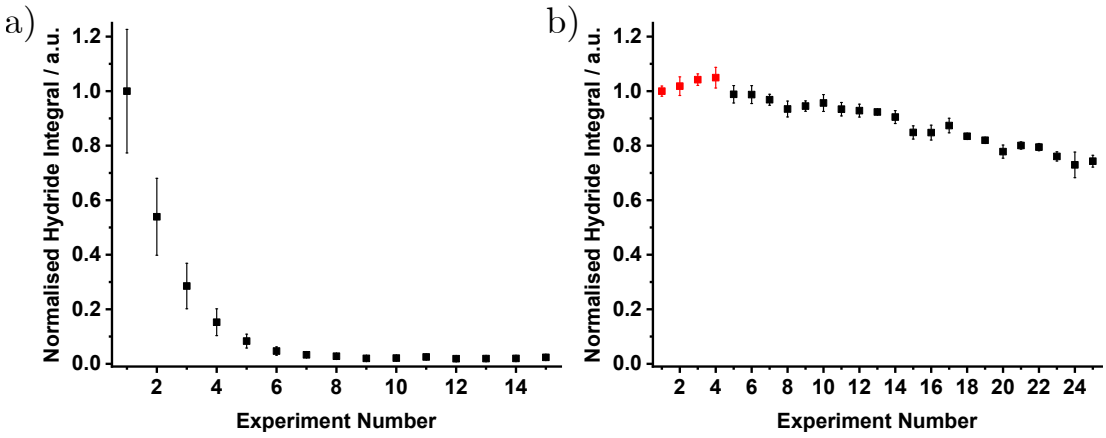

Figure 6.30: Reproducibility of *cis*$-[Ru(H)_2(dppe)_2]$ hydride peak integrals upon repeat 0.5 s irradiation periods (a) without and (b) with shaking of the sample. The data shown is the average of three repeat studies.

The second series of experiments focused on signal reproducibility if the sample is shaken between irradiation periods. These experiments were performed identically to above but with 25 steps rather than 15 and the results are shown in Figure 6.30b. From these experiments, the signal was seen to fall at a much slower rate than without sample shaking. This is because a large excess of pH$_2$ is present in the NMR tube

headspace but the gas-liquid interface has a very small surface area. By shaking the sample, dissolution of pH$_2$ is promoted and as such the ratio of pH$_2$ to oH$_2$ in the solution can be equilibrated to the ratio within the entire NMR tube. This will still lead to loss of signal upon several repeat irradiation periods (as [oH$_2$] increases becomes non-negligible). From this experiment, it was rationalised that 4 experiments could be performed before the pH$_2$ within the sample should be replaced. This value was a compromise between an acceptable level of deviation in hydride integral (<5%) and a value that was a multiple of 4 (for easy sub-division of pump-probe experiment steps).

6.6.3 Pump-Probe Observation of *cis*−[Ru(H)$_2$(dppe)$_2$]

With an appropriate irradiation time (0.5 s) and pH$_2$ replenishment period (every 4 sample shakes) being established, a variable delay pump-probe experiment could be performed on *cis*−[Ru(H)$_2$(dppe)$_2$] .

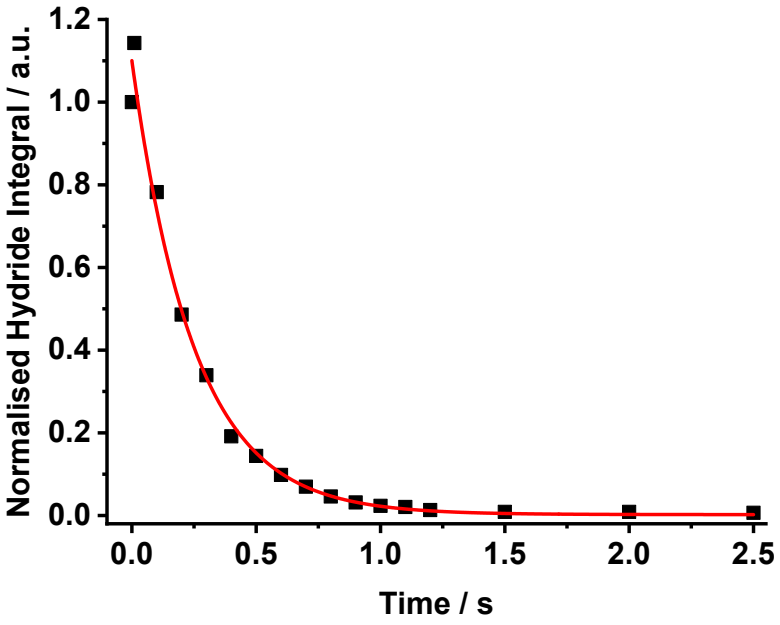

Figure 6.31: Pump-probe experiment showing the hyperpolarised signal decay for *cis*−[Ru(H)$_2$(dppe)$_2$] (2.59 mM). Performed with 17 steps and τ delays between 0 and 2.5 s.

To perform the experiment, the pump-probe pulse sequence shown in Figure 6.26b, was used with 17 steps (n_τ = 17) and τ delays from 0 to 2.5 s. From this pseudo-2D dataset, hydride peak integration was performed to give the decay curve shown in Figure 6.31.

From Figure 6.31, a decay in hydride integral is observed for *cis*−[Ru(H)$_2$(dppe)$_2$] due to the relaxation of the hyperpolarised species. To extract a hyperpolarised T_1 relaxation time for *cis*−[Ru(H)$_2$(dppe)$_2$], an exponential decay was fitted to this dataset to give a T_1 relaxation time of (250 ± 20) ms. Within this exponential decay, the hydride integral drops to <5% of the original value within 0.8 seconds. This fast rate of relaxation validates the previous discussion that the fast relaxing nature of *cis*−[Ru(H)$_2$(dppe)$_2$] was responsible for the lack of signal when performing the irradiation step manually. As user reaction times are on a similar timescale to this decay, it is likely that the majority of the signal for the hyperpolarised complex had relaxed prior to NMR observation within that setup.

From the literature, a similar hyperpolarised relaxation time for *cis*−[Ru(H)$_2$(dppe)$_2$] in C_6D_6 under *p*H_2 (4 bar absolute) was given as (301 ± 27) ms.[48] As T_1 values carry both temperature and B_0 field dependence, the value obtained is not directly comparable to this literature value which was recorded at 295 K and 600 MHz.[80] However, the values would still be expected to be of the same order of magnitude and so this comparison does provide validation for the observed T_1 value.

Overall in the current iteration, this pump-probe approach operates successfully and is able to provide general qualitative and quantitative information about a chemical system. For example, it provided evidence to support the short lifetime of the *cis*−[Ru(H)$_2$(dppe)$_2$] hyperpolarised species as to explain why no hydride signal was observed with manual irradiation. However, one issue that still has not been addressed is the potential for sample heating during irradiation which prevents temperature stabilisation during irradiation. As a result, quantitative reaction monitoring applications for this current *in situ* setup are limited as the lack of temperature stabilisation limits the accuracy to which kinetic parameters can be obtained.

6.7 Pump-Probe Application: Magnetic Coherence Evolution

6.7.1 Background Theory

A potential alternative application of the low-field pump-probe experiment is to explore the magnetic evolution of a PHIP enhanced system during pH$_2$ addition. High-field (600 MHz) laser pump - NMR probe research conducted by Torres *et al.*[47] showed that on the micro-to-millisecond timescale following pH$_2$ addition, a sinusoidal oscillation in hydride integral peaks was observed that could not be rationalised by either continued product formation or relaxation of the hyperpolarised species. From this research, it was established that these short-lived oscillations occur with a frequency that is dependent of the symmetry breaking feature during pH$_2$ addition (either chemical inequivalence, $\Delta\nu$, or magnetic inequivalence, ΔJ). Observing this phenomenon at low-field provides a route for comparison with the high-field setup. In addition, the need for evolution delays (τ) with micro-to-millisecond precision will test the time resolution of the *in situ* irradiation setup on the benchtop NMR spectrometer.

To observe magnetic coherence evolution at low-field, the origin of the effect must first be understood. Within Section 2.2, the starting density operator for singlet state pH$_2$ was established as in Equation 6.2. From this starting state, it was rationalised that this density operator would evolve over the course of the pH$_2$ addition reaction according to Equation 6.3 for an AX-type spin system.

$$\hat{\rho}_{pH_2} = \frac{1}{2}(2\hat{I}_{1z}\hat{I}_{2z}) + ZQ_x \tag{6.2}$$

$$\overline{\rho} = \frac{1}{2}2\hat{I}_{1z}\hat{I}_{2z} + \frac{1}{\xi^2+1}ZQ_x + \frac{\xi}{(\xi^2+1)}\frac{1}{2}(\hat{I}_{1z} - \hat{I}_{2z}) \tag{6.3}$$

However, Equation 6.3 was derived under the assumption that the hydrogenation reaction occurs on a relatively slow timescale and so evolution due to chemical shift or scalar coupling would be time-averaged to zero. While this assumption holds

when probing the system after a long evolution period (the second timescale), it breaks down when the system is probed at shorter micro-to-millisecond timescales. Without this assumption, terms that feature oscillations due to chemical shift or scalar coupling must now be considered and so the behaviour of the system at short timescales is different to that previously established. In order to explain how this results in observable magnetic evolution, it is necessary to reconsider the impact of the previously established free evolution Hamiltonian (Equation 6.4) on the initial $\hat{\rho}_{pH_2}$ density operator. This Hamiltonian was previously simplified in Section 2.2 to Equation 6.5, as to only show terms that do not commute with the pH$_2$ starting state. From this point, a further simplification can be made due to the reaction occurring under PASADENA conditions as this places the system into a weak coupling regime ($\delta\nu_{12} \gg J_{12}$) and so the non-secular part of the J coupling interaction (highlighted in red) can be neglected. Overall, this means that evolution of the system will only occur based on the difference in Larmor frequency between the nuclei ($\delta\omega = \omega_1 - \omega_2$).

$$\hat{H}_{free} = -\omega_1 \hat{I}_{1z} - \omega_2 \hat{I}_{2z} + \pi J_{12}(2\hat{I}_{1z}\hat{I}_{2z} + 2\hat{I}_{1x}\hat{I}_{2x} + 2\hat{I}_{1y}\hat{I}_{2y}) \tag{6.4}$$

$$\hat{H}_1 = -\frac{1}{2}\delta\omega(\hat{I}_{1z} - \hat{I}_{2z}) + \pi J_{12}(2\hat{I}_{1x}\hat{I}_{2x} + 2\hat{I}_{1y}\hat{I}_{2y}) \tag{6.5}$$

Evolution of the starting density operator by this Hamiltonian results in the formation of the spin states shown in Equation 6.6. Within this equation, there is an unchanged longitudinal 2-spin order term ($2\hat{I}_{1z}\hat{I}_{2z}$) and an oscillation between ZQ$_x$ and ZQ$_y$ at the frequency of the chemical shift difference in the AX spin system, which is highlighted in blue (where ZQ$_y$ is defined as $\frac{1}{2}(2\hat{I}_{1y}\hat{I}_{2x} - 2\hat{I}_{1x}\hat{I}_{2y})$).

$$\frac{1}{2}(2\hat{I}_{1z}\hat{I}_{2z}) + ZQ_x \xrightarrow{\frac{1}{2}\delta\omega(\hat{I}_{1z}-\hat{I}_{2z})\tau} \frac{1}{2}(2\hat{I}_{1z}\hat{I}_{2z}) + ZQ_x\cos(\delta\omega\tau) + ZQ_y\sin(\delta\omega\tau) \tag{6.6}$$

Each of these terms become observable upon application of an RF pulse in the y-direction ($\theta(\hat{I}_{1y} + \hat{I}_{2y})$). The density operators following the RF pulse for each term are given in Equations 6.7 - 6.9. Within each equation, only the terms that lead to observable NMR signal have been included to aid with clarity. A complete derivation of the effect of an RF pulse on each state, including any unobservable terms that are

generated, has been summarised Halse *et al.* within previously published literature.[48] In all cases antiphase single-quantum terms are formed (one spin along the z-direction, while the other is within the x-y plane) and so the observed NMR signal will be antiphase relative to the coupling between the two nuclei. Importantly, the terms originating from ZQ_x and ZQ_y retain their chemical shift difference dependence (in blue) and so the precession of the spins around B_0 will be modulated by this additional term. As a result of this, the observed signal from these product states will oscillate at a frequency of $\delta\omega$ during the pump-probe delay. A different RF pulse angle dependence is also observed between the $(2\hat{I}_{1z}\hat{I}_{2z})$ / ZQ_x terms and the ZQ_y terms (highlighted in red). When using a 45° pulse, signal from $(2\hat{I}_{1z}\hat{I}_{2z})$ and ZQ_x will be maximised with a small contribution from ZQ_y. However, using a 90° pulse will result in signal from ZQ_y being maximised with all other terms being cancelled out. Therefore, using a 90° pulse angle enables clean observation of the oscillation of ZQ_y due to $\delta\omega$ (often given as $\Delta\nu$, with the oscillation frequency in Hz). A full description of this theory is given in the literature by Bowers *et al.*[37]

$$\frac{1}{2}(2\hat{I}_{1z}\hat{I}_{2z}) \xrightarrow{\theta(\hat{I}_{1y}+\hat{I}_{2y})} \frac{1}{2}(2\hat{I}_{1x}\hat{I}_{2z}+2\hat{I}_{1z}\hat{I}_{2x})\frac{1}{2}\sin(2\theta) \tag{6.7}$$

$$ZQ_x\cos(\delta\omega\tau) \xrightarrow{\theta(\hat{I}_{1y}+\hat{I}_{2y})} -\frac{1}{2}(2\hat{I}_{1x}\hat{I}_{2z}+2\hat{I}_{1z}\hat{I}_{2x})\frac{1}{2}\sin(2\theta)\cos(\delta\omega\tau) \tag{6.8}$$

$$ZQ_y\sin(\delta\omega\tau) \xrightarrow{\theta(\hat{I}_{1y}+\hat{I}_{2y})} -\frac{1}{2}(2\hat{I}_{1y}\hat{I}_{2z}+2\hat{I}_{1z}\hat{I}_{2y})\sin(\theta)\sin(\delta\omega\tau) \tag{6.9}$$

An example of an AX system exhibiting this behaviour, $[Ru(H)_2(dpae)(CO)_2]$ (shown in Figure 6.32), was studied by Halse *et al.*[48] When in C_6D_6, the difference in chemical shift between the two hydride resonances is 0.4 ppm which results in an oscillation frequency ($\Delta\nu$) of 240 Hz (when in a 600 MHz spectrometer).

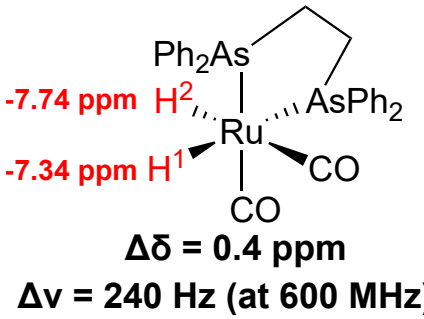

Figure 6.32: Structure of $[Ru(H)_2(CO)_2(dpae)]$ highlighting the chemical shift difference between the two hydride nuclei.

When a pump-probe experiment is performed on this system with τ delays between 0 - 60 ms, a clear oscillation of the signal is detected (Figure 6.33a) which can be fitted to give an oscillation frequency of (241.5 ± 0.1) Hz. This frequency is consistent with the expected value of $\Delta\nu$ for the system and so highlights that the observed oscillation does originate from the symmetry breaking feature within the chemical system.

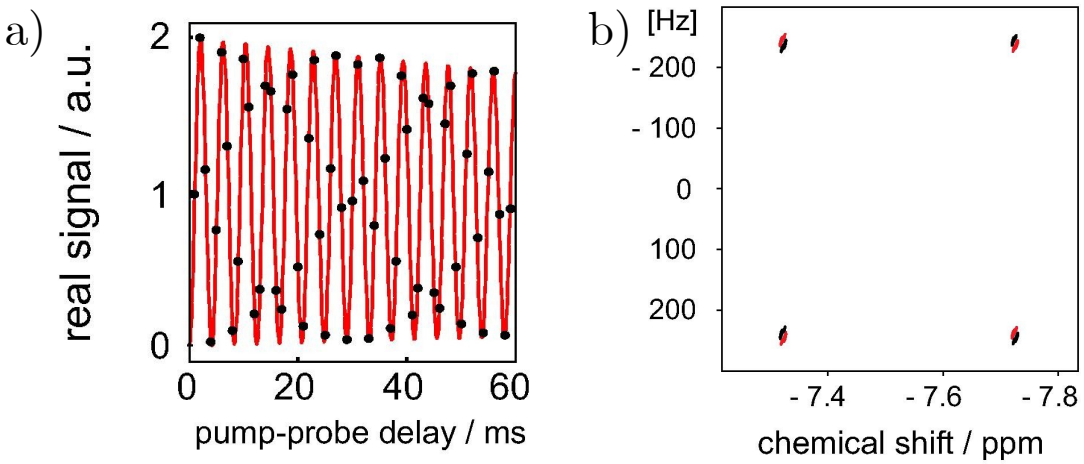

Figure 6.33: (a) 1D oscillation and (b) 2D pump-probe ^1H spectrum for $[Ru(H)_2(CO)_2(dpae)]$, recorded at 600 MHz (14.1 T) with τ = 0 - 60 ms. Reproduced from Ref. 48 with permission from Elsevier.[48]

Figure 6.33b represents an alternative way to analyse this data. By creating a 2D dataset which contains all the individual FIDs collected during the pump-probe experiment stacked according to the τ delay for each experiment, it is possible to perform a double Fourier transform of the dataset. This creates a 2D spectrum of chemical shift along the x-axis and oscillation frequency (in Hz) along the y-axis. As a result, cross-peaks are observed at the chemical shift of each hydride species at $\pm\Delta\nu$.

6.7.2 Synchronous Starting Point Development

To be able to observe these short-lived coherences, it is of vital importance that the magnetic evolution of the system occurs synchronously. Hyperpolarised species that form at different times will oscillate at the same frequency but offset from one another. As the acquired FID is of the ensemble average of spins, these offset oscillations will destructively interfere with one another obscuring the magnetic evolution feature within the pump-probe NMR experiments. A synchronous starting point is ensured when pump-probe experiments are performed using a laser due to the laser pulse occurring on a nanosecond timescale. This nanosecond pulse creates a bulk of hyperpolarised species at a very well defined time within the experiment and as such coherent evolution is observed.

Within the current *in situ* irradiation setup, irradiation periods on the second timescale are used to build up a suitable concentration of hyperpolarised species prior to detection. Within this irradiation period, complexes are continuously cycling between the starting material, which contains thermally-polarised hydrides, and the hyperpolarised product. Therefore when the irradiation ends, the solution will contain hyperpolarised species that have been formed at different times during the irradiation period. This asynchronous creation of hyperpolarisation will prevent the observation of any zero-quantum oscillations.

One route to overcome this limitation is to perform a spin-lock pulse sequence during the irradiation period. A spin-lock pulse sequence is designed to preserve a singlet state through application of specific combinations of RF pulses that control the evolution of the spin system.[243] While several specific pulse sequences exist to create long-lived states from hyperpolarised signals, these pulse sequences require precise control of the evolution of the bulk magnetisation which cannot be achieved with an asynchronous reaction starting point.[244] An alternative, more rudimentary approach to spin-locking is to apply broadband decoupling to the ^{1}H channel during the irradiation period (a method previously utilised by Blazina *et al.* to prevent dephasing during continuous irradiation).[237] NMR decoupling uses a series of RF pulses to prevent evolution due to scalar coupling. By preventing the effective formation of a scalar coupling network, decoupling can prevent magnetic inequivalence from developing between the two hydrides formed from *p*H_2 addition (i.e. it prevents $J_{H_1X} \neq J_{H_2X}$ where X is a nucleus in a different chemical environment). As magnetic inequivalence enables symmetry breaking of the singlet state of *p*H_2, preventing it from being established enables a pseudo-singlet state to

be maintained by the product molecule until the decoupling is stopped. As decoupling can be applied continuously during irradiation (as long as a sensible duty cycle is selected), this route to spin-locking is effective during the continued reactivity of the sample.

To perform a spin-lock during the pump-probe experiment at low-field, an MLEV-4 decoupling cycle was added into the pulse sequence. MLEV-4 decoupling uses a block of four 180° rotations of the magnetisation to continually invert the signal and prevent evolution due to scalar coupling (each 180° rotation is caused by a composite pulse of 90_x-180_y-90_x to minimise artifact formation).[245,246]

To apply the MLEV-4 decoupling during irradiation, a significant change had to be made to the pump-probe experiment as it required the pulse sequence to be running concurrently to the irradiation, whereas previously it had been initiated following the τ delay. To address this, the d_I and τ delays had to be placed within the pulse sequence as the Spinsolve software does not allow for several different pulse sequences to be performed within one experiment. This change enabled the d_I delay to be converted from an experimental delay into a repeating loop of MLEV-4 decoupling. For this, each MLEV-4 block (4 180° rotations) was given a duration of 2 ms with each composite pulse spaced apart by 0.5 ms. This resulted in a duty cycle of 7.5% (where each composite pulse lasts 38 μs) which was an acceptable level to not cause damage to the NMR detection coils. To calculate how many MLEV-4 cycles were needed, d_I is divided by 2 ms and this number of loops are performed by the pulse sequence. In cases where this division is not an integer value, the number of loops will be rounded up to ensure that irradiation does not end before the decoupling does (thus ensuring pseudo-singlet state preservation). The adjusted pulse sequence for the pump-probe experiment is given in Figure 6.34.

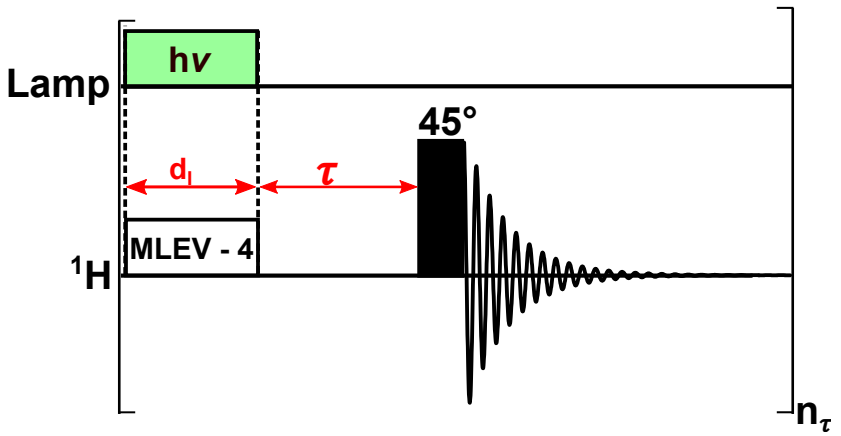

Figure 6.34: Updated pump-probe pulse sequence to include MLEV-4 decoupling during the irradiation period.

A repeat of the pump-probe experiment performed on *cis*−[Ru(H)$_2$(dppe)$_2$] (Figure 6.31) was performed using the pulse sequence controlled variant (with and without decoupling) to determine if the change in experiment affected the hydride integrals observed for each τ delay. Figure 6.35a is a comparison between the hyperpolarised signal decay curves obtained when using experimental control (EC) and pulse sequence control (PSC). While showing similar decay curves, the observed rate of decay for the PSC experiment is faster than that of the EC experiment, with calculated hyperpolarised T_1 values of (290 ± 40) ms and (249 ± 30) ms respectively. Comparing the two datasets, it appears as if the EC data is shifted relative to the PSC data on the timescale of tens of milliseconds. The major difference between these experiments is that pulse sequence initialisation occurs following the τ delay in the EC experiment whereas it occurs at the start of the irradiation period (during d_I) for PSC. The initialisation of the pulse sequence on the Spinsolve was found to add a non-negligible delay (measured to have an average value of 27 ms) within the experiment and this would explain the offset seen within the EC data. Therefore, moving to a PSC experiment is beneficial as the τ delays used within the experiment are more accurate to those set by the user. Figure 6.35b provides confirmation that changing d_I from a static delay to continuous decoupling does not impact the τ delays of the experiment.

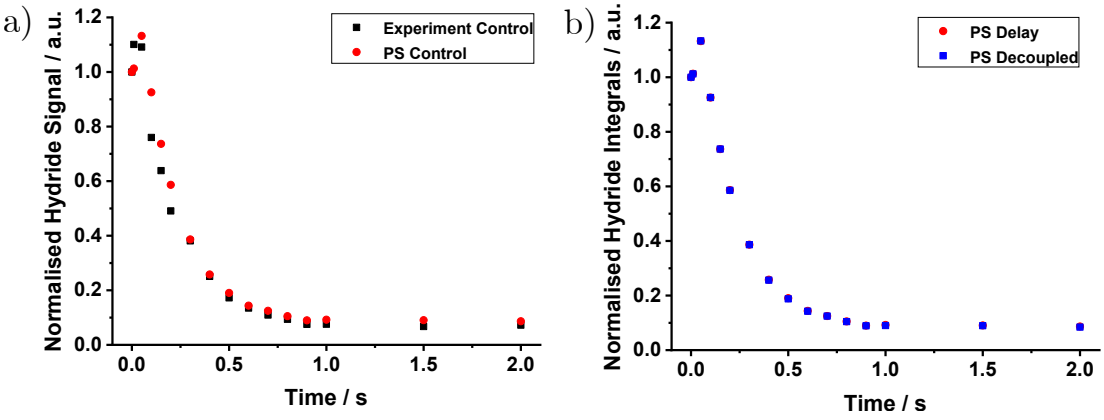

Figure 6.35: Comparisons between different pump-probe pulse sequence variants for the hyperpolarised signal decay of *cis*−[Ru(H)$_2$(dppe)$_2$] using d_I = 0.5 s and τ = 0 - 2 s. Comparisons are made between (a) experimentally and pulse sequence controlled experiments and (b) pulse sequence control with and without MLEV-4 decoupling.

With an updated pulse sequence, it was now possible to observe magnetic evolution of the *cis*−[Ru(H)$_2$(dppe)$_2$] system on the millisecond timescale. The pump-probe experiment was performed on *cis*−[Ru(H)$_2$(dppe)$_2$] with and without MLEV-4 decoupling and the resulting stack of ^{1}H spectra are shown as Figures 6.36a and b respectively. While 6.36a showed a hydride signal with minimal variation on

the millisecond timescale, the addition of decoupling in Figure 6.36b resulted in significant changes in the magnitude and sign of the NMR signals. Furthermore, much higher levels of polarisation are observed at the peak of the oscillation within Figure 6.36b (as indicated by the increased magnitude of the observed signals). This indicates that additional terms are contributing to the observed signal. Both these features were positive indicators that application of decoupling during the irradiation period enables preservation of a pseudo-singlet state until the start of the probe delay and thus a synchronous evolution of the system is observed.

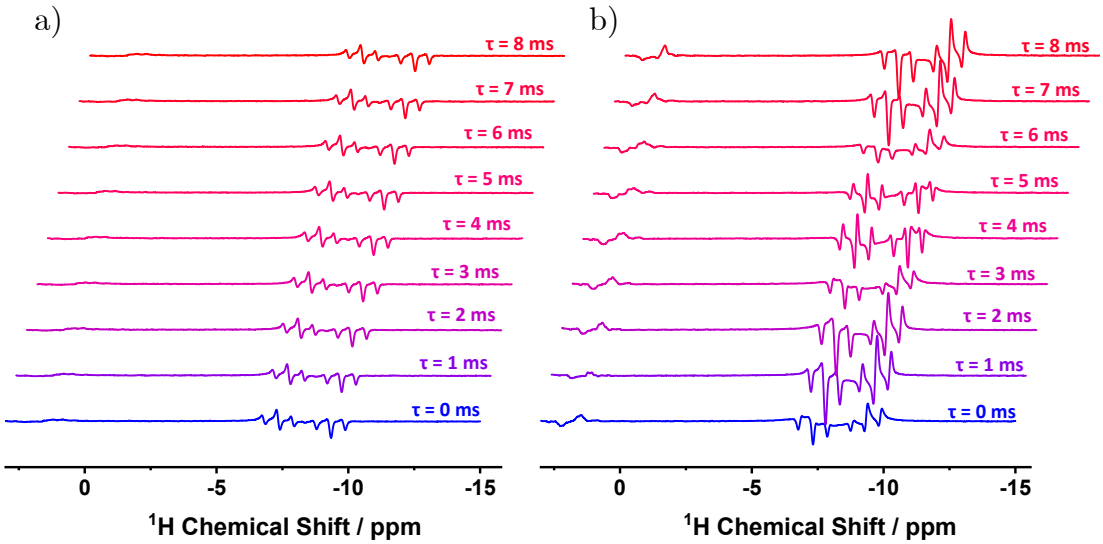

Figure 6.36: Comparison between ^{1}H spectra collected for *cis*−[Ru(H)$_2$(dppe)$_2$] (a) without and (b) with MLEV-4 decoupling during irradiation using d$_I$ = 0.5, τ = 0 - 8 ms and θ = 90°.

6.7.3 Magnetic Evolution of *cis*−[Ru(H)$_2$(dppe)$_2$]

The symmetry breaking feature of *cis*−[Ru(H)$_2$(dppe)$_2$] is magnetic inequivalence due to the AA'XX' symmetry of the complex that is formed. For reference, a diagram showing the key relationships in an AA'XX' spin system is given as Figure 6.37. The magnetic evolution for this system is different to that of the AX system example that was detailed in Section 6.7.1. A brief description of the major changes are given below but a complete description of the evolution of this system upon *p*H$_2$ addition is given in the literature by Halse *et al.*[48] Within this description, the operators $\hat{I}$ and $\hat{S}$ will be used to refer to A and X nuclei respectively, with a subscript 1 and 2 to distinguish nuclei of the same type.

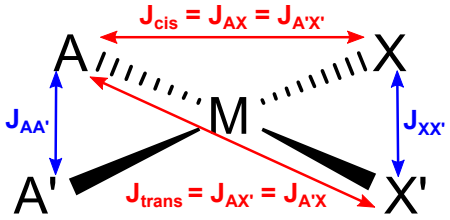

Figure 6.37: Schematic representation of the scalar coupling network present in an AA'XX' spin system with homonuclear couplings shown in blue and heteronuclear couplings shown in red.

The pH$_2$ starting state is identical to that shown previously ($\hat{\rho}_{pH_2} = \frac{1}{2}(2\hat{I}_{1z}\hat{I}_{2z}) + ZQ_x$) and this will evolve under the free evolution Hamiltonian given in Equation 6.10. The additional terms within this Hamiltonian are required to account for evolution due to chemical shift (in black), homonuclear couplings (in blue) and heteronuclear couplings (in red).

$$\begin{aligned}\hat{H}_{AA'XX'} = &-\omega_A(\hat{I}_{1z} + \hat{I}_{2z}) - \omega_X(\hat{S}_{1z} + \hat{S}_{2z}) \\ &+\pi J_{AA'}(2\hat{I}_{1z}\hat{I}_{2z} + 2\hat{I}_{1x}\hat{I}_{2x} + 2\hat{I}_{1y}\hat{I}_{2y}) + \pi J_{XX'}(2\hat{S}_{1z}\hat{S}_{2z} + 2\hat{S}_{1x}\hat{S}_{2x} + 2\hat{S}_{1y}\hat{S}_{2y}) \\ &+\pi J_{trans}(2\hat{I}_{1z}\hat{S}_{1z} + 2\hat{I}_{2z}\hat{S}_{2z}) + \pi J_{cis}(2\hat{I}_{1z}\hat{S}_{2z} + 2\hat{I}_{2z}\hat{S}_{1z})\end{aligned} \tag{6.10}$$

When this Hamiltonian is applied to $\hat{\rho}_{pH_2}$, the ZQ$_x$ term is seen to evolve at $\omega = 2\pi\sqrt{\Delta J^2 + J_{AA'}^2}$ where $\Delta J = J_{trans} - J_{cis}$. This results in the formation of a complex mixture of several other spin states. For brevity, the application of a 90° broadband pulse on the $\hat{I}$ nucleus channel results in conversion of only two spin states within this mixture into observable NMR magnetisation, and these are given in Equation 6.11. Within the equation, $\xi = \frac{\Delta J}{J_{AA'}}$ which controls the contribution of each term to the observed NMR signal.

$$\begin{aligned}\hat{\rho}_{SQ}^{AA'XX'} = &\frac{\xi}{\sqrt{1+\xi^2}}\sin(\omega\tau)\frac{1}{2}(2\hat{I}_{1y}\hat{I}_{2z} - 2\hat{I}_{1z}\hat{I}_{2y})2(\hat{S}_{1z} - \hat{S}_{2z}) \\ &-\frac{\xi}{1+\xi^2}(1-\cos(\omega\tau))(\hat{I}_{1x} - \hat{I}_{2x})(\hat{S}_{1z} - \hat{S}_{2z})\end{aligned} \tag{6.11}$$

Within both NMR observable terms, the evolution due to ω under τ (highlighted in red) will lead to oscillations of the observed NMR signal. The first term (antiphase y-magnetisation) will oscillate at a frequency of $\nu_1 = \pm\omega/2\pi = \pm\sqrt{\Delta J^2 + J_{AA'}^2}$. The

second term (in phase x-magnetisation, in blue) will also oscillate at ν_1 but will also have a component with no oscillation (which would give a cross-peak at 0 Hz in a 2D spectrum).[247]

Applying this knowledge to the *cis*−[Ru(H)$_2$(dppe)$_2$] system, an oscillation at $\nu_1 = \pm\sqrt{\Delta J^2 + J_{AA'}^2}$ would be expected from a pump-probe experiment. Using literature values of $\Delta J = |J_{HP_{trans}} - J_{HP_{cis}}|$ = 83.8 Hz and J_{HH} = 4.8 Hz, the oscillation frequency is expected to be 83.9 Hz.[48] This pump-probe experiment was performed by Torres *et al.* at 600 MHz, and the observed oscillation had a frequency of ± 84 Hz (with the literature 1D and 2D spectra shown as Figures 6.38a and b respectively).[47] Within the 2D ^{1}H pump-probe spectrum, no peak is observed at 0 Hz. This is due to the second term in Equation 6.11 having a strong ξ dependence, with large values of ξ reducing the overall contribution of this term. Due to the low strength of the hydride coupling relative to the hydride-phosphorus couplings in this system (giving a ξ of 17.5), this term only contributes to 6% of the density matrix and so no spectral feature at 0 Hz is observed.

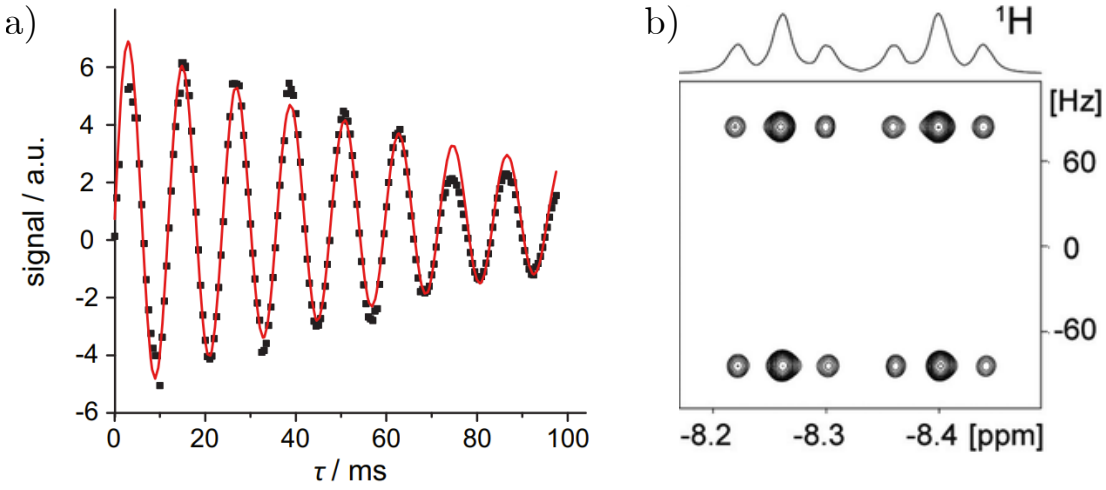

Figure 6.38: Literature data showing the (a) 1D oscillation and (b) 2D spectrum for the magnetic evolution of *cis*−[Ru(H)$_2$(dppe)$_2$] over 0 - 100 ms. Reproduced from Ref. 47 with permission from the American Chemical Society.[47]

As a comparative study, the pump-probe experiment using *cis*−[Ru(H)$_2$(dppe)$_2$] was attempted at low-field using τ between 0 and 126 ms (with an oscillation frequency of 83.9 Hz, this should allow 10 full oscillations to be observed). Based on the optimisation studies performed, the sample was shaken between each step with the pH$_2$ within the NMR tube being replenished every 4 steps. To minimise the influence of signal decay over the course of the experiment, the τ delays were performed in a randomised order. Once acquired, the ^{1}H spectra were reorganised

into a 2D dataset in sequential τ delay order. To analyse this data, the processing code for thermal reaction monitoring was modified to enable peak picking and integration of the 2D dataset. The grouping subroutine was used to separate the peaks for each hydride by their sign to allow quick summation of the peak integrals. An example *cis*−[Ru(H)$_2$(dppe)$_2$] spectrum from this experiment is given in Figure 6.39a with the full 2D dataset given in Figure 6.39b.

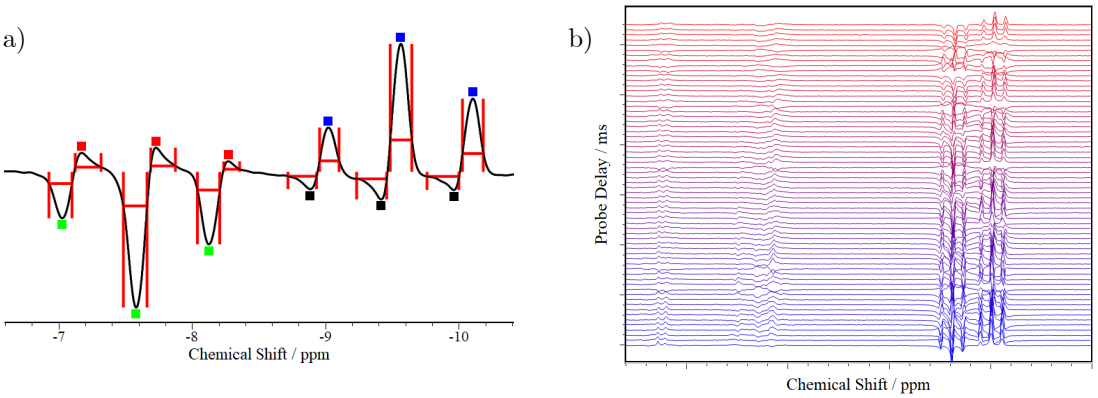

Figure 6.39: Example (a) ^{1}H spectrum and (b) 2D matrix produced during a pump-probe experiment with variable τ delays. Highlighted in (a) are the peak picking, grouping (colored squares) and integration (red lines) subroutines.

Following analysis, the integrals were plotted against τ delay and fit to a damped sine wave (Equation 6.12) where y_0 is a y-offset, A_0 is the initial amplitude, t_0 is the decay constant, x_c is the phase shift and w is the period. The period is then converted into oscillation frequency using $\nu = \frac{1}{2w}$.

$$y = y_0 + A_0 e^{(-x/t_0)} \sin\left(\pi \frac{x - x_c}{w}\right) \tag{6.12}$$

The 1D oscillation and 2D spectrum obtained for *cis*−[Ru(H)$_2$(dppe)$_2$] are given as Figures 6.40a and b respectively. The frequency of the oscillation was calculated to be (84.11 ± 0.05) Hz which is in excellent agreement with the expected value (83.9 Hz) and the value obtained experimentally using a 600 MHz spectrometer (84 Hz).[47] This experimental result is the first observation of the zero-quantum oscillation from *p*H$_2$ addition recorded at low-field and the data obtained is of a similar quality to that obtained at high-field.

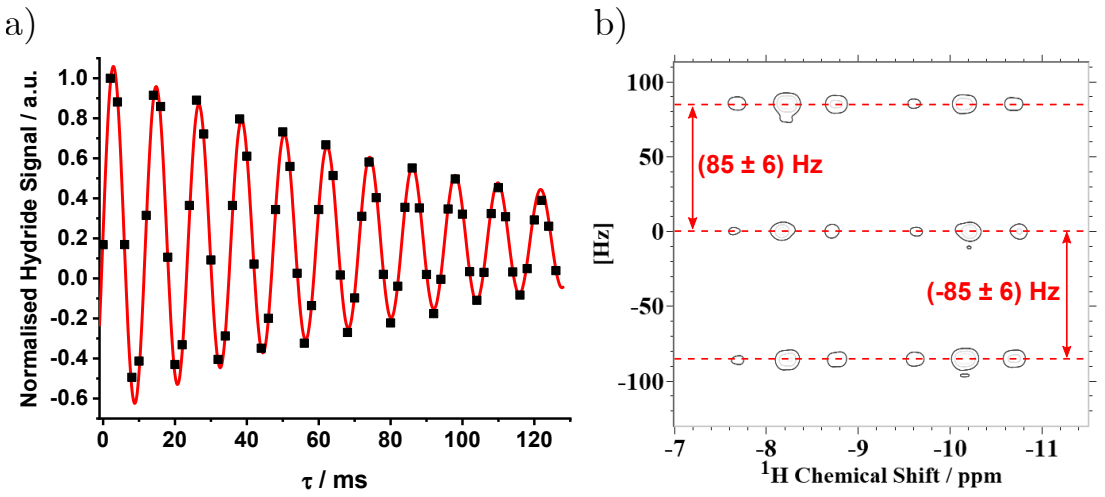

Figure 6.40: (a) 1D oscillation and (b) 2D pump-probe spectrum showing the magnetic evolution of *cis*−[Ru(H)$_2$(dppe)$_2$](3.3 mM). Data was collected in 64 steps using d$_I$ = 0.5 s and τ delays between 0 and 126 ms, in 2 ms increments.

The 2D spectrum obtained from this data (Figure 6.40b) also has a similar accuracy to that obtained at high field (where cross-peaks gave an oscillation frequency of ±(83 ± 5) Hz). However, one major difference to the high-field data is an an additional set of cross-peaks centred at 0 Hz. This cross-peak is not due to a change to ξ as the ratio of J coupling constants is magnetic field strength independent. A possible origin for these cross-peaks is that the 90° pulse did not result in complete cancellation of other potential NMR observable terms. For example, spin states that originate from the $2\hat{I}_{1z}\hat{I}_{2z}$ state (such as the observable $(2\hat{I}_{1x}\hat{I}_{2z} + 2\hat{I}_{1z}\hat{I}_{2x})$ spin state) do not evolve over time with ω and as such would contribute to cross-peaks at 0 Hz. These spin states may persist due to an imperfect 90° pulse or may be an artifact caused by the decoupling pulses during irradiation. As these additional cross-peaks are only present at 0 Hz they will not interfere with the zero-quantum oscillations and so quantitative analysis of datasets from this pump-probe technique can still be performed. One piece of evidence that supports this analysis is the offset of the 1D oscillation in Figure 6.40a, as the oscillation is not centred at 0 which suggests that there is a non-oscillating component within the signal obtained.

6.7.4 Magnetic Evolution of [Ru(H)$_2$(CO)$_2$(dpae)]

To provide further evidence that the pump-probe experiment accurately monitored zero-quantum evolution, the oscillation of [Ru(H)$_2$(CO)$_2$(dpae)] was analysed. The magnetic evolution of this AX spin system was detailed in Section

6.7.1. The oscillation of the zero-quantum terms occurs at the frequency of the difference in chemical shift ($\Delta\nu$) of the chemically inequivalent hydrides. At 600 MHz, the chemical shift difference of 0.4 ppm in C_6D_6 produced an oscillation at $\Delta\nu$ = 240 Hz (a period of 4 ms). Unlike oscillations due to scalar coupling (such as in the AA'XX' spin system), oscillations due to chemical shift will change frequency based on the B_0 field that they are evolving within. Therefore, the oscillation of $[Ru(H)_2(CO)_2(dpae)]$ at 43 MHz (1 T) would be expected to have a frequency of 17.4 Hz (a period of 57 ms).

To observe this oscillation, a sample of $[Ru(H)_2(CO)_2(dpae)]$ was prepared through prolonged irradiation of a sample of $[Ru(CO)_3(dpae)]$. The sample was irradiated until ^1H spectra gave consistent integrals upon repeat irradiation and addition of fresh pH_2 indicating that only the degenerate reaction (Figure 6.20) was occurring. After performing similar repeatability experiments to those on *cis*−$[Ru(H)_2(dppe)_2]$, it was found that 2 repeats before refreshing pH_2 could be performed before the signal dropped below 5% of the original. For this 32-step pump probe experiment, τ values were randomised to prevent signal loss from causing systematic errors in the dataset. The 1D oscillation obtained from this experiment is given in Figure 6.41b. Analysis of the oscillation gave a frequency of (17.24 ± 0.08) Hz which is in good agreement with the expected value of 17.4 Hz.

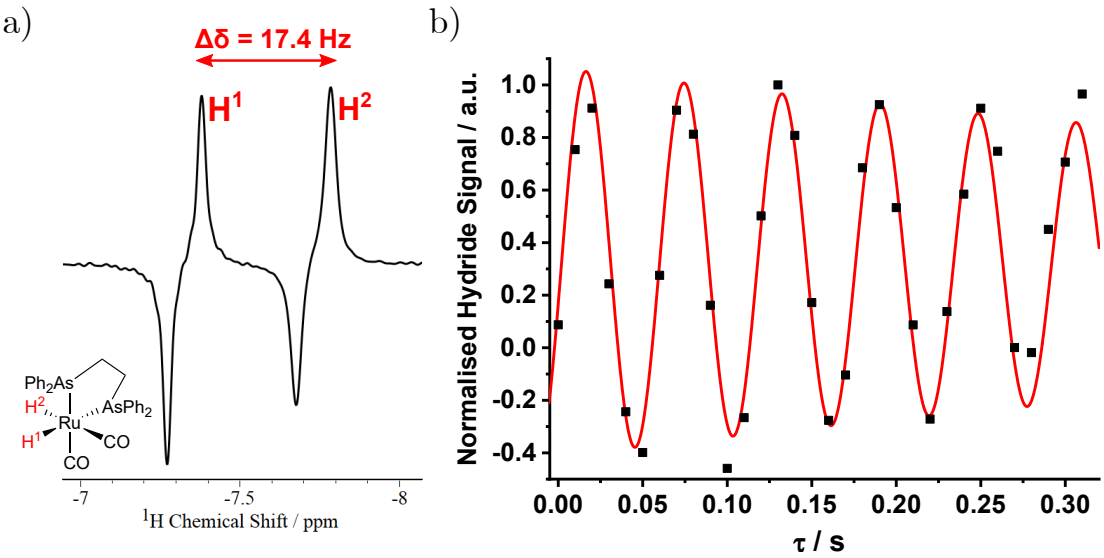

Figure 6.41: (a) Example spectrum of $[Ru(H)_2(CO)_2(dpae)]$ highlighting $\Delta\delta$ and (b) the observed 1D oscillation following a variable delay pump-probe experiment. Pump-probe data for $[Ru(H)_2(CO)_2(dpae)]$ (0.55 mM) was collected in 32 steps using θ = 90°, d_I = 2 s and τ delays between 0 and 0.31 s, in 0.01 s increments.

The pump-probe experiment was repeated using a 45° pulse angle to inspect the

difference between the 2D spectra obtained when selectively observing signals produced from ZQ_y (using 90°) and when observing signal from $2\hat{I}_{1z}\hat{I}_{2z}$, ZQ_x and ZQ_y (using 45°). The 2D spectra observed when using 90° and 45° pulses are given as Figures 6.42a and b respectively.

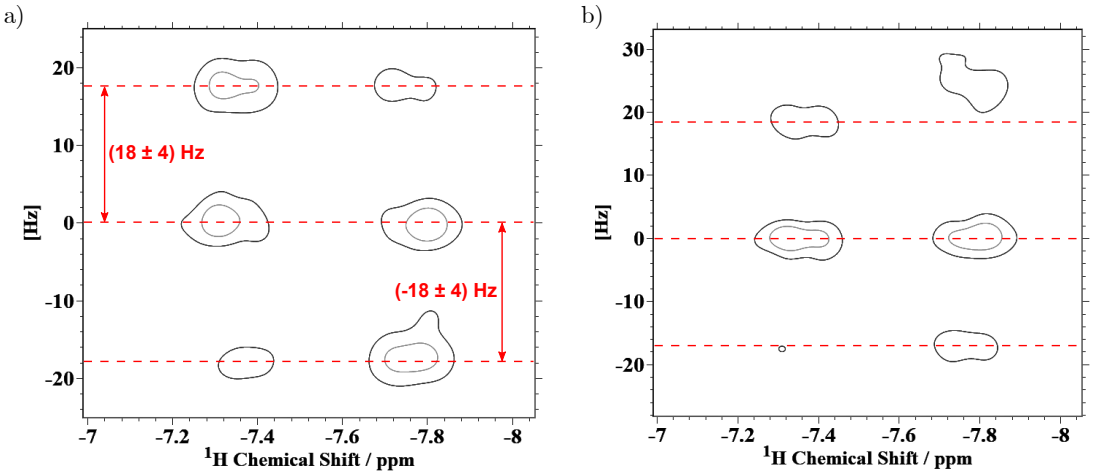

Figure 6.42: 2D pump-probe spectra for $[Ru(H)_2(CO)_2(dpae)]$ (0.55 mM) collected using a (a) 90° and (b) 45° pulse. Pump-probe data was collected in 32 steps using d_I = 2 s and τ delays between 0 and 0.31 s, in 0.01 s increments.

Figure 6.42a shows the expected cross-peaks at ±18 Hz along with a pair of strong cross-peaks at 0 Hz. Figure 6.42b shows partial cancellation of the cross-peaks at ±18 Hz with each hydride only showing a strong signal at one cross-peak frequency. This pattern indicates destructive interference of the ZQ_x and ZQ_y derived terms. Upon closer observation of 6.42a, the cross-peaks that are missing from 6.42b are also notably weaker within this spectrum. This feature, along with the presence of cross-peaks at 0 Hz, provides further evidence that the 90° pulse does not cause complete cancellation of all unwanted NMR signals. However, as the 90° pulse still strongly selects for the ZQ_y derived terms the signal cancellation is less extensive than when using a 45° pulse.

6.7.5 Magnetic Evolution of $[Ir(H)_2(CO)(PPh_3)_2I]$

The relationship between $\Delta\nu$ and B_0 provides an interesting advantage to performing the pump-probe experiment at low-field. For systems with a substantial difference in hydride chemical shift, moving to a lower B_0 can reduce the frequency of the zero-quantum evolution to an observable rate. As an example of this concept, $[Ir(H)_2(CO)(PPh_3)_2I]$, which has a $\Delta\delta$ of 6.5 ppm, was explored. This chemical shift

difference corresponds to an oscillation frequency ($\Delta\nu$) of 3900 Hz on a 600 MHz (14.1 T) spectrometer, and so a single oscillation would last 0.3 ms. For comparison, the largest oscillation frequency observed using the pump-probe technique at 600 MHz thus far is ±684 Hz for *fac*-[$Ru(H)_2(CO)(PPh_3)$(dppp)] and so a significant increase in time-resolution would be required in order for [$Ir(H)_2(CO)(PPh_3)_2I$] to be observed.[48]

Moving to 43 Hz (1 T), the chemical shift difference for [$Ir(H)_2(CO)(PPh_3)_2I$] (Figure 6.36) of 6.5 ppm corresponds to an oscillation frequency of 282 Hz. This oscillation frequency gives a period of 3.5 ms which is on a reasonable timescale for observation and provides an opportunity to test the time-resolution of the low-field pump-probe setup as it requires sub-millisecond precision of delays.

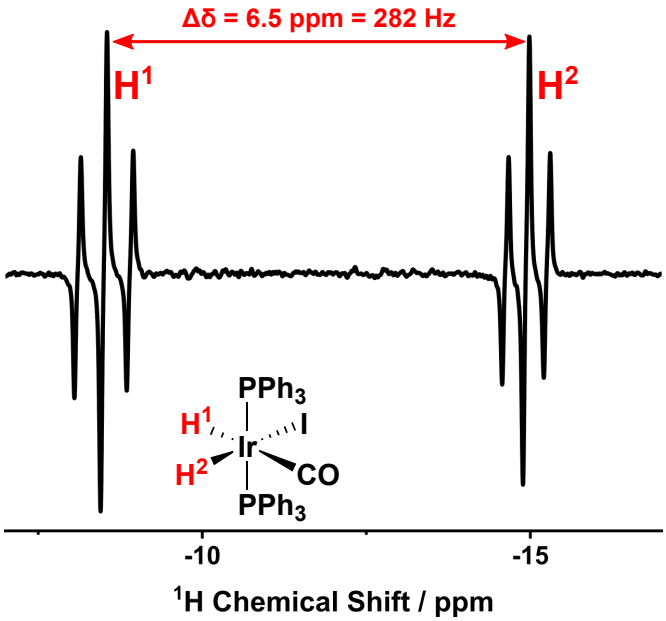

Figure 6.43: Example hydride spectrum for [$Ir(H)_2(CO)(PPh_3)_2I$](3.1 mM), highlighting $\Delta\delta$.

To measure the oscillation, a 64 step pump-probe experiment was performed using a 1 s irradiation time and τ delays between 0 and 31 ms. For the experiment, the sample was shaken after every step with pH_2 refreshment after every 4 steps (a <5% variation in signal across 4 experiments was observed within a repeatability study). The randomisation of τ values was required for this system to minimise the impact of the potential degradation of [$Ir(H)_2(CO)(PPh_3)_2I$] upon continued irradiation across the experiment (discussed in Section 6.4.3).[45]

The obtained 2D spectrum for [$Ir(H)_2(CO)(PPh_3)_2I$] is given in Figure 6.44. From

this spectrum, an oscillation frequency of (±283 ± 12) Hz was extracted for the system. A 1D oscillation was also obtained for this system, giving an oscillation frequency of (280.9 ± 1.2) Hz.

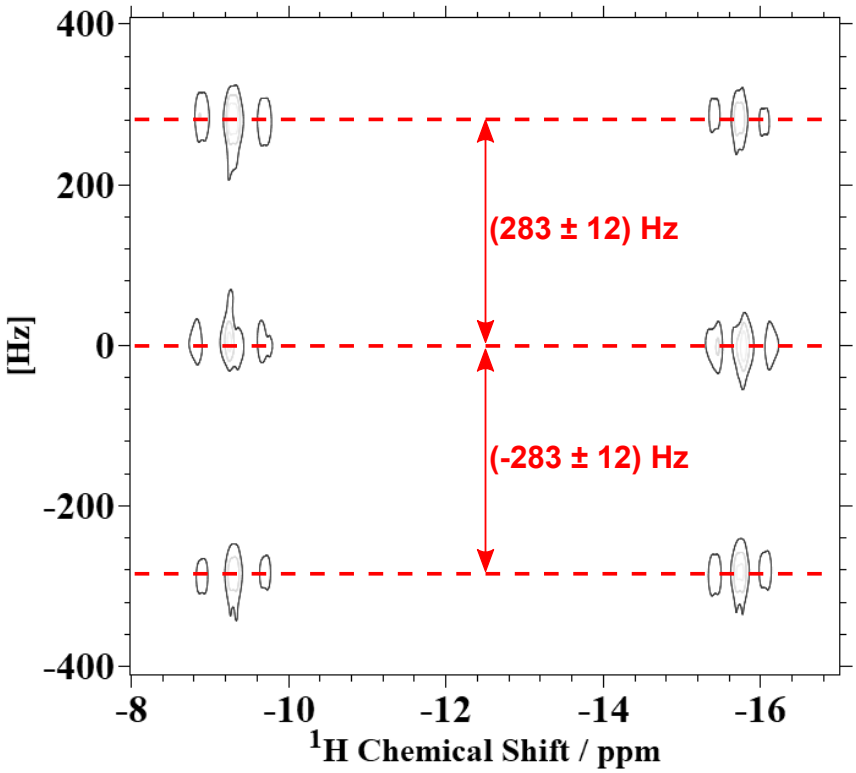

Figure 6.44: 2D pump-probe spectrum showing the magnetic evolution of $[Ir(H)_2(CO)(PPh_3)_2I]$ (3.1 mM). Data was collected in 64 steps using d_1 = 1 s and τ delays between 0 and 31 ms, in 0.5 ms increments.

A good agreement is seen between the expected value (282 Hz) and the experimentally measured values obtained from the 1D oscillation, (±280.9 ± 1.2) Hz, and the 2D spectrum, (±283 ± 12) Hz. This indicates that the pump-probe setup has successfully captured magnetic evolution using sub-millisecond τ delays, making it competitive to the high-field counterpart. Analysis of individual ^{1}H spectra recorded during this experiment showed evidence of degradation of the *trans*-$[IrI(CO)(PPh_3)_2]$ complex which could account for the increased error in the measured values relative to the Ruthenium(II) complex studies. Even with this increased error, a clear oscillation is observed within the obtained data and so the experiment is robust enough to account for slight signal deviations across the course of the experiment.

To further explore complex magnetic evolution with this pump-probe method, a ^{13}C-labelled variant of $[Ir(H)_2(CO)(PPh_3)_2I]$ was synthesised (details of the synthesis can be found in Section 8.4.4). The presence of the ^{13}CO group in the complex changes

the spin system from AX to AXY (where A and X are chemically inequivalent hydrides and Y is a coupled ^{13}C nucleus). Working through the changes to the Hamiltonian and density operators to include the additional scalar coupling to the Y nucleus results in the zero-quantum term oscillation having a frequency defined by Equation 6.13, where $\delta\omega_{AX}$ is the chemical shift difference between the hydride nuclei and $\Delta J = J_{AY} - J_{XY}$, the difference between the hydride couplings to the Y nucleus. In terms of how this changes the observed 2D spectrum, the cross-peak that is seen for an AX system is split into a doublet with a separation of ΔJ in an AXY system.[48]

$$\nu = \frac{\delta\omega_{AX}}{2\pi} \pm \frac{1}{2}\Delta J \tag{6.13}$$

The ^{1}H spectrum of [Ir(H)$_2$(^{13}CO)(PPh$_3$)$_2$I] is given in Figure 6.45. The major difference within the spectrum is the additional doublet splitting due to each hydride coupling to the ^{13}CO ligand. The J coupling constants were measured at 400 MHz with the hydride trans to ^{13}CO (δ = 8.4 ppm) having a splitting of $J_{HC_{trans}}$ = ±42 Hz while the hydride cis to ^{13}CO (δ = 14.9 ppm) has a splitting of $J_{HC_{cis}}$ = ∓2 Hz. At low-field, the reduced chemical shift dispersion leads to peak overlap of splittings resulting from $J_{HC_{cis}}$ and so this hydride appears as an apparent triplet of doublets. Using these coupling constants, ΔJ = 44 Hz for this AXY system and so, using the 282 Hz oscillation frequency of [Ir(H)$_2$(CO)(PPh$_3$)$_2$I], cross-peaks would be expected at 260 and 304 Hz for [Ir(H)$_2$(^{13}CO)(PPh$_3$)$_2$I].

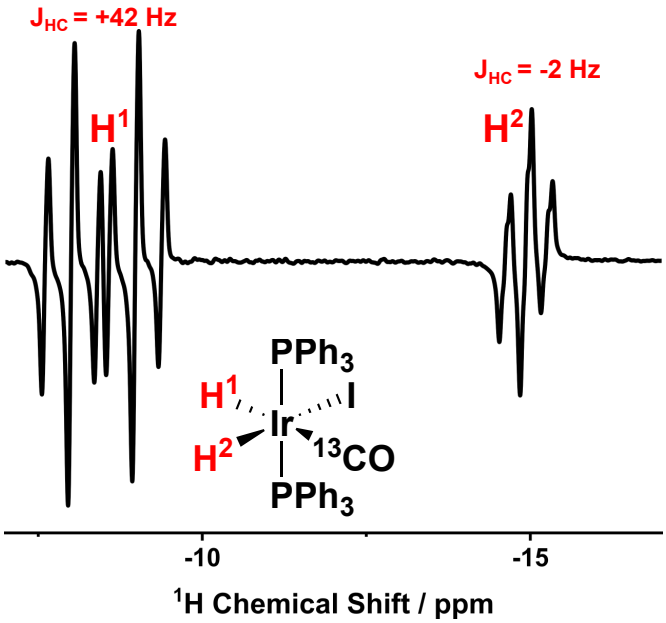

Figure 6.45: Hydride region of ^{1}H spectrum for [Ir(H)$_2$(^{13}CO)(PPh$_3$)$_2$I] (3.1 mM).

Using identical parameters to the experiment performed for $[Ir(H)_2(CO)(PPh_3)_2I]$, a pump-probe experiment was performed on $[Ir(H)_2(^{13}CO)(PPh_3)_2I]$. The resulting 2D spectrum is given in Figure 6.46. Each hydride showed cross-peaks at ±(263 ± 17) and ±(306 ± 15) Hz along with the 0 Hz artifact that has been observed in previous pump-probe experiments. 1D oscillations were obtained using the integrals from the well-resolved peaks of the H^1 hydride. The frequencies of the 1D oscillations were found to be (303.0 ± 0.06) and (257.7 ± 0.08) Hz. As the frequencies from both the 2D spectrum and 1D oscillations are well matched to the expected values of 260 and 304 Hz, this indicates another successful application of the photochemical pump - NMR probe approach at low-field.

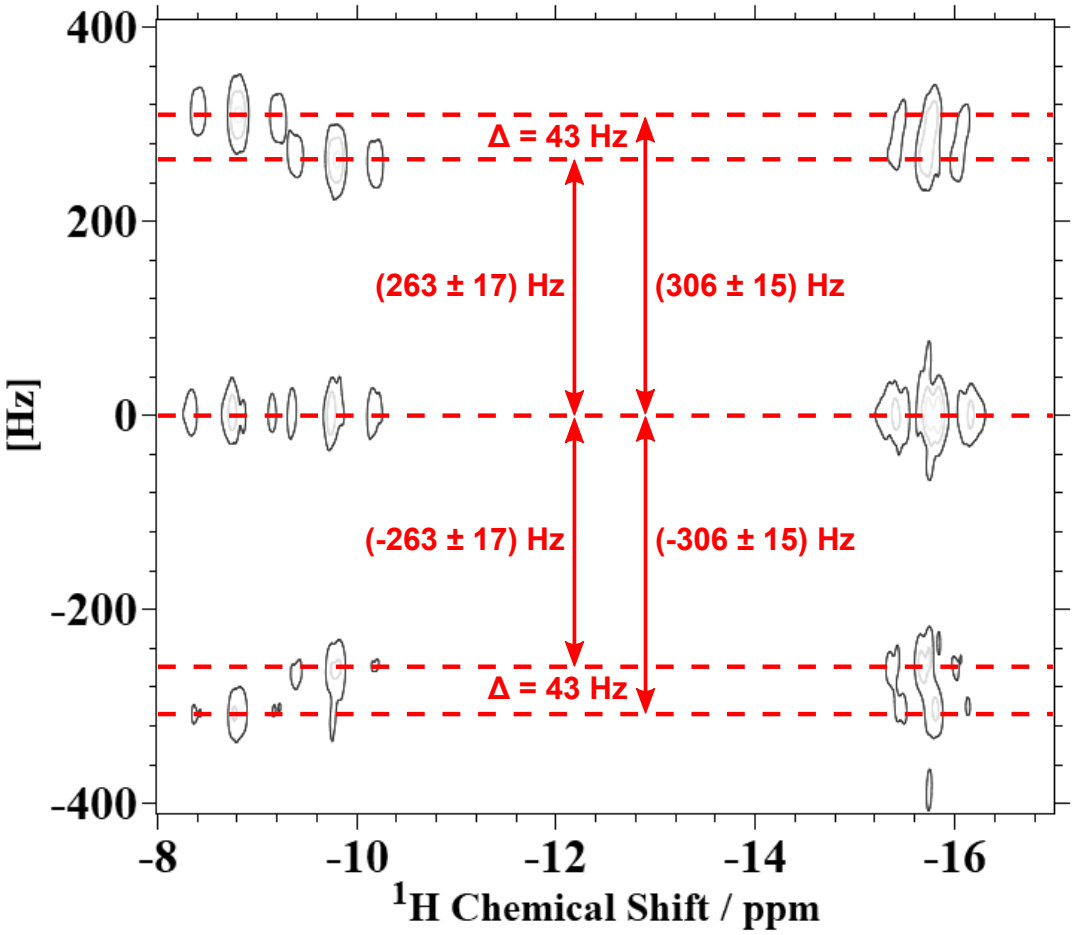

Figure 6.46: 2D pump-probe spectrum for $[Ir(H)_2(^{13}CO)(PPh_3)_2I]$ (1.6 mg, 3.1 mM). Data was collected in 64 steps using d_1 = 1 s and τ delays between 0 and 31 ms, in 0.5 ms increments.

6.8 Conclusions

An *in situ* irradiation setup was successfully implemented on a benchtop NMR spectrometer, utilising a broadband UV lamp source and a unique through-bore irradiation approach from below the NMR sample. This setup was utilised to observed enhanced hydride signals for a range of iridium and ruthenium dihydride complexes formed following photochemical reactions. Compared to the *ex situ* setup, stronger signal enhancements were observed for $[Ir(H)_2(CO)(PPh_3)_2Cl]$ and signals for faster reacting complexes, such as $[IrI(H)_2(CO)(PPh_3)_2]$, were able to be observed due to the smaller delay between irradiation and NMR observation.

Improvements to the time-resolution of the *in situ* photochemical approach were achieved through the development of a photochemical pump - NMR probe experiment at low-field. Through implementation of an Arduino-relay to allow direct control of the shutter on the UV lamp, experimental timings were able to be precisely controlled and hydride signals for fast relaxing species, such as *cis*$-[Ru(H)_2(dppe)_2]$, were able to be observed for the first time.

With the development of the photochemical pump - NMR probe experiment, magnetic evolution of several chemical systems on the micro-to-millisecond timescale have successfully been observed at low-field for the first time. Evolution from AX, AXY and AA'XX' spin systems have been observed and the calculated oscillation frequencies have matched well with theoretical predictions. Compared to the high-field pump-probe setup (which utilises a 600 MHz spectrometer and Nd:YAG laser), the oscillations of *cis*$-[Ru(H)_2(dppe)_2]$ and $[Ru(H)_2(CO)_2(dpae)]$ were obtained with a similar level of accuracy making the lower cost and more compact low-field variant a suitable alternative system to use in these types of studies. An additional advantage observed at low-field was that oscillations that have B_0 dependence (seen for systems with chemical inequivalence) will occur on a slower timescale than seen at high-field. This enabled oscillations for $[Ir(H)_2(CO)(PPh_3)_2I]$ and $[Ir(H)_2(^{13}CO)(PPh_3)_2I]$ to be observed.

One limitation of the current photochemical pump - NMR probe approach is that it is unable to properly monitor chemical evolution. This issue is not shared with the high-field counterpart with rates of formation of $[Ir(H)_2(CO)(PPh_3)_2I]$ being calculated by Procacci *et al.*[45] The main difference between these approaches is that the synchronous starting point at high-field is generated by a laser pulse on the

nanosecond timescale while the one at low-field is generated using MLEV-4 decoupling during second timescale irradiation period. While this spin-lock approach can successfully maintain a pseudo-singlet magnetic state, it cannot prevent the continued cycle of pH$_2$ loss and addition while the sample is irradiated and so there is not a synchronous starting point generated for chemical evolution. One route to address this would be to develop a series of hard pulses and gradients that effectively destroys any magnetisation formed during the irradiation period.[248,249] This would create a clear starting point for chemical evolution and prevent any previously formed hyperpolarised material from interfering with the observed integrals. Owing to the complex nature of the spin state formed upon pH$_2$ addition, the pulse sequence required to effectively remove the previous hyperpolarised signal would need to be carefully considered as to precisely destroy the unwanted terms.

7 Conclusions and Future Work

In this thesis, the development of robust quantitative techniques through which to observe both thermal and photochemical hydrogenative reactions on a benchtop NMR spectrometer has been presented. Through incorporation of PHIP hyperpolarisation methods, the inherent sensitivity limitations of transitioning to a benchtop NMR system were overcome and reactivity that was previously invisible to the benchtop NMR system became accessible. The methods development within this thesis focused on the development of low-cost and portable systems through which to achieve these goals as to align this research with the benefits of transitioning to a low-field NMR setup.

The ability of the PHIP hyperpolarised thermal reaction monitoring technique was exemplified through a model reaction system, the oxidative addition of H_2 to Vaska's complex, to allow development of the method using a well-known and simple chemical reaction.[159] The rate constant for this reaction calculated using this novel approach was determined to be (0.89 ± 0.03) $dm^3\,mol^{-1}\,s^{-1}$ which showed an excellent agreement to that presented within the literature of (0.86 ± 0.03) $dm^3\,mol^{-1}\,s^{-1}$.[111] While reaction monitoring of hydrogenation reactions using PHIP on a benchtop NMR spectrometer is starting to be utilised in a qualitative manner (in publications by Jeong *et al.*[84] and Gołowicz *et al.*[85]), this is the first study to include quantitative analysis to generate rate constants for the process being observed. As part of the experimental procedure followed, it was found to be necessary to control for temperature variations across the course of the reaction through use of a thermally-insulated holder for sample transfer and equilibration periods within the spectrometer prior to reaction monitoring. The further mitigation of these temperature effects is an area for future research, which could be achieved through the development of a route to *in situ* pH_2 bubbling at low-field (of which, examples already exist for SABRE experiments performed at high-field[187,188] and in zero-to-ultraflow-field NMR setups).[189,190]

To ensure the technique was robust, the calculated rate constant was also scrutinised against other potential sources of error such as the relaxation of the PHIP signals, the formation of thermally-polarised background signal, and variations in the enrichment level of $p\mathrm{H}_2$ used to monitor the reaction. These studies showed that each factor played a negligible role in changing the observed rate of reaction for Vaska's complex, evidencing the robustness of this technique. Within these studies, two limiting conditions under which the breakdown of the method could occur were identified. The first is low observed hyperpolarisation levels for a chemical species as this prevents the decay of PHIP activity remaining distinguished from the spectral noise. While a specific concentration limit of detection cannot be postulated, due to enhancement levels being analyte dependent, an SNR of above 30 upon initial addition of $p\mathrm{H}_2$ was found to enable accurate kinetic parameters to be obtained. The second condition occurs when the relaxation of the PHIP hyperpolarisation happens on a timescale that is competitive to the chemical reaction as the technique cannot distinguish between the two effects.

This reaction monitoring approach was successfully demonstrated to have the capability to monitor simultaneous reactions within complex mixtures which increases the scope of applications available to the method. For the system examined within this thesis, competitive hydrogenative reactions of Vaska's complex derivatives containing different phosphine ligands, reaction coordinates and rate constants were derived for each species from a single set of NMR experiments. Upon evaluation, this choice of system was found to suffer from the two limiting conditions mentioned above, with the presence of low concentration Vaska's complex derivatives and of phosphine ligand mixing on the experimental timescale. This meant that the calculated rate constants showed clear deviations from the values expected for the individual components within the sample. Further work applying this technique to mixtures which do not contain competing reaction pathways would be beneficial to clearly highlight the capabilities of the methodology developed. For example, using complexes with chelating phosphine ligands (such as dppe) as to prevent phosphine mixing within the NMR sample. Similarly, a demonstration of this technique outside of a traditional NMR laboratory (such as within a fumehood) would highlight one of the key advantages of developing this analytical technique on a benchtop NMR spectrometer.

Moving forward to observe photochemical processes in Chapters 5 and 6, low-cost *ex situ* and *in situ* photochemical setups that utilised broadband UV lamp sources were developed and optimised on the benchtop NMR system enabling the observation of

metal dihydride photochemistry for the first time on a benchtop NMR spectrometer.

Exploration of the photochemistry of $[Ir(H)_2(CO)(PPh_3)_2Cl]$ with the *ex situ* irradiation setup showed that good levels of signal enhancement (with a maximum SNR of 33) could be obtained following prolonged irradiation of the sample as to enable a significant concentration of *trans*-$[IrCl(CO)(PPh_3)_2]$ to form within the sample. The disadvantage of this irradiation period is that significant degradation of the NMR sample was observed with the formation of trisphosphine ($[IrH_2(PPh_3)_3Cl]$), trihydride ($[IrH_3(CO)(PPh_3)_2]$) and dimeric species in solution. While tuning of the irradiation wavelength was attempted using high-pass band filters, sufficient resolution was not achievable to selectively promote the H_2 loss photochemical pathway.

The *ex situ* setup also suffered from poor quantification due to the requirement for manual sample transfer following irradiation. This sample transfer requirement affected signal reproducibility (with a maximum variability of 8.8% being observed between repeat measurements) and prevented the observation of hyperpolarised species on sub-second timescales. Future advancements in the hardware associated with this method could alleviate these problems with the implementation of a pneumatically-controlled flow system for automatic sample transfer following irradiation (previously demonstrated at low-field for SABRE experiments).[99,195] While this improvement would still carry an inherent delay between initiation and observation, improving the reproducibility of the experiment would enable the setup to be used for quantitative applications. An interesting application for this setup would be in chemosensing (the detection and quantification of low concentration analytes in a solution). SABRE-enhanced chemosensing has seen interest in recent years due to the signal enhancements observed making the detection of low concentration analytes by NMR easier.[250,251] In a similar manner to how continued cycling of pH_2 and analyte molecules onto the SABRE catalyst leads to enhanced NMR signals, the *ex situ* irradiation setup could be used to generate a hyperpolarised bulk of analyte within a sample.

A novel approach was taken to the development of an *in situ* photochemical setup on the benchtop NMR spectrometer which deviated away from the currently favoured methods of using an optical fibre[26] or through-probe approach[230] to sample irradiation. By taking advantage of the continuous bore within the Spinsolve Carbon spectrometer, a through-bore approach was developed that enabled irradiation of a sample from below using an optical fibre coupled to a UV lamp

source. Unlike previous iterations of through-bore approaches utilised at high-field, the open bore of the NMR spectrometer enables this irradiation route to be used without need for permanent modification of the NMR probe. This is the second example of a *in situ* irradiation approach developed for use at low-field (the first being NMRTorch by Bramham *et al.*)[110] and the first that is compatible with the requirements of pH$_2$ hyperpolarisation. Using this approach, improved enhancements of the hydride resonances for [Ir(H)$_2$(CO)(PPh$_3$)$_2$Cl] were obtained relative to the *ex situ* approach, with a 0.43 mM sample producing a maximum SNR of 68 after only 10 seconds of irradiation. This improved enhancement can be attributed to the shorter detection delay and the more powerful lamp source used within this setup which produces a higher steady state concentration of *trans*-[IrCl(CO)(PPh$_3$)$_2$] in solution. These advantages enabled the observation of faster reacting systems with signals for [Ir(H)$_2$(CO)(PPh$_3$)$_2$I] and [Ru(H)$_2$(CO)$_2$(dpae)] dihydride complexes following irradiation being observed.

To probe dynamics on the micro-to-millisecond timescales, the development of a route to communication between the UV lamp and the computer running the spectrometer was required. This was achieved through construction of a Arduino-relay through which serial communication could be established and integrated into the design of NMR experiments. Through this setup, detection could be initiated immediately following the end of sample irradiation or after a precisely defined delay encoded into a photochemical pump - NMR probe experiment. The power of this upgrade was demonstrated through the observation of *cis*−[Ru(H)$_2$(dppe)$_2$], which was unobservable with the previous *in situ* setup, with the precise time-resolution of the technique allowing for a hyperpolarised T_1 relaxation time of (250 ± 20) ms to be measured, which was of a similar magnitude to that published within the literature.[48] The development of this Arduino-relay for communication with the NMR experiment has potential applications for the development of other hardware related improvements for the benchtop NMR spectrometer such as automated *in situ* bubbling of pH$_2$ through the sample (a technique commonly used in ultra-low field NMR via TTL pulse inputs)[190] or shuttling of the sample in and out of the spectrometer to perform magnetic field-cycling experiments.[252,253]

Using this photochemical pump - NMR probe experiment, coherent magnetic evolution due to the breakdown of the singlet state of pH$_2$ was able to be observed using a benchtop NMR spectrometer for the first time. The application of a spin-lock decoupling block during irradiation of the sample was shown to achieve

preservation of a pseudo-singlet state of pH$_2$ enabling for synchronous evolution of the magnetisation to occur. Using this technique the oscillation frequencies of the zero-quantum magnetisation were determined for the AA'XX' spin system *cis*−[Ru(H)$_2$(dppe)$_2$] to be (84.11 ± 0.05) Hz which strongly agreed with previously obtained values at obtained using a Nd:YAG laser and a 600 MHz spectrometer.[47] This value is representative of the symmetry breaking feature that causes the singlet state of pH$_2$ to breakdown and thus provides validation of the established fundamental theory of the PHIP effect.

An advantage observed for following magnetic evolution at low-field was that oscillations with a B$_0$ dependence (seen for systems with chemical inequivalence) will occur at a slower frequency. This was exemplified through the evolution of the AX spin system [Ru(H)$_2$(CO)$_2$(dpae)] which was found to evolve in C$_6$D$_6$ at (17.24 ± 0.08) Hz at 43.3 MHz rather than at 241 Hz (which was observed at 600 MHz).[48] This feature enabled the observation of [Ir(H)$_2$(CO)(PPh$_3$)$_2$I] (with an oscillation frequency of (280.9 ± 1.2) Hz) and [Ir(H)$_2$(^{13}CO)(PPh$_3$)$_2$I] (with oscillations observed at (303.0 ± 0.06) and (257.7 ± 0.08) Hz) which would oscillate a frequencies that are currently outside of the time resolution of the high-field approach. Through these studies, the use of photochemical pump - NMR probe experiments at low-field were validated and shown to be a low-cost, portable technique that produces competitive results to the currently published methods.

A natural progression for this research is to observe the magnetic evolution of heteronuclei using the photochemical pump - NMR probe approach (with high-field research demonstrating this concept with oscillations of ^{31}P signals within *cis*−[Ru(H)$_2$(dppe)$_2$]).[47] Of the heteronuclear channels available on the Spinsolve Carbon, the observation of oscillations of ^{13}C would be interesting as this could be applied to observe the CO group within [IrI(H)$_2$(CO)(PPh$_3$)$_2$]. Developing this experiment would provide an additional challenge as the lower inherent sensitivity and abundance of ^{13}C would require the pulse sequence to be modified to include polarisation transfer (for example through an INEPT pulse sequence block)[254] from ^{1}H to ^{13}C.

Another area of potential investigation is the observation of chemical evolution using the *in situ* irradiation approach. While currently inaccessible, due to the ill-defined starting point of the reaction within the irradiation period, the development of a spoiler pulse that destroys any pre-existing hyperpolarised signal could provide a route to overcome this limitation.[248,249] Alternatively, switching the light source to a

laser would provide a precise and synchronous starting point at the cost of increasing the complexity and expense of the system.

8 Experimental

8.1 Instrumentation

8.1.1 NMR Spectrometers

All high-field NMR experiments were performed on a 9.4 T AVIII spectrometer (Bruker, USA) with ^{1}H at 400.1 MHz and ^{31}P at 161.9 MHz. Prior to experimentation, the temperature of the spectrometer was set to 301.5 K (unless otherwise stated) following which the spectrometer was locked, tuned and shimmed using the experimental sample.

All benchtop NMR reaction monitoring experiments were performed on a 1 T (43 MHz) Spinsolve Carbon spectrometer (Magritek, Germany). The internal temperature of this spectrometer is fixed at 301.5 K and so all measurements were recorded at this temperature. Prior to experimentation, the spectrometer was locked, shimmed (to ensure a FWHM of <0.5ppm prior to spectral acquisition) and frequency calibrated using a 10:90 H_2O:D_2O reference sample.

Full details about the *ex situ* and *in situ* irradiation setups used with the benchtop NMR spectrometer can be found within the Instrumentation sections of Chapters 5 and 6 respectively.

8.1.2 *p*H_2 Generation

The *p*H_2 used within the experiments was generated using an in-house designed rig capable of generating up to >99% purity of *p*H_2. This is achieved through passing

H_2 gas over a paramagnetic catalyst (to allow for spin-spin interconversion) at low temperatures which favour the lowest-energy *p*H_2 spin isomer. The rig is cooled by a closed helium refrigeration system that is able to provide temperatures down to 7 K. The cooler is attached to a copper block which houses a void filled with activated charcoal (acting as the paramagnetic catalyst). Stainless steel tubing connects the base of this block to an external cylinder of H_2 (with an inlet pressure regulated to 3 bar) and the top to an outlet with an adaptor that fits Young's tap NMR tubes. For >99% purity of *p*H_2, the rig is held at 28 K. The temperature of the copper block is monitored and maintained within ±0.1 K of the desired temperature using a heater. Further details about the *p*H_2 production method are given in previous literature from Blazina *et al.*[237] and Richardson *et al.* .[195] Unless otherwise stated, a fixed pressure of (4.0 ± 0.1) bar of *p*H_2 is used within PHIP experiments which is checked during experiments using a MKS Baratron pressure gauge.

8.1.3 Analytical Techniques

IR spectra collected for characterisation of iridium complexes were collected using a Bruker Tensor 37 FT-IR spectrometer. Spectra were collected using the ATR accessory and were obtained between 450 - 4000 cm^{-1}.

UV spectra collected for *trans*-[IrCl(CO)(PPh_3)$_2$] and [Ir(H)$_2$(CO)(PPh_3)$_2$Cl] were collected using a Thermo Scientific Evolution Array UV/VIS Spectrophotometer. Spectra were collected using a quartz cell with a 1 cm pathlength and were obtained between 185 - 1100 nm.

8.2 General Experimental Procedures

8.2.1 Substrates and Solvents

The iridium complexes used within this thesis, *trans*-[IrCl(CO)(PPh_3)$_2$], *trans*-[IrCl(CO)(PBn_3)$_2$], *trans*-[IrI(CO)(PPh_3)$_2$] and *trans*-[IrI(^{13}CO)(PPh_3)$_2$] were synthesised as part of the research. The synthesis and characterisation for each complex are given in Section 8.4. The ruthenium complexes used,

cis−[Ru(H)$_2$(dppe)$_2$], [Ru(H)$_2$(CO)(PPh$_3$)$_3$] and [Ru(CO)$_3$(dpae)], were synthesised by previous members of the research group. Select characterisation information and literature references for these complexes are also given in Section 8.4.

Starting materials for iridium complex synthesis were purchased from Sigma-Aldrich (aniline), Precious Metals Online (iridium(III) chloride 3-hydrate), Fissons (sodium iodide) or synthesised by other members of the research group ([IrCl(COD)]$_2$). All solvents used within the syntheses were purchased from Sigma-Aldrich.

For the study performed on mixtures of Vaska's complex and PR$_3$ type ligands (found in Chapter 4), all PR$_3$ type ligands (PPh$_3$, P(*p*−C$_6$H$_4$OMe)$_3$, P(*p*−C$_6$H$_4$F)$_3$, P(*p*−C$_6$H$_4$(CF$_3$)$_3$, P(*p*−C$_6$F$_5$)$_3$, PCy$_3$, P(*p*−C$_{10}$H$_7$)$_3$, P(Cy)(Ph)$_2$ and PBn$_3$) were purchased from Sigma-Aldrich.

The NMR solvent, benzene-d_6, was purchased from Sigma-Aldrich. Aliquots of the solvent (10 - 15 mL) were transferred into a dried J Young sample flask under an N$_2$ atmosphere using a glass Luer-lock syringe (20 mL volume). The solvent was stored within a glovebox under an N$_2$ atmosphere.

8.2.2 PHIP Sample Preparation

Unless otherwise stated, samples for PHIP experiments were prepared as follows. The required mass of bulk analyte was weighed out (on the workbench for air-stable analytes, within a glovebox for air-sensitive analytes) and transferred into a glovebox under an N$_2$ atmosphere. The bulk analyte was then dissolved in benzene-d_6 to produce the desired concentration of the sample. 0.6 mL aliquots of this mixture were then transferred into 5 mm NMR tubes fitted with a J Young tap. Solvent transfer steps were performed using glass Luer-lock syringes.

The prepared samples were degassed using a freeze-pump-thaw method[176] on a high-vacuum line using a liquid nitrogen bath to freeze the samples. This process was repeated in triplicate to ensure the sample had been degassed sufficiently.

For the methanol thermometer experiments (Chapter 4), the 0.6 mL sample of MeOH was prepared and degassed using a freeze-pump-thaw method with a dry

ice/acetone bath.

Details about the experiments performed using these samples are given within relevant sections of the thesis.

8.3 Data Analysis

8.3.1 Spectral Characterisation

For both high-field and low-field NMR spectra, chemical shift values are given in ppm and are referenced to known chemical shift of the residual solvent peak (7.16 ppm for C_6D_6 and 4.78 ppm for MeOH in ^1H spectra). J coupling values are provided in Hz. For characterisation data, multiplicities are defined as either singlet (s), doublet (d), triplet (t) or multiplet (m).

8.3.2 Mean and Error Calculation

For experiments performed with repeat measurements, the mean ($\bar{x}$) of n repeats (x_n) was calculated using Equation 8.1. The standard deviation (SD) for the set of measurements was calculated using Equation 8.1. The error within the measurements (δ) could then be calculated using Equation 8.1.

$$\bar{x} = \frac{\Sigma x_n}{n} \tag{8.1}$$

$$SD = \sqrt{\frac{\Sigma(x_n - \bar{x})^2}{n-1}} \tag{8.2}$$

$$\text{Error} = \frac{SD}{\sqrt{n}} \tag{8.3}$$

In instances when calculations involved the addition of two values which possess their own errors, error propagation was achieved through use of Equation 8.4 where δz is the error of the new value and δx/δy are the errors associated with the original values.[255]

$$\delta z = \sqrt{(\delta x)^2 + (\delta y)^2} \tag{8.4}$$

Calculations of percentage difference between literature values (x_{lit}) and experimental values (x_{ref}) were performed using Equation 8.5.

$$\%\text{Difference} = \frac{x_{lit} - x_{ref}}{x_{lit}} \times 100 \tag{8.5}$$

8.3.3 SNR Calculations

SNR was calculated from the ratio of the observed maximum NMR signal (S) to the standard deviation of the spectral noise (Equation 8.6). The noise used within the calculation was measured between 11 and 26 ppm in the ^{1}H spectra as no NMR signals are observed within this range for the systems observed.

$$SNR = \frac{S}{SD_{noise}} \tag{8.6}$$

8.3.4 Non-linear Data Analysis

All non-linear data analysis was performed using OriginPro 2022 with the in-built non-linear fit tool. For reaction monitoring experiments, fitting was performed using the "ExpDec1" function (Equation 8.7) where y_0 is the y-offset, A_0 is the initial amplitude and t is the time constant. By taking the reciprocal of t, the k_{obs} for the reaction was obtained.

$$y = y_0 + A_0 e^{\frac{-x}{t}} \tag{8.7}$$

For magnetic evolution analysis, fitting was performed using the "SineDamp" function (Equation 8.8) where y_0 is a y-offset, A_0 is the initial amplitude, t_0 is the decay constant, x_c is the phase shift and w is the period. The period is then converted into oscillation frequency using $\nu = \frac{1}{2w}$.

$$y = y_0 + A_0 e^{(-x/t_0)} \sin\left(\pi \frac{x - x_c}{w}\right) \tag{8.8}$$

8.3.5 Software used for Coding

Pulse Sequence Design

All pulse sequences and macros build for use on the Spinsolve Carbon spectrometer were coded within the in-built programming language of the Spinsolve software, referred to as Prospa. The pulse sequences were designed to function within Spinsolve Expert Version 1.25.

MATLAB Implementation

The simulation of the reaction between pH$_2$ and Vaska's complex that was used when analysing the effect of relaxation of PHIP signals on the rate constant (Section 4.1) was originally designed within MATLAB R2018b.

To simulate spectra, the Spinach NMR simulation package for MATLAB was employed. This toolkit, developed and maintained by the research group of Ilya Kuprov, uses Liouville space simulations of spin systems to propagate a system through an NMR experiment, allowing for many liquid-state NMR experiments to be examined computationally.[177] To perform these simulations, experimentally obtained parameters for the require chemical species were stated (chemical shifts and J coupling constants) and the in-built pulse and acquire experiment (named

"hp_acquire"). To simulate standard, PASADENA and ALTADENA conditions, the starting density operator was modified within the experiment to the required combination of product operators.

Arduino Implementation

Code for the Arduino Nano board (discussed in Chapter 6, shown in Appendix A) was written within Arduino IDE Version 1.8.16. No additional libraries are required to be downloaded for the code to run.

8.4 Synthesis and Characterisation of Complexes

8.4.1 Synthesis of Vaska's Complex, *trans*-[$IrCl(CO)(PPh_3)_2$]

The synthetic procedure followed was modified and scaled down from a literature method reported by Collman *et al.*[174]

A roundbottomed flask was charged with iridium(III) chloride 3-hydrate (1.41 g, 0.004 mol) and triphenylphosphine (5.25 g, 0.02 mol). This mixture was dissolved in N,N-dimethylformaldehyde (60 mL) before addition of aniline (1.6 mL). The solution was stirred and heated to a vigourous reflux for 6 h. The resultant orange solution underwent hot filtration followed by rapid addition of warmed methanol (120 mL). The mixture then was cooled in an ice bath, filtered *in vacuo* and washed with methanol (10 mL) and diethyl ether (10 mL) to yield crude yellow crystals (2.30g, 73.7%). The crude product was heated (100 °C) *in vacuo* overnight to remove oxygen adduct by-products. Further purification was performed by dissolving the product in warm chloroform (100 mL) under an N_2 atmosphere, followed by filtering of any solid impurities and precipitation of the product using methanol (300 mL). The solution was filtered, dried and the solid yellow crystals were collected and stored (1.08 g, 35%). ^{1}H NMR (400 MHz, C_6D_6) δ: 7.96 (m, 12H, *o*-Ph), 7.03 (m, 18H, *m*-Ph and *p*-Ph). $^{31}P\{^1H\}$ NMR (162 MHz, C_6D_6) δ: 24.5. IR (ATR, cm^{-1}): 1949 (ν_{CO}).

Upon addition of H_2, $[Ir(H)_2(CO)(PPh_3)_2Cl]$ is formed. ^{1}H NMR (400 MHz, C_6D_6)

δ: 7.91 (m, 12H, *o*-Ph), 7.02 (m, 12H, *m*-Ph), 6.96 (m, 6H, *p*-Ph), -6.70 (td, 1H, J_{HP} = 17.6 Hz, J_{HH} = 4.6 Hz), -17.49 (td, 1H, J_{HP} = 13.9 Hz, J_{HH} = 4.6 Hz). $^{31}P\{^{1}H\}$ NMR (162 MHz, C_6D_6) δ: 9.9.

8.4.2 Synthesis of *trans*-[IrCl(CO)(PBn_3)$_2$]

The synthetic route to prepare *trans*-[IrCl(CO)(PBn_3)$_2$] was modified from a procedure by Burk *et al.*[199] for the synthesis of Vaska's complex derivatives.

Within a glove box, a round-bottomed flask was charged with [IrCl(cod)]$_2$ (101 mg, 0.15 mmol) and PBn_3 (183 mg, 0.60 mmol) dissolved in hexane/DCM (50:50 v/v, 20 mL). The solution was stirred for 10 min and then removed from the glovebox and placed under a a static pressure of CO (1 atm). After 1 h of stirring, the solution was concentrated *in vacuo* and then filtered to give the product. The precipitate was washed with hexane (3 x 10 mL) and dried *in vacuo* to give a pale yellow powder (173 mg, 67%). ^{1}H NMR (400 MHz, C_6D_6) δ: 7.13 (m, 12H, o-Ph), 7.09 (m, 18H, m-Ph and p-pH), 3.48 (d, 6H, J = 2.4 Hz, CH), 3.47 (d, 6H, J = 2.4 Hz, CH). $^{31}P\{^{1}H\}$ NMR (162 MHz, C_6D_6) δ: 12.7. IR (ATR, cm^{-1}): 1959 (ν_{CO}).

Upon addition of H_2, [Ir(H)$_2$(CO)(PBn_3)$_2$Cl] is formed. ^{1}H NMR (400 MHz, C_6D_6) δ: 7.14 (m, 12H, *o*-Ph), 7.09 (m, 18H, *m*-Ph and *p*-Ph), 3.43 (d, 6H, J = 2.4 Hz, CH), 3.41 (d, 6H, J = 2.4 Hz, CH), -8.37 (td, 1H, J_{HP} = 18.5 Hz, J_{HH} = 4.9 Hz), -19.61 (td, 1H, J_{HP} = 12.4 Hz, J_{HH} = 4.9 Hz). $^{31}P\{^{1}H\}$ NMR (162 MHz, C_6D_6) δ: 9.1.

8.4.3 Synthesis of *trans*-[IrI(CO)(PPh_3)$_2$]

trans-[IrI(CO)(PPh_3)$_2$] was prepared by following the synthetic procedure of Chock *et al.*[256]

trans-[IrCl(CO)(PPh_3)$_2$] (102 mg, 0.13 mmol) was dissolved in C_6H_6 (10 mL) and combined with an eleven-fold excess of NaI (215 mg, 1.43 mmol) in ethanol (5 mL) under an N_2 atmosphere. The mixture was stirred for 1 h in darkness and then the crude product was obtained *in vacuo*. The residue was dissolved in a benzene-water mixture (75:25 v/v, 13 mL), the organic layer was separated and dried *in vacuo* to

obtain the final product (73 mg, 65%).^{1}H NMR (400 MHz, C_6D_6) δ: 7.96 (m, 12H, o-Ph), 7.01 (m, 18H, m-Ph and p-pH). $^{31}P\{^{1}H\}$ NMR (162 MHz, C_6D_6) δ: 20.7. IR (ATR, cm^{-1}): 1992 (ν_{CO}).

Upon addition of H_2, $[Ir(H)_2(CO)(PPh_3)_2I]$ is formed. ^{1}H NMR (400 MHz, C_6D_6) δ: 7.89 (m, 12H, *o*-Ph), 7.02 (m, 12H, *m*-Ph), 6.95 (m, 6H, *p*-Ph), -8.49 (td, 1H, J_{HP} = 17.4 Hz, J_{HH} = 4.2 Hz), -14.90 (td, 1H, J_{HP} = 13.7 Hz, J_{HH} = 4.2 Hz). $^{31}P\{^{1}H\}$ NMR (162 MHz, C_6D_6) δ: 5.4.

8.4.4 Synthesis of *trans*-[IrI(^{13}CO)(PPh_3)$_2$]

trans-$[IrI(^{13}CO)(PPh_3)_2]$ was prepared through the combination and modification of the synthetic routes for *trans*-$[IrCl(CO)(PBn_3)_2]$ and *trans*-$[IrI(CO)(PPh_3)_2]$.

A round-bottomed flask was charged with $[IrCl(COD)]_2$ (100 mg, 0.15 mmol) and PPh_3 (165 mg, 0.63 mmol) and placed under an N_2 atmosphere. The mixture was dissolved in hexane/DCM (50:50 v/v, 20 mL) and stirred for 10 min. The resulting solution was placed under a static pressure of ^{13}CO (1 atm) and stirred for 1 h. The solution was then concentrated and the precipitate formed was collected via filtration. The precipitate was washed with hexane (3 x 10 mL) and dried *in vacuo* to give *trans*-$[IrCl(^{13}CO)(PPh_3)_2]$ (149 mg, 64%).

trans-$[IrCl(^{13}CO)(PPh_3)_2]$ (100 mg, 0.13 mmol) was placed under an N_2 atmosphere and dissolved in benzene (15 mL). The solution was charged with NaI (199 mg, 1.33 mmol) in ethanol (6 mL) and stirred in the dark for 1 h. The resulting suspension was concentrated and the precipitate was dissolved in a benzene-water mixture (75:25 v/v, 13 mL). The organic layer was separated and dried *in vacuo* to give a pale yellow powder (86 mg, 76%). ^{1}H NMR (400 MHz, C_6D_6) δ: 7.96 (m, 12H, o-Ph), 7.01 (m, 18H, m-Ph and p-pH). $^{31}P\{^{1}H\}$ NMR (162 MHz, C_6D_6) δ: 20.7. IR (ATR, cm^{-1}): 1942 (ν_{CO}).

Upon addition of H_2, $[Ir(H)_2(^{13}CO)(PPh_3)_2I]$ is formed. ^{1}H NMR (400 MHz, C_6D_6) δ: 7.89 (m, 12H, *o*-Ph), 7.02 (m, 12H, *m*-Ph), 6.95 (m, 6H, *p*-Ph), -8.49 (dtd, 1H, J_{HC} = 42.5 Hz, J_{HP} = 17.4 Hz, J_{HH} = 4.2 Hz), -14.90 (tdd, 1H, J_{HP} = 13.7 Hz, J_{HH} = 4.2 Hz, J_{HC} = 2.3 Hz). $^{31}P\{^{1}H\}$ NMR (162 MHz, C_6D_6) δ: 5.4.

8.4.5 Previously Synthesised Ruthenium Complexes

The ruthenium complexes used within this thesis were previously synthesised and characterised by other members within the Duckett research group. For each complex, the synthesis route used is given. ^{1}H and ^{31}P NMR characterisation for the hydride regions of each complex collected during the preparation of this thesis are also provided.

$[Ru(H)_2(CO)_2(dpae)]$

$[Ru(H)_2(CO)_2(dpae)]$ was synthesised through reaction of $[Ru(CO)_3(dpae)]$ with H_2. $[Ru(CO)_3(dpae)]$ was prepared following the literature procedure for the synthesis of $[Ru(CO)_3(dppe)]$.[257] Select characterisation for $[Ru(H)_2(CO)_2(dpae)]$ is as follows: ^{1}H NMR (400 MHz, C_6D_6) δ: -7.35 (d, 1H, J_{HH} = 4.7 Hz), -7.74 (d, 1H, J_{HH} = 4.7 Hz). Full NMR characterisation of both complexes ($[Ru(CO)_3(dpae)]$, $[Ru(H)_2(CO)_2(dpae)]$) are given by Adams *et al.*[239]

cis−$[Ru(H)_2(dppe)_2]$

cis−$[Ru(H)_2(dppe)_2]$ was synthesised according to a procedure by Nolan *et al.*[258] This synthesis pathway results in a distribution of *cis* and *trans* isomers of the complex. The trans isomer (observed at -8.1 ppm in ^{1}H NMR) does not hyperpolarise (has magnetic and chemical equivalence) and so does not appear within PHIP spectra. Select characterisation for the *cis* isomer is as follows: ^{1}H NMR (400 MHz, C_6D_6) δ: -8.33 (m, 2H). ^{31}P{^{1}H} NMR (162 MHz, C_6D_6) δ: 79.5 (t, 2P, J_{PP} = 16 Hz), 65.5 (t, 2P, J_{PP} = 16 Hz). Full NMR characterisation of the complexes is given by Bautista *et al.*[259]

$[Ru(H)_2(CO)(PPh_3)_3]$

$[Ru(H)_2(CO)(PPh_3)_3]$ was synthesised according to a procedure by Ahmad *et al.*[260] Select characterisation for the complex is as follows: ^{1}H NMR (400 MHz, C_6D_6) δ: -6.46 (tdd, 1H, J_{HP} = 31, 15 Hz, J_{HH} = 6 Hz), -8.3 (dtd, 1H, J_{HP} = 74, 29 Hz, J_{HH} = 6 Hz).

$^{31}P\{^{1}H\}$ NMR (162 MHz, C_6D_6) δ: 57.4 (d, 2P, J_{PP} = 17 Hz), 45.3 (t, 1P, J_{PP} = 17 Hz). Full NMR characterisation of the complexes is given by Hallman *et al.*[261]

Abbreviations

oH_2	*ortho*hydrogen.
pH_2	*para*hydrogen.
1D	1 Dimensional.
2D	2 Dimensional.
ALTADENA	Adiabatic Longitudinal Transport After Dissociation Engenders Nuclear Alignment.
Avg.	Average.
CAD	Computer Aided Design.
COD	*cis,cis*-1,5-Cyclooctadiene.
d	doublet.
DCM	Dichloromethane.
DEPT	Distortionless Enhancement by Polarisation Transfer.
DNP	Dynamic Nuclear Polarisation.
dpae	1,2-Bis(diphenylarsino)ethane.
dppe	1,2-Bis(diphenylphosphino)ethane.
DQ	Double Quantum.
EC	Experimental Control.
EPR	Electron Paramagnetic Resonance.
eq.	equivalents.
FID	Free Induction Decay.
FT	Fourier Transform.
FWHM	Full Width Half Maximum.
h	hour.

HPLC	High-performance Liquid Chromatography.
Hz	Hertz.
IFE	Inner Filter Effect.
INEPT	Insensitive Nuclei Enhanced by Polarisation Transfer.
IR	InfraRed.
m	meta.
m	multiplet.
MeOH	Methanol.
min	minute.
MQ	Multiple Quantum.
MS	Mass Spectrometry.
NC	Normally Closed.
NMR	Nuclear Magnetic Resonance.
NO	Normally Open.
nOe	Nuclear Overhauser Effect.
o	ortho.
OPSY	Only *Para*hydrogen SpectroscopY.
p	para.
PASADENA	*Para*hydrogen And Synthesis Allows Dramatically Enhanced Nuclear Alignment.
Ph	Phenyl (C_6H_5).
PHIP	*Para*Hydrogen Induced Polarisation.
ppb	parts per billion.
ppm	parts per million.
PSC	Pulse Sequence Control.
RASER	Radiofrequency Amplification by Stimulated Emission of Radiation.
RF	Radiofrequency.
ROCHESTER	Rates of Catalytic Hydrogenation Estimated Spectroscopically Through Enhanced Resonances.

SABRE	Signal Amplification by Reversible Exchange.
SEOP	Spin-Exchange Optical Pumping.
SNR	Signal-to-Noise Ratio.
SPDT	Single Point Double Throw.
SQ	Single Quantum.
t	triplet.
TR	Time Resolved.
UV	UltraViolet.
v/v	volume per volume.
ZQ	Zero Quantum.

Appendices

A MATLAB Hyperpolarised Relaxation Simulation

```
function [x] = Optimising_PHIP_Simulation_Demo
%% Definition of parameters

%Experimental Parameters
kobs = 0.01; % kobs of reaction
R1 = 1.5; %R1 Relaxation rate of hyperpolarisation
Vaska0 = 0.000427; %Concentration of starting material
Leftover = 0.5; %Proportion of signal destroyed upon detection

%Simulation Sampling Parameters
TotTime = 640; %Total time of reaction, in s
Interval = 0.1; %Timestep for simulation, in s
SamplingRate = 5; %How often NMR detection is performed, in s
NoPoints = SamplingRate/Interval; %How many steps NMR detections

%Setting up of data storage
Time = 0:Interval:TotTime;
TotalPoints = length(Time);
Sampling = SamplingRate:SamplingRate:TotTime;
Samples = length(Sampling);
Detect = zeros(Samples,1);
Spectrum = zeros(Samples,1);
Datapoints = length(Spectrum);

%Simulation concentration storage
Vaska = zeros(TotalPoints,1); %Conc. of Starting Material
VaskaH2 = zeros(TotalPoints,1); %Conc. of Product
VaskaH2hyp = zeros(TotalPoints,1); %Conc. of Hyp. Product for Experiment without NMR
    detection
VaskaH2hypDetect = zeros(TotalPoints,1); %Conc. of Hyp. Product for Experiment with
    NMR detection

%Setting up noise
NoiseStart = ((Vaska0*Interval*kobs)/62);
Noise = -NoiseStart + (NoiseStart+NoiseStart)*rand(Samples,1);

%Initial state of system
Vaska(1) = Vaska0;
VaskaH2(1) = 0;
VaskaH2hyp(1) = 0;
Sample_count = 0;
Detect_count = 0;
```

```
%% Start of simulation

for nn = 2:TotalPoints
    %Evolve starting material and product concentrations
    Sample_count = Sample_count + 1;
    Vaska(nn) = Vaska(nn-1) - (Vaska(nn-1)*Interval*kobs);
    VaskaH2(nn) = VaskaH2(nn-1) + (Vaska(nn-1)*Interval*kobs);

    %Check to see if hyperpolarised product exists
    Hyp_test = VaskaH2hyp(nn-1)*Interval*R1;

    %Loop for hyperpolarised signal variation without detection
    if Hyp_test == VaskaH2hyp(nn-1)
        %No hyp product exists so only new product is formed
        VaskaH2hyp(nn) = (Vaska(nn-1)*Interval*kobs);
    else
        %Hyperpolarised product exists so formation and relaxation occur
        VaskaH2hyp(nn) = (VaskaH2hyp(nn-1)- (VaskaH2hyp(nn-1)*Interval*R1)) + (Vaska(
            nn-1)*Interval*kobs);
    end

    %Loop for hyperpolarised signal variation with detection
    if Sample_count == NoPoints
        %Reset counter for detection
        Sample_count = 0;
        %Progress counter for spectral acquisition
        Detect_count = Detect_count + 1;

        %Hyperpolarised signal is detected and leftover parameter applied
        if Hyp_test == VaskaH2hypDetect(nn-1)
            Detect(Detect_count) = (Vaska(nn-1)*Interval*kobs)+Noise(Detect_count);
            VaskaH2hypDetect(nn) = Leftover*(Vaska(nn-1)*Interval*kobs);
        else
             Detect(Detect_count) = (VaskaH2hypDetect(nn-1) - (VaskaH2hypDetect(nn-1)
                 *Interval*R1)) + (Vaska(nn-1)*Interval*kobs)+Noise(Detect_count);
            VaskaH2hypDetect(nn) = Leftover*((VaskaH2hypDetect(nn-1) - (
                VaskaH2hypDetect(nn-1)*Interval*R1)) + (Vaska(nn-1)*Interval*kobs));
        end

        %Accumulate detected signal for product formation curve
        if Detect_count == 1
            Spectrum(Detect_count) = Detect(Detect_count);
        else
            Spectrum(Detect_count) = Detect(Detect_count) + Spectrum(Detect_count-1);
        end
    else
        %Hyperpolarised signal evolves without application of leftover term
        if Hyp_test == VaskaH2hypDetect(nn-1)
        VaskaH2hypDetect(nn) = (Vaska(nn-1)*Interval*kobs);
        else
        VaskaH2hypDetect(nn) = (VaskaH2hypDetect(nn-1) - (VaskaH2hypDetect(nn-1)*
            Interval*R1)) + (Vaska(nn-1)*Interval*kobs);
        end
    end
end
```

```
%% Plot data

%Plot datasets collected during simulation
figure('Name','Vaska Consumption and Vaska(H)2 Formation')
plot(Time,Vaska,'ok')
hold on
plot(Time,VaskaH2,'ob')
figure('Name','Hyperpolarised Vaska(H)2 Complex Build-up')
plot(Time,VaskaH2hyp,'or')
figure('Name','Build-up of Hyp with Detection')
plot(Time,VaskaH2hypDetect)
figure('Name','Detected Hyp Signal for Vaska(H)2')
plot(Sampling,Detect)
figure('Name','Cumulative Signal for Vaska(H)2')
plot(Sampling,Spectrum)

%% Determine observed rate constant

%Plot product concentration against time
SpectrumScaled = zeros(Samples,1);
for nn = 1:Datapoints
    SpectrumScaled(nn) = (Spectrum(nn)/Spectrum(Datapoints))*Vaska0;
end
plot(Sampling,SpectrumScaled)

% Fit product concentration against time
[xData, yData] = prepareCurveData(Sampling,SpectrumScaled);

% Set up fit type and options
ft = fittype( 'a*(1-exp(-kobs*x))', 'independent', 'x', 'dependent', 'y' );
opts = fitoptions( 'Method', 'NonlinearLeastSquares' );
opts.Display = 'Off';
opts.Lower = [0 0];
opts.StartPoint = [0 0.01];

% Fit model to data.
[fitresult, gof] = fit( xData, yData, ft, opts );

% Plot fit with data.
figure( 'Name', 'Simulation Fit to Exponential' );
h = plot( fitresult, xData, yData );
legend( h, 'y vs. x', 'kobs', 'Location', 'NorthEast' );

%Print the obtained value of kobs
SimCoeff = coeffvalues(fitresult);
SimRate = SimCoeff(2)
end
```

B Vendor Provided Spectral Irradiance Plots of Lamp Sources

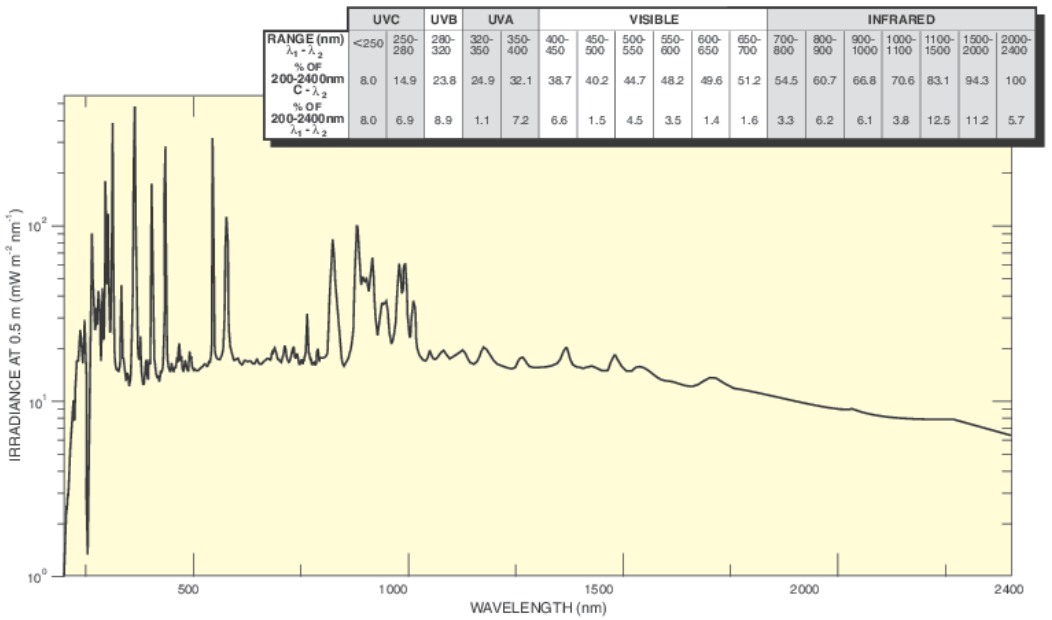

Figure B.1: Spectral irradiance plot of the output of an Oriel 200 W Hg-Xe lamp. Image courtesy of Newport Corporation (www.newport.com).

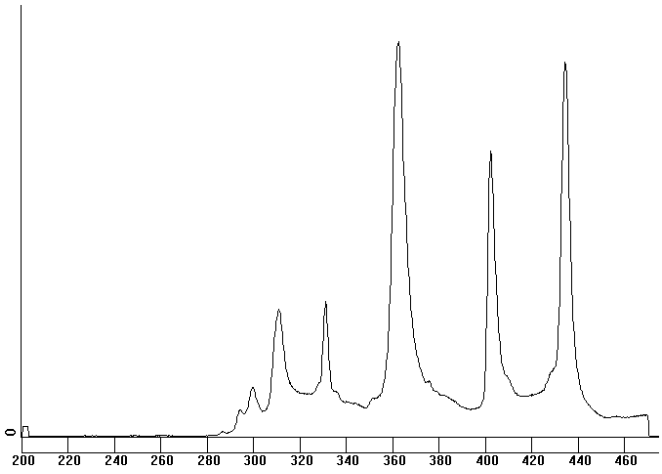

Figure B.2: Spectral irradiance plot of the output of a Dymax Bluewave 75 lamp. Image courtesy of Intertronics (www.intertronics.co.uk).

C Lamp Shutter Control: Arduino Code

```
1  //Code for Pump-Probe Experiments Involving Prospa-Arduino Communications.
2
3  //Definition of all experimental variables.
4  const int RELAY_PIN = 2;
5  int currentMillis;
6  int startMillis;
7  String dInput = "500";
8  int dIrrad = "500";
9  int start;
10 int finish;
11 int dur;
12 char input;
13
14 //Initial Arduino setup (Runs once).
15 //Opens up serial connection to PC and sets PIN 2 (connected to relay) as an output.
16 void setup() {
17 Serial.begin(19200);
18 Serial.println("Ready");
19 pinMode(RELAY_PIN, OUTPUT);
20 }
21
22 //Main Arduino loop (Runs continuously).
23 //Runs handleSerial command then checks current shutter time.
24 //If shutter open for over 30 s, shutter closes as a safety measure.
25
26 void loop() {
27   handleSerial();
28   currentMillis = millis();
29   if(currentMillis-startMillis > 30000){
30     digitalWrite(RELAY_PIN,LOW);
31     startMillis = currentMillis;
32   }
33 }
34
35 //Handle Serial: Checks to see if any data from Serial port. If yes, will read and
       execute on input.
36 void handleSerial(){
37     if (Serial.available() > 0) {
38         input = Serial.read();
39 //Switch...case commands allow for different commands to be performed depending on
       serial input.
40 //Switch...case will react to inputs of 0,1,2,3,4 and 5 only.
41         switch(input){
42
43 //Case '0': Closes shutter.
44          case '0':
```

```
45            digitalWrite(RELAY_PIN,LOW);
46            finish = millis();
47          break;
48
49 //Case '1': Opens shutter. Resets internal timer to 0 seconds.
50          case '1':
51            digitalWrite(RELAY_PIN,HIGH);
52            start = millis();
53            startMillis = millis();
54          break;
55
56 //Case '2': Checks to see if shutter is open or closed and then prints result to
       serial.
57          case '2':
58            if(digitalRead(RELAY_PIN)== LOW){
59              Serial.println("Idle");}
60            else if(digitalRead(RELAY_PIN) == HIGH){
61              Serial.println("On");}
62            else{Serial.println("Error");}
63          break;
64
65 //Case '3': Allows user to set pre-defined irradiation delay for shutter to be open
       between 0 - 30 seconds.
66          case '3':
67            while(Serial.available() == 0){}
68            while(Serial.available() > 0){
69              dInput = (Serial.readString());
70              dIrrad = dInput.toInt();
71             if(dIrrad > 30000 || dIrrad < 0){
72                dIrrad = 1000;
73                Serial.println("NA");}
74              else{
75                Serial.println("SET");}}
76          break;
77
78 //Case '4': Automatically opens and closes shutter based on user input irradiation
       delay.
79          case '4':
80            digitalWrite(RELAY_PIN,HIGH);
81            start = millis();
82            delay(dIrrad);
83            digitalWrite(RELAY_PIN,LOW);
84            finish = millis();
85            startMillis = millis();
86          break;
87
88 //Case '5': Checks to see how long the shutter was open for. Prints result to serial.
89          case '5':
90            dur = finish - start;
91            Serial.println(dur);
92          break;}
93   }
94 }
```

D Lamp Shutter Control: Prospa Code

D.1 Prospa Code Part 1: Additional Procedures for Arduino Integration

```
1
2  ##########################
3  ####Initialise Arduino####
4  ##########################
5
6  procedure(initialiseArduino,port,baudrate,databits,parity,stopbit,STATUS)
7  # Open Arduino Connection
8     try
9        closeserial(port)
10    catch
11       message("Error","Unable to close "+port)
12    endtry
13
14    try
15       openserial(port,baudrate,databits,parity,stopbit)
16    catch
17       message("Error", "No arduino is connected to "+port)
18       abort("")
19    endtry
20
21 stat = :replytoArduino(port,STATUS)
22 pr("Initial status: $stat$\n")
23 endproc()
24
25
26
27 ######################
28 ####Close Arduino####
29 ######################
30
31 procedure(closeArduino)
32 closeserial("com3")
33 endproc()
34
35
36
37
38
39
```

```
40
41
42 ########################
43 ####Reply to Arduino####
44 ########################
45
46 procedure(replytoArduino,port,str)
47    writeserial(port,str)
48    pause(3)
49    rslt = readserial(port)
50 endproc(rslt)
51
52
53
54 ########################
55 ####Send to Arduino#####
56 ########################
57
58 procedure(sendtoArduino,port,str,dIrrad)
59    writeserial(port,str)
60    writeserial(port,dIrrad)
61    pause(3)
62    rslt = readserial(port)
63    pr(rslt)
64 endproc()
65
66
67
68 ########################
69 ####Write to Arduino####
70 ########################
71
72 procedure(writetoArduino,port,str)
73    writeserial(port,str)
74 endproc()
```

D.2 Prospa Code Part 2: Commands Required within a Pump-Probe Experiment

```
### 0) Define Before NMR Experiment (Required parameters in experiment) ###

 w1 = Pump Delay (in s)
 w2 = Probe Delay (in s)

### 1) Start of NMR Experiment ###
#Define serial connection
    port = "com3"
    baudrate = 19200
    databits = 8
    parity = "none"
    stopbit = "1"

#Define Arduino commands
    RUN = "1"
    STOP = "0"
    STATUS = "2"
    DELAY = "3"
    RUND = "4"
    TIME = "5"

### 2) Immediately Before Pulse Sequence  ###
#Open serial port connection to the Arduino
     :initialiseArduino(port,baudrate,databits,parity,stopbit,STATUS)

#Send delay to Arduino
     dIrrad = w1*1000
     :sendtoArduino(port,DELAY,"$dIrrad$")

#Open shutter on lamp for set delay
     start = time()
     :writetoArduino(port,RUND)

#Wait for pump pulse (w1) and then probe delay (w2) before acquisition
    pause(w1)
    pause(w2)
    end = time()

### 3) End of Pulse Sequence ###
#Define irradiation length from Arduino and Pump-Probe timing from Prospa
   durP = end - start
   durA = :replytoArduino(port,TIME)

#Save timings to data folder
   dur = matrix(2)
   dur = ["durP = $durP$","durA = $durA$"]
   cd("$dataDirectory$\\$expName$\\$expNr$")
   save("durations.par",dur)

#Close serial port connection to Arduino
   :closeArduino()
```

References

(1) M. P. Johnson, *Essays Biochem.*, 2016, **60**, 255–273.

(2) M. Boggio-Pasqua, C. F. Burmeister, M. A. Robb and G. Groenhof, *Phys. Chem. Chem. Phys*, 2012, **14**, 7912–7928.

(3) D. Phillips, *Photochem. Photobiol. Sci.*, 2010, **9**, 1589–1596.

(4) K. Plaetzer, B. Krammer, J. Berlanda, F. Berr and T. Kiesslich, *Lasers in Medical Science*, 2009, **24**, 259–268.

(5) M. Fischer, *Angew. Chem., Int. Ed. Engl.*, 1978, **17**, 16–26.

(6) A. Basso and P. Capurro, in *Photochemistry: Volume 48*, 2021, pp. 293–321.

(7) C. E. Wayne and R. P. Wayne, *Photochemistry*, Oxford University Press, Oxford, 1996.

(8) T. Maschmeyer, L. P. Yunker and J. E. Hein, *React. Chem. Eng.*, 2022, **7**, 1061–1072.

(9) T. Rob and D. J. Wilson, *Eur. J. Mass. Spectrom.*, 2012, **18**, 205–214.

(10) G. Gauglitz and W. Schmid, *Chromatographia*, 1987, **23**, 395–400.

(11) H. Kodamatani, Y. Iwaya, M. Saga, K. Saito, T. Fujioka, S. Yamazaki, R. Kanzaki and T. Tomiyasu, *Anal. Chim. Acta*, 2017, **952**, 50–58.

(12) B. Li, W. Guo, H. Chi, M. Kimura and E. D. Ramsey, *Chromatographia*, 2017, **80**, 1179–1188.

(13) B. Behera and P. Das, *MethodsX*, 2022, **9**, 101847.

(14) U. Sachs, G. Schaper, D. Winkler, D. Kratzert and P. Kurz, *Dalton Trans.*, 2016, **45**, 17464–17473.

(15) L. Zhu, S. Saha, Y. Wang, D. A. Keszler and C. Fang, *J. Phys. Chem. B*, 2016, **120**, 34.

(16) C. Fang, L. Tang, B. G. Oscar and C. Chen, *J. Phys. Chem. Lett*, 2018, **9**, 3.

(17) B. Roig, E. Touraud and O. Thomas, *Spectrochim. Acta. A Mol. Biomol. Spectrosc.*, 2002, **58**, 2925–2930.

(18) E. Stadler, A. Eibel, D. Fast, H. Freißmuth, C. Holly, M. Wiech, N. Moszner and G. Gescheidt, *Photochem. Photobiol. Sci*, 2018, **17**, 660.

(19) S. Sivakesava, J. Irudayaraj and D. Ali, *Process Biochem.*, 2001, **37**, 371–378.

(20) U. Holzgrabe, R. Deubner, C. Schollmayer and B. Waibel, *J. Pharm. Biomed.*, 2005, **38**, 806–812.

(21) R. W. Darbeau, *Appl. Spectrosc. Rev.*, 2006, **41**, 401–425.

(22) M. Khajeh, M. A. Bernstein and G. A. Morris, *Magn. Reson. Chem.*, 2010, **48**, 516–522.

(23) M. V. Gomez and A. De La Hoz, *Beilstein J. Org. Chem.*, 2017, **13**, 285–300.

(24) A. L. Dunn and C. R. Landis, *Magn. Reson. Chem.*, 2017, **55**, 329–336.

(25) D. A. Foley, A. L. Dunn and M. T. Zell, *Magn. Reson. Chem.*, 2016, **54**, 451–456.

(26) G. E. Ball, *Spectrosc. Prop. Inorg. Organomet. Compd.*, 2010, **41**, 262–287.

(27) C. Wolff, J. Kind, H. Schenderlein, H. Bartling, C. Feldmeier, R. M. Gschwind, M. Biesalski and C. M. Thiele, *Magn. Reson. Chem.*, 2016, **54**, 485–491.

(28) W. B. Swords, S. J. Chapman, H. Hofstetter, A. L. Dunn and T. P. Yoon, *J. Org. Chem*, 2022, **2022**, 11776–11782.

(29) Y. Ji, C. Bottecchia, F. Ois Lévesque, K. Narsimhan, D. Lehnherr, J. P. Mcmullen, S. M. Dalby, K.-J. Xiao and M. Reibarkh, *J. Org. Chem.*, 2022, **87**, 2055–2062.

(30) T. Paululat, M. Rabe and D. V. Berdnikova, *J. Magn. Reson.*, 2021, **327**.

(31) M. Thaning, M. H. Lerche, B. Fridlund, K. Golman, L. Hansson, J. H. Ardenkjaer-Larsen, G. Hansson, R. Servin and A. Gram, *Proc. Natl. Acad. Sci. U.S.A.*, 2003, **100**, 10158–10163.

(32) A. Abragam and M. Goldman, *Rep. Prog. Phys.*, 1978, **41**, 395–467.

(33) M. A. Bouchiat, T. R. Carver and C. M. Varnum, *Phys. Rev. Lett.*, 1960, **5**, 373–375.

(34) T. G. Walker and W. Happer, *Revi. Mod. Phys.*, 1997, **69**, 629–642.

(35) S. I. Hommeltoft, D. H. Berry and R. Eisenberg, *J. Am. Chem. Soc.*, 1986, **108**, 5345–5347.

(36) T. C. Eisenschmid, R. U. Kirss, P. P. Deutsch, S. I. Hommeltoft, R. Eisenberg, J. Bargon, R. G. Lawler and A. L. Balch, *J. Am. Chem. Soc.*, 1987, **109**, 8089–8091.

(37) C. R. Bowers and D. P. Weitekamp, *Phys. Rev. Lett.*, 1986, **57**, 2645–2648.

(38) R. A. Green, R. W. Adams, S. B. Duckett, R. E. Mewis, D. C. Williamson and G. G. Green, *Prog. Nucl. Magn. Reson. Spectrosc.*, 2012, **67**, 1–48.

(39) R. W. Adams, S. B. Duckett, R. A. Green, D. C. Williamson and G. G. Green, *J. Chem. Phys.*, 2009, **131**, 194505.

(40) S. K. Hasnip, S. A. Colebrooke, C. J. Sleigh, S. B. Duckett, D. R. Taylor, G. K. Barlow and M. J. Taylor, *J. Chem. Soc., Dalton Trans.*, 2002, 743–751.

(41) S. B. Duckett and R. E. Mewis, *Acc. Chem. Res.*, 2012, **45**, 1247–1257.

(42) S. B. Duckett and N. J. Wood, *Coord. Chem. Rev.*, 2008, **252**, 2278–2291.

(43) R. N. Perutz and B. Procacci, *Chem. Rev.*, 2016, **116**, 8506–8544.

(44) P. Nitschke, N. Lokesh and R. M. Gschwind, *Prog. Nucl. Magn. Reson. Spectrosc.*, 2019, **114-115**, 86–134.

(45) B. Procacci, P. M. Aguiar, M. E. Halse, R. N. Perutz and S. B. Duckett, *Chem. Sci.*, 2016, **7**, 7087–7093.

(46) B. Procacci, S. B. Duckett, M. W. George, M. W. Hanson-Heine, R. Horvath, R. N. Perutz, X. Z. Sun, K. Q. Vuong and J. A. Welch, *Organometallics*, 2018, **37**, 855–868.

(47) O. Torres, B. Procacci, M. E. Halse, R. W. Adams, D. Blazina, S. B. Duckett, B. Eguillor, R. A. Green, R. N. Perutz and D. C. Williamson, *J. Am. Chem. Soc.*, 2014, **136**, 10124–10131.

(48) M. E. Halse, B. Procacci, S. L. Henshaw, R. N. Perutz and S. B. Duckett, *J. Magn. Reson.*, 2017, **278**, 25–38.

(49) E. E. Brown, I. Mandzhieva, P. M. Tomhon, T. Theis and F. N. Castellano, *ACS Cent. Sci.*, 2022, **8**, 1548–1556.

(50) B. Blümich, *J. Magn. Reson.*, 2019, **306**, 27–35.

(51) E. Danieli, J. Mauler, J. Perlo, B. Blümich and F. Casanova, *J. Magn. Reson.*, 2009, **198**, 80–87.

(52) E. Danieli, J. Perlo, B. Blümich and F. Casanova, *Angew. Chem. Int. Ed.*, 2010, **49**, 4133–4135.

(53) K. Halbach, *Nucl. Instrum. Methods*, 1980, **169**, 1–10.

(54) H. Raich and P. Blümler, *Concept Magn. Reson. B*, 2004, **23**, 16–25.

(55) A. J. Parker, W. Zia, C. W. Rehorn and B. Blümich, *J. Magn. Reson.*, 2016, **265**, 83–89.

(56) K. Singh and B. Blümich, *Trends. Anal. Chem.*, 2016, **83**, 12–26.

(57) S. K. Küster, E. Danieli, B. Blümich and F. Casanova, *Phys. Chem. Chem. Phys.*, 2011, **13**, 13172–13176.

(58) B. Blümich, G. K. M. Verzijl, V. M. Litvinov, E. Danieli, F. Casanova, A. L. L. Duchateau, J. Perlo, A. L. L. Duchateau, G. K. M. Verzijl, V. M. Litvinov, B. Blümich and F. Casanova, *ChemPhysChem*, 2014, **15**, 3060–3066.

(59) P. Giraudeau and F. X. Felpin, *React. Chem. Eng.*, 2018, **3**, 399–413.

(60) M. V. Silva Elipe and R. R. Milburn, *Magn. Reson. Chem.*, 2016, **54**, 437–443.

(61) H. Kim, Y. Yonekura and J. I. Yoshida, *Angew. Chem. Int. Ed.*, 2018, **57**, 4063–4066.

(62) M. Goldbach, E. Danieli, J. Perlo, B. Kaptein, V. M. Litvinov, B. Blümich, F. Casanova and A. L. Duchateau, *Tetrahedron Lett.*, 2016, **57**, 122–125.

(63) S. T. Knox, S. Parkinson, R. Stone and N. J. Warren, *Polym. Chem.*, 2019, **10**, 4774–4778.

(64) M. Leutzsch, A. J. Sederman, L. F. Gladden and M. D. Mantle, *Magn. Reson. Imaging*, 2019, **56**, 138–143.

(65) E Danieli, J. Perlo, A. L. L. Duchateau, G. K. M. Verzijl, V. M. Litvinov, B. Blümich and F Casanova, *ChemPhysChem.*, 2014, **15**, 3060 –3066.

(66) K. Singh, E. Danieli and B. Blümich, *Anal. Bioanal. Chem.*, 2017, **409**, 7223–7234.

(67) W. G. Lee, M. T. Zell, T. Ouchi and M. J. Milton, *Magn. Reson. Chem.*, 2020, **58**, 1193–1202.

(68) K. A. Farley, U. Reilly, D. P. Anderson, B. P. Boscoe, M. W. Bundesmann, D. A. Foley, M. S. Lall, C. Li, M. R. Reese and J. Yan, *Magn. Reson. Chem.*, 2017, **55**, 348–354.

(69) Y. Chae, S. Min, E. Park, C. Lim, C. H. Cheon, K. Jeong, K. Kwak and M. Cho, *Anal. Chem.*, 2021, **93**, 2106–2113.

(70) D. Galvan, L. M. de Aguiar, J. J. R. Rohwedder, D. Borsato and M. H. M. Killner, *Fuel Process. Technol.*, 2020, **208**, 106511.

(71) L. Porwol, A. Henson, P. J. Kitson, D. L. Long and L. Cronin, *Inorg. Chem. Front.*, 2016, **3**, 919–923.

(72) J. F. Araneda, T. Mendonça Barbosa, P. Hui, M. C. Leclerc, J. Ma, A. F. Maier and S. D. Riegel, *J. Chem. Educ.*, 2021, **98**, 1227–1232.

(73) T. H. Rehm, C. Hofmann, D. Reinhard, H. J. Kost, P. Löb, M. Besold, K. Welzel, J. Barten, A. Didenko, D. V. Sevenard, B. Lix, A. R. Hillson and S. D. Riegel, *React. Chem. Eng.*, 2017, **2**, 315–323.

(74) B. Musio, E. Gala and S. V. Ley, *ACS Sustain. Chem. Eng.*, 2018, **6**, 1489–1495.

(75) B. Ahmed-Omer, E. Sliwinski, J. P. Cerroti and S. V. Ley, *Org. Process Res. Dev.*, 2016, **20**, 1603–1614.

(76) A. Friebel, E. Von Harbou, K. Münnemann and H. Hasse, *Ind. and Eng. Chem. Res.*, 2019, **58**, 18125–18133.

(77) B. Gouilleux, B. Charrier, E. Danieli, J. N. Dumez, S. Akoka, F. X. Felpin, M. Rodriguez-Zubiri and P. Giraudeau, *Analyst*, 2015, **140**, 7854–7858.

(78) B. Charrier, B. Gouilleux, S. Akoka, M. Rodriguez-Zubiri, P. Giraudeau and F.-X. Felpin, *TrAC Trends Anal. Chem.*, 2016, **83**, 65–75.

(79) T. Castaing-Cordier, D. Bouillaud, J. Farjon and P. Giraudeau, *Annu. Rep. NMR Spectrosc.*, 2021, **103**, 191–258.

(80) M. H. Levitt, *Spin Dynamics*, John Wiley & Sons Ltd, Chichester, 2nd, 2008.

(81) M. E. Halse, *Trends Anal. Chem.*, 2016, **83**, 76–83.

(82) K. H. Kim, J. W. Choi, C. S. Kim and K. Jeong, *Fuel*, 2019, **255**, 115845.

(83) K. Jeong, S. Min, H. Chae and S. K. Namgoong, *Magn. Reson. Chem.*, 2018, **56**, 1089–1093.

(84) K. Jeong, S. Min, H. Chae and S. K. Namgoong, *Magn. Reson. Chem.*, 2019, **57**, 44–48.

(85) D. Gołowicz, K. Kazimierczuk, M. Urbańczyk and T. Ratajczyk, *ChemistryOpen*, 2019, **8**, 196–200.

(86) K. Them, F. Ellermann, A. N. Pravdivtsev, O. G. Salnikov, I. V. Skovpin, I. V. Koptyug, R. Herges and J. B. Hövener, *J. Am. Chem. Soc.*, 2021, **143**, 13694–13700.

(87) B. Joalland, N. M. Ariyasingha, S. Lehmkuhl, T. Theis, S. Appelt and E. Y. Chekmenev, *Angew. Chem. Int. Ed.*, 2020, **59**, 8654–8660.

(88) N. M. Ariyasingha, B. Joalland, H. R. Younes, O. G. Salnikov, N. V. Chukanov, K. V. Kovtunov, L. M. Kovtunova, V. I. Bukhtiyarov, I. V. Koptyug, J. G. Gelovani and E. Y. Chekmenev, *Chem. Eur. J.*, 2020, **26**, 13621–13626.

(89) P. Spannring, I. Reile, M. Emondts, P. P. Schleker, N. K. Hermkens, N. G. van der Zwaluw, B. J. van Weerdenburg, P. Tinnemans, M. Tessari, B. Blümich, F. P. Rutjes and M. C. Feiters, *Chem. Eur. J.*, 2016, **22**, 9277–9282.

(90) A. B. Schmidt, H. De Maissin, I. Adelabu, S. Nantogma, J. Ettedgui, P. Tomhon, B. M. Goodson, T. Theis and E. Y. Chekmenev, *ACS Sens.*, 2022, **7**, 3430–3439.

(91) D. A. Barskiy, L. A. Ke, X. Li, V. Stevenson, N. Widarman, H. Zhang, A. Truxal and A. Pines, *J. Phys. Chem. Lett.*, 2018, **9**, 2721–2724.

(92) P. M. Richardson, S. Jackson, A. J. Parrott, A. Nordon, S. B. Duckett and M. E. Halse, *Magn. Reson. Chem.*, 2018, **56**, 641–650.

(93) J. F. Colell, A. W. Logan, Z. Zhou, R. V. Shchepin, D. A. Barskiy, G. X. Ortiz, Q. Wang, S. J. Malcolmson, E. Y. Chekmenev, W. S. Warren and T. Theis, *J. Phys. Chem. C*, 2017, **121**, 6626–6634.

(94) B. Chapman, B. Joalland, C. Meersman, J. Ettedgui, R. E. Swenson, M. C. Krishna, P. Nikolaou, K. V. Kovtunov, O. G. Salnikov, I. V. Koptyug, M. E. Gemeinhardt, B. M. Goodson, R. V. Shchepin and E. Y. Chekmenev, *Anal. Chem.*, 2021, **93**, 8476–8483.

(95) T. M. Alam, A. Duchowny, J. Denninger, L. Lohmann, T. Theis, S. Lehmkuhl and A. Adams, *Int. J. Mol. Sci.*, 2023, **24**, 2465.

(96) S. Nantogma, B. Joalland, K. Wilkens and E. Y. Chekmenev, *Anal. Chem.*, 2021, **12**, 30.

(97) S. Lehmkuhl, M. Wiese, L. Schubert, M. Held, M. Küppers, M. Wessling and B. Blümich, *J. Magn. Reson.*, 2018, **291**, 8–13.

(98) P. M. Richardson, A. J. Parrott, O. Semenova, A. Nordon, S. B. Duckett and M. E. Halse, *Analyst*, 2018, **143**, 3442–3450.

(99) A. D. Robinson, P. M. Richardson and M. E. Halse, *Appl. Sci.*, 2019, **9**, 1173.

(100) I. Adelabu, P. TomHon, M. S. Kabir, S. Nantogma, M. Abdulmojeed, I. Mandzhieva, J. Ettedgui, R. E. Swenson, M. C. Krishna, T. Theis, B. M. Goodson and E. Y. Chekmenev, *ChemPhysChem*, 2022, **23**, 131–136.

(101) O. G. Salnikov, N. V. Chukanov, A. Svyatova, I. A. Trofimov, M. S. Kabir, J. G. Gelovani, K. V. Kovtunov, I. V. Koptyug and E. Y. Chekmenev, *Angew. Chem. Int. Ed.*, 2021, **60**, 2406–2413.

(102) J. R. Birchall, M. S. Kabir, O. G. Salnikov, N. V. Chukanov, A. Svyatova, K. V. Kovtunov, I. V. Koptyug, J. G. Gelovani, B. M. Goodson, W. Pham and E. Y. Chekmenev, *Chem. Commun.*, 2020, **56**, 9098–9101.

(103) A. I. Silva Terra, M. Rossetto, C. L. Dickson, G. Peat, D. Uhrín and M. E. Halse, *ACS Meas. Sci. Au*, 2023, **3**, 73–81.

(104) H. Chae, S. Min, H. J. Jeong, S. K. Namgoong, S. Oh, K. Kim and K. Jeong, *Anal. Chem.*, 2020, **92**, 10902–10907.

(105) O. Semenova, P. M. Richardson, A. J. Parrott, A. Nordon, M. E. Halse and S. B. Duckett, *Anal. Chem.*, 2019, **91**, 6695–6701.

(106) P. M. Richardson, W. Iali, S. S. Roy, P. J. Rayner, M. E. Halse and S. B. Duckett, *Chem. Sci.*, 2019, **10**, 10607–10619.

(107) T. Tennant, M. C. Hulme, T. B. Robertson, O. B. Sutcliffe and R. E. Mewis, *Magn. Reson. Chem.*, 2020, **58**, 1151–1159.

(108) R. Sakla and D. A. Jose, *Inorganica Chim. Acta*, 2021, **516**, 120134.

(109) M. W. Dale, D. J. Cheney, C. Vallotto and C. J. Wedge, *Phys. Chem. Chem. Phys*, 2020, **22**, 28173.

(110) J. E. Bramham and A. P. Golovanov, *Commun. Chem.*, 2022, **5**, 1–10.

(111) P. B. Chock and J. Halpern, *J. Am. Chem. Soc.*, 1966, **88**, 3511–3514.

(112) P. J. Hore, *Nuclear Magnetic Resonance*, Oxford University Press, Oxford, 2015.

(113) B. M. Dale, M. A. Brown and R. C. Semelka, *MRI Basic Principles and Applications*, John Wiley & Sons, Chichester, 2015.

(114) H. Schwalbe, *Angew. Chem. Int. Ed.*, 2017, **56**, 10252–10253.

(115) M. Edgar, *Annu. Rep. Prog. Chem., Sect. B: Org. Chem*, 2012, **108**, 292–315.

(116) J. Keeler, *Understanding NMR Spectroscopy*, John Wiley and Sons, Chichester, 2010.

(117) A. W. Overhauser, *Phys. Rev.*, 1953, **92**, 411–415.

(118) T. R. Carver and C. P. Slichter, *Phys. Rev.*, 1953, **92**, 212–213.

(119) W. A. Anderson and R. Freeman, *J. Chem. Phys.*, 1962, **37**, 85–103.

(120) G. A. Morris and R. Freeman, *J. Am. Chem. Soc.*, 1979, **101**, 760–762.

(121) D. M. Doddrell, D. T. Pegg and M. R. Bendall, *J. Magn. Reson.*, 1982, **48**, 323–327.

(122) P. Nikolaou, B. M. Goodson and E. Y. Chekmenev, *Chem. Eur. J.*, 2015, **21**, 3156–3166.

(123) C. J. Gorter, *Phys. Z.*, 1934, **35**, 928.

(124) M. L. Hirsch, N. Kalechofsky, A. Belzer, M. Rosay and J. G. Kempf, *J. Am. Chem. Soc.*, 2015, **137**, 8428–8434.

(125) M. L. Hirsch, B. A. Smith, M. Mattingly, A. G. Goloshevsky, M. Rosay and J. G. Kempf, *J. Magn. Reson.*, 2015, **261**, 87–94.

(126) T. Maly, G. T. Debelouchina, V. S. Bajaj, K.-N. Hu, C.-G. Joo, M. L. Mak–Jurkauskas, J. R. Sirigiri, P. C. A. van der Wel, J. Herzfeld, R. J. Temkin and R. G. Griffin, *J. Chem. Phys.*, 2008, **128**, 052211.

(127) B. Plainchont, P. Berruyer, J. N. Dumez, S. Jannin and P. Giraudeau, *Anal. Chem.*, 2018, **90**, 3639–3650.

(128) J. Bargon, U. Johnsen and H. Fischer, *Z. Naturforsch. A.*, 1967, **22**, 1551–1555.

(129) F. R. Ward and R. G. Lawler, *J. Am. Chem. Soc.*, 1967, **89**, 5518–5519.

(130) M. Goez, *Concepts Magn. Reson.*, 1995, **7**, 69–86.

(131) K. H. Mok and P. J. Hore, *Methods*, 2004, **34**, 75–87.

(132) P. J. Rayner and S. B. Duckett, *Angew. Chem. Int. Ed.*, 2018, **57**, 6742–6753.

(133) W Pauli, *Z. Phys.*, 1925, **31**, 765–783.

(134) M. Born and J. R. Oppenheimer, *Ann. Phys.*, 1927, **389**, 457–484.

(135) J. Natterer and J. Bargon, *Prog. Nucl. Magn. Reson. Spectrosc.*, 1997, **31**, 293–315.

(136) A. H. Schmauch and G. E. Singleton, *Ind. Eng. Chem.*, 1964, **56**, 21–31.

(137) A. J. Parrott, P. Dallin, J. Andrews, P. M. Richardson, O. Semenova, M. E. Halse, S. B. Duckett and A. Nordon, *Appl. Spectrosc.*, 2019, **73**, 88–97.

(138) A. B. Schmidt, J. B. Hövener, C. R. Bowers, K. Buckenmaier, E. Y. Chekmenev, H. de Maissin, J. Eills, F. Ellermann, S. Glöggler, J. W. Gordon, S. Knecht, I. V. Koptyug, J. Kuhn, A. N. Pravdivtsev, F. Reineri, T. Theis and K. Them, *Anal. Chem.*, 2022, **94**, 479–502.

(139) B. A. Tom, S. Bhasker, Y. Miyamoto, T. Momose and B. J. McCall, *Rev. Sci. Instrum.*, 2009, **80**, 016108.

(140) M. Matsumoto and J. H. Espenson, *J. Am. Chem. Soc.*, 2005, **127**, 11447–11453.

(141) J. W. Leachman, R. T. Jacobsen, S. G. Penoncello and E. W. Lemmon, *J. Phys. Chem. Ref. Data*, 2009, **38**, 721.

(142) S. Wagner, *MAGMA*, 2014, **27**, 195–199.

(143) C. R. Bowers and D. P. Weitekamp, *J. Am. Chem. Soc.*, 1987, **109**, 5541–5542.

(144) M. G. Pravica and D. P. Weitekamp, *Chem. Phys. Lett.*, 1988, **145**, 255–258.

(145) M. Sender and D. Ziegenbalg, *Chem. Ing. Tech.*, 2017, **89**, 1159–1173.

(146) K Holz, J Lietard and M. M. Somoza, *ASC Sustainable Chem. Eng.*, 2017, **5**, 828–834.

(147) D. L. Andrews, *Lasers in Chemistry*, Springer, Berlin, 1997.

(148) R. N. Perutz, *Pure Appl. Chem.*, 1998, **70**, 2211–2220.

(149) M. C. Heitz, D. Guillaumont, I. Cote-Bruand and C. Daniel, *J. Organomet. Chem.*, 2000, **609**, 66–76.

(150) B. A. Arndtsen, R. G. Bergman, T. A. Mobley and T. H. Peterson, *Acc. Chem. Res.*, 1995, **28**, 154–162.

(151) B. J. Fisher and R. Elsenberg, *Organometallics*, 1983, **2**, 764–767.

(152) C. Giannotti and M. L. Green, *J. Chem. Soc., Chem. Commun.*, 1972, **0**, 1114b–1115.

(153) B. J. Tickner and V. V. Zhivonitko, *Chem. Sci.*, 2022, **13**, 4670–4696.

(154) M. S. Chinn and R. Eisenberg, *J. Am. Chem. Soc.*, 1992, **114**, 1908–1909.

(155) P. Hübler, R. Giernoth, G. Kümmerle and J. Bargon, *J. Am. Chem. Soc.*, 1999, **121**, 5311–5318.

(156) L. Vaska and J. W. DiLuzio, *J. Am. Chem. Soc.*, 1961, **83**, 2784–2785.

(157) M. Angoletta, *Gazz. Chim. Ital.*, 1959, **89**, 2359–2370.

(158) R. U. Kirss, *Bull. Hist. Chem.*, 2013, **38**, 52–60.

(159) L. Vaska and J. W. DiLuzio, *J. Am. Chem. Soc.*, 1962, **84**, 679–680.

(160) L Vaska, *Science*, 1963, **140**, 809–10.

(161) L. Vaska, *Acc. Chem. Res.*, 1968, **1**, 335–344.

(162) L. Vaska and R. E. Rhodes, *J. Am. Chem. Soc.*, 1965, **87**, 4970–4971.

(163) L. Vaska, *Science*, 1966, **152**, 771–773.

(164) Y. Une, A. Tahara, Y. Miyamoto, Y. Sunada and H. Nagashima, *Organometallics*, 2019, **38**, 852–862.

(165) S. K. Hasnip, S. B. Duckett, C. J. Sleigh, D. R. Taylor, G. K. Barlow and M. J. Taylor, *Chem. Commun.*, 1999, **0**, 1717–1718.

(166) B. A. Messerle, C. J. Sleigh, M. G. Partridge and S. B. Duckett, *J. Chem. Soc., Dalton Trans.*, 2005, 1429.

(167) R. Eisenberg, *Isr. J. Chem.*, 2017, **57**, 932–936.

(168) M. Selke and C. S. Foote, *J. Am. Chem. Soc.*, 1993, **115**, 1166–1167.

(169) G. L. Geoffroy, G. S. Hammond and H. B. Gray, *J. Am. Chem. Soc.*, 1975, **97**, 3933–3936.

(170) R. Ugo, A. Pasini, A. Fusi and S. Cenini, *J. Am. Chem. Soc.*, 1972, **94**, 7364–7370.

(171) A. L. Sargent, M. B. Hall and M. F. Guest, *J. Am. Chem. Soc.*, 1992, **114**, 517–522.

(172) A. L. Sargent and M. B. Hall, *Inorg. Chem.*, 1992, **31**, 317–321.

(173) C. A. Tolman, *Chem. Rev.*, 1977, **77**, 313–348.

(174) J. P. Collman, C. T. Sears, M. Kubota, A. Davison, E. T. Shawl, J. R. Sowa and R. J. Angelici, in *Inorganic Syntheses, Volume 28*, ed. R. J. Angelici, John Wiley & Sons Ltd, New York, 2007, pp. 92–94.

(175) P. P. Deutsch and R. Eisenberg, *Chem. Rev.*, 1988, **88**, 1147–1161.

(176) R. Shaver, S. Van Wallendael and D. P. Rillema, *J. Chem. Educ.*, 1991, **68**, 604.

(177) H. J. Hogben, M. Krzystyniak, G. T. Charnock, P. J. Hore and I. Kuprov, *J. Magn. Reson.*, 2011, **208**, 179–194.

(178) C. L. Young, in *IUPAC Solubility Data Series*, ed. C. L. Young, Pergamon Press, Oxford, 1981, vol. 5/6, pp. 159–160.

(179) W. Henry, *Phil. Trans. R. Soc.*, 1803, **93**, 29–274.

(180) P. Anastas and N. Eghbali, *Chem. Soc. Rev.*, 2010, **39**, 301–312.

(181) J. A. Aguilar, P. I. Elliott, J. López-Serrano, R. W. Adams and S. B. Duckett, *Chem. Commun.*, 2007, 1183–1185.

(182) J. A. Aguilar, R. W. Adams, S. B. Duckett, G. G. Green and R. Kandiah, *J. Magn. Reson.*, 2011, **208**, 49–57.

(183) A. N. Pravdivtsev, V. P. Kozinenko and J.-B. Ho, *J. Phys. Chem. A*, 2018, **122**, 8948–8956.

(184) S. Bussandri, L. Buljubasich and R. Acosta, *J. Magn. Reson.*, 2019, **299**, 28–32.

(185) C. Ammann, P. Meier and A. E. Merbach, *J. Magn. Reson.*, 1982, **46**, 319–321.

(186) A. L. Van Geet, *Anal. Chem.*, 1970, **42**, 679–680.

(187) A. S. Kiryutin, G. Sauer, A. V. Yurkovskaya, H.-H. Limbach, K. L. Ivanov and G. Buntkowsky, *J. Phys. Chem. C*, 2017, **121**, 9879–9888.

(188) J. W. Blanchard, B. Ripka, B. A. Suslick, D. Gelevski, T. Wu, K. Münnemann, D. A. Barskiy and D. Budker, *Magn. Reson. Chem.*, 2021, **59**, 1208–1215.

(189) D. A. Barskiy, K. V. Kovtunov, I. V. Koptyug, P. He, K. A. Groome, Q. A. Best, F. Shi, B. M. Goodson, R. V. Shchepin, M. L. Truong, A. M. Coffey, K. W. Waddell and E. Y. Chekmenev, *ChemPhysChem*, 2014, **15**, 4100–4107.

(190) F. Hill-Casey, A. Sakho, A. Mohammed, M. Rossetto, F. Ahwal, S. B. Duckett, R. O. John, P. M. Richardson, R. Virgo and M. E. Halse, *Molecules*, 2019, **24**, 4126.

(191) G. Buntkowsky, B. Walaszek, A. Adamczyk, Y. Xu, H. H. Limbach and B. Chaudret, *Phys. Chem. Chem. Phys.*, 2006, **8**, 1929–1935.

(192) M. E. Tadros and L. Vaska, *J. Colloid Interface Sci.*, 1982, **85**, 389–410.

(193) J. Matthes, T. Pery, S. Grü, G. Buntkowsky, S. Sabo-Etienne, B. Chaudret and H.-H. Limbach, *J. Am. Chem. Soc.*, 2004, **126**, 8366–8367.

(194) J. Matthes, S. Gründemann, G. Buntkowsky, B. Chaudret and H. H. Limbach, *Appl. Magn. Reson.*, 2013, **44**, 247–265.

(195) P. M. Richardson, R. O. John, A. J. Parrott, P. J. Rayner, W. Iali, A. Nordon, M. E. Halse and S. B. Duckett, *Phys. Chem. Chem. Phys.*, 2018, **20**, 26362–26371.

(196) J. D. Atwood, *Inorganic and Organometallic Reaction Mechanisms*, Wiley, Germany, 1997.

(197) J. S. Thompson and J. D. Atwood, *J. Am. Chem. Soc.*, 1991, **113**, 7429–7430.

(198) C. A. Miller, T. S. Janik, C. H. Lake, L. M. Toomey, M. R. Churchill and J. D. Atwood, *Organometallics*, 1994, **13**, 5080–5087.

(199) M. J. Burk and R. H. Crabtree, *Inorg. Chem.*, 1986, **25**, 931–932.

(200) H. Eyring, *J. Chem. Phys.*, 1935, **3**, 107.

(201) P. Atkins and J. de Paula, *Physical Chemistry*, Oxford University Press, Oxford, 2014.

(202) R. L. Rominger, J. M. McFarland, J. R. Jeitler, J. S. Thompson and J. D. Atwood, *J. Coord. Chem.*, 2007, **31**, 7–18.

(203) B. Gouilleux, B. Charrier, S. Akoka, F. X. Felpin, M. Rodriguez-Zubiri and P. Giraudeau, *Trends Analyt. Chem.*, 2016, **83**, 65–75.

(204) B. Procacci, S. S. Roy, P. Norcott, N. Turner and S. B. Duckett, *J. Am. Chem. Soc.*, 2018, **140**, 16855–16864.

(205) L. Bliumkin, R. Dutta Majumdar, R. Soong, A. Adamo, J. P. D. Abbatt, R. Zhao, E. Reiner and A. J. Simpson, *Environ. Sci. Technol.*, 2016, **50**, 5506–5516.

(206) A. M. R. Hall, R. Broomfield-Tagg, M. Camilleri, D. R. Carbery, A. Codina, D. T. E. Whittaker, S. Coombes, J. P. Lowe and U. Hintermair, *Chem. Commun.*, 2018, **54**, 30–33.

(207) K. A. M. Ampt, S. Burling, S. M. A. Donald, S. Douglas, S. B. Duckett, S. A. Macgregor, R. N. Perutz and M. K. Whittlesey, *J. Am. Chem. Soc.*, 2006, **128**, 7452–7453.

(208) D. Blazina, J. P. Dunne, S. Aiken, S. B. Duckett, C. Elkington, J. E. McGrady, R. Poli, S. J. Walton, M. S. Anwar, J. A. Jones and H. A. Carteret, *Dalton Trans.*, 2006, 2072–2080.

(209) S.-L. Henshaw, Ph.D. Thesis, University of York, 2016.

(210) V. Esen, Sağlam and B. Oral, *Renew. Sust. Energ. Rev.*, 2017, **77**, 1240–1250.

(211) S. Kumar Panigrahi and A. Kumar Mishra, *J. Photochem. Photobiol. C*, 2019, **41**, 100318.

(212) C. Hu, F. E. Muller-Karger and R. G. Zepp, *Limnol. Oceanogr.*, 2002, **47**, 1261–1267.

(213) S. Bouguet-Bonnet, F. Reineri and D. Canet, *J. Chem. Phys*, 2009, **130**, 234507.

(214) R. E. Mewis, K. D. Atkinson, M. J. Cowley, S. B. Duckett, G. G. Green, R. A. Green, L. A. Highton, D. Kilgour, L. S. Lloyd, J. A. Lohman and D. C. Williamson, *Magn. Reson. Chem.*, 2014, **52**, 358–369.

(215) C. P. Casey and E. W. Rutter, *Inorg. Chem.*, 1990, **29**, 2333–2335.

(216) D. A. Wink and P. C. Ford, *J. Am. Chem. Soc.*, 1985, **107**, 5566–5567.

(217) S. Hasnip, S. B. Duckett, D. R. Taylor and M. J. Taylor, *Chem. Commun.*, 1998, 923–924.

(218) J. Hore and R. W. Broadhurst, *Prog. Nucl. Magn. Reson. Spectrosc.*, 1993, **25**, 345–402.

(219) R. Kaptein, K. Dijkstra, F. Müller, C. G. Van Schagen and A. J. Visser, *J. Magn. Reson.*, 1978, **31**, 171–176.

(220) R Kaptein, K Dijkstra and K Nicolay, *Nature*, 1978, **274**, 293–294.

(221) R. J. Miller and G. L. Closs, *Rev. Sci. Instrum.*, 1981, **52**, 1876–1885.

(222) B. Koeppe, P. M. Tolstoy and H. H. Limbach, *J. Am. Chem. Soc.*, 2011, **133**, 7897–7908.

(223) P. M. Tolstoy, B. Koeppe, G. S. Denisov and H. H. Limbach, *Angew. Chem.*, 2009, **48**, 5745–5747.

(224) C. L. Lerman and M. Cohn, *Biochem. Biophys. Res. Commun.*, 1980, **97**, 121–125.

(225) J. E. Scheffler, C. E. Cottrell and L. J. Berliner, *J. Magn. Reson.*, 1985, **63**, 199–201.

(226) K. Maeda, C. E. Lyon, J. J. Lopez, M. Cemazar, C. M. Dobson and P. J. Hore, *J. Biomol. NMR*, 2000, **16**, 235–244.

(227) J. Wirmer, T. Kühn, H. Schwalbe, H Schwalbe, J Wirmer and T Kühn, *Angew. Chem. Int. Ed*, 2001, **40**, 4248–4251.

(228) I Kuprov and P. J. Hore, *J. Magn. Reson.*, 2004, **171**, 171–175.

(229) Y. Ji, D. A. DiRocco, J. Kind, C. M. Thiele, R. M. Gschwind and M. Reibarkh, *ChemPhotoChem*, 2019, **3**, 984–992.

(230) S. B. Duckett, M. W. George, O. S. Jina, S. L. Matthews, R. N. Perutz, X. Z. Sun and K. Q. Vuong, *Chem. Commun.*, 2009, 1401–1403.

(231) E. Stadler, M. Dommaschk, P. Frühwirt, R. Herges and G. Gescheidt, *ChemPhysChem*, 2018, **19**, 571–574.

(232) J. L. Clark and S. B. Duckett, *Dalton Transactions*, 2013, **43**, 1162–1171.

(233) C. Godard, P. Callaghan, J. L. Cunningham, S. B. Duckett, J. A. Lohman and R. N. Perutz, *Chemical Communications*, 2002, **2**, 2836–2837.

(234) O. Torres, J. A. Calladine, S. B. Duckett, M. W. George and R. N. Perutz, *Chem. Sci.*, 2014, **6**, 418–424.

(235) M. V. Câmpian, R. N. Perutz, B. Procacci, R. J. Thatcher, O. Torres and A. C. Whitwood, *J. Am. Chem. Soc.*, 2012, **134**, 3480–3497.

(236) E. Hecht, *Optics*, Pearson Education Limited, Harlow, 2017.

(237) D. Blazina, S. B. Duckett, T. K. Halstead, C. M. Kozak, R. J. K. Taylor, M. S. Anwar, J. A. Jones and H. A. Carteret, *Magn. Reson. Chem.*, 2005, **43**, 200–208.

(238) M. S. Anwar, D. Blazina, H. A. Carteret, S. B. Duckett, T. K. Halstead, J. A. Jones, C. M. Kozak and R. J. Taylor, *Phys. Rev. Lett.*, 2004, **93**, 040501.

(239) R. W. Adams, R. O. John, D. Blazina, B. Eguillor, M. C. Cockett, J. P. Dunne, J. López-Serrano and S. B. Duckett, *Eur. J. Inorg. Chem.*, 2022, **2022**, e202100991.

(240) L. Cronin, M. C. Nicasio, R. N. Perutz, R. G. Peters, D. M. Roddick and M. K. Whittlesey, *J. Am. Chem. Soc*, 1995, **117**, 10047–10054.

(241) D. Schott, C. J. Sleigh, J. P. Lowe, S. B. Duckett, R. J. Mawby and M. G. Partridge, *Inorg. Chem.*, 2002, **41**, 2960–2970.

(242) H. Günther, *Angew. Chem. Int. Ed. Engl.*, 1972, **11**, 861–874.

(243) M. Carravetta and M. H. Levitt, *J. Am. Chem. Soc.*, 2004, **126**, 6228–6229.

(244) A. M. Olaru, S. S. Roy, L. S. Lloyd, S. Coombes, G. G. Green and S. B. Duckett, *Chem. Commun.*, 2016, **52**, 7842–7845.

(245) M. H. Levitt, R. Freeman and T. Frenkiel, *J. Magn. Reson.*, 1982, **47**, 328–330.

(246) M. H. Levitt and R. Freeman, *J. Magn. Reson.*, 1981, **43**, 502–507.

(247) M. E. Halse, B. Procacci, R. Perutz and S. B. Duckett, *Faraday Discuss.*, 2019, **220**, 28–44.

(248) B. A. Rodin, K. F. Sheberstov, A. S. Kiryutin, L. J. Brown, R. C. Brown, M. Sabba, M. H. Levitt, A. V. Yurkovskaya and K. L. Ivanov, *J. Chem. Phys.*, 2019, **151**, 234203.

(249) S. J. Elliott, O. Cala, Q. Stern, S. F. Cousin, D. Eshchenko, R. Melzi, J. G. Kempf and S. Jannin, *Phys. Chem. Chem. Phys.*, 2021, **23**, 9457–9465.

(250) N. K. Hermkens, N. Eshuis, B. J. Van Weerdenburg, M. C. Feiters, F. P. Rutjes, S. S. Wijmenga and M. Tessari, *Anal. Chem.*, 2016, **88**, 3406–3412.

(251) L. Sellies, I. Reile, R. L. Aspers, M. C. Feiters, F. P. Rutjes and M. Tessari, *Chem. Commun.*, 2019, **55**, 7235–7238.

(252) A. S. Kiryutin, A. V. Yurkovskaya, H. Zimmermann, H. M. Vieth and K. L. Ivanov, *Magn. Reson. Chem.*, 2018, **56**, 651–662.

(253) P. TomHon, E. Akeroyd, S. Lehmkuhl, E. Y. Chekmenev and T. Theis, *J. Magn. Reson.*, 2020, **312**, 106700.

(254) D. T. Pegg, D. M. Doddrell and M. R. Bendall, *J. Magn. Reson.*, 1983, **51**, 264–269.

(255) J. R. Taylor, *Introduction to Error Analysis*, University Science Books, Sausalito, 1997.

(256) P. B. Chock and J. Halpern, *J. Am. Chem. Soc*, 1966, **88**, 3511–3514.

(257) R. A. Sanchez-Delgado, J. S. Bradley and G. Wilkinson, *J. Chem. Soc., Dalton Trans.*, 1976, 399–404.

(258) S. P. Nolan, T. S. R. Belderrain and R. H. Grubbs, *Organometallics*, 1997, **16**, 5569–5571.

(259) M. T. Bautista, J. Zubkowski, A. Sella, E. P. Cappellani, C. T. Schweitzer, R. H. Morris and S. D. Drouin, *J. Am. Chem. Soc.*, 1991, **113**, 4876–4887.

(260) N. Ahmad, S. D. Robinson and M. F. Uttley, *J. Chem. Soc., Dalton Trans.*, 1972, 843–847.

(261) P. S. Hallman, B. R. McGarvey and G. Wilkinson, *J. Chem. Soc. A*, 1968, 3143–3150.